UNDERSTANDING, MODELING AND PREDICTING HIDDEN SOLDER JOINT SHAPE USING ACTIVE THERMOGRAPHY

A Dissertation

by

JOSE BENJAMIN DOLORES GIRON PALOMARES

Submitted to the Office of Graduate Studies of
Texas A&M University
in partial fulfillment of the requirements for the degree of

DOCTOR OF PHILOSOPHY

May 2012

Major Subject: Mechanical Engineering

Understanding, Modeling and Predicting Hidden Solder Joint Shape

Using Active Thermography

UNDERSTANDING, MODELING AND PREDICTING HIDDEN SOLDER JOINT SHAPE USING ACTIVE THERMOGRAPHY

A Dissertation

by

JOSE BENJAMIN DOLORES GIRON PALOMARES

Submitted to the Office of Graduate Studies of
Texas A&M University
in partial fulfillment of the requirements for the degree of

DOCTOR OF PHILOSOPHY

Approved by:

Chair of Committee,	Sheng-Jen Hsieh
Committee Members,	Jorge Alvarado
	Je-Chin Han
	Chii-Der Suh
Head of Department,	Jerald A. Caton

May 2012

Major Subject: Mechanical Engineering

ABSTRACT

Understanding, Modeling and Predicting Hidden Solder Joint Shape
Using Active Thermography. (May 2012)
Jose Benjamin Dolores Giron Palomares, B.A.; M.S., The University of Guanajuato
Chair of Advisory Committee: Dr. Sheng-Jen Hsieh

Characterizing hidden solder joint shapes is essential for electronics reliability. Active thermography is a methodology to identify hidden defects inside an object by means of surface abnormal thermal response after applying a heat flux. This research focused on understanding, modeling, and predicting hidden solder joint shapes. An experimental model based on active thermography was used to understand how the solder joint shapes affect the surface thermal response (grand average cooling rate or GACR) of electronic multi cover PCB assemblies. Next, a numerical model simulated the active thermography technique, investigated technique limitations and extended technique applicability to characterize hidden solder joint shapes. Finally, a prediction model determined the optimum active thermography conditions to achieve an adequate hidden solder joint shape characterization.

The experimental model determined that solder joint shape plays a higher role for visible than for hidden solder joints in the GACR; however, a MANOVA analysis proved that hidden solder joint shapes are significantly different when describe by the GACR. An artificial neural networks classifier proved that the distances between experimental solder joint shapes GACR must be larger than 0.12 to achieve 85% of accuracy classifying. The numerical model achieved minimum agreements of 95.27% and 86.64%, with the experimental temperatures and GACRs at the center of the PCB assembly top cover, respectively. The parametric analysis proved that solder joint shape discriminability is directly proportional to heat flux, but inversely proportional to covers

number and heating time. In addition, the parametric analysis determined that active thermography is limited to five covers to discriminate among hidden solder joint shapes. A prediction model was developed based on the parametric numerical data to determine the appropriate amount of energy to discriminate among solder joint shapes for up to five covers. The degree of agreement between the prediction model and the experimental model was determined to be within a 90.6% for one and two covers. The prediction model is limited to only three solder joints, but these research principles can be applied to generate more realistic prediction models for large scale electronic assemblies like ball grid array assemblies having as much as 600 solder joints.

DEDICATION

To my mother

ACKNOWLEDGEMENTS

I would like to thank my committee chair, Dr. Hsieh, and my committee members, Dr. Alvarado, Dr. Han, Dr. Suh, and Dr. Fang, for their guidance and support throughout the course of this research.

Thanks also to my friends and colleagues and the department faculty and staff for making my time at Texas A&M University a great experience. I also want to extend my gratitude to the Mexican National Council of Science and Technology, which provided the financial support.

Finally, thanks to my mother and father for their encouragement and to my wife for her patience and love.

NOMENCLATURE

a_i	Neural network hidden layer output i
ANN	Artificial neural network
ANOVA	Analysis of variance
AOI	Automatic optical inspection
A_{solder}	Base surface area of the solder joint
AXI	Automatic x-ray inspection
BGA	Ball grid array
BPNN	Back propagation neural network
C_i	Grand average cooling rate at i·20 s of cooling
C_N	Number of covers for the PCB assembly
c_{pi}	Specific heat for material i
CR_{A-B}	Grand average cooling rate difference between closest or contiguous classes A and B
d	Number of dimensions
df_h	Hypothesis degrees of freedom
df_e	Error degrees of freedom
D_{A-B}	Discriminability index between contiguous curves or classes A and B
e_{ij}	Error for response variable j and class i
E_{ij}	Relative error from grid i to grid j
FEA	Finite element analysis
F_{i-j}	View factor from surface i to surface j
f_i	Finite element solution for grid i
F	Beta distribution
GACR	Grand average cooling rate
GCI_{ij}	Grid constant index from grid i to grid j
h	Convection coefficient of heat transfer

h_r	Radiation coefficient of heat transfer
h_T	Total coefficient of heat transfer
H_F	Heat flux at the top cover of the finite element model
H_i	Average heating rate at i·20 s of cooling
H_{oi}	Thermal irradiation for isothermal surface area i
H_0	Null hypothesis
HR_i	Heating rate at i·20 s of cooling
H_T	Heating time during heating process for finite element model
I	Total number of classes
IC	Integrated circuit
J_i	Radiosity for isothermal surface area i
k	Thermal conductivity
k_i	Thermal conductivity for material i
L	Characteristic length
n_i	Total number of observations for class i
n	Overall number of observations
MANOVA	Multivariate analysis of variance
MCM	Multi chip packages
p	Total number of response variables
P	Probability
PC	Personal computer
PCB	Printed circuit board
PGA	Pin grid array
p_i	Polynomial constant coefficient i
PWB	Printed wiring board
Q	Uniform irradiation per unit area
Q_o	Constant heat flux o
Q_{cover}	Total amount of energy provided to the top cover
q_i	Heat flux for isothermal surface area i

r_j	Polynomial constant coefficient j
r_{ij}	Refinement factor from grid i to grid j
RBF	Radial basis function
RC_{i-j}	Average of the rate of change in grand average cooling rate from i to j
RTD	Resistance temperature detector
R^2	Coefficient of determination
$\vec{r}$	Vector position
S_{cover}	Top cover horizontal face surface area
S_i	Section i of the copper wire
S_{solder}	Lateral surface area of the solder joint
$SS_{between}$	Summation of variances between classes
SS_{within}	Summation of variances within classes
SAM	Scanning acoustic microscopic
SVM	Support vector machine
t	Time
T_{A-B}	Average temperature difference between closest or contiguous classes A and B
T_{solder}	Temperature at the solder joint surface
tansig	Hyperbolic tangent sigmoid transfer function
TDR	Time domain reflectometry
T_i	Average temperature at i·20 s of cooling
T_∞	Ambient temperature
trainrp	Resilient backpropagation training function
traincgb	Powell-Beale conjugate gradient backpropagation training function
trainbfg	Quasi-Newton backpropagation training function
trainlm	Levenberg-Marquardt backpropagation training function
u_i	Representative grid size for grid i
w	Order of accuracy
w_i	Neural network weight for input i

WinTES	Windows thermal evaluation software
X_i	Neural network input i
x, y, z	Cartesian coordinates
$\vec{x}$	Vector of predictors
y_i	Neural network output i
y_{ij}	Response variable j for class i
$\bar{y}_i$	Response average for class i
$\bar{y}$	Overall response average
Y	Response variable
ΔT_{60}	Average temperature difference between experimental and numerical models at 60° solder joint position
ΔT_{90}	Average temperature difference between experimental and numerical models at 90° solder joint position
ΔT_{120}	Average temperature difference between experimental and numerical models at 120° solder joint position
ΔCR_{60}	Grand average cooling rate difference between experimental and numerical models at 60° solder joint position
ΔCR_{90}	Grand average cooling rate difference between experimental and numerical models at 90° solder joint position
ΔCR_{120}	Grand average cooling rate difference between experimental and numerical models at 120° solder joint position
ε_i	Thermal emissivity for isothermal surface area i
ξ	Linear regression disturbance term
γ	Cone angle
σ	Stefan-Boltzmann constant
λ_v	Wilks criterion eigenvalue v
ρ_i	Density for material i
μ_i	Response mean for class i

θ	Temperature difference with respect to the ambient temperature
$\tau_{A\text{-}B}$	Time required to achieve a zero temperature difference between curves or contiguous classes A and B
φ_{ij}	Difference between finite element solution i and finite element solution j
Λ	Wilks lambda value

TABLE OF CONTENTS

Page

Page

LIST OF FIGURES

FIGURE Page

FIGURE Page

FIGURE Page

LIST OF TABLES

TABLE Page

TABLE Page

TABLE Page

TABLE Page

1. INTRODUCTION

1.1. Motive: The Importance of Proper Solder Joints

There are diverse electronic products that made human life more comfortable. Electronics applications are radio, television, satellites, control systems, micro devices like watches, computers, and diverse appliances. Electronic products are composed by various printed circuit boards that interconnect multiple electronic components: capacitors, resistors, integrated circuits, etc. Electronic components are attached to the PCB by means of two different methods (surface mount technology and through hole technology) that used a molten metal solder to generate a solder joint between the electronic component and the PCB. An appropriate solder joint is vital for the correct function of electronic products, because every single component in the PCB has a specific task that affects the correct behavior of the other components. The next few subsections will expose in a little more detail the importance of proper solder joints, the problems encounter to assure a proper solder joint between the PCB and the component, and the existing methodologies to assure solder joint integrity. Finally, Section 1.1.4 summarizes the nature of the problem to achieve an adequate solder joint.

1.1.1. Solder Joint Reliability

Electronic products reliability is one of the most important tasks of the electronics industry. Reliability is the capability of a product to function as intended for a specified amount of time under specified conditions. Electronic products failures lead to financial losses caused by the loss of market share due to damage confidence, increase in insurance rates, cost to replace parts, claims for damages, among others [1-3]. In order to improve electronics reliability, electronic products are tested for defects after assembly.

This thesis follows the style of Nondestructive Testing and Evaluation.

In particular, chip solder joint integrity is one of the most important factors for the proper reliability of electronics. According to a study conducted on 200 Surface mounted/leaded assemblies with a total of 552,600 parts placed, the largest defects found were: open solder joints (71%), insufficient solder (23%), and missing components (6%) [4]. Therefore, it is important to assure a good solder shape that guarantees a correct solder joint between the chips and printed circuit boards. An adequate solder joint shape is very important because a poor solder shape can lead to early cracks, abnormal temperatures, and of course unexpected failures and malfunctions in electronic products [4-8].

1.1.2. Popularity of Multi-PCB Integrated Electronics

With the shrinking of electronics packages and the need of more compact and powerful assembled printed circuit boards, managing of space on the printed circuit board is vital. A very common technique used in microelectronics is the stacking of components that makes possible a better management of space by using the third dimension. Stacking is not only done in the component level but also in the board level [9-13]. Stacking of boards saves on space just like tall buildings take advantage of the air space when there is not more available space at the ground level. Increasing speeds in the backplanes (printed circuit board that connects several connectors in parallel) are gotten by connecting multiple printed circuit boards together [14]. In addition, stacking of boards makes the expandability of boards as easy as a plug in task. Embedded systems (computer systems designed to do one or few dedicated systems) are usually composed of multiple parallel stacked boards (mezzanine boards) to reduce cost and product size. Applications of board stacking include: machine tool-computer numerical control, ultrasound equipment, measurement equipment, LCD television, computerized tomography scanner, mobile phone, digital cameras, copy machine and laser printer, notebook PC, PDA, DVD recorder, Router and LAN, and portable medical devices [15]. Major companies as 3M, Hirose, and SAMTEC keep working in the development of

connectors that make possible the integrity of signals between board to board applications, reducing of size of connectors, increasing of pitch between connector (to accommodate tall components like heat sinks), and connector reliability [16-18]. However, the use of multiple boards keeps the solder joint hidden from view for inspection, in special, when pitch between boards is small.

1.1.3. Difficulty and Significance of Hidden Solder Joints

As explained before, it is important to assure a good solder shape that guarantees a correct solder joint between the chips and printed circuit boards. Multiple methods have been used to detect chips solder joint quality after its assembly on PCB. However, the growing used of surface mount technology and multi-PCB integrated electronics (board stacking) keep solder joints hidden from view making methodologies like Automatic Optical Inspection (AOI) [19-22] not adequate (i.e. AOI relies completely in the visibility of the solder joints). Not only the chip surface keeps hidden the solder joints, but also the high amount of solder joints and small pitch among them made even difficult to see the inner solder joints for lateral inspections. Detection methods like X-ray [23-29], scanning acoustic microscopic (SAM) [26, 30-39], and laser ultrasound systems [40-43] that can detect joints hidden from view have grown in importance, but there are some limitations in these inspection methods [22, 41, 43]: x-ray is slow to implement, can not detect open solder joints (solder joint is not in contact with one of the surfaces), and needs human interpretation of images; SAM is slow and destructive for some assemblies because the sample must be submerge in a liquid; laser ultrasound needs multiple inspection points for large chips and can detect only missing solder joints or more than two adjacent open solder joints.

1.1.4. Problem Statement

Solder joint integrity is one of the most important factors for the proper reliability of electronics. However, the growing use of surface mount technology and Multi-PCB integrated electronics (board stacking) keep solder joints hidden from view making methodologies like machine vision obsolete (i.e. machine vision relies completely in the visibility of the solder joints). Multiple methods have been used to detect electronic components solder joint quality after assembly, but there are limitations in these inspection methods. An approach easy to perform, low cost, and automated (i.e. no human interpretation should be required to decide if there is a variation in the solder joint shape) to characterize hidden solder joint shape variations is essential to improve electronic products reliability.

1.2. Infrared Thermography and Hidden Solder Joint Characterization

Infrared thermography is a technique that has been widely used to characterize objects and even subsurface hidden defects. Among the current applications for infrared thermography are: detection, diagnosis and prognosis of breast cancer [44, 45], study of skin toxicities and tumor control in melanoma treatments [46], plant species identification [47], solar physics [48], astronomy [49], civil engineering [50], athmospherical wind velocity detection [51], maritimal surveillance systems [52], imaging missile seekers [53], gas detection [54, 55], and nondestructive detection in multiple fields of technology [56-82]. From all of the applications mentioned, nondestructive detection is what makes very interesting infrared imaging as a tool for the inspection of hidden solder joints. Thermography base nondestructive methodologies are successfully used to characterize not only hidden defects sizes but also their depth by means of the thermal behavior of the surface of gears, transpiration panels, car bonnet, glass platelet, tiles, Plexiglas, carbon fiber reinforce plastics, among other materials [57, 59, 60, 64, 66, 70, 73, 75, 77, 79, 83]. Some attempts have been done to detect abnormal

thermal behavior in electronics by means of infrared imaging too [56, 62, 79, 84-88]. Some of the most important researches on electronics are:

- Wiecek *et al.* [88] used a thermographic camera to characterize the solder thickness on printed circuit boards by means of its thermal transient response; this thermal transient response varies with the solder thickness as a consequence of the thermal conductivity and capacity.
- Chai *et al.* [84] were able to detect solder joint cracks in flip chip packages by means of infrared thermal imaging; the solder cracks were detected as clear high temperature areas in the thermal images caused by an increase in thermal resistance.
- King *et al.* [86] showed anomalous temperature spots in infrared images of photovoltaic systems; these anomalous temperatures were due to resistive or failed solder bonds, short circuits, resistive battery terminals, and shunts.
- Breitenstein *et al.* [56] detected current leakage in integrated circuits, such current leakage are heat sources shown as high temperature regions in infrared images.
- Artificial solder defects in ball grid array electronic components were detected by Varis *et al.* [87], but the abnormal thermal signature was detected only retiring a thick plastic cover from the electronic components.
- Finally, Hsieh *et al.* [85] characterized the thermal profile on a chip under vibration stress; spots more susceptible to vibration stress presented an evident increase in temperature that was monitored by means of infrared thermography.

As seen in the previous paragraph, infrared thermography has been successfully used to detect subsurface defects in several applications. Thermography is a technique that takes advantage of the capacity of bodies to emit radiation in the infrared range (invisible to human eye with a wavelength in the range 0.75-100 μm) to inspect the internal structure of materials; such radiative energy is captured and transformed into a temperature

distribution by means of an infrared camera (the measurement wavelength range for common cameras is from 3-14 μm; a wide description of the infrared cameras can be fount at [89]). Thermography can be divided in two kinds, active and passive thermography. Thermography is called passive thermography if no external energy is provided to the object under study. On the contrary, active thermography requires using an external source of energy to generate a thermal variation in the object under study. For example, if heat is applied on the surface of a plate with air voids inside, the thermal waves will travel fast until they reach a void that slows down the heat diffusion; this behavior will be captured in the surface thermal distribution as a higher temperature region. There are different kinds of external sources (optical, mechanical, electromagnetic, etc.), but a halogen lamp (optical) is the most simple to apply [58, 61, 67, 69]. The most expensive element is the camera, but it is small, light, and can be adapted to a total automated system to analyze the thermal images. Therefore, active thermography is a very useful tool to show not only visible defects but also hidden defects, because the anomalous temperature caused by defects affect the areas surrounding them. In particular, active thermography seems a good option to characterize solder joint shapes in electronics. If an external heat source is apply to the board surface, the heat will diffuse in a different rate in the regions where the solder joint is in perfect contact from the regions where the solder joint is in partial contact or no contact at all; this variation in the diffusion rate will cause a surface temperature variation over time (temperature variation that can be capture by means of the infrared camera) that will depend on the solder joint shape. This variation in the temperature over time is called heating rate and is defined by the next expression:

$$HR_i = \frac{T_i - T_{i-1}}{\Delta t} \qquad i = 1, 2, \ldots, n\text{-}1 \tag{1}$$

where i denotes the number of thermal image, n is the total number of images captured, Δt is the interval of time between thermal images, and T is the temperature of a region of

interest in the thermal image. Another useful variable is the grand average heating rate that is defined in terms of the heating rate by the next expression:

$$H_i = \frac{\sum_{k=1}^{i} HR_k}{i} \qquad i = 1, 2, \ldots, n\text{-}1 \tag{2}$$

Hsieh *et al.* [85] have already shown the usefulness of using heating rate to characterize thermal processes. This research will investigate grand average heating rate usefulness to characterized hidden solder joints.

In summary, active thermography can be used to characterize solder joint shapes by means of its grand average heating rate. It is relatively easy to implement, not harmful for technicians, portable, low cost, and automated; these are characteristics suitable for a good nondestructive detection system. However, the capabilities of the technique to characterize solder joints shapes hidden below the chip body must be widely investigated.

1.3. Objective

The objectives of this research are to understand, model, and predict hidden solder joint shapes in order to achieve better electronics reliability. To understand how the solder joint shapes affect the component surface transient temperature after applying a heat flux, an experimental model will be developed by means of a low cost but effective active infrared thermography nondestructive experimental setup. Transient thermal behavior will be characterized by means of grand average cooling rate (grand average cooling rate is the additive inverse of grand average heating rate). The solder joint shapes will be assumed as cones with the same volume and three different angles (60°, 90°, and 120°) to account for the solder joint integrity (60° represents an adequate solder joint). As the solders are attached to the same board, interaction among solders will be neglected. In

addition, solder joints thermal properties are identical. These solder joints will be visible and hidden by one and two covers. The addition of the covers will assess how the grand average cooling rate signal strength will be affected as the solder joints are blocked by more objects, while the absent of cover will serve as a benchmark criterion. Ten different electronic board prototypes and 15 experiments will be performed in an active thermography detection system. Five of the experiments will be performed on boards without a cover, while the rest of the experiments will be performed on boards with one and two covers. The cover and the PCB are considered made of the same material. The experiments will be performed inside an environmental chamber with two sections (heating and cooling sections). The experimental procedure will consist of heating the PCB assembly by a halogen lamp inside the heating section, moving the PCB assembly into the cooling section, and monitoring the thermal transient behavior during the cooling process by means of an infrared camera. The thermal irradiation from the lamp will be considered uniform. A multivariate analysis of variance (MANOVA) will be performed on the experimental data to determine if the solder joint geometries are statistically different when described by the grand average cooling rate. After proving that the solder joint shapes can be described by the grand average cooling rates, classifying models will be developed to test and establish the capability of grand average cooling rate to describe the different hidden solder joint shapes as the PCB assembly complexity increases.

After the experimental model establishes the relationship between the different solder joint shapes and grand average cooling rate, a numerical model will be used to simulate the heat transfer phenomena during the application of the active thermography technique. Sources of uncertainties during active thermography application (e.g. uneven heating, sample movement, and dead time between heating and cooling processes) will not be modeled. First, the numerical model will be validated with respect to the experimental model; second, a numerical parametric analysis will be performed to further investigate the limitations and extend the applicability of active infrared thermography to

characterize hidden solder joint shapes by means of grand average cooling rate. The parameters to vary will be:

- Number of covers. The number of covers blocking the solder joint shapes will diminish the strength of the grand average cooling rate signal.
- Amount of heat flux provided. It is expected that increasing the number of covers will increase the amount of heat flux needed to reach an adequate solder joint shape characterization.
- Heating time. As the heat flux and number of covers vary, the time needed to reach an adequate solder joint shape characterization will vary too.

The number of covers is constrained by the nature of the problem (multi cover PCB assembly), while the heating time is constrained by the speed of the active infrared thermography inspection required. Therefore, as a final step, a prediction model will be developed to predict the optimum amount of heat flux required to achieve an adequate hidden solder joint shape characterization in function of the number of covers and heating time. In summary, this research will provide the electronics industry with the knowledge to develop better infrared thermography techniques to address hidden solder joint shapes quality inspection and improve electronics reliability.

1.4. Sections Description

Sections are organized as follows:

- Section 2 presents the literature review on electronic solder joints characteristics, existing solder joint characterization methodologies, infrared thermography as a methodology to describe surface and sub-surfaces defects or shapes, neural networks as a classification methodology, and numerical methodologies to

characterize the thermal phenomena involved in the application of infrared thermography.

- Section 3 describes the methodologies applied to understand and characterize hidden solder joint shapes.
- Section 4 shows and analyzes the experimental and numerical data describing hidden solder joint characterization.
- Finally, Section 5 presents a summary, conclusions, and future work.

2. LITERATURE REVIEW

2.1. Solder Joint [90-93]

Solder joint characteristics depend mainly on the objects being joined; in the case of electronics, the objects being joined are the printed circuit board and the integrated circuit chip (one of the most important electronic component). Subsection 2.1.1 describes the relationship between the solder joint and the PCB, while subsection 2.1.2 exposed the relationship between the solder joint and the integrated circuit chip.

2.1.1. Solder Joint and Printed Circuit Board

A printed circuit board (PCB) or printed wiring board (PWB) provides mechanical support as well as electrical interconnections for electronic components. Printed circuit board technology include single-side boards, double side plated through hole boards, multilayer boards, surface mount technology, and flexible. Printed circuit boards are designed and fabricated as layered structures. Typically, a PCB is composed of conducting layers made of thin copper foil, insulated dielectric layers that are laminated together with epoxy resin prepreg, and a coating solder mask green in color. There are two techniques to add electronic components to the PCB: surface mount technology and through hole technology. In through hole technology, leaded components are inserted in holes. In the case of surface mount technology, the components are placed on pads on the outer surface of the PCB. However, a molten metal solder is used to fix the component in both techniques. In recent years, surface mount technology is widely used because surface mounted devices are smaller than the through hole component version, but several PCB use both kind of components. Through hole technology is mainly used for big components like electrolytic capacitors or semiconductors in large packages. The solder joint shape that attaches the component to the PCB depends mainly on the component; single surface mount components sizes are in the range of 0.4×0.2 mm

(resistor) to 19×19 mm (aluminum capacitors). Solder joints are particularly small in BGA integrated circuit semiconductors where solder ball joints arrays are used to attached the component to the board (solder ball joints pitch is usually 1 mm). Next section gives details about the most common integrated circuit semiconductors used up to date.

2.1.2. Solder Joint and Integrated Circuit

Integrated circuit chips perform logic and/or memory operation in a PCB assembly. IC are created bipolar, bipolar-complementary MOS, gallium arsenide, and MOS (metal-oxide semiconductor); being the most popular MOS. Integrated circuits (IC) can be attached directly to the PCB or by means of a substrate or carrier that interconnects the chips and provide a bridged to larger widths and spacings in the PCB. The IC is packaged in order to be used in electronic assemblies. The packaging has the function of protecting it from the environment and providing electrical connections for a substrate or PCB, while keeping a good dissipation of the heat generated. Packaging materials are usually plastics or ceramics. Ceramics possess a combination of electrical, thermal mechanical and dimensional stability properties; however, plastic offers many advantages like weight, performance cost, reliability, and availability (97% of the worldwide packaging material used is plastics). IC packaging can be divided in two categories: single chip packaging and multi chip packaging. Single chip packaging can be divided in the next categories: in-line, small outline, quad surface mount, and grid array. Multi chip packages can be divided in MCM-L, MCM-C, and MCM-D. Inline packages can be single or double and use through hole mount technology with 2.54 mm pitch between its side body leads. Small outline packages are surface mount technology devices with leads on two sides of the body (standard pitch among leads is 1.27 mm). Quad surface mount packages have a larger body than small outline package and leads in the four sides of the body; the pitch among leads is usually in the range of 0.65 to 0.2 mm. Array packages are characterized by pins or pads place on a regular array on the

package body. The array packages can be pin grid array (PGA) and ball grid array (BGA). PGA packages have pins arrange across the bottom of its body. PGA packages are mounted by through hole technology with 100×100 mil or staggered 50×100 mil centers. BGA packages use solder balls in the bottom part of their body instead of pins. This solders balls are cheaper than pins and are surfaced mounted. Solder ball pitches are usually 1 mm and counted as much as 600 balls. BGA packages are replacing quad surface mount packages because they are low cost, 20% smaller, and have no leads. Leads pitch for QFP are as small as 0.5 mm making leads as small as 0.1 mm, thin, and fragile. On the other hand, solder balls can not be inspected visually because the solders are high on count and they are hidden by the package making difficult the solder joint quality inspection.

Multi chip modules interconnect and package more than one integrated circuit chip. This leads to a considerable reduction in size. MCM-L packages are constructed with printed circuit board laminates; interconnections are made from copper and created by photo imaging; vias are created by platting and electroplating; integrated circuits are attached through wire bonding or flip chip process. MCM-C packages are made with ceramics or glass ceramics as substrate; conductors and vias are fireable metal materials like tungsten or molybdenum. In MCM-D, integrated circuits are deposited on the substrate using thin film technology. Vias are made of copper or nickel. MCM-D are high performance modules used in military and space applications.

The solder joint shape depends largely in the component and the kind of mounting technology used to attach the component. In surface mount technology, the components are to place on flat pads without holes (pads made of tin-lead, silver, or gold copper); pads that are called solder pads. A solder paste, composed of flux and tiny solder particles, is first applied to the solder pads with a stencil using screen printing process. After solder paste placement, numerical control pick-and-place machines place the components on the PCB. In the next step, the boards, components, and solder paste are

preheated and heated just enough to melt the solder particles; the molten solder surface tension keeps the components in place and aligned the components in well designed solder pads. Finally, the boards are inspected for missing components or misaligned components. In the case of through hole technology, the components leads are inserted into holes drilled on the PCB and soldered to the pads. Although this technique offer a strong mechanical bond, the additional drilling made this process more expensive and limit the availability of routing area for signal traces as holes have to go through all the PCB thickness. Shapes of the final solder joint depend on the component leads. Solder joint shape can be though as a triangular prism on rectangular leads for surface mount technology, conical in through hold technology, and spheroid on BGA. Solder joint shapes deviating from these morphologies are related to poor solder, excessive solder, and no solder. Solder joint sizes will depend on the component size.

2.1.3. Summary

Integrated circuit components are attached to PCB by means of two techniques: surface mount technology and through hole technology. Although through hole technology has been almost displaced by surface mount technology, through hole technology is still been used for big components. Solder is used to attach the integrated circuit components to the PCB in both mounting techniques. BGA components are one of the most used electronic components in actuality. These components are attached to the PCB by means of solder balls that are high on count and very small making visual inspection almost impossible. The shape of the final solder joint depends on the component and component leads. Solder joint shape can be modeled as a triangular prism on rectangular leads for surface mount technology, conical for through hold technology, and spheroid for BGAs. Solder joints are in a wide range of sizes down to 0.1 mm depending on the component attached.

2.2. Inspection Methods

Multiple methods have been used to detect hidden solder defects on electronics. Among the most important are: automatic optical inspection, automatic X-ray inspection, laser ultrasound, and infrared thermography. Next subsections, will present some of the most significant investigations existing in relation to this inspection methodologies.

2.2.1. Automated Optical Inspection (AOI)

Automated optical inspection is a very important methodology to inspect microelectronics in the integrated circuit and PCB levels. AOI consist of comparing images obtained by multiple optical cameras with image references of good components called templates. Several illumination systems are tested to improve the images quality. In particular, automated optical inspection is widely used to asses the right solder joint and position of visible components after its assembly on boards. Its capacity to speed the detection of improper solder joints and characterize them is evident, and has surpassed that of traditional contact detection techniques or human inspection [94]. However, its applicability for solder joint quality in components hiding the solder joints is completely impossible. Its role is only for solder balls quality inspection on BGAs before its assembly on PCB or visible components on PCB after assembly. For example, Cao *et al.* [20] used a binocular machine vision system to characterize solder balls in BGA before assembly. Their methodology consisted of illuminating the BGA chip with LED ring lights while a CCD camera capture ranged images from certain side orientation. Ranged images were analyzed by means of the Otsu method to obtain the geometrical size. In order to determine oversized or undersized balls, the obtained dimensions were compared with the specification sizes. The positions of the pins were determined by comparing centroid position. Co planarity was assessed by determining the solder balls height. However, no information about repeatability is provided. The camera should be located at the right position and, as the authors explained, the margin of field of view is

fuzzy. Considering that this technique is completely base on the field of view of the balls this is a major drawback. In a similar investigation, Gao [19] used two images of a BGA connector with the same light source but different light angles to characterized the solder joint balls. They were able to obtain a precision measurement of the balls of 1%. However, these techniques need to have a view of the balls and it is only to check the quality of the solders balls before their assembly on the PCB. A complete description of their discrimination methodology is given in their work [19, 20].

Koh *et al.* [95] studied the use of a statistical learning-based object recognition algorithm to identify an appropriate component position in surface mounted technology. However, they only addressed the improvement of the components classification by proposing a new methodology to discriminate and analyze the resistors components images. No experiments were performed. In another interesting research on surface mount components with visible solder joints, Yun *et al.* [96] proposed a circular illumination technique to obtain a 3D shape of the solders. Circular blue, red and green light lamps were used. After obtaining the images by means of a CCD camera, the circular paths on the solder surface were used to infer the 3D characteristics of the solder joint. Solder joints observed in the images were divided by categories: excessive, good, insufficient, and not solder. Characteristic features of the solder joint images were determined base on the intensity of light value and percentage of highlights. The classification of the solder joint quality was made by means of support vector machines. A six dimensional feature vector was used as input for the classifier. Size of training data was addressed. 402 solder joints were collected from PCBs. 201 were used for training and 201 for testing. The accuracy of classification obtained were 96.07%, 98%, 100%, and 100% for the excessive, good, insufficient, and no solder classes, respectively. The support vector machines classifier was compared with k-means (4 classes) and back propagation classifiers showing a better accuracy. Another effort to extend the AOI inspection of surface mounted components from 2D imaging to 3D imaging was performed by Hong *et al.* [97]. Their methodology was based on a phased-measuring profilometer method

and a stereo vision system. The distortion of fringes (one of the alternate light and dark bands produce by diffraction or interference) on the electronic components surfaces is used as a characterization of the object morphology. The stereo vision cameras were used to develop images to characterize the height of the surface mount components at different depths forming a 3D shape of them. Heights were calculated with 10 μm accuracy. Calculated dimensions were compared with two coordinate measuring machines (contact and noncontact types) proving similar values. In a research more related to solder joint shape, Kong [98] reconstructed the solder joint shape by means of shape from shading technology. Shape from shading determines the shape from a gradual variation of the shading from two or more 2D images. The technique success is based on the different lightness between the component and the solder joint. The images were process on a pixel level methodology. Three different illumination directions were used and four images were used to reconstruct the solder joint shape on surface mounted resistors and capacitors. 3D graphics of the solder joint shape are presented. In a different research trend, Ayoub [99] addressed the correct flux deposition just before the components placement. As the authors explained, some of the defects on the final assembly were caused by poor flux alignment with the intended pads, insufficient thickness/amount of the flux material, excessive amount of flux, or from smearing. The authors proposed the use of an ultraviolet illumination system because the common systems are not able to image the flux material correctly. Such ultraviolet based AOI system was apply in-line inspection with success for three years keeping up with the production line speed and a low false call rate. Further reading to exemplify the use of AOI on the IC level and its applicability for on line inspection to increase the yield production can be found at [100] and [94], respectively.

As seen in the investigations described, AOI is a valuable inspection methodology for visible surface mount technology components, and solder balls quality before its assembly on PCBs. Attempts to use the methodology to characterized hidden solder

shapes are impossible and the great majority of efforts are to improve the AOI capability to classify the visible components and solder joint shapes, and illumination systems.

2.2.2. Automated X-Ray Inspection (AXI)

X-ray imaging is the most widely nondestructive technique used up to date. X ray imaging has been used as an important medical diagnosis tool since is early discovery in 1985. There are two kinds of X-ray imaging techniques: radiography and tomography; both techniques use a highly penetrating X-rays to record the internal structure of an object. Images can be detected by film or in real-time by video signal conversion. The object is put in contact with the film in radiography. X-rays are pass through the object producing the image on the film; image that is possible because of the different absorption of X-rays in the heterogeneous structures of the object. When objects are not visible by eye or light microscopic, projection radiography is used. In this technique, the diverging angle of the X-ray beam is used to magnify the image of the object. Projection radiography is generated by X-rays coming from a single point. Size detection depends in the X-ray source size and the film contrast for this technique. Film contrast will depend on the relative mass absorption coefficient of the objects. Resolution depends on the film and the material under evaluation (typically 5μm). Magnifications of 200x and resolutions below 5μm are possible with real time projection. Real time projection radiography can be used with objects of any size. Nondestructive evaluations of soldered semiconductors, substrate bondings, PCBs, wire bondings, among other components are possible. Finally, X-ray computed tomography is a technique to determine 3D representations of true objects by means of 2D projections in several planes. However, this technique is slow and the computing resources required to analyze the images is vast [23].

As explained in the previous section, AOI is a technique that lacks the capability to detect hidden solder joints. The capability of X-rays to image the internal structure of an

object makes it the natural technique to inspect solder joints hidden from view. X-ray inspection is widely used to detect failures in microelectronics in the IC level and the PCB level. Upton [94] gives a good example on how automatic X-ray inspection is used by manufacturing companies to inspect complex boards like BGAs, CGAs, and CSPs while increasing the company product yield. Next paragraphs give some of the most important trends on X-ray inspection of electronics.

Zhen *et al.* [22] make a comparison among different techniques to detect Opens and cracks in BGAs. 30 pins BGA from 10 PCBs were tested by means of time domain reflectometry (TDR), Automatic X-ray inspection (AXI), and transmission X-ray (2DX). PCBs were tested by destructive techniques to corroborate results given by nondestructive techniques. Authors determined that TDR can detect BGA opens and large cracks, but 2DX performs better detecting opens and smaller cracks. Open and cracks down to 30 μm were found by 2DX. However, 2DX can not detect opens on PCBs made of FR-4, because FR4 is invisible to X-rays. It is important to mention that oblique perspectives give better imaging of the solder integrity; as Brundy [23] and Feng *et al.* [24] explained, this is done by tilt and twists the sample or the X-ray tube.

A micro focus X-ray fluoroscopy system was used by Hirakimoto *et al.* [25]. As explained by the authors, LSI surface mount components are very difficult to inspect by optical inspection methods because the several solder balls are hidden between the component and the PWB. Even destructive inspection is difficult because the destructive cutting generates deformation and stress, and the trial and cut process is time consuming. They were able to obtain the 3D geometry of the solder ball in a printed wire board (PWB) within 400 s and using 1800 view angles of the board (a computer with dual processors of 3 GHz was used). However, 6.67 min looks like a high amount of time for online nondestructive inspection system. In addition, the automatization of inspection systems required classifiers that can discriminate adequate solder joints without the need of human discerning.

Another application for the X-ray methodology is found in reliability test of solder joints. For example, Ladani *et al.* [28] used X-ray methodology to determine the voids on the solder balls of a BGA. After determining the percentage of voids in the solder balls, the authors performed thermal cycling test to characterize the durability of the solder balls in function of the void percentage. Lo *et al.* [29] used X-ray to make sure different kind of surface mount components were in perfect conditions before mechanical test and thermal cycling test. Finally, Kangasvieri *et al.* [26] performed X-ray inspections after ball attachments process and thermal cycling test on BGAs with plastic core solder balls. They were able to detect voiding and misaligned plastic spheres after the thermal cycling.

As seen in the reported investigations, X-ray is a good tool to identify misaligns of solder balls, cracks, voids, and missing solder balls on BGAs. However, open bumps are very complicated to detect on the PCB side as the PCB is almost invisible to X-rays. In addition, X-ray is slow and human interpretation is needed to identify the defects. Although X-ray computed tomography offers a more detailed inspection, it is slow to implement on an automatic technique.

2.2.3. Laser Ultrasound Inspection

A more recent technique to detect solder joint defects on electronic components (particularly BGA mounted components) is laser ultrasound [41-43, 101]. The laser ultrasound technique consists of generating ultrasound in the chip surface by means of a laser pulse that excites the chip in a vibration motion. The out-of plane vibration (vertical to the chip surface) can be measured by means of an interferometer. Under the premise that solders with defects generate different vibration pattern, the chips with solder defects can be differentiate from the chips without defects.

A typical laser ultrasound experimental setup has the next elements:

- Fixture. This component holds the chip allowing the interferometer to be scanned over the whole chip surface. In this way, data can be acquired at multiple points on the surface. The fixture consists of a right angle platform that is used to position each sample and a xy-positioning stage where the angle platform is mounted. The xy-positioning stage is controlled by two stepper motors from a computer. The fixture allows a position accuracy of 12μm.
- Nd : YAG infrared laser. This is the source of ultrasound. An optical fiber is used to deliver the infrared energy. This optical fiber permits flexibility in the positioning of the test fixture and the location of the chip. The fiber is very close to the chip and approaches it with a 45° angle. The angle prevents the reflected laser pulses from damaging the interferometer detector.
- Interferometer. This laser interferometer is used to record the surface displacement of the chip at specific points. The interferometer is in a perpendicular direction to the chip surface.

The environmental vibration is considered small enough to be neglected; moreover, the environmental vibration may be rejected by the interferometer or removed with filters. Sheng *et al.* [43] compare vibration signals among two good chips with no missing solder balls and two bad chips with missing solder balls. Measurements were acquired in four different positions per chip. A comparison among signals showed that good chips generate enough different signals from bad chips, allowing discrimination between good and bad chips. An error ratio was proposed to compare signals quantitatively; error ratio that is given by the next expression:

$$ERR = \frac{\int |f(t) - r(t)| dt}{\int |r(t)| dt}$$

where r(t) is the reference signal, an f(t) is another signal. Good chips signals were compared to generate a threshold value to determine acceptable and unacceptable solder

joins. A comparison among the threshold value and the characteristic ERR for the bad chips showed a much higher ERR value than the threshold value. Sheng *et al.* [43] generated an inspection method capable of detecting bad chips, although only bad chips with missing solders. The time to take data at one point and process it was about 2 s. One inspection point will be sufficient for small chips, and more than one inspection point will be necessary only if there is a need to isolate the bad solder joint.

In a subsequent research, Liu *et al.* [101] performed a vibrational modal analysis for two flip chips (one with a solder ball missing and one without a solder ball missing). The chip was modeled as a rectangular plate with pin supports by means of the finite element method. The different frequencies obtained for the good flip chip and the bad flip chip proved the feasibility of vibration frequencies as a mean to detect chips with missing solder defects.

The laser ultrasound technique has been used not only to detect missing solders, but also to detect open solder balls. Using a very similar procedure to the one exposed in [43, 101], Erdahl *et al.* [41] showed that the laser ultrasound technique can be used to detect open solder balls. Two sample boards were tested. Each of the boards had three reference chips and seven chips with open solder bumps. Consistency and repeatability were proven by testing ten times all ten chips in both boards. A statistical analysis show that this technique can detect successfully two or more adjacent open solder balls, but not one open solder ball. To find a clear difference between good chips and chips with only one open solder ball, multiple tests of the specimen should be done.

In summary, laser ultrasound can detect missing and more than one open solder balls, but multiple tests should be done to locate the position of the defectuous solder joints.

2.2.4. Active Thermography Technique

Thermography is a technique that takes advantage of the capacity of bodies to emit radiation in the infrared range (invisible to human eye with a wavelength in the range 0.75-100 μm) to inspect internal structure of materials; such radiative energy is captured and transformed into a temperature distribution by means of an infrared camera (the measurement wavelength range for common cameras is from 3-14 μm; a wide description of the infrared cameras can be fount at [89]). Thermography can be divided in two kinds, active and passive thermography. If no external energy is provided to the object under study the technique is called passive thermography, while active thermography requires using an external source of energy to generate a thermal variation in the object under study. Active thermography base nondestructive methodologies are successfully used to characterize not only hidden defects sizes, but their depths too. Hung *et al.* [67] present an excellent literature review on active thermography. Active thermography can be divided in long time excitation or short time excitation. Long time excitation requires higher input of energy with lower powerful heat sources. The object is irradiated (~2 kJ) for long times (~1-30 min). This technique is useful for sandwich structures, deep flaws and high thermal conductivity materials. Location and size of flaws can be determined from the thermal images and the depth can be determined from the thermal transient behavior after localizing the defect position. Transient pulse excitation is a fast inspection technique, full field interrogation, and no interaction with the sample. Usually pulses are very short (~3 ms) and large power of transient light sources (~9.6 kJ). This technique is useful for surface flaws, subsurface flaws, and high thermal conductivity materials. The transient behavior of the pixels in the image is compare to the transient behavior where there are no defects in the material (1D approach). In this way, the defect can be detected without any reference to neighbor pixels. The depth of the defect can be determined comparing the thermal transient time too.

Sections 2.2.4.1 and 2.2.4.2 show some of the most significant researches related to active thermography and the detection of hidden defect shapes; literature sources are divided by excitation time. On the other hand, Section 2.2.4.3 shows some of the most relevant researches of the application of thermography on electronics.

2.2.4.1. Long Excitation Time

The practical application of active thermography or any inspection method is highly linked to a fast detection development. The great majority of investigation effort on active thermography is focused on short time excitation procedures. Therefore, only two of the most interesting researches are presented for long time excitation.

Kurita *et al.* [73] used active infrared imaging to show the hidden defects in an elevated railway bridge. They used a remote heating system consisting of 6-kW air xenon arc lamp. The covered area for each inspection was 16.8 m^2 corresponding to half of the middle of a slab. Irradiation and image acquisition were performed at the same time. This methodology was able to detect the defects at depths of 3 cm successfully.

Kamoi *et al.* [70] study the capacity of infrared thermography to detect hidden defects in concrete blocks. Air and steel objects were buried in the concrete. The objects were detected after 150 min of heating (500 W/m^2), but only the air objects were detected after 20 mm depth. A better performance was obtained with higher energy source (1500 W/m^2 with standard electrical bulbs) at low times of heating. A numerical model was developed too showing same behavior on temperature profiles, but with higher values of temperature caused by no accurate thermal properties.

2.2.4.2. Short Excitation Time

Short excitation times can be divided in two classes of active thermography: lock-in and pulse thermography [69]. Lock in Thermography is a nondestructive detection technique in which the specimen is heated periodically and the oscillating surface temperature is captured by an infrared camera. Pulse thermography is easier to perform, but the data acquired is affected by non uniform heating. On the other hand, lock-in thermography needs a separate experiment for each inspected depth and there is a stabilization time before reaching a steady state regime; a direct relationship between the specimen depth and inspection frequency that allows defect detection is needed. The energy needed to perform lock-in thermography is less than in other techniques. In the next paragraphs, some of the most significant investigations on pulse and lock-in thermography are summarized.

Active lock-in thermography was used by Giorleo *et al.* [63] to detect inclusions, delaminations, and lack or excess of resin in carbon-epoxy laminates. The thermography system is coherently couple to a thermal wave source which is operate so that a temperature modulation results. The thermal wave is extremely damped so that it penetrates into the object only to a certain depth (slower waves give deeper penetrations). Modulation frequencies were used from 0.0098 -0.47 Hz. Specimens with holes ranging from 3 mm to 8 mm in diameter and depths ranging from 2 to 6.4 mm were studied. They were able to detect only defects at a depth that does not exceed the diameter of the defects.

Ibarra-Castanedo *et al.* [69] used pulse thermography and lock-in thermography to nondestructively evaluate honey comb structures. Two specimens were used with delaminations, core unbounds, excessive adhesive, and crush core. Six lamps providing 1000 W each were used as the modulated heating source for the lock-in thermography test. Two high-power flashes (Balcar FX 60, 6.4 kJ, 2 ms pulse) were used as the heating

source for the pulsed thermography tests. They were able to detect the different artificial defects by both techniques. They conclude that pulse thermography was easier to perform but the data acquired is affected by nonuniform heating, emissivity variations, environmental reflections, and surface geometry. On the other hand, lock-in thermography needs a separate experiment for each inspected depth and there is a stabilization time before reaching a steady state regime. A direct relationship between the specimen depth and inspection frequency that allows defect detection is needed. The energy needed to perform lock-in thermography is less than in other techniques.

Busse *et al.* [57] proposed the combination of phase images obtained at different lock-in frequencies to improve the hidden defects characterization. They were able to characterized three back holes at different depths on the specimen.

Hierl *et al.* [66] used active thermography to detect hidden solid material non uniformities. A flash heater was used as irradiation source and located in the same side as the camera. The temperature transient behavior was monitored by the infrared camera (camera with a 20 ms temporal resolution). An air void of 4.15 mm diameter and 0.95 mm depth void was detected in a glass platelet. Thermal images were taken after 2 s of the flash heating. The glass platelet has a homogeneous constitution with exception of the air void. The transient temperature was determined analytically neglecting heat losses at the surface and neglecting the heat conduction in the void. A clear different behavior in the surface temperature was obtained after 0.7 s from heating when the heat wave reaches the void.

Marinetti and Vavilov [75] used infrared active thermography to characterize hidden corrosion in metals. Inversion formulas were developed to determine material loss for both flash and squared-pulse heating. A flash heater (two tubes 4.8 kJ each delivered in 5 ms) and a quartz lamp heater (30 kW continuous energy) were used as the external heat sources. Infrared images were acquired with a frequency of 1 to 30 Hz. Rectangular

holes ranging in different sizes and depths (deeper holes simulate higher corrosion percentage) were inspected in a 3mm thick steel plate by means of flash heating. The heating source and the camera were kept in the same side. The surface of the plate was painted black to improve absorption. For the square-pulse heating, a 10 mm thick steel plate was inspected. 20 and 40 mm diameter holes at different depths were perforated in the plate. The plate was heated for 20 s. Flash heating allow the detection of up to 10% material loss in steel samples with thickness up to 3 mm. In thicker samples (up to 5 mm) the limit worsens to 25%. Squared-pulse heating showed a detection limit of 25% for material loss in plates thicker than 5mm.

Chen *et al.* [59] propose an ultrasonic burst phase thermography. This methodology uses an ultrasonic burst as the external heat source. The defects are detected because of the heat generation caused by friction, clapping, and thermo elastic effects. 18 different bottom holes in sized and depth in a transpiration sample were inspected by ultrasonic burst phase thermography and pulse thermography. The burst phase thermography was unable to heat all of the holes and only five of the holes were visible. However, pulse thermography was able to show 15 of the 18 holes.

Montanini *et al.* [77] detected flat-bottomed holes in a Plexiglas specimen by means of lock-in and pulse thermography. The specimen consists of a circular plate with sixteen 10 mm circular holes with depths ranging from 0.6 mm to 3.6 mm. The surface under inspection was painted black to uniform emissivity and reduce reflections. For the lock-in thermography experiments, 4 halogen lamps (1 kW) were used and were synchronized by a lock-in amplifier integrated in the camera. For lock-in thermography, the correct detection of the defect depends directly on the excitation frequency; therefore, the authors performed several tests changing the modulation frequency. In the case of pulsed thermography, the specimen is heated using halogen lamps (500 ms pulses) or high power xenon tube ring flashes (1 ms pulse). The transient response in the temperature was obtained by recording a sequence of infrared images. A Fourier transform method

was used to characterize the temperature values by means of amplitude and phase values for each thermogram. Phase values based images were better because they are independent of non uniform heating infrared surface properties. Every hole was detected by this techniques but better contrast was obtain by lock-in thermography, although in different modulated frequencies so multiple test must be performed for the different depths. The defects size (digital image processing software) and depths (1D heat transfer model) were determined. The errors on the estimation of depths range from -0.1% to 9.7%. The increase of error as depth increases were attributed to the 1-D approach. Errors ranging from 2% to 28% were estimated for the determination of the defects size. Errors are attributed to the radial heat transfer. Lock-in was able to detect all the defects, but multiple experiments were carried out. Pulse thermography is fast but not all of the defects were detected; this poor detection capability can be improved by increasing the heat intensity that might damage the specimen.

Finally, Gleiter *et al.* [64] give some examples of the use of pulse, lock-in thermography and ultrasound lock-in thermography to detect cooling channels of turbine blades (lock-in), hidden bonded areas on aircraft wings (lock-in), riveted fuselages in aeronautics (optical and ultrasound source), and gearwheel cracks (ultrasound).

2.2.5. Active Thermography and Electronics Inspection

Wiecek *et al.* [88] used a thermographic camera to characterize the solder thickness on printed circuit boards by means of its thermal transient response; this thermal transient response varies with the solder thickness as a consequence of the thermal conductivity and capacity. The authors model the solder as solder layers with 400, 700, and 1200 μm of thickness and located on the top of the PCB. The thermography technique was developed on transmission by heating the back of the PCB and monitoring the front of the PCB where the solder is located. The infrared camera used has a 0.2 K temperature resolution and a 20 μm spatial resolution. A 1-D model of the solder-PCB assembly was

developed too. Major assumptions on the development of the 1-D analysis were: the copper pad was neglected because of his high thermal conductivity in comparison to the solder and PCB thermal conductivities, the thermal convection is uniform over time, and the energy by radiation from the lamp can be modeled as a uniform heat flux because the temperature of the heat source is very high. The 1-D analysis was solved by finite differences and a system of linear equations was generated. This system of linear equations was fed with the experimental temperature and an estimate of the solder thickness was obtained. A comparison between the estimate thickness and the real thickness give errors from 10 to 25%.

Chai *et al.* [84] were able to detect hidden solder joint cracks in flip chip packages by means of infrared thermal imaging; the solder cracks were detected as clear high temperature areas in the thermal images caused by an increase in thermal resistance. The flip chip package under investigation consisted of 4 x 4 mm die with 60 peripheral solder bump forming a single daisy chain when attached to a Bismaleimide-Triazine (BT) substrate. The solder bumps have a 100 μm size and a 200 μm pitch, and were hidden by the silicon die. Flip chip samples were subject to an intensive thermal cycling; subsequently, the daisy chain resistance was measured to identify possible chips with solder joint cracks. Chips with solder joint cracks presented an increment of daisy chain resistance of 20% after thermal cycling. After identifying defective and normal chips, a current was apply to the daisy chain and the temperature at the top of the flip chip was monitored during transient behavior with a thermal imager capable of storing 16 frames per second and with a field of view of 6×3 mm. 10 normal and 29 defective units were inspected. 100% of the units with defects presented a localized heating area, while 100% of the normal units did not. The effect of the increment of the electric current on the temperature of the localized heating area was determined. The difference of the temperatures among the defective samples and the normal samples increased as the current increased providing a better discriminability among defective and non defective

samples. Finally, the location of the solder joint with a crack was corroborated by cross-section and micro-probing studies.

Breitenstein *et al.* [56] detected current leakage in integrated circuits, such current leakage are heat sources shown as high temperature regions in infrared images. The authors were able to achieve detection limits down to 10 μK by using a high speed infrared camera in conjunction with a microscope objective and a lock-in thermography system. The technique allows to localized leakage currents of about 1 mA in 1 s and currents on the order of μA in less than 1 hour. The camera used was a camera with 128×128 pixels and running at 217 Hz. The camera could reach spatial resolutions of 0.23 mm and 13 μm by adding a normal 25 mm objective or a two-stage microscope objective, respectively. The specimen was uniformly heated by means of a 5 mm wide and 230 μm thick Ni stripe. A leakage of 60 μA was detected in an IC by using a lock-in frequency of 13.5 Hz and a measure time of 36 min. In addition, a leakage of 1 mA was detected in a CMOS at a lock-in frequency of 54 Hz, spatial resolution of 5 μm, and test duration of 10 min. Finally, two CMOS ICs, one defective and one functioning normally, were investigated by a lock-in frequency of 54 Hz for 2 min and a pixel resolution of 50 μm. The defective CMOS IC showed clearly higher temperatures with respect to the intact one.

Artificial solder defects in ball grid array electronic components were detected by Varis *et al.* [87], however the abnormal thermal signature was detected only retiring a thick plastic cover from the electronic components. The two electronic components inspected were BGA mounted components with a 27 mm in diameter. One of the components was cover by a 2 mm thick plastic package and the other with a 0.75 mm thick copper heat slug. Both components were attached to PCBs 1 mm thick and made of glass fiber composite. Multiple solder balls were retired of three different regions of the components. The electronic components were heated using a 25 W CO_2 laser operated at a wavelength of 10.6 μm. The laser beam was expanded to 35 mm by means of two

ZnSe lenses. The infrared camera was located in the same side of the sample as the laser. The camera had a 16º field of view and a minimum focal length of 20 cm. The samples were heated for 5 s and left to cool down. In the case of the first component, the missing solder joints were clearly detected and it was determined that the visibility of the solder joints is higher at a determine time during heating. A time of 1.5 s, after heating was started, was determined as the optimal time for solder joints visibility. An attempt to monitor the temperature on the opposite side of the component was performed, but not traces of the solder balls were obtained (the energy transfer to the PCB is very low). In the case of the second component, no traces of the solder joints were found, perhaps because of the thick cover blocking the solder joints from view.

Finally, Hsieh *et al.* [85] characterized the thermal profile on a chip under vibration stress; spots more susceptible to vibration stress presented an evident increase in temperature that was monitored by means of infrared thermography. The test subject was a parallel processor (surface mount device with leads on the sides) on a networks communication card. Vertical vibration was induced on the component by means of a sonifier unit. Gray scale images of the component were obtained by means of a ThermoSonix imaging system. The gray scale values were transform to temperature values by measuring the temperatures on the component by means of platinum-film and resistive temperature detectors. Three temperature sensors were used to measure the temperatures at the component surface, leads, and ambient temperature. The amplitude and duration of the vibration were increase, corroborating an increment of temperature caused by the vibration stress as the amplitude and duration increase. Next, 30 experiments were conducted varying the amplitude of the vibration (25, 35, and 50%). 21 of the experiments were used to develop an artificial neural network to model the amplitude of vibration or stress level in function of the thermal response (average heating rate) at the corner of the component (this location is the highest stress point). Finally, the neural network model was tested with the rest of the experimental data

providing an overall error rate of 15.3% on the determination of the stress level in function of thermal response.

2.2.6. Summary

Table 2.1 shows a comparison of the advantages and disadvantages of the more common inspection methodologies for solder joints. A more detail summary is given for infrared thermography in this paragraph. Infrared thermography has been used to characterize hidden defects in different ranges of size and depth. The ability of the technique to detect the defects depends on the material properties, excitation time, and defects size and depth. In particular, long excitation times of exposure are used in applications where the inspection time is not an important variable to consider. Short times of heating or excitation are applied by lock-in thermography and pulse thermography. Lock-in thermography is more complicated to perform and time consuming, because the depth detection capability depends on the modulated frequency used. Pulse thermography is simpler to perform, but a very high energy is applied in very short times (*ms*) compromising the non invasive characteristic of the detection system and increasing its cost. Infrared thermography has been successfully used to detect hidden solder joint defects with sizes down to 0.1 mm. However, the capability to detect these defects depends highly on the component configuration, infrared camera sensitivity and speed, and heat source. Providing energy directly to the solder joint by means of an electric current gives better results than using lamps, because energy is generated directly in the solder joint. It is important to remark that the active thermography methodology is quite easy to implement, because only an infrared camera and a heating source, as simple as a halogen lamp, can achieve defects visibility.

Table 2.1. Comparison among inspection methodologies.

Technique	**Advantages**	**Disadvantages**
AOI	Spatial resolution is down to 10 μm.	Only visible solder joints can be inspected
AXI	Can detect solder joints hidden from view; proportionate a direct view of the solder joints; spatial resolution down to 5 μm.	It is slow to implement; PCB material is invisible to X-ray; no open solder joints are detected; equipment is expensive; human interpretation is needed.
Laser ultrasound	Can detect missing solder joints and open solder joints on BGAs.	The location of defective solder joints needs multiple inspections and it is not directly visible; only more than one open solder joints can be detected.
Infrared Thermography	Possible to detect hidden defects size and depth; location of defective solder joint is shown by abnormal temperature regions; spatial resolution down to 13 μm is possible.	Effectiveness to show hidden defects on the size of solder joints is not clear; high accuracy systems are slow (lock-in test is in the range of min); fast techniques are affected by non uniform heating, emissivity variations, environmental reflections and surface geometry.

2.3. Numerical Method

Almost every phenomenon of nature can be modeled by means of laws of physics or other fields in terms of algebraic, differential and/or integral equations relating various quantities of interest. An analytical description of a particular phenomenon is called a mathematical model. A mathematical model of a process is developed by doing assumptions with respect to the process and using different laws governing the process. Mathematical models are usually characterized by very complex differential and/or integral equations apply to complex geometrical domains. Usually, very simplify versions of the mathematical models can be solved analytically. However, with the invention of the computer and the use of numerical methods, the accurate solutions for much more complex mathematical models can be achieved. Therefore, numerical methods are widely used in the actuality because: several practical problems involved very complicated domains and nonlinearities that prohibit the use of analytical solutions and a numerical method can be used to study the effects of multiple parameters gaining a

better understanding of the process being analyzed saving time and material resources [102]. In the case of this research, the phenomenon to analyze is the heat exchange by radiation and convection between the PCB assembly and the surroundings when applying active thermography technique. Analyzing heat exchange by radiation in enclosures composed of multiple and complex geometries is not an easy task. In addition, couple heat exchange mechanisms make it even more complicated to analyze (i.e. heat exchange involving conduction, convection, and radiation). One of the most difficult tasks is the determination of view factors (parameter that accounts for how heat is exchange by radiation among surfaces). The simplest way to determine view factors is by means of tables, but unfortunately view factors for complex geometries are not available. Other methods required the determination of fourth order integrals, or second order integrals if contour integration is used. Commercial and non commercial software is available too, but any method involves the use of numerical methods. In addition, radiation and conduction heat exchange governing equations must be solved simultaneously. Such a huge task is only possible by means of numerical methods. In the majority numerical solutions for couple heat exchange transfer, radiation is usually considered as exchange by radiation between a surface and the ambient simplifying the problem at hand [103-105]. More complicated numerical radiation analyses usually involve participating medium, semi transparent medium, and porous medium [106-108]. In the next two subsections, some of the few researches involving numerical analysis related to electronics, heat exchange by radiation and/or convection, and the application of infrared thermography are presented.

2.3.1. Numerical Methods in Electronics

In the field of electronics solder joints, numerical methods are usually employed to model fatigue damage by torsion in plastic board grid array solder joints [109], thermal cycling test in flip chip ball grid array solder joints [110], effects of flip chip solder geometry on the reliability of solder joints [111], elastic and plastic deformation of

solder joints in a printed wiring board under vibration stress [112], prediction of solder joint shapes during reflow processes and their reliability [113], and the modeling of solder joint geometry in surface mount technology [114]. Although the great majority of numerical research is focus in failures of solder joints by fatigue, elastic or plastic deformation, and geometry determination during soldering or reflowing processes, some efforts have been done to model heat exchange of printed circuit boards in enclosures. Eveloy *et al.* [115], modeled the transient heat transfer in a board-mounted plastic quad flat pack under natural and forced convection. The printed circuit board was enclosed in an enclosure whose ambient conditions resemble reliability screening and surface-mount assembly processes. The reliability tests were performed in three different situations: component power dissipation and fixed ambient conditions, passive component operation in dynamic ambient conditions, and component power dissipation in dynamic ambient conditions. For surface mount assembly, a typical solder reflow profile was applied. Benchmark criteria are based on component junction temperature and component printed circuit board surface temperature, measure experimentally using thermal test dies and infrared thermography. The test board was a 1.6 mm thick FR-4 design with a plastic quad flat pack containing a 7.5 mm square thermal test die with an accuracy ±0.4 °C. The board and component surfaces temperatures were recorded using an infrared camera (AGEMA operating in the 8-12 μm spectrum with a ±2 °C accuracy) and thermocouples (±1 °C accuracy) located on the component and several board locations. Free and forced convection characterizations were performed in a still-air enclosure and variable speed wind tunnel. The numerical model was performed using Flotherm CFD code. Dimensions and properties were taken according to vendor specifications with exception of FR-4 thermal conductivity that follows an anisotropic value. For free convection modeling, only the air in the vicinity of the PCB was modeled to allow a dense mesh. Artificial free convection was used on the boundaries of the computational domain. For steady state free convection heat transfer, the board Grashof number was determined from the thermographic measurements to be 10^6. The Reynolds number for the board was calculated as 2×10^5. Radiative heat transfer was modeled

from the component top and bottom surfaces, PCB FR-4 substrate and copper tracking surfaces, although, as usually, the radiative heat transfer was considered only between the component surfaces and the environment. Higher density mesh was used in component body and near wall regions. The time increment was smaller when high temperature variations are expected. Time increments ranged from 3 ms to 5 s. Junction temperatures were determined with 3.6%, 6.4% and 2.9% accuracy for free convection, laminar flow, and turbulent flow, respectively. Errors in the prediction during reliability test were attributed to experimental errors caused by the wind tunnel velocity variations, while errors in the reflow process were attributed to the copper lead thermocouples used to measure temperature in the component and printed circuit board.

2.3.2. Numerical Methods in Infrared Thermography

Numerical methods have been used to characterize thermographic analysis for the detection of defects morphology; however, as seen in the next couple of researches, radiation is again avoided considering a uniform heat flux and exchange by radiation only between a surface and the environment. Galietti *et al.* [116] used finite element method to determine the mathematical relationships that correlates data taken from thermography tests with the characteristics of the defects in composite materials. Authors aimed in developing a hybrid numerical-experimental methodology that is cheaper than the expensive and complicated lock-in and pulse thermography by reducing equipment cost and number of experiments performed. The composite material consisted of carbon/epoxy laminate with inclusions of extraneous materials resembling the degradation of mechanical properties. The effects of the defects on the temperature profile in a line, along the composite surface and in the position of the defect, were analyzed. A parameter called thermal contrast was used to characterize the effective detection of the defects. This parameter is the difference between the temperature in a zone with defects (T_d) and the temperature in a free defects zone (T_s). Authors determined the apparent dimension of the defect as the distance between the

intersections of the tangent lines with the thermal profile in the points with the maximum thermal gradient. In order to develop an accurate FEA model, preliminary experiments on non defective specimens were carried out determining the thermal heat flux of the source. In addition, preliminary experiments on specimens with defects were performed to determine defects thermal resistance by means of their maximum temperature. Multiple finite element analyses were done varying depth and dimensions of the defect; the coefficients of the correlation equations among the thermal parameters (obtained from FEA models) and defects parameters are determined by multiple linear regression. Such coefficients are used to calculate the geometrical parameters of unknown defects by means of the thermal contrast and apparent sized obtained from the thermography experiments of samples with unknown defects. The infrared camera, a non cooled microbolometric sensor 610-TVS AVIO camera, was a no particularly sensitive camera in order to test its capability to describe accurately the defects. Carbon resin plate samples with multiple square Teflon inserts ranging in sizes from 0.25 in to .75 in and different depths were analyzed by transmission active thermography (camera is in the opposite side of the heating source). Smoothing of thermal profile curve was necessary because of the irregularities caused by noise from the camera results. Images with the best thermal profile were chosen to determine the apparent dimensions. The numerical analysis was performed using 1-D and 3-D modeling. The 1-D analysis was developed for a specimen with no defects considering heat exchange by convection and radiation with the surroundings and a constant heat flux in the heated surface. This model was developed with the intention of performing a fast analysis to determine possible errors before developing 3-D simulations. The 3-D model was performed adhering the closest possible to the characteristic of the experimental thermographic test of specimens with defects. Before performing simulations varying defects geometric characteristics, the thermal resistance of the defects was determined by comparing iteratively the thermal contrast in the simulations with that of the experimental test in a known defect. After calibrating the FEA model, a 3-D graph representing the thermal contrast in terms of depth and defect size was developed by means of multiple simulations varying size and

defect depth. This graph showed clearly the defects more likely to be detected by the thermography camera. Regression curves for thermal contrast and apparent dimension were done in function of depth and defect size. Therefore, the defect size and depth were determined by solving the regression equations simultaneously by knowing the experimental values of the thermal contrast and the apparent dimension. Errors in the prediction of size were high as the tangent of the thermal profile is quite variable because of the no so sensitive camera. The depth was determined more accurately because the thermal contrast values are more stable during experiments. Although certain success was achieved by this no so expensive and no complicated methodology, pulse and lock-in thermography is more successful in characterizing not only defect sized, but also defects depth. The authors proposed a neural network modeling to improve the prediction accuracy in future related research.

In a more recent research, Marinneti and Vavilov [75] developed 1-D, 2-D, and 3-D thermal numerical models for the characterization of corrosion in metals. Inversion equations were determined from the simulation thermal results in order to determine defects geometrical characteristics (absence of metal caused by corrosion). All numerical models were developed considering heat diffusion only due to conduction with a uniform heat flux in the sample surface (eliminating necessity of determining the heat transfer by radiation from the heat source to the sample surface), heat exchange by convection on sample boundaries, and adiabatic surfaces in the boundaries between defect and sample. Sample was composed of a material with homogeneous composition with exception of the air defects. The heating function was characterized by a square pulse with a maximum absorbed power and a specified pulse duration. Normalize surface differential temperature signal ($(T_{defect} - T_{no\_defect}) / \dim ensionless\ absorbed\ heat\ energy\ density$) and running surface temperature contrast ($(T_{defect} - T_{no\_defect}) / T_{no\_defect}$) were selected as the features characterizing the defects. The 1-D model was limited to large defects avoiding boundary heat diffusion phenomena. The 1-D model was defined as the analytical heat

conduction solution for a plate with adiabatic boundary conditions and square-pulse heating in one of its surfaces. The 1-D model is adequate for defects in steel with defect size (diameter) that is five times larger than sample thickness. A 3-D model was done by a finite difference scheme and an implicit solution method, while a 2-D model was done by finite differences using COMSOL multiphysics. Numerical solutions were compared to classical solution for heating an adiabatic plate with square pulse to be better than 1%. Temperature solutions were compared between 2-D and 3-D models finding a maximum difference between models of less than 1%. After the 3-D numerical model was corroborated, multiple simulations varying defects dimensions were performed. Adiabatic conditions were determined to be accurate by comparing with a convective boundary conditions case (10 $Wm^{-2}K^{-1}$). Thermal conductivity showed not to affect the running surface temperature contrast and corrosion (defects geometry) estimation. The 3-D numerical analysis made possible to determine the adequate time for the detection of the defects as the instant when the running thermal contrast reach the maximum. In addition, this model corroborate that heat diffusion made more difficult the accuracy in the detection of large defects and the inability to detect small defects as the time from beginning of heating increases. However, small times will require higher power heating sources. An inversion formula from the 3-D simulations proved to give an overall accuracy better than 20%. To corroborate the applicability of the inversion formulas, two thermography tests were performed: one was performed in a steel plate with bottom square holes at different depths using a flash heater (two tubes 4.8 *kJ* each delivered in 5 *ms*), and the other on a metallic specimen with circular bottom holes at different depths by means of a 30 *kW* tubular quartz lamp heater (square pulse) providing up to 15 kW/m^2 of absorbed energy for 5 to 20 *s*. Flash heating was found to be adequate to detect up to 10% material loss in steel plates up to 3mm in thickness, but in thicker samples the detection limit worsens up to 25%. To assure detection in samples thicker than 5 mm, square pulse heating must be employed. Another way to improve detection is painting the surface in black to improve emissivity/absorptivity and reduce the surface emissivity non uniformities.

Table 2.2. Potential benefits of using numerical methods on electronics and infrared thermography.

Application	**Potential Benefits**
Electronics	Very complex shapes for the solder joints can be created; effects of the solder joint shape on the electronic component function can be investigated during thermal cycling and reflow processes; virtual prototyping can be used reducing cost on the design process..
Infrared thermography	The thermal process during an infrared thermography test can be simulated; parametric analysis can be used to investigate the relationship between the thermography conditions and the capability to detect hidden solder joint shapes; numerical methods can be used in conjunction to moderate experimental thermography models to generate more complete thermography mathematical models.

2.3.3. Summary

Numerical methods are used to model complex nature phenomena involving very complicated domains and nonlinearities that prohibit the use of analytical solutions. Heat exchange by radiation is a phenomenon usually avoided because of the difficulties to model the interaction among multiple and complex geometries. In addition, radiation analysis rarely involves more than two mediums exchanging heat by radiation (surface and surroundings or environment). Some specialize numerical researches analyze more complicated problems involving participating medium, semi transparent medium, and porous medium. In relation to electronics, numerical methods are usually employed to model failure by fatigue or elastic/plastic strain, and solder shapes during reflow. On the other hand, numerical methods have been successfully used to analyze the effects of defects on the thermal behavior of plates considering a constant heat flux on the surface, and convection and radiation exchange with the environment. More over, numerical methods are used to simulate thermography methodologies. These simulations relate thermal parameters to defects geometrical parameters in order to investigate the optimal configuration for thermography methodologies. Table 2.2 shows a summary of the potentials of numerical methods on electronics and infrared thermography.

2.4. Classification Method

Pattern recognition is the study of how machines can observe the environment, learn to distinguish patterns of interest from their background, and make sound and reasonable decisions about the categories of the patterns. Automatic (machine) recognition, description, classification, and grouping of patterns are important problems in biology, psychology, medicine, marketing, computer vision, artificial intelligence, and remote sensing. According to the pattern, its recognition/classification can consist of one of the next tasks: ***supervised classification*** (discriminate analysis) in which the input pattern is identified as a member of a predefined class, and ***unsupervised classification*** (clustering) in which the pattern is assigned to an unknown class. In the particular case of this research, supervised classification will be used. The design of a classification system can be divided into three steps: data acquisition and preprocessing, data representation, and decision making (refer to [117, 118] for more information). In this research, the classification of solder joint shapes by means of the grand average cooling rate data is one of the goals (grand average cooling rate is a predetermined feature describing solder joint shape classes). The data acquisition is made by means of infrared thermography experimental technique, the preprocessing is the thermography images manipulation to get the grand average cooling rate data, data representation is the definition of the predefine classes (solder geometries), and decision making is made by the supervised classification or pattern recognition algorithm used. Three of the most common used classification methods are statistical, artificial neural networks, and genetic algorithm. Statistical classification is one of the earliest methods to classify data. Statistical classification is the problem of identifying the sub-population to which new observations belong. The identification of the new observations is done on the basis of a training set of data containing observations whose sub-population is known. Statistical classification is based on a Bayesian approach; this means that the population to which a subject belongs is a random variable. In statistics, the procedure of classifying a group of data is called discriminant analysis. Discriminant analysis is a parametric statistical classifying method that fits a parametric model to the training data and interpolates to classify the

new data. According to the parametric function or discriminant function, the discriminant analysis can be linear or quadratic. A linear discrimination analysis is used when the variance-covariance matrix does not depend on the population from which the data are obtained, while a quadratic discriminant analysis is used for heterogeneous variance-covariance populations. One of the major drawbacks of the statistical discriminant analysis is the assumption of a Gaussian distribution for the data to classify that usually is not adequate [117]. On the other hand, genetic algorithm is one of the most recent techniques used for the development of classifiers. According to Cantu [119], genetic algorithms are stochastic search algorithms based on principles of natural selection and combination. These algorithms try to find a solution for a problem by manipulating a population of candidate solutions. The best solutions are selected to reproduce and mate to form the next generation. As the generations continue, good traits dominate the population providing quality solutions, while bad traits are eliminated from the population. The size of the population is directly proportional to the quality of solutions and the time to achieve adequate solutions. Although genetic algorithm is usually used as an optimizer, a variant called genetic programming has been used recently as a classifier. Genetic programming has the advantage of flexibility. According to Espejo *et al.* [120], genetic programming can be used to construct classifiers using decision trees, classification rules, and discriminant functions. However, genetic algorithm base classifiers have the disadvantage of the computational cost and achieving a solution might take even days; computational cost is a genetic algorithm issue that has been handle by using multiple parallel genetic algorithms improving running time [120]. Finally, artificial neural networks is a classifier that avoids any assumptions regarding the data to classify and can handle highly nonlinear classification functions. Moreover, artificial neural networks are originally massively parallel computing systems consisting of an extremely large number of simple processors with many interconnections [117]. This classifier has been widely used by the scientific community for years because it is simple, reliable, and fast. Therefore, this classifier has been selected by this research to

generate the classification procedure. In the next subsection, a survey on the most recent researches on this classifier will be presented on detail.

2.4.1. Artificial Neural Networks Classifier

Artificial neural networks, as its name indicates, makes use of very low level programming (additions, multiplication and fundamental logic elements) to solve complex problems by imitating the biological neural network. An artificial neural network is basically composed by multiple inputs with different importance (weights), a cell body where the inputs are processed, and multiple outputs carrying the results of the computations made in the cell body. The most accepted neuron model is the perceptron (see Figure 2.1). Although high level mathematics and logic can yield a broad general frame for solutions and can be reduced to specific but complicated algorithmization, artificial neural networks algorithmic structure is very simple and highly adaptable to a broad range of data problems. ANNs are perfectly suited to solve non-analytical, nonlinear, nonstationary, and stochastic problems or a combination of these kinds of problems (see [121] for a more detailed description of ANN structure). In special, artificial neural networks are commonly used to solve problems of recognition or classification, filtering and control. The popularity of ANNs in classification or pattern recognition is due to their low dependence on domain-specific knowledge and the availability of efficient learning algorithms.

Up to date, one of the most used neural networks for classification is one base in three layers (one output layer, one hidden layer, and one input layer) and a back propagation learning algorithm [122-132]. A three layers neural network has proven to be adequate for several complex classification problems. Some other learning algorithms used in three layer neural networks are cross validation [133] and scale conjugate algorithm [134]. However, when comparing back propagation to other algorithms, back propagation usually outperformed them or presents a very similar performance.

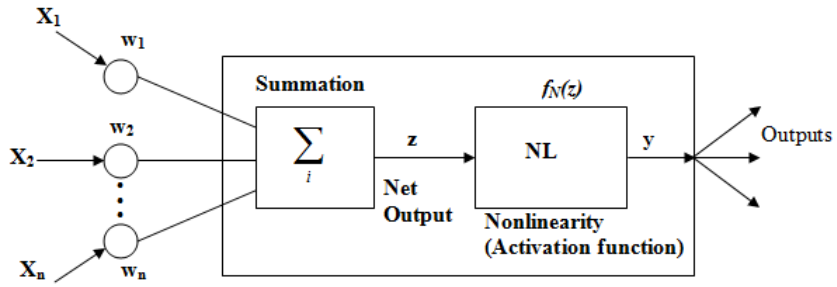

Figure 2.1. Perceptron model.

A successful design of a neural network or any classifier depends highly on the data acquisition and preprocessing. Therefore, feature extraction from data to use as input nodes in neural networks is highly investigate because the neural networks are very dependant on the input data quality and quantity. The quantity of data limits the number of features that should be used; it is advised to use at least ten times as many training samples per class as the number of features. Quality of the data is controlled by the feature extraction. Feature extraction depends on the data type and data type depends on the scientific field. A common feature extraction tool for time-frequency signals and data images type is the wavelet transform. The wavelet transform plays an important role in signal analysis and feature extraction. It can be used to detect the singularity of a signal and to identify a small difference between two signals. For example, Cheng *et al.* [124] used the wavelet transform to extract the features from the infrared spectroscopy signal of stomach tissue samples to discriminate among normal, early gastric cancer, and gastric cancer samples. Using a Morlet wavelet analysis, three of the wavelets coefficients showing a high influence in the signals pick were used as input for a back-propagation neural network classifier. The BPNN classifier was composed of three layers of nodes: an input layer, hidden layer, and an output layer. The hidden layer was composed of 20 neurons. The mean square error was 0.005. The output values were selected as 0.3 for normal tissues and 0.7 for abnormal tissues. They used the resilient

backpropagation algorithm because is a better option to gradient descent that points to local minimum. The initial number of hidden nodes (10) was determined by means of a formula in terms of output nodes and input nodes. Optimal hidden layer neurons number is determined by increasing and decreasing the initial number calculated (in this case 10) until the best accuracy of prediction is obtained. Learning speeds were studied and were found only important for convergence speed. Classification accuracies of 94.1%, 100%, and 100% were obtained for the early gastric cancer, advanced gastric cancer, and normal tissue, respectively. In a similar research, Gope *et al.* [126] classified electroencephalogram (EEG) non-stationary signals obtained from human subjects performing two mental tasks (relaxing and multiplying). In this case, the authors represented the non-stationary signals in its time frequency representation that resembles an intensity image. Next, the wavelet transform (Daubechies second order wavelet db2) was applied to the images and four features were extracted for each EEG channel. The features were used as the input for three different classifiers: Bayes, k-nearest-neighbor (kNN), and neural network (NN). The data set was randomly divided into 75% for training and 25% for testing in the Bayes and kNN classifiers. For the neural network classifier the data set was randomly divided into 75% for training, 10% for validation, and 15% for testing. For kNN and NN the data in each class was normalized to have zero mean and unit variance to avoid any feature dominating the classification outcome. In the case of the kNN classifier, the highest classification rate was obtained for k = and the classification rate was found to decreased as k increases its values. The neural network classifier used was a standard feed forward with three layers using a back propagation training algorithm. The hidden nodes were varied until the best performance was obtained (4 nodes). The neural network was performed by means of LabVIEW. LabVIEW offers two classes of learning modes: stochastic or batch. The learning process can be done for a fix or adaptive learning rate. Adaptive learning for the next iteration is based on the previous slope of the derivative of error (with respect to network weights). In addition, a momentum term can be used to speed the learning process. Finally, the best accuracy in the predictions was obtained for the neural network model

with 96% of accuracy. In another kind of scientific field, Gonzalez-Garcia *et al.* [134] used wavelet transformation to classify different landscape images. Features from the image like the distribution and size of the objects were represented by the wavelets coefficients of the Daubechies 4 wavelet transform. The extraction of the features procedure consisted of splitting the images in its three channels (red, green, and blue), then a histogram was generated for every channel, and finally the wavelet transform was applied to obtain 48 wavelet coefficients (16 per channel). The 48 wavelet coefficients were used as the input for the neural network model. The neural network model was composed of three layers: a 48 nodes input layer, a 49 nodes hidden layer (number determined as the one giving the best performance), and 6 output nodes (six different kind of landscapes). Cross validation neural network training was performed. 192 images were divided into 5 sets. Next, four sets were chosen to train the network five times leaving out a different set each time. Finally, after confirming a similar behavior for every training performed, the whole set of images was used to train the neural network. The landscapes were classified with a minimum accuracy of 96.875% for the same set of images, but very low accuracies (50%) were obtained when a new set of images was tested. This might be due to a not very good generalization or over fitting.

Another research demonstrating feature and class selection was performed by Hsieh [127] who used artificial neural networks and statistical analysis to predict or classify the stress-level under voltage stress. The author proposed the thermal profile on the electronic component as the feature that characterize the voltage stress-level on the electronic after performing a statistical analysis that suggested a strong correlation between stress-level and thermal profile. Experiments were performed to determine current readings and the transient temperature behavior for electronic components with nine different levels of stress. After determining the mean and standard deviation for the whole experimental data, the data was divided in three reasonable levels of stress (high, medium, and low levels) or classes out of the nine levels or classes. Three different neural network topologies were proposed: three input nodes, two hidden nodes, and one

output node; three input nodes, three hidden nodes, and one output node; and three input nodes, two hidden layers with two hidden nodes each one, and one output node. The feature variables characterizing better the stress level were the average heating rates (variable depending on electronic temperature profile) for the electronic component at two consecutive times and their summation; these three feature variables were used as the three input nodes. The hidden nodes were chosen to keep a ratio greater or equal to one between the input nodes and the hidden nodes. The output was considered a node with three possible outcomes: high, medium, or low level of stress. Several training functions were tested and the best topology was determined to be the one with three input nodes, two hidden nodes, and one output, because this topology presented a lower average error rate. A statistical analysis was performed for comparison purposes by means of multivariate analysis and factor contribution. The two statistical analyses proved to have a higher average error rate. An analysis of the neural network tolerance to noise was performed too. The author fitted the three classes (low, medium, and high level of stress) grand average cooling rates data to a distribution function. The means and standard deviations for each class were determined, and new sets of data were generated by increasing the standard deviations by 0.2, 0.4, and 0.6; this increases the overlap among classes making difficult to distinguish among classes. The best neural network topology was tested with these sets of data resulting in similar average error rates.

As seen in the previous described researches, artificial neural networks structure is basically base on rule of thumbs like keeping a similar number of hidden nodes as the number of input nodes or classes. Some efforts have been done to use scientific methodologies to determine the best neural network methodology. For example, Cazorla *et al.* [122] used artificial neural networks to characterize the cloud cover in the sky. An all-sky imager was developed to obtain TIFF images from the sky. The authors characterized the clouds in the sky in two steps: development of artificial neural network and optimization of artificial neural network by means of genetic algorithm. A neural

network of perceptrons with three layers was used for the classification task. A total of 18 initial input nodes base on the signal values, mean values for pixel and neighbors, variance values for pixel and neighbors in the gray scale, R channel, G channel and B channel, as well as a dual ratio of the signals for the RGB channels (R/G, R/B, G/R, G/B, B/R, and B/G) were used. Three output classes were defined as opaque cloud, thin cloud, and clear sky. The number of hidden nodes selected was 18 after several tests were performed. A data set of 1000 images was randomly divided in two sets: one for training and one for testing. Different training algorithms were tested and the resilient back propagation algorithm provided the best performance. A linear function for the input layer and a log-sigmoid function for the open layer were determined as the best combination after several tests. After the first neural network configuration with 18 input nodes was determined, a genetic algorithm was used to determine the best inputs or features from the 18 initial inputs. The Genetic algorithm determined the best neural network as a network with three input nodes out of the 18 initial nodes used. The optimized neural network presents an accuracy of 85% versus an 82% obtained for the initial 18 input nodes neural network. The most important benefit of using the Genetic algorithm was the reduction of time to acquire the features or inputs from the images. Another example of the use of genetic algorithm to optimize the neural network structure is shown by Kucuk *et al.* [135]. Kucuk *et al.* [135] used the genetic algorithm to train a three layers feed forward network. The genetic algorithm was basically used to determine the weights giving the best prediction for the structure. The Genetic algorithm begins with an initial configuration or population that is improved by specific fundamental processes which are reproduction based on fitness, crossover and mutation. 1000 epochs were used and hidden nodes were assigned by trial and error as usually. The best topology found was a five input nodes, ten hidden nodes, and one output node. The predicted values were obtained with a 99% of accuracy. In another interesting investigation, Maglogiannis *et al.* [136] used fuzzy logics in conjunction with artificial neural network to generate a more complete classifier. Maglogiannis *et al.* [136] used a Radial Basis Function Neural Network to classify lung tissue with idiopathic pulmonary

fibrosis. They used a fuzzy means clustering algorithm to group the input data into different classes and a fuzzy optimization method to determine the best number of hidden nodes for the neural network. The RBF neural network is a three layer network that is linear with respect to the output parameters. The hidden layer performs a nonlinear transformation and maps the input space onto a new space. The output layer then implements a linear combiner on this space, where the only adjustable parameters are the weights of the linear combiner. The input nodes are passed to the hidden nodes and the hidden nodes response is weighted and passed to the output nodes where and addition process is performed. The training of the RBF network consists of calculating the hidden layer parameters and determining the connection weights between the hidden layer and the output layer. The hidden layers number is usually determined by trial and error. The centers of the hidden nodes are determined iteratively by an unsupervised classifier (usually k-means classifier). The authors proposed a fuzzy means algorithm to determine the centers and hidden nodes improving the speed of selection as no multiple classifications of the whole data are required. However, the best fuzzy centers selection is selected by trial and error (the neural network with the best accuracy). 83700 pixels characterizing the areas of interest were used as the training set. Several RBF neural networks were developed with and average training time of 3 min. A neural network with 13 fuzzy sets in each input dimension and 197 hidden nodes was proven to provide the best performance. Accuracy results were compared with support vector machine (SVM) classifier as being slightly better for the Radial Basis Network.

Another way to improve neural networks classifiers is by using classification in two steps. After classifying the firs set of data, data classified with similar probability between two classes can be classified again. Mittal *et al.* [128] developed a two step neural network model to classify focal liver diseases by means of ultrasound images. 65 typical and 46 atypical images were used to extract 208 texture based features from 800 non-overlapping segmented regions of interest in such images. The texture features were obtained by means of five different extraction techniques: first order statistics, spatial

gray level dependency matrix, gray level run-length matrix, texture energy measures, and Gabor wavelet. The neural network model consisted of an input layer with 208 inputs, a hidden layer and an output layer with five classes (four diseases and normal liver). 20 hidden neurons were determined by a trial and error process to be the best in accuracy and convergence time. The output desired was set to one and the others as zero. The learning algorithm used was based on back propagation with adaptive learning and momentum. A training set of 250 segmented regions of interest with 50 of each class, a validation set of 50 segmented regions of interest having 10 of each class, and a testing set 500 segmented regions of interest were used in the classification procedure. 401 segmented regions of interest where classified correctly out of 500. In a second classification step, a binary neural network was implemented to classify between classes having two very similar high probabilities. For example, if an input was misclassified as class one but the next highest probability is class four, the binary neural network developed was used to classify between classes one and four correctly. By using the 10 binary classifiers among classes, the accuracy percentage was increased in 6.2%.

One of the major issues on artificial neural networks is over fitting. The error on the training set can be very small, but the developed neural network can not classified new situations adequately (i.e. it is a network with poor generalization). This issue was addressed by Vilar *et al.* [137] for the classification of weld defects in radiography images. The authors used three methods to improve generalization: regularization, Bayesian regularization, and early stopping. Regularization consist of modifying the performance function by adding a term consisting of the mean of the sum of squares of the network weights and biases, as well as a performance parameter; this smoothes the network response, but an erroneous performance parameter leads to over fitting or poor fitting. Bayesian regularization implements this performance parameter automatically. Early stopping is the simplest and is implemented by dividing the data sets into a training set, a validation set, and a testing set. The training set is used to train the network, while the validation set is used to test the network during training. The training

and validation sets error reduce as the training progress, but the validation sets error begin to increase when the network over fits the data. The best network topology is returned as the one with the minimum validation error. Neural networks were developed using the generalization methods as well as no generalization method. Regularization and early stopping presented higher mean accuracy in the classification of multiple welding defects. Bayesian low performance in the identification of some defects was attributed to the lack of data samples.

Table 2.3. Requirements to develop or improve neural networks performance.

Requirement or improvement procedure	**Comments**
Training and testing samples should be characteristic of population.	Random training and test samples should be similar in sized so the probability to obtain characteristic samples is high.
Adequate ratio of training sample to inputs.	The ratio of training sample to inputs should be at least 10 to avoid the curse of dimensionality.
Hidden nodes should be limited	Twice the number of input nodes plus one is a sufficient number of hidden nodes to model any continuous function. Too high number of nodes can caused poor generalization.
Good generalization	Early stopping should be used to improve neural network performance for data never seen before.
Classification in two steps	A new classifier can be generated for samples that have very similar probability to belong to two different classes after the first classification is performed.
Optimization procedures	Instead of selecting randomly the number of hidden nodes, optimization procedures like genetic algorithm and fuzzy logics can be used to optimize the neural network performance.

2.4.2. Summary

Neural network is one of the most widely used classifier up to date. In order to improve the performance of neural network classifiers, the selection of features characterizing the data is of great importance. The selection of these input features is performed by means of statistical analysis, supervised classification, and optimization methodologies like genetic algorithm. Although the feature (grand average cooling rate) defining the solder

joint shapes (classes) is already selected in this research, a special section will be reserved to statistically analyze the quality of cooling rate as a feature describing the solder joint shape classes. On the other hand, another way to improve neural network performance is by using two steps neutral network classifiers; the first classifier is used to classify among original classes, and the second classifier is used to classified erroneous classifications on data with similar probabilities of pertaining to two classes. In order to avoid random selection of hidden nodes, neural networks have been trained by means of fuzzy logics and genetic algorithm. Finally, poor neural network generalization (issue that characterizes several developed neural networks) can be improved by means of a technique called early stopping. Table 2.3 shows some of the techniques to develop and improve neural networks performance.

3. METHODOLOGY

3.1. Introduction

The objectives of this research are to understand, model, and predict hidden solder joint shapes in order to achieve better electronics reliability. In order to accomplish these objectives, a methodology compose of three models is proposed. The three models are: an experimental model, a numerical model, and a prediction model (See Figure 3.1 for models relationship). The objective of the experimental model is to understand how the solder joint shapes affect the component surface transient behavior after applying a heat flux. In addition, the experimental model will provide the adequate variable to characterize hidden solder joint shapes as well as the tool to validate the numerical model.

The objective of the numerical model is to simulate the experimental active thermography model and develop a parametric analysis; this analysis will determine the limitations and extend the applicability of infrared thermography. First, the numerical model will be fed with the characteristics of the experimental model; among these characteristics are: experimental setup geometry, experimental conditions, and the experimental results. Among the experimental conditions are: the ambient temperature and the temperatures of the PCB assemblies top surfaces at the beginning of the cooling process. The experimental results used for the numerical model are the temperatures during the cooling process on the top of the PCB assembly as well as the grand average cooling rates. The experimental conditions will be used to develop the numerical model and the experimental results will be used to validate the numerical model. Second, as the classification accuracies will determine the characteristics that the thermal response should meet in order to discriminate adequately among hidden solder joint shapes, these thermal response characteristics will be fed to the validated numerical model to perform a parametric analysis. The parametric analysis will determine the adequate active

thermography parameters needed to achieve a good characterization of solder joint shapes according to the classification accuracies.

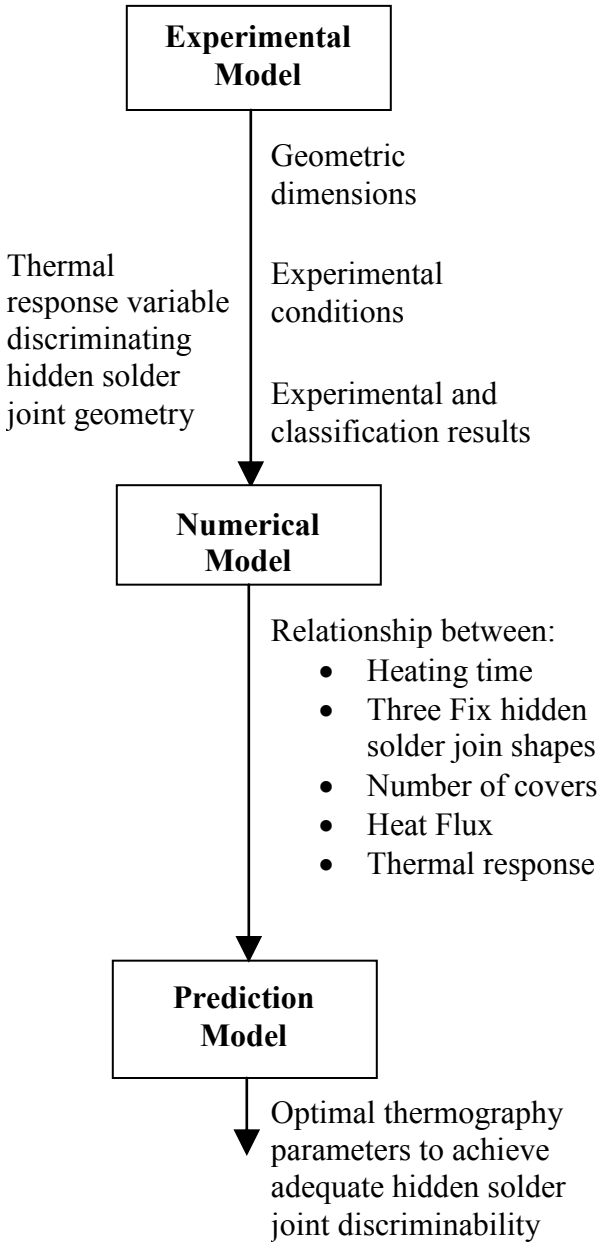

Figure 3.1. Diagram showing the relationship between the models conforming the methodology.

Finally, the objective of the prediction model is to predict the optimum characteristics of the active thermography to discriminate among hidden solder joint shapes. The parametric analysis relationships between the active thermography and the PCB assembly parameters will be provided to the prediction model. The prediction model will generate a parametric equation to determine the adequate active thermography parameter for the hidden solder joint shapes discrimination. This model will provide the electronic industry a methodology to discriminate among hidden solder joint shapes and to determine the quality of hidden solder joints by means of its shape. Sections 3.2, 3.3, and 3.4 show details of the methodology followed to generate the experimental, numerical, and prediction models, respectively.

3.2. Experimental Model

The experimental methodology will be implemented by means of a low cost and effective active infrared thermography nondestructive experimental setup. The experimental setup will be based on the common knowledge about infrared thermography systems on the technical literature (see Sections 2.2.4 and 2.2.5). After the experimental results are obtained, the experimental data capability to discriminate among different solder joint shapes will be evaluated by means of qualitative and statistical analyses, and the classification models. The assumptions used in the experimental model are as follows:

- The solder joint shape will be considered as cones with three different cone angles (60°, 90°, and 120°) but same volume. The 60° solder joint will be considered as a good solder joint in contact with the chip and the chip carrier. The rest of them will be considered as solder joints that are not in contact with both surfaces. The cone angle will provide a different depth from the chip surface. The solder joint shapes and dimensions were motivated by the necessity of a chip

fabricant to analyze the effect of this solder joint defects and the availability of 60º, 90º, and 120º drill bits to fabricate shaping molds.

- ❖ The solder joint surfaces have the same emissivity.
- ❖ When irradiated, the solder joint, board, and cover surfaces are being irradiated uniformly by the external heat source (halogen lamp).
- ❖ The chip carrier and the chip have the same composition.
- ❖ The solder joints are hidden from view.
- ❖ The solder will behave qualitatively in a similar way as in real chips assemblies.
- ❖ The solder joint with no cover is useful as a benchmark criterion for the solder joint discrimination.

According to the assumptions mentioned above, experiments will be conducted and the experimental data will be evaluated by means of qualitative and statistical comparisons, and artificial neural networks classification. In the experimental analysis, board samples will be heated and the cooling process will be recorded by means of an infrared camera. The experimental methodology is organized as follows: Section 3.2.1 describes the experimental setup, Section 3.2.2 explains the boards prototype construction, Section 3.2.3 describes the experimental procedure, Section 3.2.4 explains the experimental raw data (thermal images) processing, Section 3.2.5 describes the design of experiments, Section 3.2.6 indicates the statistical analysis performed, and Section 3.2.7 contains the classification procedure.

3.2.1. Experimental Setup

The experimental setup consists of three main components: a microcontroller, a chamber, and a PC for data acquisition. The chamber consists of two sections, the heating section and the cooling section. The heating section is equipped with a 150 Watt halogen lamp (halogen lamps are commonly used as the heat source for active thermography [69]) to heat the boards and a mechanical fixture that holds the PCB on position. The heating

section walls are composed of three layers: an outer acrylic layer, a middle Styrofoam layer, and an inner Mylar layer. The Styrofoam layer has the purposed of avoiding heat losses from the heating section to the environment, while the Mylar layer is intended to reflect the radiative energy from the lamps to the board.

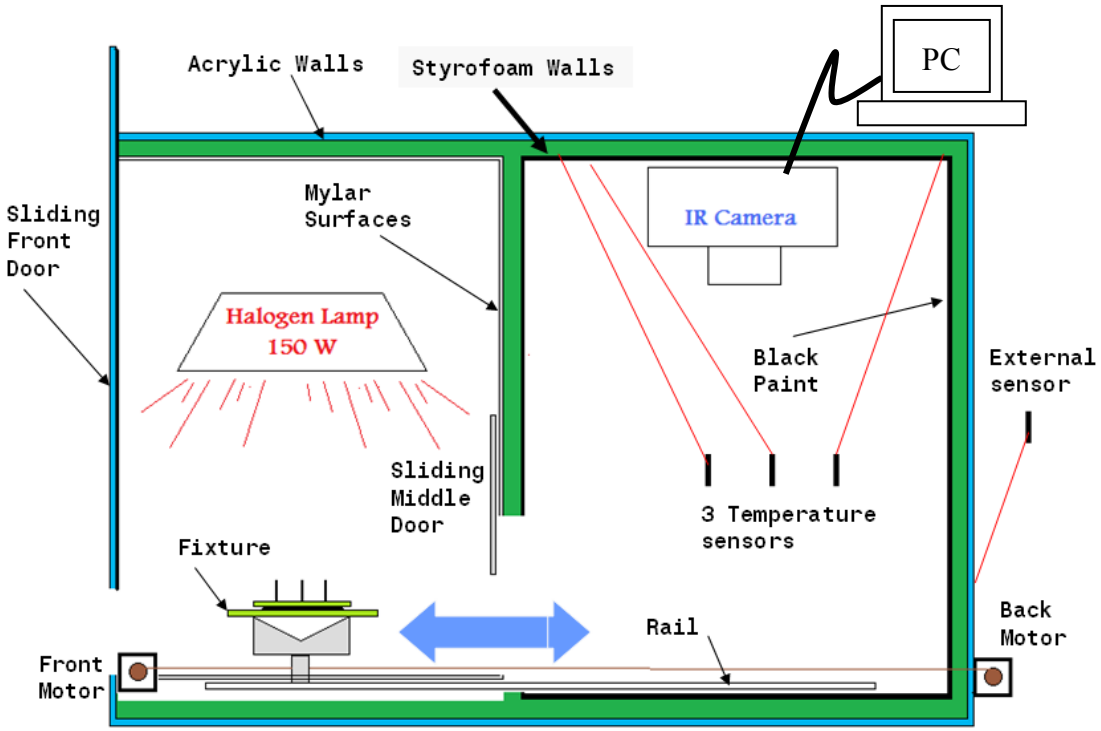

Figure 3.2. Experimental Setup.

In addition to the Mylar layer in the walls, the fixture structure surface is coated with a Mylar layer too. The top surface of the boards and fixture platform are covered with black tape in order to get a maximum amount of the energy absorbed by the board and a uniform emissivity. On the other hand, the cooling section is equipped with an infrared camera on its ceiling and RTD sensors to monitor the temperature inside (three sensors) and outside (one sensor) of the chamber. The cooling section walls are composed of

three layers: an outer acrylic layer, a middle Styrofoam layer to avoid heat losses from the cooling section to the environment, and an inner black mate paint layer to avoid reflections from the cooling section walls. The infrared camera is a Compix PC2100 with a resolution of 244×193 pixels. The measuring temperature ranges are from 17 to 150 °C. The infrared camera can detect small temperature changes (0.2 °C) of an object's surface and capture a complete image in 12 seconds. There is a flexible door that connects the heating section with the cooling section; such door separates both sections during each process, but allows the easy automatic translation of the assembly from section to section. The movement of the fixture is managed by means of a rail (rail that goes from the heating section to the cooling section), pulley-belt system, and two small electrical motors. The microcontroller manages all of the electronic components in the right sequence by means of two switches: switch 1 (green led) starts the experimental process, and switch 2 (red led) returns detection system to initial condition. The PC allows acquiring the images from the camera as well as processing the images to extract the temperatures and grand average cooling rates. Figure 3.2 shows the experimental chamber and its components.

3.2.2. Board Prototypes

Three kinds of PCB assemblies will be made for the experimental model: no cover assembly, one cover assembly, and two covers assembly. The PCB and covers dimensions are 44.45 mm width, 44.45 mm length, and 1.6 mm thickness. As mentioned before, the top surface of the board and the covers will be covered with black tape allowing a more uniform heating and material surface properties. After the tape is collocated, three different solder joints will be attached to the board. In difference to the board surface, the solder joints are kept with its inherent properties as the main objective is to study the solder behavior. The solder joints will be shaped by a compression method. First, the solder will be attached to a copper wire; second, the solder paste will be rapidly shaped by the mold before the solder cools down; finally, the excessive solder

will be retired by polishing with a small precision file set. Velcro slices will be attached to the bottom surface of the board and the top surface of the fixture in order to keep both parts attached during experiments. A schematic view of the board, solder joints, and molds can be seen in Figure 3.3. Figure 3.4 shows the schematic for no cover, one cover, and two covers assemblies.

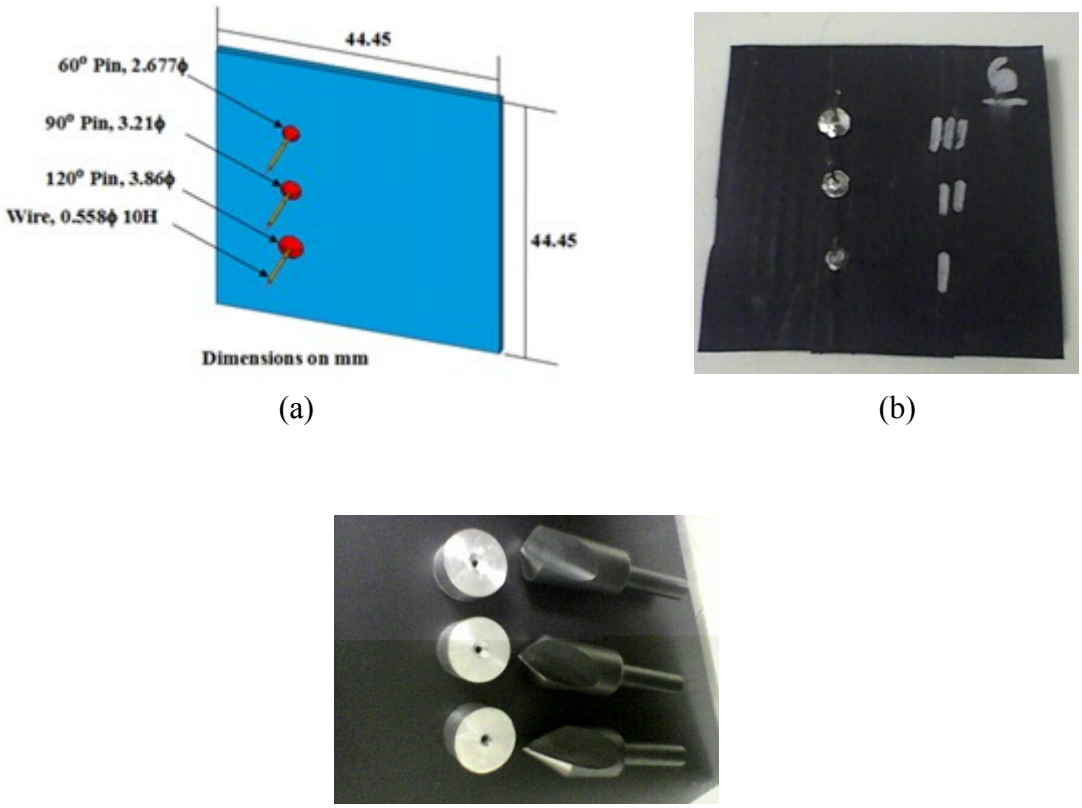

(a) (b)

(c)

Figure 3.3. Schematic of the Board. (a) Dimensions, (b) actual board, (c) and molds. (Dimensions are in millimeters. ϕ and H means diameter and height, respectively)

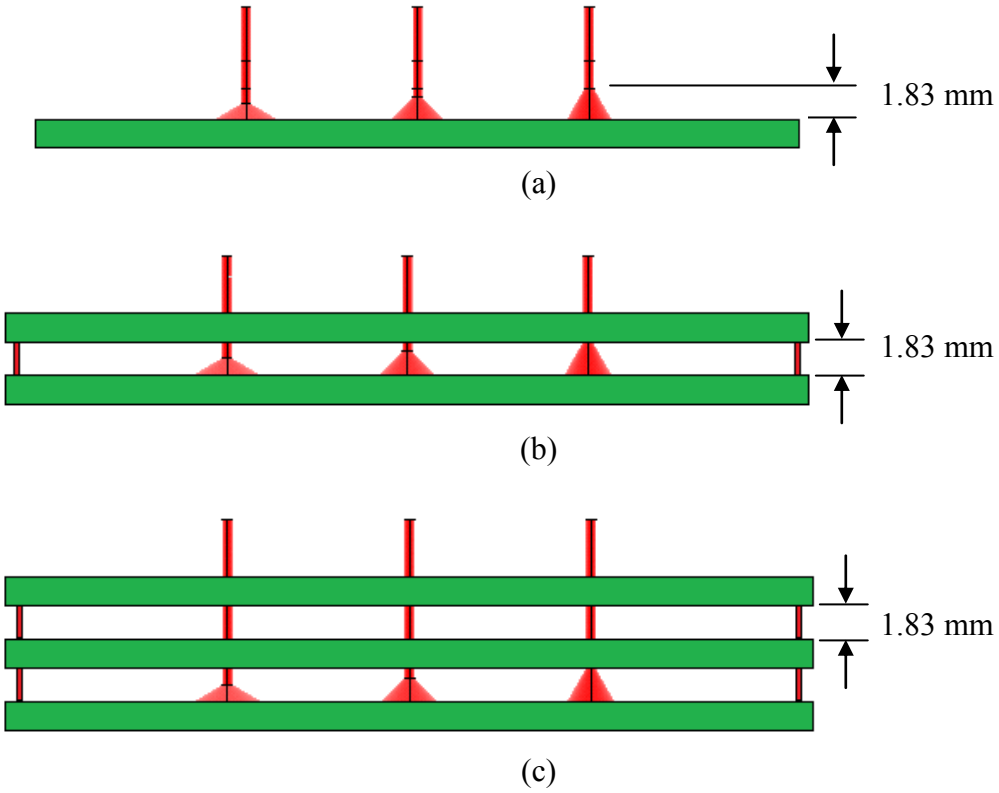

Figure 3.4. PCB assemblies: (a) no cover, (b) one cover, (c) and two covers.

3.2.3. Experimental Procedure

The experimental procedure consists of a certain amount of heating time and a certain amount of cooling time or scanning time. These times will be determined after performing some preliminary experiments. The experimental procedure can be divided in the next steps:

1. Start system detection by turning on main switch, computer, and open the Windows Thermal Evaluation Software (call from now on WinTES). WinTes controls the infrared camera in order to take automatically thermal images in the time interval required. It is important to mention that variables as the ambient temperature, focus, emissivity of the object, and scanning interval are the same

and established by means of WinTes for every one of the 15 experiments performed. All WinTes parameters should be established in this step, so image acquisition can be started by clicking “START” automatic scanning button.

2. Set the board on the top surface of the fixture. The board is cautiously located so that its top surface is parallel to the lamps and lens of the infrared camera. There are some alignment marks in the top surface of the fixture platform to assure the same board position every time that a board is collocated. Finally, front gate is closed.
3. Monitor temperatures in chamber. After the board is set in the correct position, the chamber is sealed and the temperature in the chamber is monitored by means of three thermocouples to assure that every experiment is conducted under the same initial conditions. The temperature is considered steady when does not change for around five minutes.
4. Flip up switch 1. The heating process is initialized by means of this switch that turns the lamps on and off after the required heating time is completed. Next, the middle door is opened, the back motor pulls the PCB assembly to the cooling section, the middle door is closed, and a green led lights indicating heating process is finished.
5. Initialize images acquisition by means of WinTes and flip down switch 1. The frequency of acquisition will be determined according to the classification procedure and the preliminary experiments.
6. Stop image acquisition and flip switch two up when the required cooling time is reached. This switch will open the middle door, bring back the fixture to the heating chamber by means of the front motor, close middle door, and turn on a red led indicating that the system is ready for another experiment.
7. Take off board and begin from step 2 the next experiment.

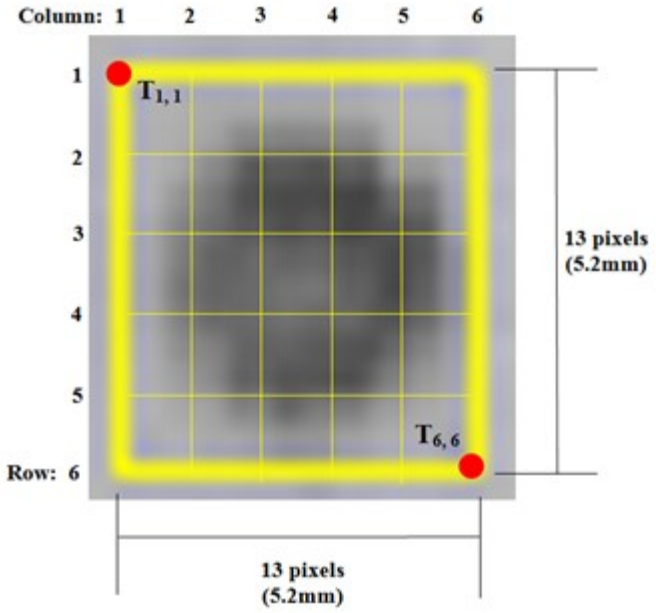

Figure 3.5. Region selected to obtain temperatures for solder joints thermal signatures.

3.2.4. Experimental Data Processing

After the experimental procedure is performed, the thermal images must be processed in order to obtain the solder thermal behavior. In particular, the experimental methodology can be considerate as a semi automated methodology, because human interaction is needed to identify the thermally abnormal zones in the thermal images. Although an automated methodology to identify and to characterize the thermally abnormal zones is desirable, developing such method is challenging and out of the scope of this investigation; further information about the identification methods can be found in the technical literature [67]. The thermal images are processed by means of ThermalView computational software. In order to obtain the temperature of the solder joint thermal signature, a square region surrounding the area of interest was selected (See Figure 3.5). The selected square region and the solder joint zone symmetry lines should approximately overlap each other. It is important to mention that the selected area dimensions were kept constant among solder joints (13×13 pixels) at the maximum

spatial resolution of the camera. Next, the square region is divided in 6 rows by 6 columns. Temperatures were obtained in the intersection among the rows and columns; therefore, 36 readings were acquired and averaged over the square region according to the next expression:

$$T = \frac{\sum_{j=1}^{6} \sum_{k=1}^{6} T_{k,j}}{36} \tag{3}$$

Similarly, grand average heating rate is defined in function of the average temperatures and is given by Equation (2).

Figure 3.6 shows an example of a thermal image taken by means of the infrared camera; this picture shows three black spots marking the solder shape thermal signature. The smallest one is the 60° solder joint, the biggest one is the 120° solder joint, and the middle size one is the 90° solder joint. Here and after, the solder joint shape positions will be referred as 60, 90, or 120 positions. The average temperature or average of the grand average heating rates at the 60, 90, and 120 positions will refer to the average values of these variables for the region enclosed by the yellow square at such positions. At the end of the thermal image processing, curves for the average temperatures and grand average heating rate can be generated for each experiment (See Figure 3.7 for the average of grand average heating rate sample). As seen in Figure 3.7, a grand average heating rate per solder joint position is obtained every 20 seconds; according to this, the next notation will be used when referring to individual grand average heating rates:

$$\begin{aligned} H_1 &= \textit{grand average heating rate at 20 seconds of cooling} \\ H_2 &= \textit{grand average heating rate at 40 seconds of cooling} \\ &\vdots \\ H_i &= \textit{grand average heating rate at } i{\cdot}20 \textit{ seconds of cooling} \end{aligned} \tag{4}$$

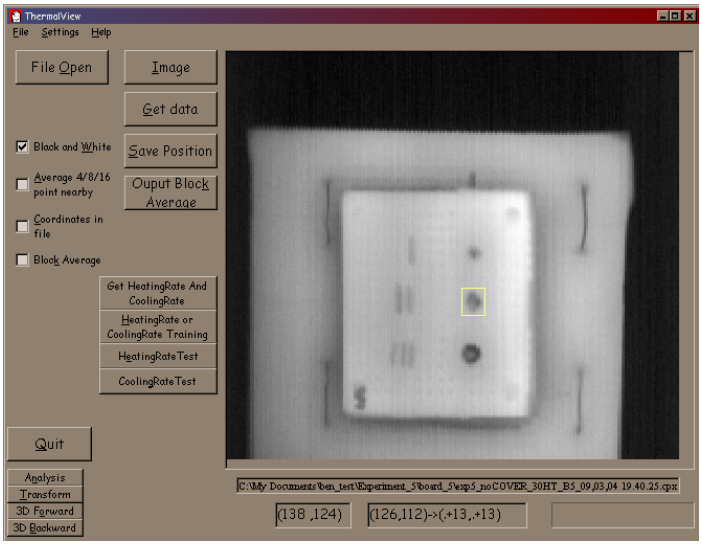

Figure 3.6. Thermal image of PCB assembly.

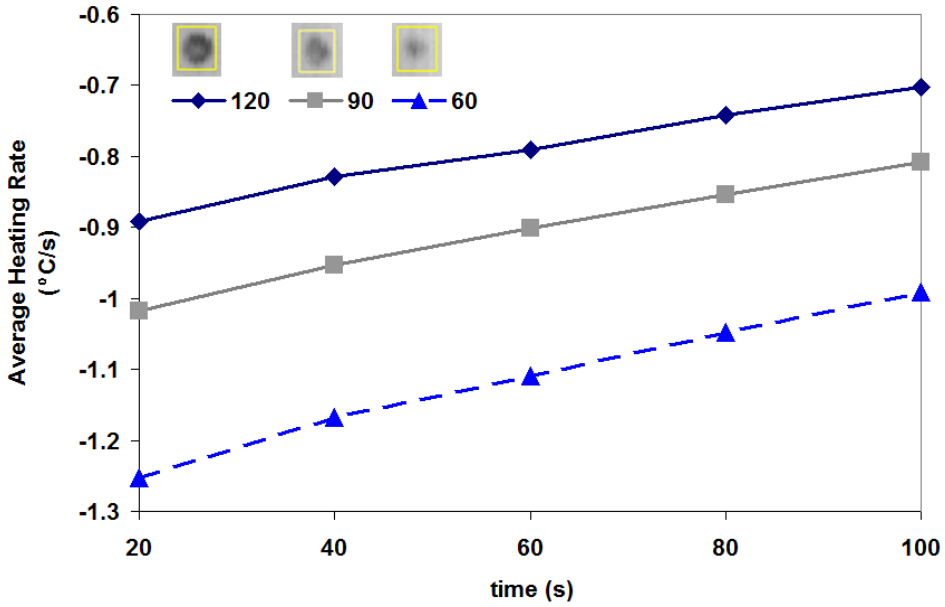

Figure 3.7. Square region grand average heating rate for 60, 90 and 120 positions.

Finally, as this work deals only with a cooling process, a new variable called grand average cooling rate is defined as the negative of the average heating rate; this will avoid negative values in graphs and results presented in the results section. Therefore, the grand average cooling rate is defined as:

$$C = -H \tag{5}$$

Similarly as with grand average heating rate:

$$C_i = \textit{grand average cooling rate at } i \cdot 20 \textit{ seconds of cooling} \tag{6}$$

As mentioned before, cooling rate is used as the main variable to characterize the solder joint thermal behavior, because cooling rate is a signal that interprets how fast and object surface is cooling down. Object properties affecting directly this variable are thermal conductivity, thermal diffusivity, and geometry.

3.2.5. Design of Experiments

In order to determine the adequate parameters for the experimental thermography procedure, hypotheses must be formulated regarding the parameters affecting the capability to differentiate among solder joint shapes. After hypotheses are formulated, preliminary experiments should be performed to confirm hypotheses and to determine optimum values for such parameters. Finally, multiple experiments should be performed under the optimal configuration to prove repeatability.

3.2.5.1. Hypotheses

According to the literature review on infrared thermography, there is an adequate amount of heating time when the visibility of a hidden defect is the highest. In this case,

it is of interest the capability to differentiate among the signals for three different solder joint shapes. As the solder joints are affected in different ways by the heating time, there must be an adequate heating time when the differences among solder joint shapes signals are the highest. On the other hand, the signals for the solder joint shapes are monitored after the heating is ended during cooling process. During the cooling process, the system cool downs until the steady state is reached and the signals for every solder joint shape are the same; therefore, there must be an appropriate scanning time during which the signals differences among solder joint shapes is still significant. An additional parameter to determine is the scanning frequency, but this parameter depends highly on the scanning time, and the number of total experiments planned to prove repeatability and to generate a classification methodology. In summary, two hypotheses are formulated:

- The amount of heating time will depend on the capability of the signals to discriminate among solder joint shapes.
- The total scanning time will depend on the time during which there is a significant difference among solder joint shape signals.

3.2.5.2. Preliminary Experiments

According to the two formulated hypotheses on section 3.2.5.1, two preliminary experiments will be performed:

Preliminary experiment 1: the amount of heating time will be varied from 10 to 30 s in intervals of 10 seconds. These times are chosen because too low heating times might not provide enough energy to the sample, and too high heating times will increase test length.

Preliminary experiment 2: the cooling process will be monitored after the heating times are applied on the preliminary experiment 1. The cooling process will be monitored for 600 s to ensure the signals are reaching the steady state.

3.2.5.3. Experiments

Ten boards with three different solder shapes will be constructed; 15 experiments will be performed in each of them for a total of 150 samples (50 for visible solder joints, 50 for solder joints hidden by one cover, and 50 for solder joints hidden by two covers). Optimum amount of heating time and scanning time determined on preliminary experiments will be used to perform these 15 experiments. After the experiments are finished, the experimental data will be analyzed to determine if the solder joint shapes are statistically different when described by such data. After proving that solder joint shapes are statistically different, a classification methodology will be performed to determine the degree of discriminability provided by the experimental data as well as the parameter characterizing such degree of discriminability.

3.2.6. Statistical Analysis

One of the most used ways to determine if classes are different when describe by a dependant variable is one way ANOVA. An analysis of variance (ANOVA) does not only determine if the classes are statistically different, but gives also a numerical measure of the grand average cooling rate differences that will permit to discriminate among the different solder joint shapes (classes). In this case, a multivariate analysis of variance (MANOVA) is required, because multiple dependant/response variables will be used to discriminate among solder joint shapes or classes. A multivariate analysis of variance will test whether there are statistically significant means differences among classes on a combination of multiple response variables. Next, the procedure to develop a multivariate analysis of variance is described in detail.

Assume that there are I classes of multivariate observations with n_i observations in class I, $i=1,...,I$. Then, the statistical model is given by the next expression:

$$y_{ij} = \mu_i + e_{ij}, \quad Var(e_{ij}) = \sum \tag{7}$$

The hypothesis of no class difference at all is given as

$$H_0: \quad \mu_1 = \cdots = \mu_I \tag{8}$$

Next, the class and overall averages are determined as:

$$\bar{y}_i = \frac{1}{n_i}\sum_{j=1}^{n_i} y_{ij}, \quad \bar{y} = \frac{1}{n}\sum_{i=1}^{I} n_i \bar{y}_i \tag{9}$$

where $n = n_1 + \cdots + n_I$. Now, the summations of the variance between and within classes are given by the next expressions:

$$\begin{aligned} SS_{between} &= \sum_{i=1}^{I} n_i \left(\bar{y}_i - \bar{y}\right)\left(\bar{y}_i - \bar{y}\right)^T \\ SS_{within} &= \sum_{i=1}^{I} \sum_{j=1}^{ni} \left(\bar{y}_{ij} - \bar{y}_i\right)\left(\bar{y}_{ij} - \bar{y}_i\right)^T \end{aligned} \tag{10}$$

The more used criterion to test the hypothesis that the classes have identical means is the Wilks criterion and is given by the next expression:

$$\Lambda = \frac{\left|SS_{within}\right|}{\left|SS_{between} + SS_{within}\right|} \tag{11}$$

The Wilks lambda values can be approximate by means of a central Beta distribution (F) under the null hypothesis, assuming independent units, multivariate normality, and homogeneous covariance matrices. The Beta distribution is given by the next expression:

$$F = \frac{1-\Lambda^{1/s}}{\Lambda^{1/s}} \frac{m(s) - \frac{p(df_h)}{2} + 1}{p(df_h)},$$

$$m = df_e - \frac{p - df_h + 1}{2}, \tag{12}$$

$$s = \sqrt{\frac{p^2\left(df_h^2\right) - 4}{p^2 + df_h^2 - 5}},$$

where p, df_h, and df_e are the number of response variables, the hypothesis degrees of freedom, and the error degrees of freedom, respectively. According to the values taken by F, the probability of the null hypothesis can be determined with the 1% level of confidence by means of a table for the F distribution listing the degrees of freedom, and the values of F with 5% and 1% levels of confidence. If $F<F_{1\%}$ the null hypothesis can be accepted and therefore the classes means are the same. Next, a series of statistical tests can be done to determine the dimensions needed to interpret the classes differences. This procedure is done by partitioning the Λ statistic for every *n-dimension* tested and generating new values of F to test the hypothesis that at least *n-dimensions* are needed to interpret classes differences. Such partitioning can be expressed by the next expression:

$$\Lambda = \prod_{v=n}^{r} \left(\frac{1}{1+\lambda_v} \right) \tag{13}$$

where $r=min\ (p,\ df_h)$ and λ_v are the eigenvalues for the matrix:

$$\left(SS_{within}\right)^{-1} SS_{between} \tag{14}$$

More details about this procedure can be found at [138]. In this research the MANOVA will be performed by means of the MATLAB statistics toolbox function "*manova1*". A simple command line, "*[d, P] = manova1 (x, classes)*", will perform the MANOVA;

here ***x*** is a matrix containing *m-observations×n-response variables*, *classes* is an array containing the corresponding classes for each component of the matrix ***x***, and *d* and *P* are two parameters describing the MANOVA results. A *d=0* indicates the classes of data have the same means. A *d>0* indicates that the data has different means, and that *d-dimensions* are needed to describe the differences. The *P* values describe the results of testing if at least *d-dimensions* are needed to interpret classes differences. A *P* value less than 0.05 rejects the hypothesis of a *d-dimensional* space with a 95% level of confidence.

3.2.7. Classification Procedure

Artificial neural networks are widely used to characterize experimental data describing hidden defects properties [135, 137, 139-147]. Artificial neural networks, as its name indicates, makes use of very low level programming to solve complex problems by imitating the biological neural network. In special, artificial neural networks are perfectly suited for problems of recognition, filtering and control. An artificial neural network is basically composed by multiple inputs with different importance (weights), a cell body where the inputs are processed, and multiples outputs carrying the results of the computations made in the cell body. Three layers neural networks have proven to be adequate for several complex classification problems and are widely used by the scientific community (see Section 2.4.1). In this research a neural network of perceptrons is used (see Figure 2.1). The perceptron computations consist of setting the weights of the inputs until the appropriate outputs are obtained. The act of setting the weights is called training the neural network. In this particular case, the inputs will consist of the experimental grand average cooling rates, while the outputs will be the solder joint shapes angles (60°, 90°, and 120°). Basically, the artificial neural network procedure will be able to classify the solder joint shape by means of its grand average cooling rate. High predictions ratios by the model are expected for consistent data; therefore, high prediction ratios for the experimental data under evaluation will prove the

capacity of the methodology to characterize different solder joint shapes. Figure 3.8 shows a scheme of the neural network used in this research.

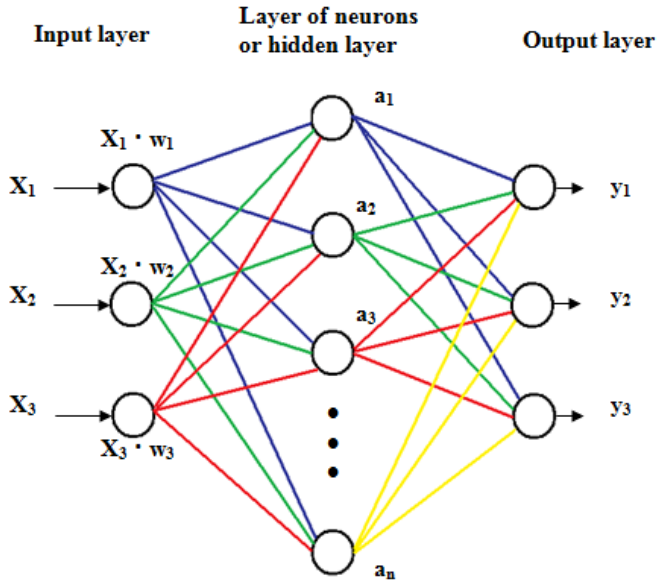

Figure 3.8. Three layers artificial neural network structure (a and y are the outputs of the perceptrons in layers 2 and 3).

A feed-forward back propagation network is developed for the experimental set of data by means of the Neural Network Toolbox of MATLAB. Multiple parameters are involved in the development of an adequate neural network model; such parameters include number of input nodes, number of hidden nodes, training function, among others. Several functions were tested to be the transfer or activation function for the input and output layers, and the "tansig" function was the one providing a better performance. The learning function for the weights and biases used was a gradient descent learning function that is very fast; this training function (trainrp) iteratively adjusts the weights and biases of the network to minimize the network performance function gradient. The gradient is determined using a technique called backpropagation that involves

performing computations backward through the network. According to Jain *et al.* [117], it is recommended that the ratio of the samples for training to the number of inputs is higher than 10 to allow a proper classification or prediction. In this case, the number of training samples per class is 30, therefore a maximum of three inputs should be used (more than three input nodes will worsen prediction accuracy). In relation to the three input nodes, different alternatives (alternatives 1, 2, and 3) were selected according to Hsieh *et al.* [85] who used heating rates as input nodes too. In addition to the alternatives used by Hsieh *et al.* [85], four additional alternatives (alternatives 4, 5, 6, and 7) were tested to analyze the effects of the number of input nodes in the network behavior. Such input nodes alternatives are:

Alternative 1

- Input node 1: grand average cooling rate at *20 s* (C_1).
- Input node 2: grand average cooling rate at *40 s* (C_2).
- Input node 3: summation of grand average cooling rates at *20* and *40 s* (C_1+C_2).

Alternative 2

- Input node 1: grand average cooling rate at *20 s* (C_1).
- Input node 2: grand average cooling rate at *40 s* (C_2).
- Input node 3: standard deviation of grand average cooling rate values.

Alternative 3

- Input node 1: summation of grand average cooling rates at *80* and *100 s* (C_4+C_5).
- Input node 2: average for the rate of change in grand average cooling rate from *20 s* (C_1) to *60 s* (C_3), which is given by the next expression:

$$RC_{(1-3)} = \frac{|C_3 - C_2| + |C_2 - C_1|}{2} \tag{15}$$

- Input node 3: grand average cooling rate from *20* (C_1) to *40 s* (C_3).

Alternative 4

- Input node 1: grand average cooling rate at *20 s* (C_1).
- Input node 2: grand average cooling rate at *40 s* (C_2).
- Input node 3: grand average cooling rate at *60 s* (C_3).
- Input node 4: grand average cooling rate at *80 s* (C_4).

Alternative 5

- Input node 1: grand average cooling rate at *20 s* (C_1).
- Input node 2: grand average cooling rate at *40 s* (C_2).
- Input node 3: grand average cooling rate at *60 s* (C_3).

Alternative 6

- Input node 1: grand average cooling rate at *20 s* (C_1).
- Input node 2: grand average cooling rate at *40 s* (C_2).
- Input node 3: grand average cooling rate at *60 s* (C_3).
- Input node 4: summation of grand average cooling rates from *20* to *60 s* ($C_1+C_2+C_3$).

Alternative 7

- Input node 1: grand average cooling rate at *20 s* (C_1).
- Input node 2: grand average cooling rate at *40 s* (C_2).

The number of hidden nodes will be varied from five to nine. According to the Kolmogorov's Theorem [148], twice the number of input nodes plus one is a sufficient number of hidden nodes to model any continuous function; therefore, nine nodes is the maximum number of hidden nodes used. In summary, a neural network with three layers,

variable number of hidden nodes and input nodes, “tansig” transfer function, and a backpropagation algorithm to train the network is used.

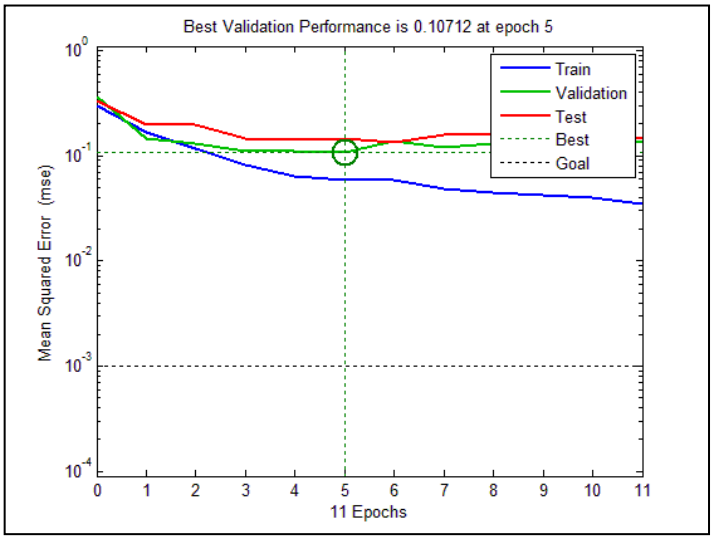

Figure 3.9. Validation performance for the feed-forward backpropagation network.

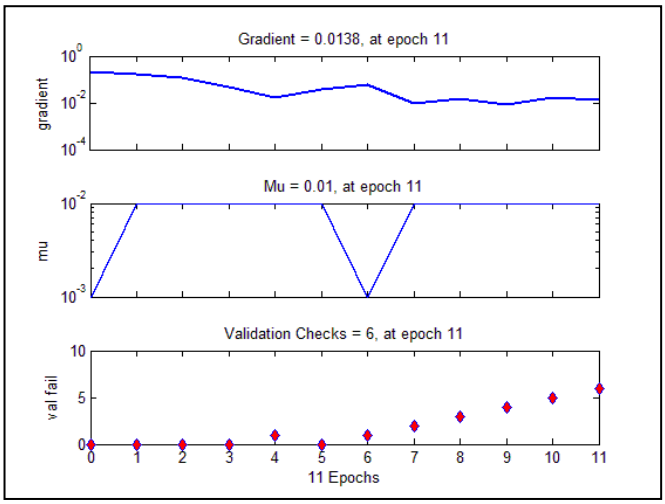

Figure 3.10. Typical training state for the feed-forward backpropagation network.

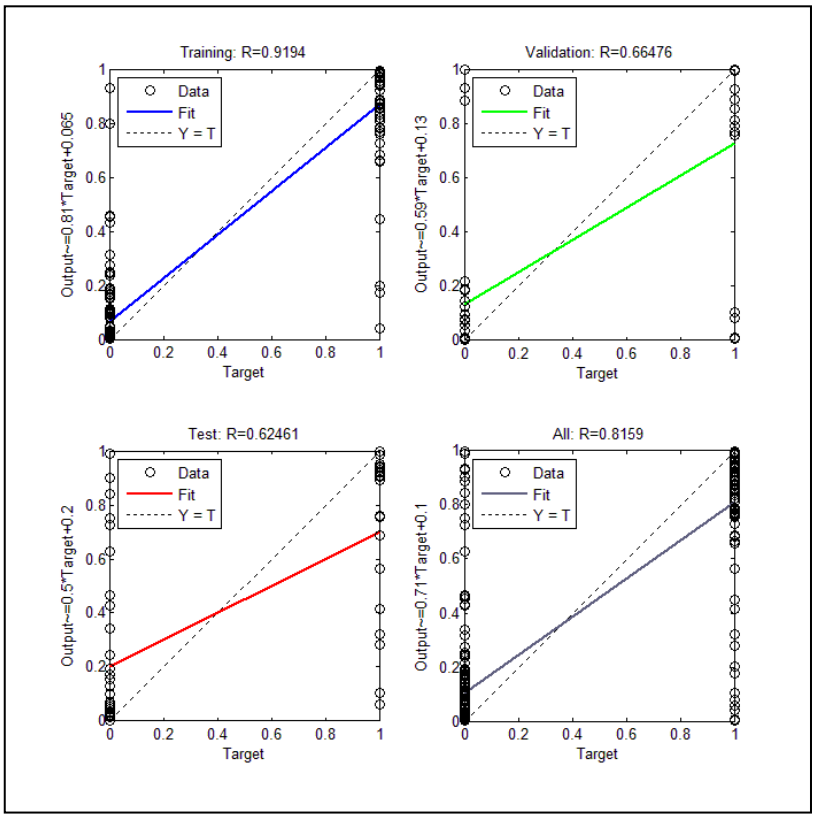

Figure 3.11. Typical linear regression for the feed-forward backpropagation network.

In order to test the neural network, the sets of data are divided in: 60% of the data to develop a network, and 40% to test such network. First, the 60% of the data is used to develop a network by means of the training function, "train", which is incorporate in MATLAB; second, the network was tested for the rest of the data by means of the MATLAB command "sim". As an example of the results obtained with MATLAB, Figures 3.9 to 3.11 show an example of the performance, training state, and linear regression for a neural network developed using MATLAB. There are three lines in the performance and linear regression plots, because the input sets of data are randomly divided into three sets by the Neural Network Toolbox of MATLAB. 60% of the data are used to train the network. 20% of the data are used to validate how well the network generalized. Training on the training data continues as long as the training reduces the

network's error on the validation data. After the network learns the training set (at the expense of generalizing better), training is stopped. Finally, the last 20% of the data provide an independent test of the network generalization for data never seen. This technique automatically avoids the problem of over fitting already mentioned on the literature review [149]. Figure 3.9 shows the best validation performance, while Figure 3.10 shows when the training is stopped; training stops when the validation error increased for six iterations or epochs (i.e. the increment in the validation error implies poor generalization). Figure 3.11 shows the linear regression results for the training, validation, and test data. Regression is a function integrated into the Neural Network Toolbox of MATLAB that analyzes the feed-forward backpropagation network response; the closer the solid line is to the dashed line, the better the performance of the network. Finally, the network developed by MATLAB is tested. If the prediction accuracy of the network is low, the neural network is initialized iteratively until the best accuracy is obtained. Appendix A shows an example of the MATLAB script developed for alternative 3 and no cover results.

3.2.8. Summary

The experimental model has the objective to understand how the solder joint shapes affect the component surface transient behavior after applying a heat flux. In addition, the experimental model will provide the adequate variable to characterize hidden solder joint shapes, as well as a tool to validate the numerical model. The experimental methodology will be implemented by means of a low cost, but effective, active infrared thermography nondestructive experimental setup. The experimental setup consists of an infrared camera, an environmental chamber, a halogen lamp, a microcontroller, and a PC for data acquisition. The experimental PCB assembly prototypes will consist of PCB assemblies with no cover, one cover, and two covers; the PCB assemblies will have three solder joint shapes with 60°, 90°, and 120° cone angles. The experiments will be performed inside an environmental chamber with two sections (heating and cooling

sections). The experimental procedure will consist of heating the PCB assembly by a halogen lamp inside the heating section, moving the PCB assembly to the cooling section, and monitoring the thermal transient behavior during the cooling process by means of an infrared camera. Two preliminary experiments will be performed to determine the adequate heating time and scanning time for the active thermography methodology; after these two parameters are established, multiple experiments will be performed in no cover, one cover, and two covers PCB assemblies to determine the thermal response variation with the solder joint shapes. A multivariate analysis of variance (MANOVA) will be done on the experimental data to prove that the solder joint shapes are statistically different when described by the grand average cooling rates. Finally, an artificial neural networks based classifier will be used to classify the solder joint shapes in function of the grand average cooling rates. This classification procedure will serve to determine the adequate parameters to achieve a good discriminability of the solder joint shapes.

3.3. Numerical Model

The main objective of the numerical methodology is to develop a numerical parametric model that can be useful to further investigate the limitations of the solder joint shape characterization infrared thermography methodology proposed. As explained in Section 1.2, the infrared thermography methodology requires heating up the object under study by means of a halogen lamp; next, the object temperature behavior is obtained as the object cools down. The most important thermal process is the thermal exchange by radiation in the heating section with a special emphasis in the energy gained by the solder surfaces. The thermal process in the heating chamber is a combined transfer phenomena, because heat transfer by radiation, convection and conduction is exchanged among the different elements of the heating section. Although the most important mechanism exchange is the radiation heat transfer, the heat transfer by conduction among the solder joints and the boards is vital for the correct determination of the solder

joints behavior. The solder joints have similar length in the three dimensions and the low conductivity of the board material in comparison to the solder material makes even more important to consider the solder joints conduction 3D behavior. Radiation exchange participation of the air can be neglected because air behaves as a nonabsorbing and nonscattering medium at moderate temperatures [150]. The air is not in movement and to simplify the analysis, the natural convection will be considered according to convective empirical correlations; therefore, only the radiation among surfaces and the conduction process will be analyzed in detailed. The empirical convective correlations depend on the surfaces geometries and were established at:

- Horizontal surfaces at the top cover, chamber top and bottom surfaces, and fixture top surface.
- Vertical cylinder at the exposed parts of the wires.
- Vertical surface at lateral surfaces of the covers, walls, air gaps, fixture, and board.

The convective equations correlations for every kind of surface can be found in the technical literature on heat transfer [151-153] and are given on Appendix B. It is important to mention that convective coefficients are updated as time progresses, because the convective coefficient depends on the surface temperature (variable over time) and the ambient temperature (constant over time).

The radiation exchange among surfaces must be analyzed as a close enclosure. In this case, the surfaces are considered gray and diffuse surfaces. This assumption is quite common to simplify radiation analysis. The equation governing the radiation exchange in close enclosures for gray diffuse surfaces is given by the next expression:

$$\frac{q(\vec{r})}{\varepsilon(\vec{r})} - \int_A \left(\frac{1}{\varepsilon(\vec{r}')} - 1 \right) q(\vec{r}') dF_{dA \to dA'} + H_o(\vec{r}) = E_b(\vec{r}) - \int_A E_b(\vec{r}') dF_{dA \to dA'} \qquad (16)$$

where q is the heat flux on the surface, ϵ is the thermal emissivity, *Ho* is the thermal irradiation, E_b is the thermal emission, dF is the differential view factor from dA to dA', and $\vec{r}$ and $\vec{r}'$ are the position vectors for the differential areas dA and dA', respectively. Figure 3.12 shows a schematic of the enclosure.

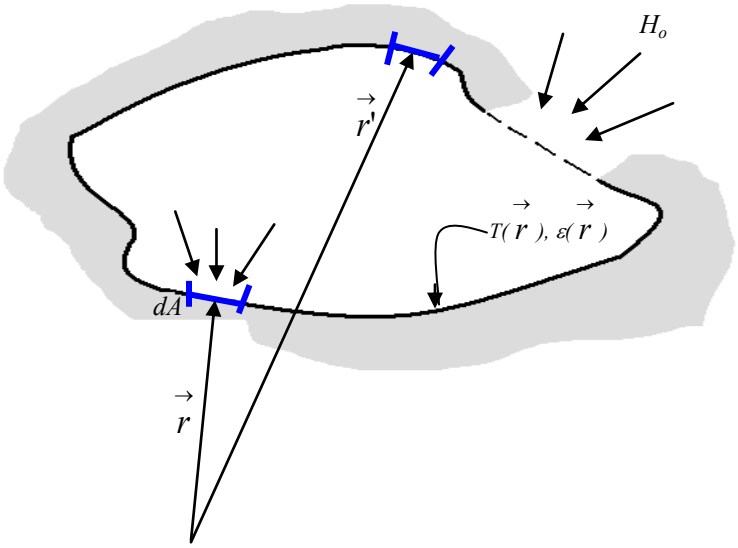

Figure 3.12. Close enclosure representation in thermal radiation exchange.

If the enclosure is break into N-isothermal surfaces and properties are average over each surface, the previous equation is simplified to the next expression:

$$\frac{q_i}{\varepsilon_i} = E_{bi} - \sum_{j=1}^{N} J_j F_{i \to j} - H_{oi} \qquad i = 1, 2, \ldots, N \qquad (17)$$

although previous expression looks quite simple, the determination of the view factors is the most difficult task to solve such equation. In addition, the temperature over the chamber is only uniform at the beginning of the heating process; after the heating process starts, the temperatures of each surface will vary according to each surface thermal property. The simplest way to determine view factors is by means of tables. Unfortunately, view factors for the geometries as the cones are not available. Other methods required the determination of fourth order integrals, or second order integrals if contour integration is used. Commercial and non commercial software is available too, but any method involves the use of numerical methods. Therefore, a completely analytical solution is only possible by doing several undesirable assumptions. In addition, the previous equation should be solved simultaneously with the conductive heat transfer governing equations for every single solid component involved in the thermal process.

Table 3.1. Maximum Biot numbers achievable by every PCB assembly component.

Component	**Bi**
60 solder joint	0.00023
90 solder joint	0.00022
120 solder joint	0.00019
Cover	0.04233
Copper wire or rod	0.00075

Figure 3.13 shows an assembly of one cover assembly with the right geometrical proportions for one of the solder joints (90). Four components can be identified. The fourth component is neglected and considered as insulation or a material with a very low thermal conductivity in comparison to solder joint and copper wire. An estimation of the maximum Biot number for each PCB assembly component can be determined by considering the maximum temperatures achieved in the PCB assemblies for no cover, one cover, and two covers. The maximum temperatures achieve in the solder joints for the experimental procedure with no cover was 37 °C. Although the maximum temperatures achieve by the top cover were around 70 °C, the maximum Biot number for

the cover was determined with the glass transition temperature for the cover (140 °C). According to these considerations, the maximum Biot numbers for every component were determined and are shown in Table 3.1. Although the Biot numbers are much lower than 0.1, caution should be used when neglecting temperature gradients within the solids in systems composed of different materials. It is well known that high thermal conductivity differences between materials in direct contact will lead to significant dimensional temperature variations. For instance, the dimensional temperature variations near the interface between the top cover (k = 0.81 W/m°C) and the copper wire (k = 401 W/m°C) are essential to differentiate among solder joints by means of their thermal signature. Therefore, it is important to consider the temperature dimensional variation close to the interfaces between the cover and the copper wire.

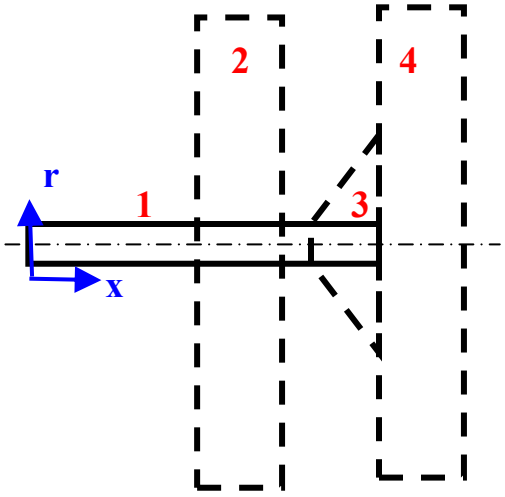

1. Copper rod or wire.
2. Cylindrical portion of top cover
3. solder joint
4. printed circuit board body

Figure 3.13. Simplified PCB assembly.

Next, the heat diffusion governing equations will be presented for every component of the PCB assembly. It is important to mention that parameters *m* and *n* were defined in order to differentiate between cooling and heating boundary conditions. Parameters *m* and *n* will have values of zero and one for heating process, and one and zero for cooling

process. The first component of the simplified cover-board-assembly (copper rod) is very important because it is in contact with the rest of the elements. Figure 3.14 shows a sketch of the copper rod, the boundary conditions, and the sections (S_1 to S_4) in which is divided:

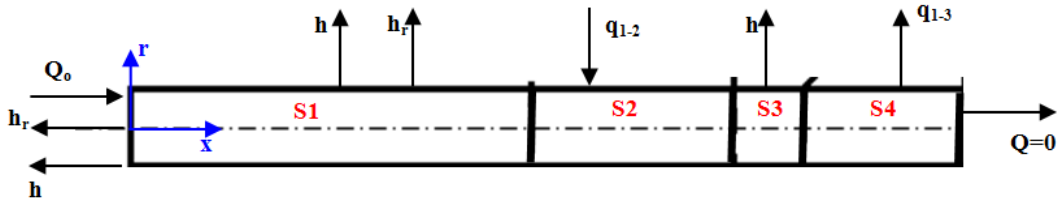

Figure 3.14. Copper rod.

For this problem, thermal conduction is considered important in the axial direction and the radial direction to allow continuity in the rod sections interfaces and components interfaces. Rod section one could be considered as linear flow close to the tip of the copper, but not close to the interface between rod sections S_1 and S_2; the heat exchange between components one and two causes an important variation in the radial direction (i.e. this is the phenomenon that this research is particularly interested in). In general, the governing equation for the rod in any section is giving by the next expression:

$$\frac{1}{r}\frac{\partial}{\partial r}\left(r\frac{\partial\theta}{\partial r}\right)+\frac{\partial^2\theta}{\partial x^2}=\frac{\rho c_p}{k}\frac{\partial\theta}{\partial t} \qquad (18)$$

where $\theta = T-T_\infty$. If the rod has a radius a and the lengths of its sections are L_1, L_2, L_3, and L_4, the boundary conditions for each section are:

- S_1

$q = nQ_o - m(h+h_r)\theta$ at x=0 and $h_r = \varepsilon\sigma(T^2+T_\infty^2)(T+T_\infty)$

$q_{s1} = q_{s2}$ at $x = L_1$

$\theta_{s1} = \theta_{s2}$ at $x = L_1$

$\frac{\partial \theta}{\partial r} = 0$ at r=0

$-k\frac{\partial \theta}{\partial r} = (h + mh_r)\theta$ at r=a and $h_r = \varepsilon\sigma(T^2 + T_\infty^2)(T + T_\infty)$

- S_2

$q_{s1} = q_{s2}$ at $x = L_1$

$\theta_{s1} = \theta_{s2}$ at $x = L_1$

$q_{s2} = q_{s3}$ at $x = L_1 + L_2$

$\theta_{s2} = \theta_{s3}$ at $x = L_1 + L_2$

$\frac{\partial \theta}{\partial r} = 0$ at r=0

$\theta_{c1} = \theta_{c2}$ at r=a

$k_{c1}\left(\frac{\partial \theta}{\partial r}\right)_{c1} = k_{c2}\left(\frac{\partial \theta}{\partial r}\right)_{c2}$ at r=a

- S_3

$q_{s2} = q_{s3}$ at $x = L_1 + L_2$

$\theta_{s2} = \theta_{s3}$ at $x = L_1 + L_2$

$q_{s3} = q_{s4}$ at $x = L_1 + L_2 + L_3$

$\theta_{s3} = \theta_{s4}$ at $x = L_1 + L_2 + L_3$

$\frac{\partial \theta}{\partial r} = 0$ at r=0

$-k\frac{\partial \theta}{\partial r} = h\theta$ at r=a

❖ S_4

$q_{s3} = q_{s4}$ at $x = L_1 + L_2 + L_3$

$\theta_{s3} = \theta_{s4}$ at $x = L_1 + L_2 + L_3$

$\frac{\partial \theta}{\partial x} = 0$ at $x = L_1 + L_2 + L_3 + L_4$

$\frac{\partial \theta}{\partial r} = 0$ at r=0

$k_{c1}\left(\frac{\partial \theta}{\partial r}\right)_{c1} = k_{c3}\left(\frac{\partial \theta}{\partial r}\right)_{c3}$ at r=a

The second of the components is the most important, because the temperature of its top surface is the temperature detected by the infrared camera. For simplicity, only a cylindrical portion of the cover surrounding the copper rod will be considered. It is assumed that in the external surface of the cylinder there is not a significant heat flux in the transversal direction and that the external radius is not big enough to interfere with the rest of the cylinders (there is one cylinder per each solder joint shape). A sketch of a circular section of the cover is shown in Figure 3.15. The governing equation and the initial condition for this component are the same as for the component one (rod), but the boundary conditions are given by the next expressions:

$q = nQ_o - m(h + h_r)\theta$ at $x = L_1$ and $h_r = \varepsilon\sigma(T^2 + T_\infty^2)(T + T_\infty)$

$-k\frac{\partial \theta}{\partial x} = h\theta$ at $x = L_1 + L_2$

$\theta_{c1} = \theta_{c2}$ at r=a

$k_{c1}\left(\frac{\partial \theta}{\partial r}\right)_{c1} = k_{c2}\left(\frac{\partial \theta}{\partial r}\right)_{c2}$ at r=a

$\frac{\partial \theta}{\partial r} = 0$ at r=b, where b is the outer radius of the hollow cylinder.

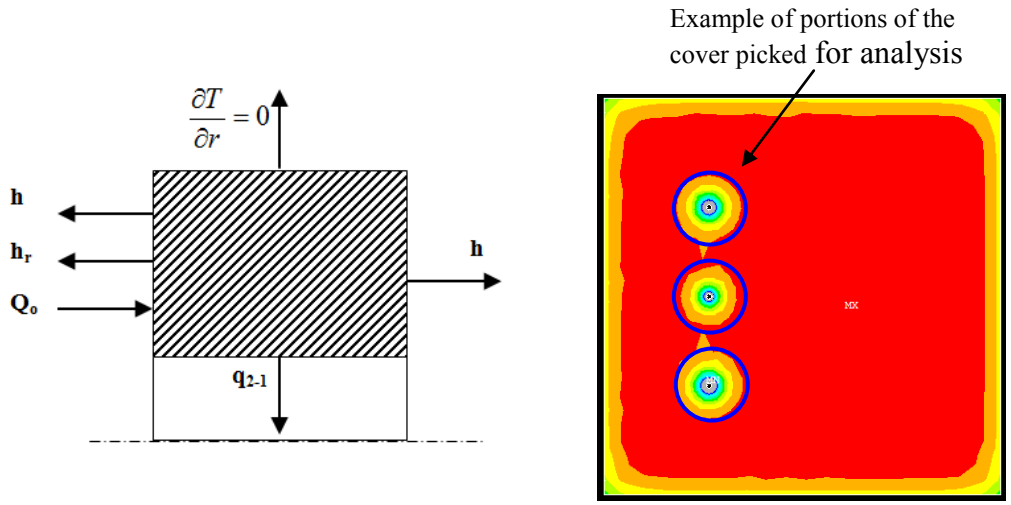

Figure 3.15. Cylindrical portion of cover.

The third component is the solder joint. This component is what makes the heat transfer from the rod to every selected cylindrical portion in the cover to vary causing different surface temperatures at every solder joint location on the top cover. Figure 3.16 shows a sketch of this component. Next expressions are the boundary conditions for the solder Joint:

q=0	at x= L_1+ L_2+L_3+L_4
$\theta_{c1} = \theta_{c2}$	at r=a
$-k\frac{\partial\theta}{\partial r} = h\theta\cos(\gamma/2)$	at $r-a=\frac{b-a}{L_4}(x-L_1-L_2-L_3)$, where b and γ are the major radius and angle of the cone
$-k\frac{\partial\theta}{\partial x} = h\theta\sin(\gamma/2)$	at $r-a=\frac{b-a}{L_4}(x-L_1-L_2-L_3)$, where b and γ are the major radius and angle of the cone

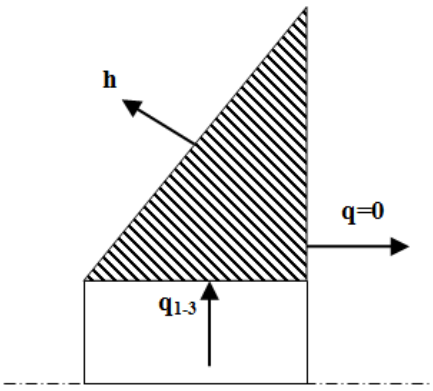

Figure 3.16. Solder joint schematic.

All of the previous boundary conditions and an initial condition given by the next expression:

$$\theta = mT_o + nT(30s,r,x) - T_\infty \tag{19}$$

form the complete set of equations to solve the governing equations for all of the components. Solving this system of partial differential equations is not an easy task. Solutions can be represented in products of series, but interface boundary conditions should be accounted for. A more adequate and simple method to solve this system of partial differential equations is the use of finite differences or, as in this research, finite element method. In the finite element method, the domain is separated in subdomains. The governing equations are applied for every single subdomain and approximated into algebraic equations by means of variational methods. Next, the subdomains are assembled, and a solution for the whole domain is obtained. The advantages of the finite element method are that the division of the domain in subdomains allows representing very complicated geometries and the inclusion of dissimilar materials [102]. The finite element model was developed in ANSYS. The next assumptions were considered in the development of the finite element model:

- During heating process, a uniform heat flux was considered. Such heat flux was determined iteratively to match the experimental results for one and two covers.
- Radiation, convection and conduction thermal processes are modelled.
- Convective coefficients are determined according to empirical correlations.
- Only the solid elements are considered.
- The bulk temperature is taken as the air initial temperature.
- All surfaces are gray-diffuse. *Emissivity = absorptivity*; *emissivity + reflectivity = 1*.
- The initial temperature for the whole system is a uniform temperature of 28.7 °C.
- Emissivity coefficients are selected according to the technical literature. Table 3.2 show the values used for every material the system is made of.
- As the distance between cover and PCB or between two consecutive covers is small (1.8 mm), only thermal conduction is considered in the air located in the air gaps.
- A list of the material properties for each of the elements of the model are shown in Table 3.2.

Table 3.2. Material properties for finite element model.

Component	**ρ (kg/m^3)**	**k (W/m K)**	**cp (J kg/K)**	**ε (Obtained from [150])**
Acrylic chamber walls and fixture [151]	105	0.036	795	------
Styrofoam walls and fixture [151]	16	0.04	1210	1 (Painted walls)
Solder [154]	8420	51	176	0.63
Board substrate [155]	1870	0.525	*f(T)*	0.9 (black tape)
Velcro (Nylon) [156]	1150	0.25	1883.95	--
Air [151]	1.1769	0.02624	1007.3	--
tin-plated copper wires [151]	10500	429	235	0.182
Mylar Surfaces [151]	--	--	--	0.37

The heat transfer by radiation in the system can be solved by means of the radiosity solver method provided with ANSYS Multiphysics. The radiosity solver method accounts for the heat exchange between radiating bodies by solving for the outgoing radiative flux for each surface, when the surface temperatures for all surfaces are known. The surface fluxes provide boundary conditions to the finite element model for the conduction process analysis. When new surface temperatures are computed, due to either a new time step or iteration cycle, new surface flux conditions are found by repeating the process. The element used for the geometrical model was SOLID90 which is a 3-D 20-Node element with a single degree of freedom, temperature, at each node. The 20-node elements have compatible temperature shapes and are well suited to model curved boundaries. The development of the finite element analysis is basically composed of three parts: pre-processing (started by command: /prep7), solution (started by command: /solu), and post-processing (started by command: /post1). The pre-processing part consists of generating the geometrical model by means of geometrical primitives like cones, cubes, areas, lines, etc., assigning material properties, defining the adequate element (solid90), defining the mesh size, and applying the loads. The loads are the boundary conditions of the model and in this case are: heat fluxes (command example: sfa,all,,hflux,1000), convective heat transfer (command example: sfa,all,,conv,2,27), and radiation heat transfer (command example: sfa,all,,rdsf,0.9,2). The mesh is generated by using the command “vmesh” and the mesh size is determined by using the command “smrtsize,10” (the size of the mesh is decided by the number following the comma and can be from 10 to 1, where 10 means a coarse mesh and 1 means a very fine mesh). In the solution part of the analysis, the type of the solution and solution options are defined. In this case the type of solution is a full transient analysis (command example: antype,transient,new), because the temperatures in the models are solved over time. In the post-processing part, variables in function of basic variables like time or temperature can be generated to describe the part of the model of interest. Appendix C shows an example of the scripts generated for every single models developed in this research; in such script, every part of the finite element modeling can be identify by the

adequate starting command (/prep7, /solu, or /post1) and the "finish" command. In addition, some of the commands indicated in this paragraph can be identified too. Comments were added to the scripts where they are considered relevant. Although these scripts can be used to run the ANSYS analysis directly, it is important to mention that different versions of the software or different computers can lead to errors caused by some version and computing unit dependant commands. Next section explains the procedure used to generate the finite element models step by step.

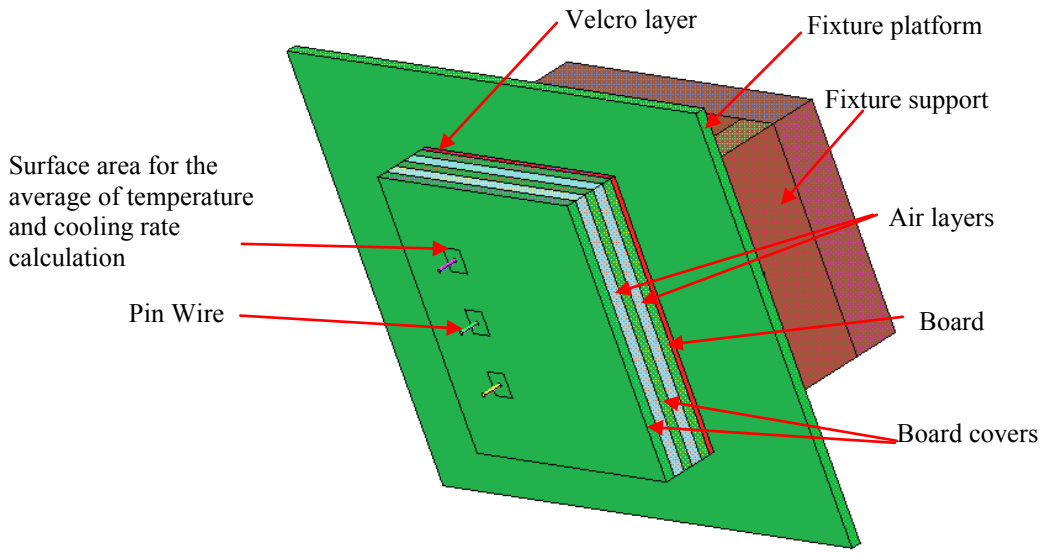

Figure 3.17. Solid model for the fixture-board-covers assembly.

3.3.1. Finite Element Model Development

As explained in the experimental methodology, the active thermography methodology requires heating the surface of the cover for certain amount of time and monitoring the

cooling process to obtain cooling rates and temperatures over time. The finite element models to follow these two processes were generated in the next steps:

- The solid model was generated with small square surfaces at every solder joint position. This will allow comparing the average temperatures between the experimental and numerical results. In accordance to the experimental methodology, this square region was selected with sides lengths equal to the 120° solder joint radius. Figure 3.17 shows the solid model for the fixture-board-cover assembly for two covers.
- The mesh was generated according to the model parts importance in the processes. A coarse mesh (smart size 10) was used in the walls of the chamber, because these parts do not play and important role during the heating and cooling process, because the energy is focused on the board and fixture. In addition, the Mylar on the walls reduces highly the energy gained by the heating section walls. A medium mesh size (smart size 7) was used in the support of the fixture platform, because this part only catches energy by reflection of the floor and does not exchange energy by radiation with the top part. A fine mesh (smart size 4) was used for the PCB assembly and fixture because these components play the most important role in the heat exchange process. It is important to mention that smart size option generates automatically higher mesh density close to the junctions between different parts like the solder joints, wires, covers, etc. For example, Figure 3.18 shows the nodes for the surface at the top cover close to the 90 solder joint position of the finite element model for an assembly of two covers; it can be seen that distance between nodes grows as the distance from the wire increases.

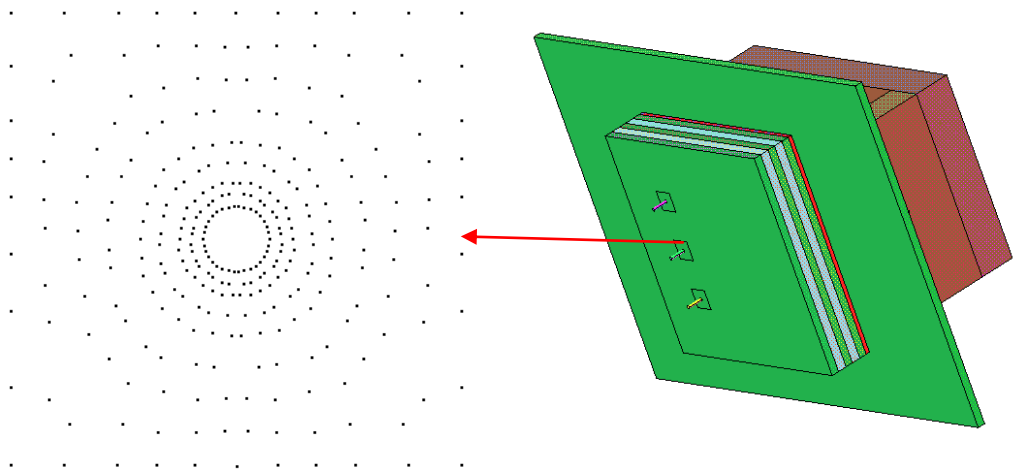

Figure 3.18. Nodes forming the square surface on the top cover at the 90 solder joint position.

- After the mesh is generated, the loads are specified in every surface of the model. This is the main difference between cooling and heating models. During the heating process, only convective loads are applied in the walls of both chambers and not radiation is modeled at the cooling chamber. In addition, radiation is modeled as a heat flux applied at the top of the board and the fixture. This assumption is done, because the main goal of the active thermography methodology is to provide the same amount of energy to the solder joints so the only parameters affecting temperature and grand average cooling rate are the shapes of the solder joints. Figure 3.19 shows the heat flux loads used at the cover-board-fixture assembly as well as the convective loads.
- After the loads are applied, the transient thermal analysis is solved to obtain the temperature transient behavior considering and initial temperature uniform for all the parts of the model. The amount of time for the solution is dictated by the amount of heating time needed. Solution controls are set “on” so the optimal values for the solution methodology of the full transient analysis are used. Only the initial time increment is needed and was established as 0.5 or 1 s minimum.

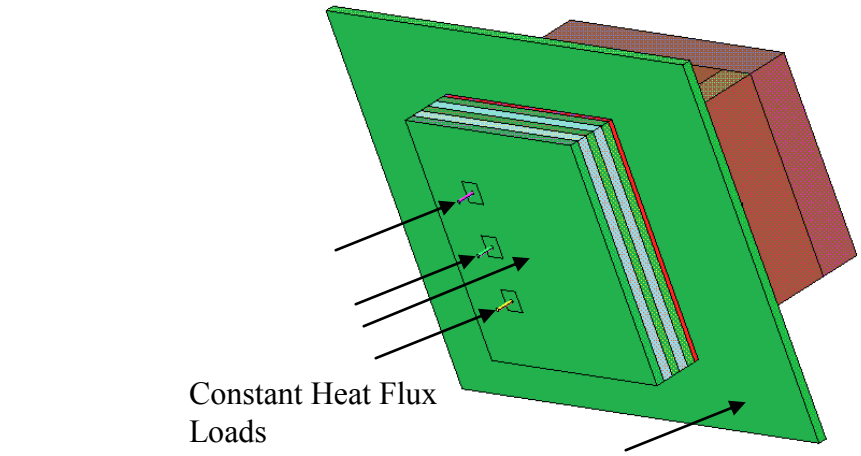

(a)

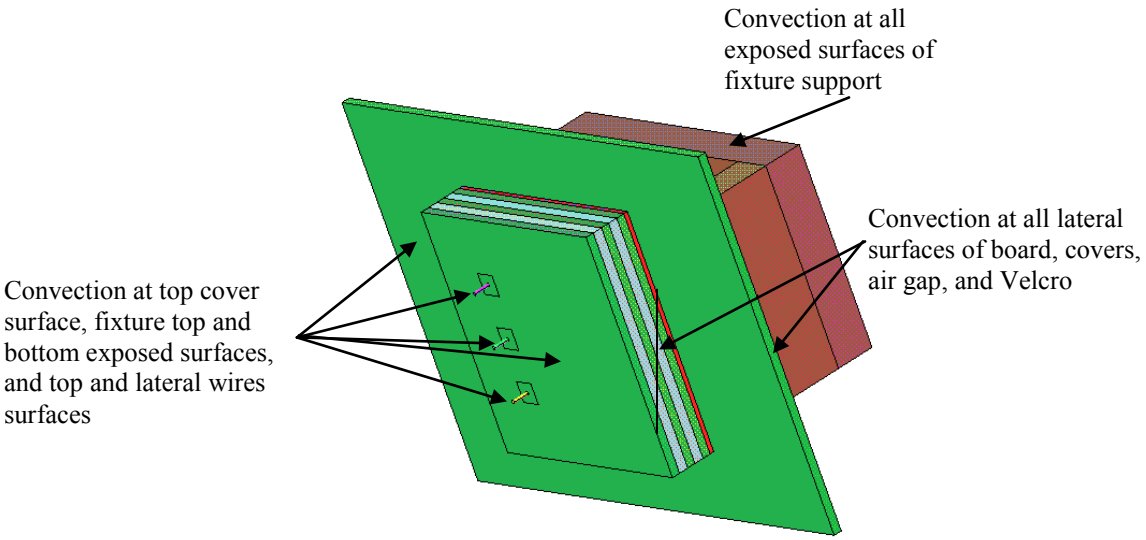

(b)

Figure 3.19. Model showing surfaces where: (a) the constant heat flux, and (b) convection loads were applied during heating process.

- After the solution for the heating process is completed, the cover-board-fixture assembly is moved to the cooling chamber and all heat flux loads are erased. Radiation loads are established at the top surface of the cover, exposed top surface of the fixture, and exposed surfaces of the wires. The radiative surfaces of the walls of the cooling chamber are modeled as ambient radiation, because the walls are much bigger than the other radiative surface areas that are completely surrounded for such walls. The radiative loads are shown in Figure 3.20, while convective loads are the same as in the heating analysis (see Figure 3.19 (b)).

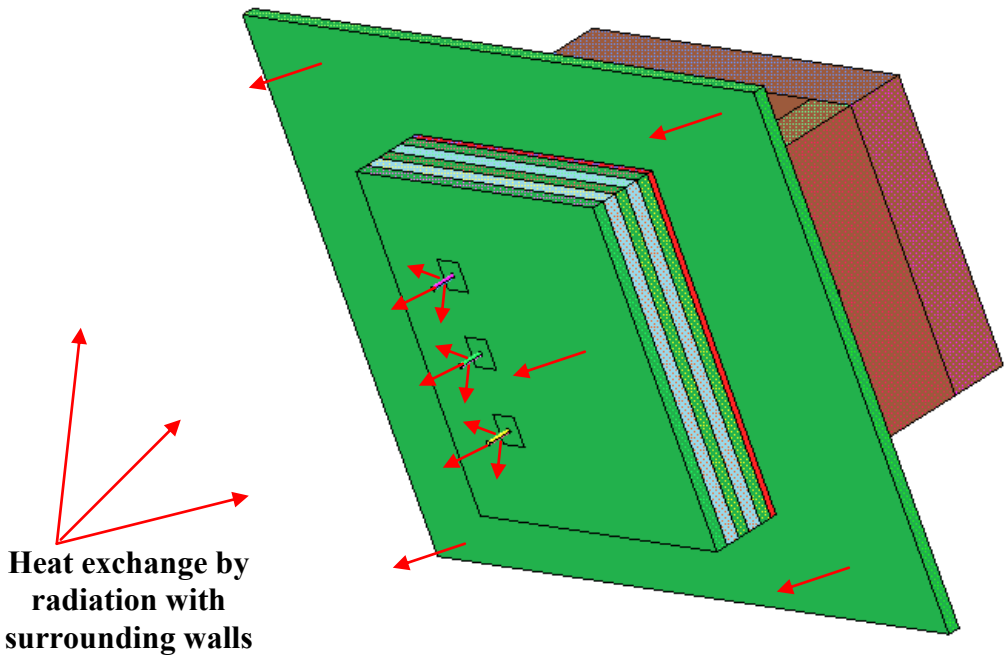

Figure 3.20. Radiative loads at the top surfaces of cover and fixture platform, and at the exposes areas of the wires.

- ❖ After loads are updated, the final temperature profile solution of the heating process is used as an initial condition for the cooling process. The transient temperature is determined for 100 seconds establishing a minimum time increment of 2 seconds. Solution controls is established as "on" again, so ANSYS uses the optimal parameters and solvers.
- ❖ After the solution is obtained for the cooling process, average temperatures and cooling rates are determined at the square surface areas on the top of the cover.

Two main tasks are intended to be fulfilled by the finite element models: generate a numerical model that is consistent with experimental results, and develop a parametric analysis. The parametric analysis will determine the active thermography limitations and generate a linear regression model to predict the right active thermography settings to discriminate among solder joint shapes. In the next two subsections, the corroboration of the numerical model procedure is presented.

3.3.2. Finite Element Model Verification

Verification is defined as the process of determining that a model implementation accurately represents the developer's conceptual description of the model and the solution to the model [157]. Two aspects of the verification should be addressed:

- ❖ Verification of the code. This involves error evaluation, which is looking for bugs, incorrect implementation of conceptual models, and error in inputs. This is typically a task of the developers prior to release the code. A qualitatively examination is required to check basic behaviors expected in the solutions. Next, the code is used to check highly accurate verification cases (analytical solutions or numeric solutions to ordinary and partial differential equations). One of the most used verification methods is by comparison of two different codes.

- Verification of calculation. This involves error estimation. The approach requires performing a grid convergence study and determining the grid convergence indices (GCI). The grid convergence study should be performed with at least three or more grid solutions. The refinement factor (r) between the coarse and the fine grid should be at least 1.1. Finally, if the grid convergence study is performed among three different grids, the grid convergence indexes can be calculated by the next group of equations:

$$
\begin{aligned}
&GCI_{21} = \frac{3E_{21}}{r_{21}^{w}-1} \qquad GCI_{32} = \frac{3E_{32}}{r_{32}^{w}-1} \\
&E_{21} = \left|\frac{f_1 - f_2}{f_1}\right| \qquad E_{32} = \left|\frac{f_2 - f_3}{f_2}\right| \\
&w = \frac{1}{\ln(r_{21})}\left|\ln\left|\varphi_{32}/\varphi_{21}\right| + \ln\left(\frac{r_{21}^{w} - sign(\varphi_{32}/\varphi_{21})}{r_{32}^{w} - sign(\varphi_{32}/\varphi_{21})}\right)\right. \\
&r_{21} = u_2/u_1 \qquad r_{32} = u_3/u_2 \\
&\varphi_{21} = f_2 - f_1 \qquad \varphi_{32} = f_3 - f_2
\end{aligned}
\tag{20}
$$

where the subscripts 1, 2, and 3 indicate the fine, medium, and coarse grids; f indicates a main or critical variable calculated by the numerical simulation and u is the representative grid size given by the next expression:

$$
u = \left(\frac{1}{N}\sum_{i=1}^{N} V_i\right)^{1/3} \tag{21}
$$

where N, and V_i are the number of elements, and the volume of the i^{th} element, respectively. It is important to mention that the numerical uncertainty of the fine grid solution will be calculated by the grid convergence index. A low index is expected for

spatial convergence. More detail information on verification of numerical models can be obtained at [158, 159].

3.3.3. Finite Element Model Validation

In order to validate the finite element models, two of the most representative experiments for one and two covers were selected. The finite element model validation is made based on the average temperature at the 90 position for the experimental results with one and two covers. As only the temperature and cooling rate variations over time were determined for the cooling process, the validation of the models are done by comparing the average temperatures and cooling rates at the 90 position during the cooling process. The 90 position was chosen, because the lamp used in the experimental procedure is characterized by an uneven heating that provides different amounts of energy for the solder joints positions in the sides (60 and 120 positions). Therefore, it is expected that providing the same amount of energy by means of a uniform heat flux in the finite element model will cause higher differences for the temperatures and cooling rates at the 60 and 120 positions when comparing with the experimental results. The procedure to validate the finite element model follows the next steps:

- First, the finite element model for the heating process is solved iteratively varying the constant heat flux until the average temperature at the end of heating for the 90 position is the same as the one in the experimental model. When the same average temperature in the 90 position is achieved, the heat flux determined is considered as the numerical heat flux equivalent to the one provided with the lamp in the experiment.
- After the same initial average temperature in the 90 position is determined, the temperatures solution at 30 s for the heating finite element model is used as the initial temperatures conditions for the cooling finite element model.

- ❖ Finally, average temperatures and cooling rates over time for 100 s are compared between finite element models and experimental models for one and two covers at the 90 position.

3.3.4. Summary

The active thermography technique will be simulated by means of the finite element method. The advantage of the finite element method is that the division of the domain in subdomains allows representing very complicated geometries and including dissimilar materials. The main objective of the numerical model is to develop a numerical parametric analysis. This analysis will investigate the limitations of the infrared thermography methodology proposed to characterize hidden solder joint shapes. First, it will be verified that the finite element model solves adequately for the heat exchange during the application of the active thermography technique. Next, the numerical model will be validated by comparing the temperature at the center of the top cover with that one of the experimental models for one and two covers. This validation will corroborate the real applicability of the numerical model for an actual inspection system.

3.4. Prediction Model

The prediction model has the objective to predict the optimum characteristics of the active thermography to discriminate among hidden solder joint shapes. The numerical model relationships between the active thermography and the PCB assembly parameters for a good discrimination of the solder joint shapes will be provided to the prediction model; next, a parametric equation to predict the adequate active thermography parameters for hidden solder joint shapes discrimination. Section 3.4.1 describes the procedure followed to perform a numerical parametric analysis that establishes the relationship between the optimum active thermographic characteristics and the PCB assembly characteristics. Section 3.4.2 explains the methodology followed to generate a

mathematical prediction model to determine the optimum characteristics of the infrared thermography for adequate discrimination. Finally, the procedure followed to validate the mathematical prediction model is explained in Section 3.4.3.

3.4.1. Finite Element Parametric Model

One of the main tasks of the parametric model is to investigate which parameters affect the capability of the infrared thermography methodology to discriminate among solder joint shapes. Three main parameters are varied:

- *Number of covers*. Number of covers is the most important parameter to vary, because multi-PCB integrated electronics use not only one or two boards, but several boards up to six. It is expected that the increments of the thermal resistance and the transversal conduction, as the number of covers increases, will decrease the capability to reach the solder joints and therefore reduce the capability to discriminate among solder joints.
- *Amount of heat flux*. The amount of heat flux is the main variable that should be increased to reach the solder joints in order to make up for the energy lost by the transversal conduction and the increase of thermal resistance. It is expected that increasing the amount of heat flux will increase the discriminability among solder joint shapes.
- *Amount of heating time*. The amount of heating time will increase or reduce the amount of time needed during a solder joint inspection. In addition, there is a different time to reach the solder joint when the number of covers increases. Amount of heating time is important when different energy sources are used; for example, flash lamps use a very high energy source in very short time periods, while halogen lamps use a low energy source in large time periods.

In addition to investigate the effects of the three parameters already mentioned in the discriminability of the solder joint shapes, the limitations of the thermography methodology to discriminate adequately among solder shapes is investigated. The criterion to decide, if a "good discrimination" among solder joint shapes is achieved, is determined according to the accuracy in the classification for the experimental data for no cover, one cover, and two covers. No cover accuracy is used as the benchmark criterion because it is the highest possible accuracy achievable (i.e. with no cover is easier to see the difference among solder joint shapes than when the solder joint shapes are hidden). After the right "good discriminability" criterion is decided, the optimum conditions for the active thermography methodology to discriminate among solder joints will be determined in function of the parameters varied in the parametric analysis (heating time, heat flux, and number of covers).

3.4.2. Prediction Model Development

A linear regression procedure will be used to fit the parametric numerical results data and generate an equation to predict the optimum characteristics of the active thermography methodology. Linear regression is an approach to model the relationship between a scalar variable Y and one or more explanatory variables denoted $\vec{x}$. Generally speaking, Y and $\vec{x}$ are called the response and a vector of predictors, respectively. A linear regression model takes the next form:

$$Y = r_1 f_1(\vec{x}) + \cdots + r_{pr} f_{pr}(\vec{x}) + \xi \tag{22}$$

where $f_{pr}(\vec{x})$ is a function of the predictor that can be nonlinear. If n independent observations of the predictor $\vec{x}$ and the response Y are considered, the linear regression model becomes a n by pr system of equations given by the next expression:

$$\begin{pmatrix} Y_1 \\ \vdots \\ Y_n \end{pmatrix} = \begin{pmatrix} f_1(\vec{x}_1) & \cdots & f_{pr}(\vec{x}_1) \\ \vdots & \ddots & \vdots \\ f_1(\vec{x}_n) & \cdots & f_{pr}(\vec{x}_n) \end{pmatrix} \begin{pmatrix} r_1 \\ \vdots \\ r_{pr} \end{pmatrix} + \begin{pmatrix} \xi_1 \\ \vdots \\ \xi_n \end{pmatrix} \tag{23}$$

Because the predictor $\vec{x}$ is multidimensional, the predictor functions should be too. For example, if two predictors are contained in the model, the next functions of the predictor might be included: $f_1(\vec{x}) = x_1$, $f_2(\vec{x}) = x_2$, $f_3(\vec{x}) = x_1^2$, $f_4(\vec{x}) = x_2^2$, $f_5(\vec{x}) = x_1 x_2$, $f_6(\vec{x}) = x_1^2 x_2$, $f_7(\vec{x}) = x_1 x_2^2$, and $f_8(\vec{x}) = 1$. Finally, the system of equations can be solved by a least-squares procedure that can be found elsewhere. In this research, the appropriate form of the statistical linear model will be established, and the coefficients of the linear model will be determined by the excel function "LINEST" that has a built in least-squares procedure. After "LINEST" performs the fitting procedure, the coefficient of determination is determined (a coefficient of determination of one means a perfect fitting).

3.4.3. Prediction Model Validation

The validation of the prediction model will be done by comparing the predicted values for one and two covers with the experimental values for one and two covers. One and two covers are chosen because the experimental model is limited to one and two covers PCB assemblies. Six experiments will be conducted for one and two covers in order to corroborate there is repeatability on the experimental results.

3.4.4. Summary

After the numerical FEA model is verified and validated, a parametric numeric analysis will determine the relationships between active thermography and PCB assembly parameters needed for a good discrimination of the solder joint shapes. The parameters varied are the heat flux, heating time, and number of covers. The heat flux is a parameter

characterizing the active thermography heat source, the heating time is a parameter that depends on the camera capabilities and the inspection duration desired, and the number of covers is a parameter specifying the difficulty to detect the hidden solder joints. There must be adequate combinations of these parameters to achieve good discrimination among solder joint shapes. Next, the relationship among these parameters will be fitted by means of a multiple linear regression methodology; this methodology will generate a mathematical model to predict the optimum conditions for adequate hidden solder joint shapes discrimination. The prediction model will be validated by comparison with the experimental models for one and two covers. This validation will test the capability of the prediction model to determine the optimum parameters for a real active thermography detection system.

3.5. Summary

An active thermography based methodology is proposed to characterize solder joint shapes hidden from view. This methodology is composed of three main models: experimental, numerical, and prediction models. The objective of the experimental model is to understand how three different hidden solder joint shapes (60°, 90°, and 120° cones) affect the surface transient thermal behavior of a multi cover PCB assembly after applying a heat flux. Transient thermal behavior will be characterized by means of the grand average cooling rate. Five experiments will be performed on a PCB assembly without a cover, five on a PCB assembly with one cover, and five in a PCB assembly with two covers. The PCB assembly with no cover will serve as a benchmark criterion and the assemblies with covers will increase the difficulty to detect the solder joint shapes. The experiments will be performed inside an environmental chamber with two sections (heating and cooling sections). The experimental procedure will consist of heating the PCB assembly by a halogen lamp inside the heating section, moving the PCB assembly to a cooling section, and monitoring the thermal transient behavior during the cooling process by means of an infrared camera. A multivariate analysis of variance

(MANOVA) will be performed on the experimental data to determine if the solder joint geometries are statistically different when describe by the grand average cooling rates. If the solder joint shapes are statistically different, defective hidden solder joints can be detected by means of the grand average cooling rate. Artificial neural networks classifying models will be developed based on the grand average cooling rate experimental data. These models will test and establish the capability of grand average cooling rate to describe the different hidden solder joint shapes as the PCB assembly complexity increases.

The numerical model will be used to simulate the heat transfer phenomena during the application of the active thermography technique. The main objectives of the numerical model are to increase the complexity of the PCB assembly, and to determine the optimum active thermography conditions to achieve adequate hidden solder joint shapes discrimination. The complexity will be augmented by increasing the number of covers to a maximum of eight. The optimum conditions will be achieved when the distances among grand average cooling generate good solder joint shapes discrimination. Sources of uncertainties during active thermography application (e.g. uneven heating, sample movement, and dead time between heating and cooling processes) will not be modeled. Major assumptions used in the development of the numerical model are: energy transfer by convection is determined according to empirical correlations, only heat transfer by conduction is considered in the air gaps between covers, and emissivity of the top cover is equal to 1. The numerical model will be validated with respect to the experimental model; next, a numerical parametric analysis will investigate the technique limitations and extend its applicability to characterize hidden solder joint shapes by means of grand average cooling rate. The parameters varied were the number of covers, amount of heat flux, and amount of heating time. The heat flux is a parameter characterizing the active thermography heat source, the heating time is a parameter that depends on the camera capabilities and the inspection duration desired, and the number of covers is a parameter

specifying the difficulty to detect the hidden solder joints. An adequate combination of such parameters will allow an adequate hidden solder joint shape characterization.

Finally, the prediction model will determine the optimum amount of heat flux required to achieve an adequate hidden solder joint shape characterization in function of the number of covers and heating time. The prediction model will fit the numerical parametric analysis results by means of a multiple linear regression methodology. Finally, the prediction model will be validated by comparison with the experimental model for one and two covers. This validation will test the capability of the prediction model to determine the optimum parameters for a real active thermography detection system.

4. RESULTS AND ANALYSIS

In this section, the results and their analysis are presented. In order to explain the different behavior of the solder shapes base on the heat transfer theory, comparative graphs of the experimental temperature and grand average cooling rate are presented in Section 4.1. Results of the statistical and classification procedures performed on the experimental grand average cooling rates are presented in Section 4.1 too. Section 4.2 presents the results of the verification and validation procedures conducted on the finite element model. Finally, the parametric finite element model analysis results, details about the prediction methodology development, and prediction model corroboration are presented in Section 4.3.

4.1. Experimental Model

The transient temperature and the grand average cooling rate were determined for every board by means of ThermalView. Five experiments were performed for ten boards with three solder joints in order to obtain 50 samples for the boards with one cover, 50 samples for the boards with two covers, and 50 samples for the boards without cover. According to the preliminary experiments, Section 4.1.1 shows the amount of heating time and scanning time used to perform these 15 experiments. Section 4.1.2 shows the comparative graphs of the average of 50 samples of temperature and grand average cooling rate over time for the three solder joint shapes. Section 4.1.3 contains the results of performing a multivariate analysis of variance to determine if the solder joint shapes classes are statistically different when describe by the 50 samples of grand average cooling rates for no cover, one cover, and two covers. Finally, Section 4.1.4 presents the classifiers developed to discriminate hidden solder joint shapes, the accuracies that such classifiers achieved, and an analysis to determine the parameters governing a good discrimination among solder joint shapes.

4.1.1. Preliminary Experiments

According to the two formulated hypotheses on section 3.2.5.1, two preliminary experiments were performed:

- ❖ Preliminary experiment 1: the amount of heating time was varied from 10 to 30 s in intervals of 10 seconds.
- ❖ Preliminary experiment 2: the cooling process was monitored for 600 s during the cooling process after the heating times are applied on the preliminary experiment 1.

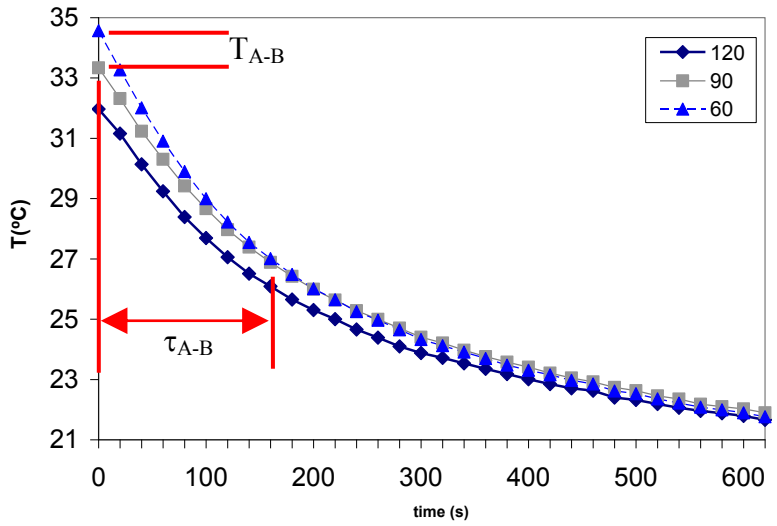

Figure 4.1. Variables affecting the capability to discriminate between contiguous curves.

On the other hand, Figure 4.1 shows an example of the temperatures obtained during cooling process for 30 seconds of heating time and no cover (no cover was chosen for clarity, because the difference among curves is clearer). According to Figure 4.1, the temperature difference between contiguous curves is a measurement of how different is

the temperature for the solder joint shapes. In addition, this difference reduces as the time progresses (e.g. the temperature difference between 60 and 90 curves has almost vanished after 100 seconds of cooling). Therefore, the temperature difference at the beginning of cooling process as well as the time a significant temperature difference is observed are parameters qualifying a level of discriminability between contiguous curves; a variable to evaluate the ability to discriminate between contiguous curves was defined and called discriminability index. The discriminability index is given by the next expression:

$$D_{A-B} = T_{A-B} \times \tau_{A-B} \tag{24}$$

Were T_{A-B} is the temperature difference between contiguous curves A and B and, and τ_{A-B} is the time required to achieve a zero temperature difference between curves A and B. D_{A-B} can be used to assess which amount of heating time should be chosen. τ_{A-B} should be used directly to determine the scanning time, because this variable is a direct measurement of how long the differences between signals are significant. Table 4.1 shows the discriminability index values obtained for the preliminary experiment 1 and one cover. As can be seen, the total discriminability index is higher for 30 s of heating time confirming the hypothesis that increasing the heating time allows higher differences between signals. Therefore, 30 s of heating time was used to perform the experimental procedure on this research.

Table 4.1. Total discriminability index in function of heating time.

Heating time	D_{90-60}	D_{60-120}	Total D_{A-B}
10	40	36	76
20	32	158	190
30	31.3	318.13	631.13

Table 4.2 shows the time required to achieve a zero temperature difference between curves A and B for preliminary experiment 2 and one cover. It can be seen that the minimum τ_{A-B} for 30 s of heating time is 100 s. Therefore, 100 s was chosen as the scanning time. The minimum was chosen because it is not valuable to scan the sample when there is not a significant different signal among all the solder joint shapes. According to the preliminary experiments, five experiments were perform for the no cover, one cover, and two covers PCB assemblies using 30 s of heating time and 100 seconds of scanning time. In the case of the scanning frequency, although the camera can take pictures every 12 s, 20 s was selected to allow an adequate difference among temperature readings; in addition and as explain in section 3.2.7, no more than three individual cooling rates are necessary as inputs to perform the solder joint classification (20 s will provide five readings in 100 s of scanning time). Next sections will present the results obtained in such experiments.

Table 4.2. Time to achieve a zero temperature difference between curves A and B.

Heating time	τ_{90-60}	τ_{60-120}	Minimum τ_{A-B}
10	150	150	150
20	100	200	100
30	100	240	100

4.1.2. Thermal Response

Figures 4.2 and 4.3 show a comparison among solder joints of the average temperature and the average of the grand average cooling rate for all the experiments performed in the boards without cover. It can be seen that temperature in the 60° solder joint decreases faster over time than the temperature for 90°, and that temperature in the 90° solder joint decreases faster over time than the temperature for 120° solder joint (See Figure 4.2). This indicates that as the cone angle decreases, the solder joint cools down faster.

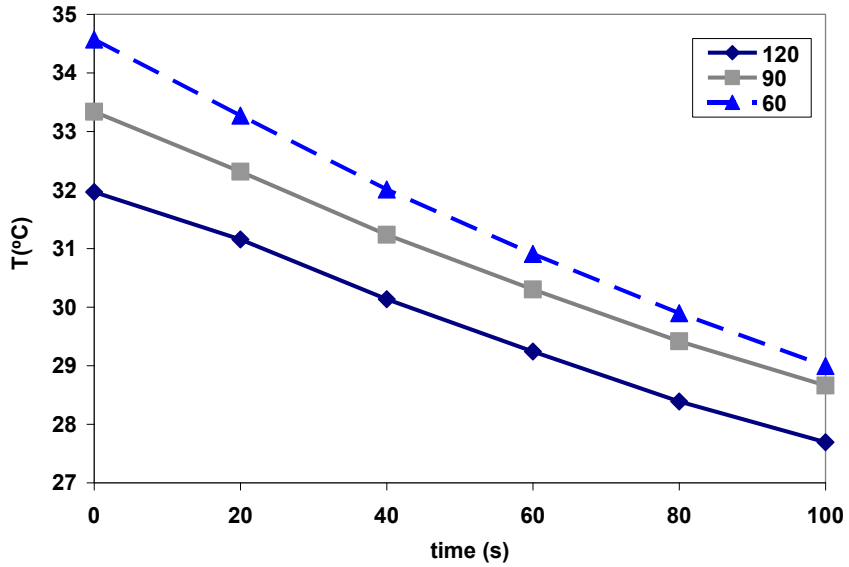

Figure 4.2. Comparison of average temperature among different solder joints (no cover).

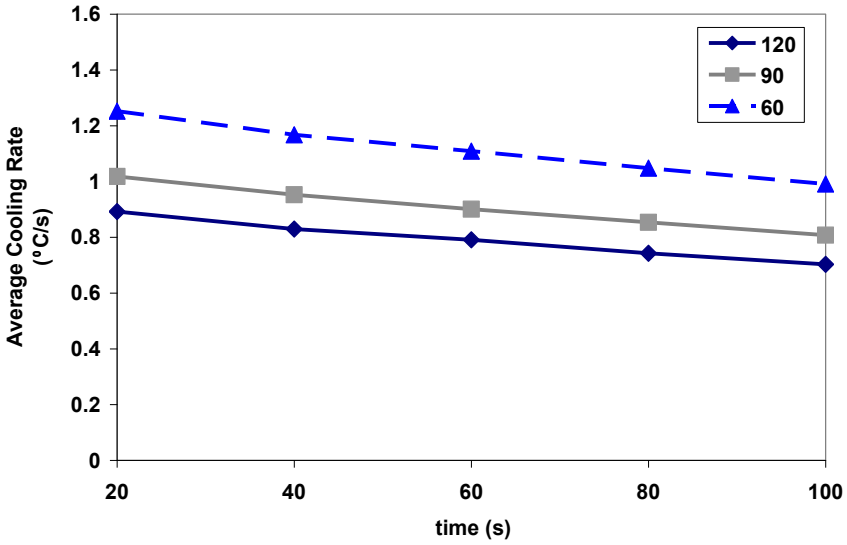

Figure 4.3. Comparison of grand average cooling rate among different solder joints. (no cover).

This behavior is more evident in Figure 4.3 that shows clearly how grand average cooling rate is higher as the cone angle decreases. It is very important to mention that average temperature difference among solder joints decreases as time increase; this behavior must be considered when predictive models are developed, because models using temperatures at early stage of cooling are most likely to succeed discriminating among solder shapes. Another matter to point out is the link between temperature and cooling rate, classes with different curve slopes on temperature will present a major difference in cooling rate too; for example, the temperature curve slope of classes 60 and 90 are much more different than the slope between 90 and 120 classes, therefore a major difference in grand average cooling rate between 60 and 90 is found as seen in Figure 4.3. In conclusion, it is clearly not possible to discriminate by means of cooling rate between two classes if their temperature curves run parallel to each other.

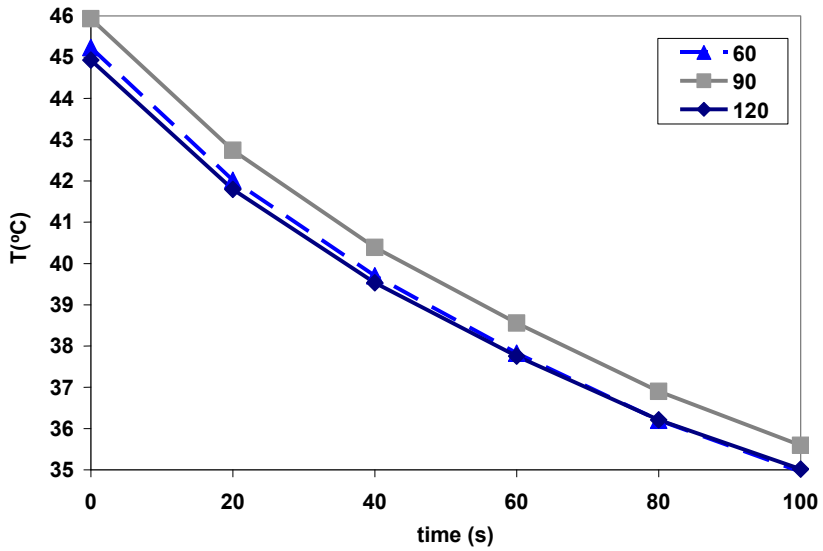

Figure 4.4. Comparison of average temperature among different solder joints (one cover).

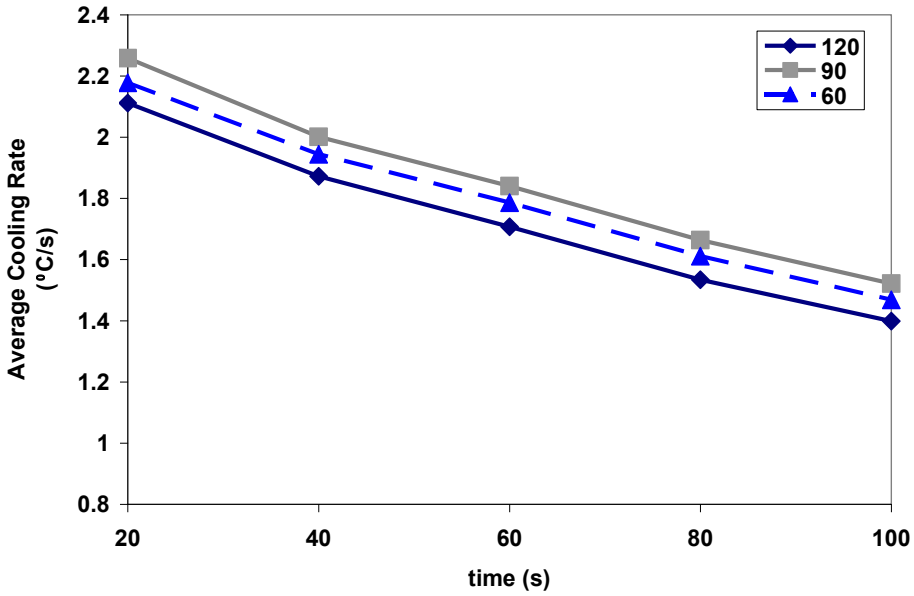

Figure 4.5. Comparison of grand average cooling rate among different solder joints (one cover).

As seen in Figure 4.4, the temperature difference among contiguous classes in the board with one cover diminishes with respect to that one in the board with no cover. In fact, no clear difference between 60 and 120 is shown. Figure 4.5 shows the average of the grand average cooling rate for all the experiments performed in the boards with cover. It can be seen that grand average cooling rate in the 90 solder joint position is higher than the 60 solder joint position, and that grand average cooling rate in the 60 solder joint position is higher than the grand average cooling rate for 120 solder joint position. This does not indicate a clear variation of the cooling rate with the solder joint angle, but at least there is a clear difference among contiguous classes. However, this behavior is completely normal as the solder joints surface area is not a variable involved in the energy added by radiation anymore. In this experiment configuration, the energy is transferred by radiation to the cover and wires (very thin and reflective wires). All the energy added to the solder joints is added either by the thin wire or by conduction from the board to the air, then from the air to the solder joint. So it is expected that energy transfers slowly in

the 120 position, because a higher air quantity is between the board and the solder joint. The shift between 90 and 60 positions with respect to the grand average cooling rate for no cover is explained by the fact that a bigger amount of energy by radiation is being provided to this 90 central position. In addition, the energy is mostly transferred in the axial direction and the effective transversal area available for conduction is bigger in the 90 position than in the 60 position. Finally, the link between temperature curve slope and grand average cooling rate is corroborate, because the classes with higher difference in their temperature slope have a higher difference between grand average cooling rates too.

After the grand average cooling rate difference between 90° and 60° positions in the cover was proven to be not particularly high, the experimental setup was cautiously investigated to determine possible components affecting the experimental results. One of the most important factors for the successful discrimination of the solder joint shapes by means of the grand average cooling rate is to provide the same amount of energy to the different solder joint positions so their thermal behavior can be compare; therefore, the halogen lamp was analyzed to determine if a uniform heat flux from the lamp was being obtained. Experiments were performed in a cover with no solder joints to determine if the temperature distribution caused by the lamp was uniform; however. the temperature was determined to be higher in the center of the cover and decreasing towards the edges of the cover. This means that a higher amount of energy is being provided to the central solder joint. In order to solve this uneven distribution of energy, an optical diffuser and a focus lens were investigated. The focus lens was found to worsen the uneven heating by providing a higher difference between the central temperature and sides temperatures. The optical diffuser improved the temperature distribution at expenses of reducing in a high degree the energy provided to the cover. Finally, a new structure to support and align the lamp was constructed and used for the experimental procedure for two covers.

Experimental results for two covers are presented in Figures 4.6 and 4.7, respectively. As seen in Figure 4.6, the temperature difference among contiguous classes in the board

with two covers increases a little bit with respect to that one in the board with one cover. Figure 4.7 shows the average of the grand average cooling rate for all the experiments performed in the boards with two covers. It can be seen that grand average cooling rate in the 90 solder joint position is higher than the 60 solder joint position, and that grand average cooling rate in the 60 solder joint position is higher than the grand average cooling rate for 120 solder joint position. As with one cover, this does not indicate a clear variation of the cooling rate with the solder joint angle, but at least there is a clear difference among contiguous classes. The reason for this behavior was already explained for one cover results; however, it is more interesting to analyze why there is a little increase in the space among contiguous classes with respect to one cover. First, the improvement was attached to the better alignment for this experimental procedure, but the reason is an increment in the energy provided to the surface area. This increment of energy is caused by the reduction of the distance with respect to the lamp (i.e. distance from lamp is inversely proportional to the amount of energy provided).

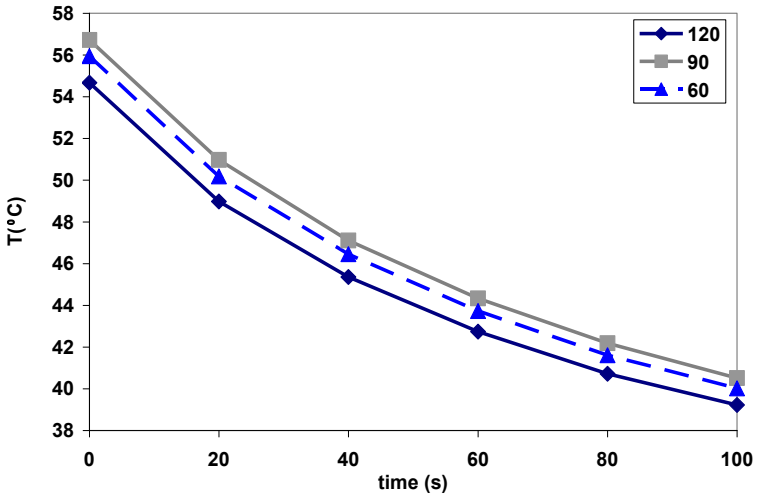

Figure 4.6. Comparison of average temperature among solder joints (two covers).

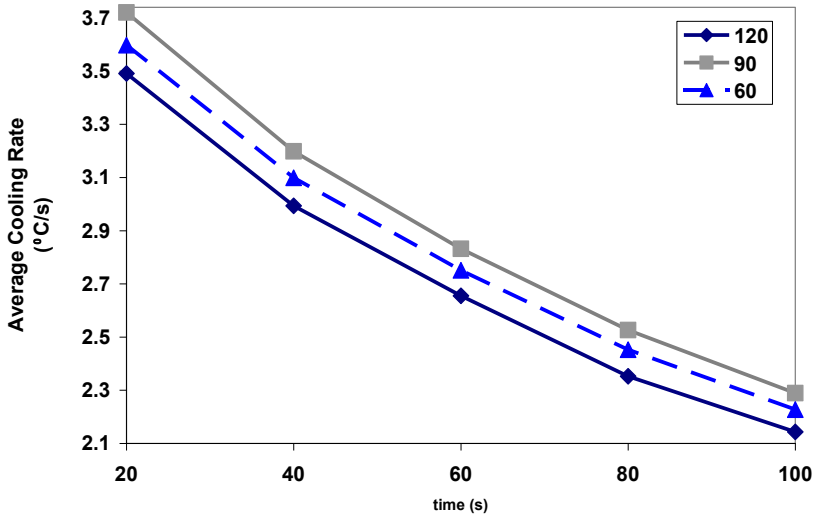

Figure 4.7. Comparison of grand average cooling rate among solder joints (two covers).

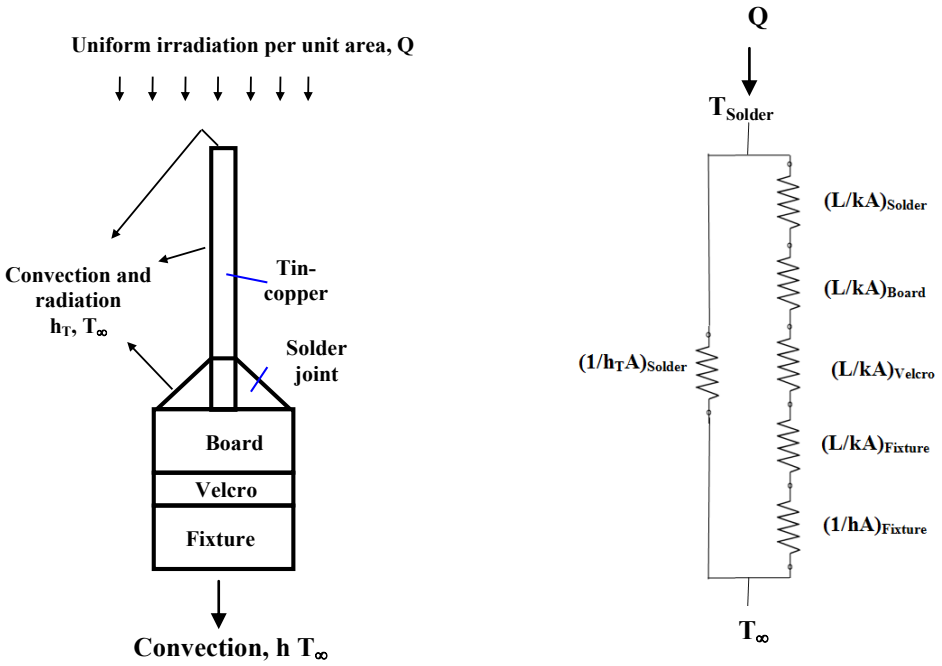

(a) (b)

Figure 4.8. (a) No cover Board-solder joint assembly and (b) its equivalent thermal circuit.

The addition of the covers produces a change on the trend between no cover and cover models. As the covers increase, the energy from the lamp can only get to the solder joint surfaces indirectly. Therefore, the temperature in the top cover is not affected directly by the solder joint shape. In order to illustrate this, consider the no cover configuration shown in Figure 4.8 (a) that is under irradiation from a lamp and dissipating energy by convection from its surface. Now, if the next assumptions are considered: energy going into the solder joint from the copper wire is small in comparison to the energy absorbed by the solder joint lateral surface, one dimensional conduction, and steady state process; the equivalent thermal circuit for no cover configuration is given by Figure 4.8 (b). According to the thermal circuit, the total energy received by irradiation is given by the next expression:

$$Q = \frac{1}{S_{solder}}\left(\frac{T_{solder} - T_{\infty}}{(h_T S)_{solder} + 1/R_1}\right)$$
$$R_1 = \frac{1}{A_{solder}}\left((L/k)_{solder} + (L/k)_{board} + (L/k)_{velcro} + (L/k)_{Fixture} + (1/h)_{Fixture}\right) \quad (25)$$

where S_{solder}, A_{solder}, T_{solder}, L, h, k, T_{∞} are the lateral surface area, base area, surface temperature of the solder joint, effective thickness, total coefficient of heat transfer, thermal conductivity, and ambient temperature, respectively. It is not difficult to infer from this equation, that the only terms that will vary among solder joints are the lateral surface area and the base area. For instance, the highest summation of these two areas (solder joint total surface area) will lead to a lower thermal resistance and temperature at the solder joint surface. As an example, the temperature at the solder joint lateral surface was determined for typical values of the thermal irradiation (2000 W/m^2) and convection coefficients (30 W/m^{2}K at the solders and 3.12 W/m^{2}K at the fixture bottom surface). Table 4.3 shows the overall thermal resistance and the temperatures determined at the solder joints. It can be seen that the temperature is directly proportional to thermal resistance, but inversely proportional to the cone angle, the lateral surface area, and base surface area. This proves that the solder joint shape has a direct impact in the solder joint

temperature and the temperature trend obtained by means of the experimental results for the PCB assembly with no cover. Now, it is clear that the heat transport phenomenon for the heating process is a transient process. However, the temperature variation with the solder joint angle should remain the same as the components among every solder joint have the same volumes and thermal properties; therefore, they are expected to storage energy in a very similar manner. Another fact to point out is that the temperatures at the solder joints are particularly high with respect to the experimental values; this is explained as this analysis is considered for steady state after a several time of heating when the temperature has reached its maximum value possible. If the solder joint temperature is determined by a lumped capacitance model for the 90º solder joint, a steady state temperature of 68.97 ºC will be achieved at 159 seconds of heating time; temperature that agrees with the temperatures obtained by the 1-D model, although it is a little over determined, because the lost of energy by conduction in the solder base was neglected (12% of difference between 1-D model and lumped capacitance model temperatures). Moreover, the time to achieve steady state temperature by the solder joints characterize the speed of the process as being completely transient during 30 s of heating.

Table 4.3. Temperature at the solder joint surface for no cover.

Solder Joint angle	Tsolder	Overall resistance	Surface area
60	63.0	2578.6	1.69E-05
90	61.2	2403.0	1.96E-05
120	59.9	1961.6	2.52E-05

In the case of the printed circuit board assembly with one cover, the process is more complicated. Figure 4.9 shows a schematic of the printed circuit board assembly for one cover. In order to be able to apply a 1-D steady state analysis, the energy lost by convection in the copper wire before reaching the top of the cover is neglected; this

assumption is the same for each solder joint and will not affect a comparison among solder joints. Additionally, the energy lost by convection in the transversal direction will be considered as energy lost on the immediately previous isothermal plane; Figure 4.10 shows an example of how this procedure was performed on the cover. Referring to Figure 4.10, q_2 is the energy lost by convection in the transversal direction and it is at a lower average temperature than the top of the cover; therefore, the energy lost by convection in the transversal direction will be over determined by the 1-D model. However, this model will give an idea of the effect of this energy lost on the temperatures at the solder joints at the extremes.

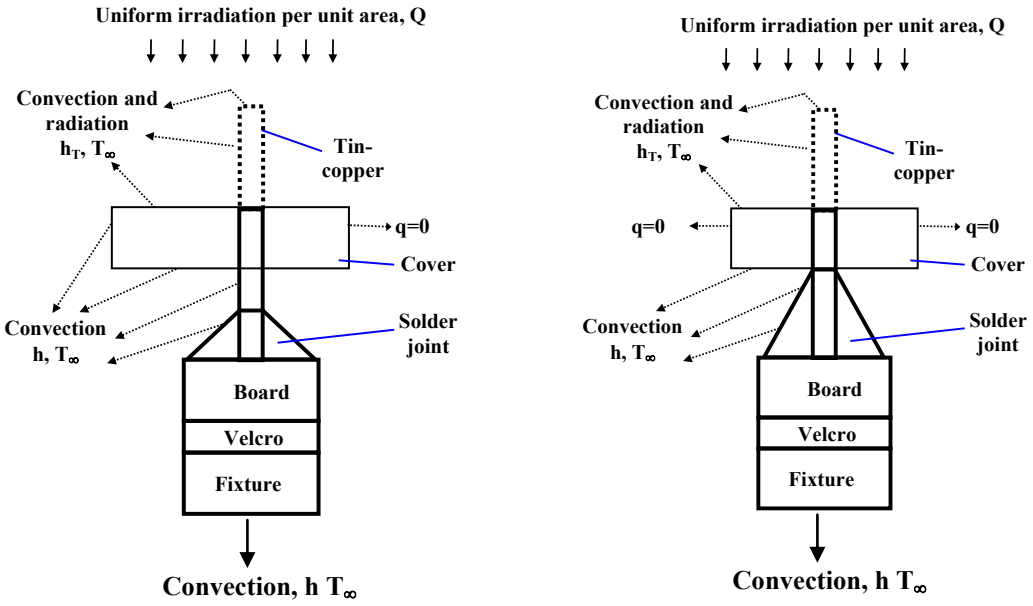

(a) (b)

Figure 4.9. Schematic of one cover PCB assembly for: (a) 90° and 120° solder joints, and (b) 60° solder joint.

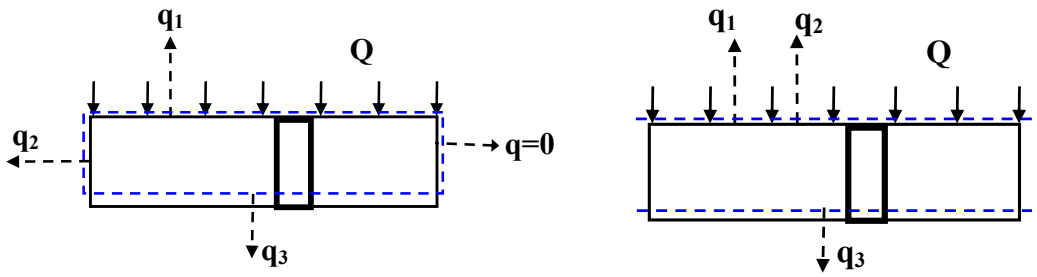

(a) (b)

Figure 4.10. Models of the cover for: (a) 2-D model, and (a) approximate 1-D model accounting for transversal convection lost.

Now, as the energy lost by convection in the transversal direction is by convection with the ambient at T_∞, any transversal convection can be considered as a resistance in parallel. Considering these assumptions, an equivalent thermal circuit for one cover assembly, as the one shown in Figure 4.11, can be obtained and solved for the total irradiation as:

$$Q = \frac{1}{A_{cover}} \frac{T_{cover} - T_\infty}{R_T}$$

where

$$R_T = \left(\frac{1}{1/R_3 + (hA)_{top\,cover} + (hS)_{side\,cover}} \right)$$

$$R_3 = \left(\frac{1}{1/R_2 + (hS)_{bare\,wire} + (hA)_{bottom\,cover}} \right) + (L/kA)_{wire} + (L/kA)_{cover} \qquad (26)$$

$$R_2 = \left(\frac{1}{1/R_1 + (hS)_{solder}} \right) + (L/kA)_{bare\,wire}$$

$$R_1 = (L/kA)_{board} + (L/kA)_{velcro} + (L/kA)_{Fixture} + (1/hA)_{Fixture} + \left(\frac{1}{(kA/L)_{wire} + (kA/L)_{solder}} \right)$$

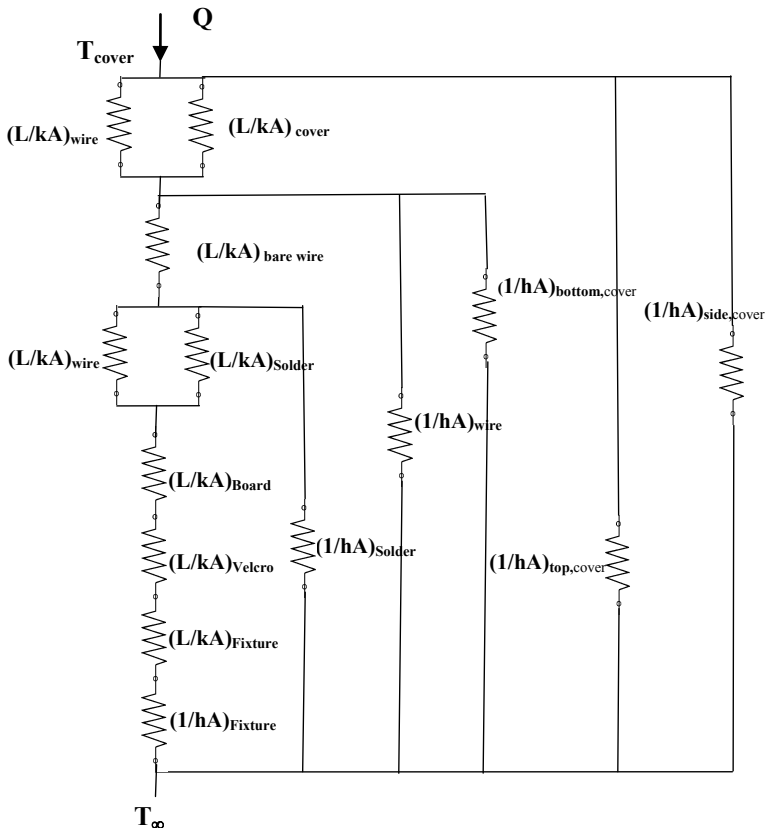

Figure 4.11. Equivalent thermal circuit for one cover PCB assembly.

The temperature at the cover and the total thermal resistance were determined for typical values of the thermal irradiation (2000 W/m^2) and convective coefficients (30 W/m^{2}K at lateral surfaces, 16.54 W/m^{2}K at the top cover (radiation and convection), 10 W/m^{2}K at the solder joints, 4.8 W/m^{2}K at the wire, and 3.12 W/m^{2}K at the fixture bottom surface). These convective coefficients were selected according to the typical temperatures reached in every section of the assembly and were updated if the calculated temperature at the cover was significantly different. Table 4.4 shows the temperatures determined at the cover for every solder joint position and the total resistance obtained. It can be seen that the variation of the temperature at the cover agrees with the experimental results. The temperature at the 90 position is higher than that one at the 60 position, while the temperature at the 60 position is higher than that one at the 120 position. Again, the

temperatures calculated are much higher than the experimental values and the reason for this behavior is the steady state assumption. For instance, considering a lumped capacitance model for the cover, a steady temperature of 117.04 °C is determined after 1010 s of heating (this value has a maximum 1.8% difference with the temperatures calculated at the cover considering a steady state 1-D model). A higher time to achieve steady state temperature by the cover implies that the transient process on the covers is slower than the process in the solder joint.

Table 4.4. Temperatures at every solder position for one cover 1-D model.

Solder Joint angle	T_{cover}	Overall resistance	$\lvert T-T_{90} \rvert$
60	117.35	63.79	1.82
90	119.18	112.10	0.00
120	116.88	63.46	2.29

Basically, the energy lost at the extremes closed to the 60 and 120 positions causes a reduction on the temperature for these two positions, while the 90 position is unaffected. This can be easily inferred by inspecting the temperature profile for a wall that is subject to convection in both extremes; basically, the temperature is higher in the center and drops toward the ambient temperature at the extremes. In order to prove this phenomenon, a 1-D model of the cover neglecting the energy lost at the extremes was developed. The temperatures obtained are shown in Table 4.5. Temperature at the 60 position now is the highest as with no cover assembly. However, the temperatures are very close to each other than considering a lost of energy in the extremes. This proves the importance of the transversal energy lost in the change of the temperature behavior with the solder joints when adding the cover.

Table 4.5. Temperatures at every solder position for one cover 1-D model (no lateral energy lost).

Solder Joint angle	T_{cover}	Overall resistance
60	120.18	65.79
90	119.18	112.10
120	119.68	65.44

Next, to prove that the main cause of the highest temperature in the central position is the energy lost at the extremes (caused by a location condition) and not the solder joint shape, the 1-D model was solved considering only one solder joint shape (90° cone angle). Table 4.6 shows the results for the temperatures obtained for this case. It can be seen that the temperature at the center (90) is the highest and that the temperatures at the extremes are the same (60 and 120). The temperatures at the extremes are the same because the solder joint geometries are identical and their location is symmetrical. Therefore, it is reliable to compare temperatures between the solder joint geometries located on the sides, but not between a solder joint shape in the central location and a solder joint shape on the side location (i.e. they are not subject to the same conditions). In addition, this proves the main role of the energy lost by convection at the extremes for the temperature difference between the solder joints at the sides (60 and 120) and the solder joint at the center (90), and a minor role of the solder joint shape for this difference in temperatures.

Table 4.6. Temperatures at every solder position for one cover 1-D model (same solder joint shape).

Position	T_{cover}	Overall resistance
90 (side position)	114.5	106.4
90 (center position)	119.2	112.1
120 (side position)	114.5	106.4

Finally, to investigate the relationship among the number of covers and the temperatures at the top of the cover, a 1-D model for a PCB assembly with two covers was developed by means of a similar procedure. Table 4.7 shows the temperatures and the total thermal resistance obtained. It can be seen that the temperature behavior agrees with the experimental results too. In addition, the differences between temperatures decrease as the number of covers increases (Compare $|T-T_{90}|$ between Table 4.7 and Table 4.4). Something to note is the reduction of the overall thermal resistance caused by the capacity to dissipate energy by convection in the transversal direction as the number of covers increases (i.e. the increment of the surface area in contact with the fluid increases the capacity to dissipate energy because of the fin effect). As will be seen and corroborated in the numerical parametric analysis, increments on the amount of energy provided to the cover allows a better discriminability for the solder joint position because the energy provided to the solder joints increases.

Table 4.7. Temperatures at every solder position for two covers 1-D model.

Solder Joint angle	T_{solder}	Overall resistance	$\lvert T-T_{90} \rvert$
60	96.05	48.75	0.67
90	96.72	84.79	0.00
120	95.86	48.62	0.86

Finally, if an energy balance is performed in the top cover and the dimensional effects are neglected, an empirical model for the temperatures at the top cover for one and two covers assemblies can be generated. Next expressions are the governing equations for the heating and cooling processes considering a lumped capacitance model (no dimensional effects):

- heating

$$\frac{d\theta}{dt} + A\theta - B = 0 \tag{27}$$

where $A = h\left(L^2 - \pi a^2\right)/\rho Vc$ and $B = \left(Q_o\left(L^2 - \pi a^2\right) - q''_{2-1}\left(2\pi a L_2\right)\right)/\rho Vc$. The solution for Equation (27) is given by

$$\frac{\theta}{\theta_o} = e^{-At} + \frac{B/A}{\theta_o}\left(1 - e^{-At}\right) \tag{28}$$

The only unknown in the previous equation is the heat flux from the cover to the copper wire (q''_{2-1}), but it can be determined according to the experimental results for one cover and two covers respectively (i.e. q''_{2-1} will have different values for each solder joint shape position).

- cooling

$$\frac{d\theta}{dt} + C\theta - D = 0 \tag{29}$$

where $C = \left(2h + h_r\right)\left(L^2 - \pi a^2\right)/\rho Vc$ and $D = -q''_{3-1}\left(2\pi a L_2\right)/\rho Vc$ and its solution is given by Equation (28) and replacing A and B for C and D, respectively. Based on Equation (28), an empirical correlation could be developed to fit the experimental results for one and two cover models. Tables 4.8 and 4.9 show the constants C and D determined by means of the experimental data during cooling in one and two covers.

Table 4.8. Fitting parameters for the empirical model (one cover).

solder Joint	A	B	R^2	h+hr (W/m^2K)	q"2-1 (W/m^2)	%Δ(h+hr)	%Δq"2-1
60	0.00979	1.582E-11	0.998	18.9	1.53E-07	0.00	0.00
90	0.00922	1.024E-11	0.998	17.8	9.90E-08	-5.82	-35.29
120	0.00953	1.164E-11	0.997	18.38	1.13E-07	-2.75	-26.47

Table 4.9. Fitting parameters for the empirical model (two covers).

solder Joint	A	B	R^2	h+hr (W/m^2K)	q"2-1 (W/m^2)	%Δ(h+hr)	%Δq"2-1
60	0.00932	1.200E-10	0.982	17.99	1.16E-06	0.00	0.00
90	0.00889	8.450E-11	0.979	17.16	8.17E-07	-4.61	-29.57
120	0.00935	1.779E-10	0.979	18.05	1.72E-06	0.33	48.28

As seen in Tables 4.8 and 4.9, the coefficients of determination R^2 are very high indicating a good correlation between the experimental temperature results and Equation (28), but Equation (28) was developed neglecting thermal conduction effects; therefore, the results obtained for the heat flux and the thermal convective coefficients cannot be used to characterize the thermal phenomena involved in the cooling process. For instance, it is clear that there must be a heat flux in the interface between the rod and the cover, because the thermal conductivity of the rod is very high in comparison to that one of the cover. In addition, an increment of the convective coefficient for one cover with respect to that one of two covers is not possible. In the reality, the convective coefficient should be higher for two covers as the temperature difference between the ambient temperature and the top cover surface is higher for two covers assembly.

4.1.3. Statistical Analysis

As seen in Section 4.1.2, the average of the temperature and heating rate seems to be different among solder joint shapes (classes). A comparison of all of the samples will give more insight in relation to this difference. Figures 4.12 to 4.14 show the scatter plot of the different cooling rates C_1 to C_5 for no cover, one cover, and two covers. Comparing these figures, it can be seen a clear cooling rate difference between solder joint shapes for the samples belonging to the experiments with no cover (a clear separation between the blue plus signs , green crosses, and red circles can be clearly seen). In the case of the results for one cover and two covers, separation between classes (solder joint shapes) is hardly visible.

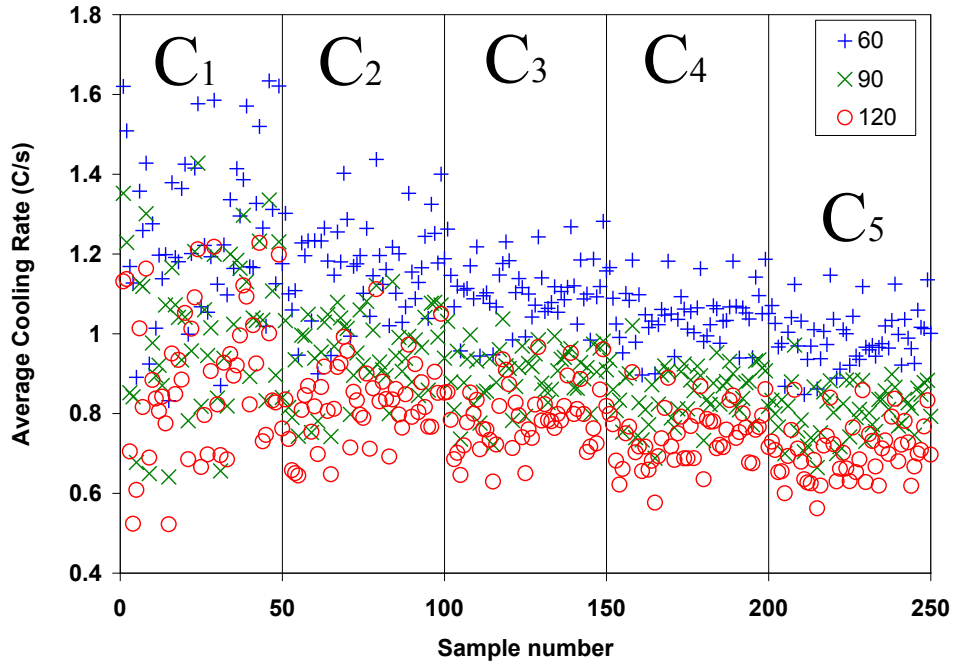

Figure 4.12. Scatter plot for the cooling rates C_1 to C_5 (no cover).

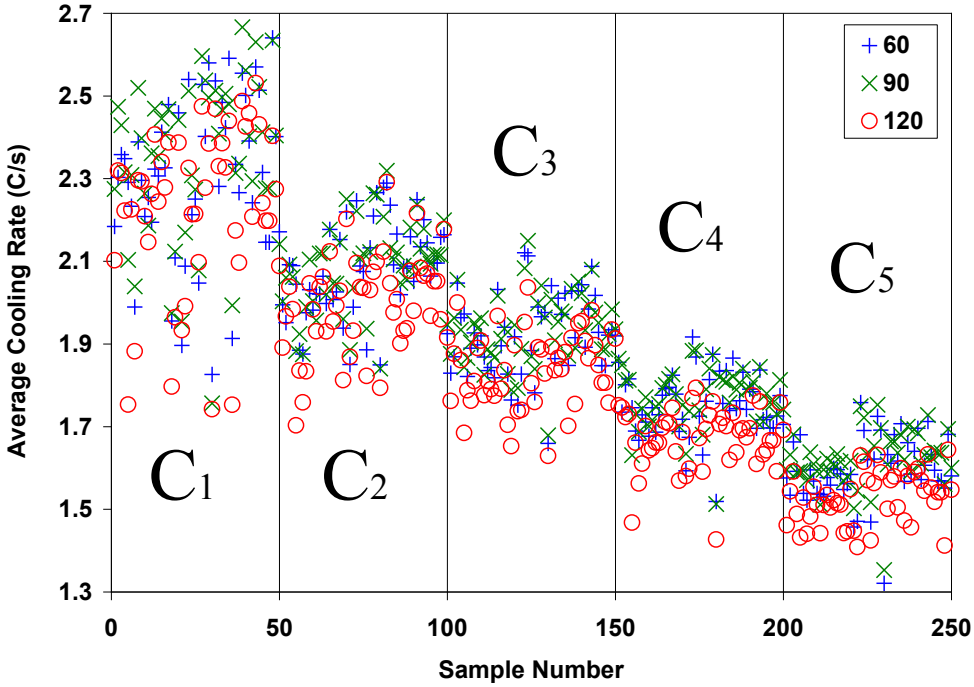

Figure 4.13. Scatter plot for the cooling rates C_1 to C_5 (one cover).

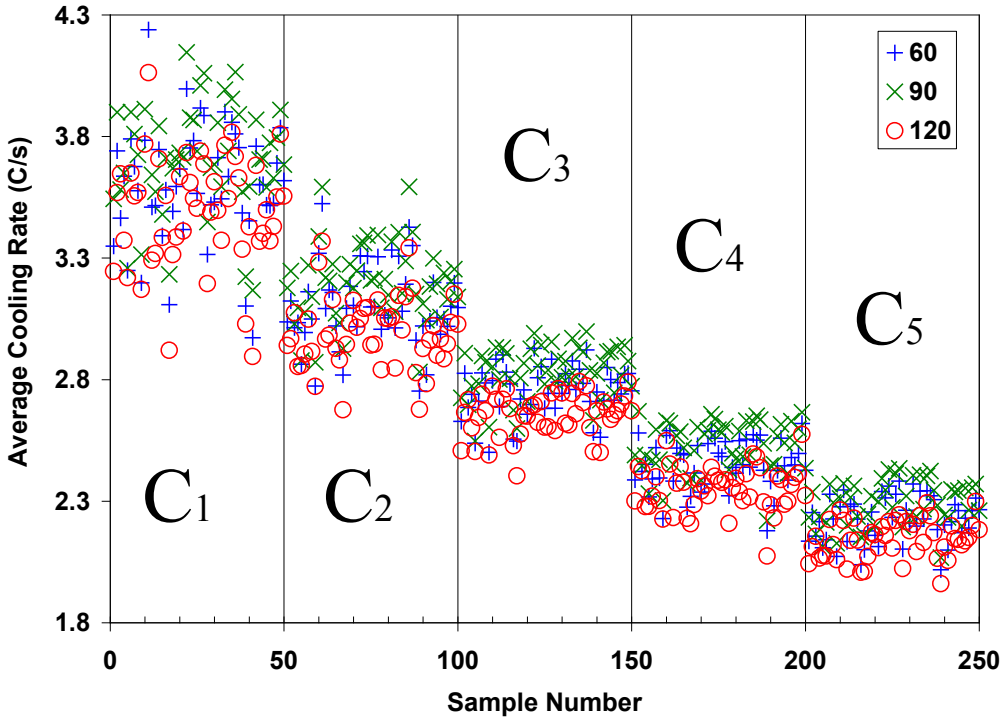

Figure 4.14. Scatter plot for the cooling rates C_1 to C_5 (two covers).

One of the most used ways to determine if classes are different is one way ANOVA. An analysis of variance (ANOVA) will not only determine if the classes are statically different, but also will give a numerical measure of the difference permitting to compare among the different solder joint shapes (classes) capability to discriminate. For example, Kang *et al.* [160] used ANOVA to determine if there was a statistical significant difference in the performance of multiples classifiers. In this case, a multivariate analysis of variance (MANOVA) was required because there are five different cooling rates or variables (C_1, C_2, C_3, C_4, and C_5) that will be used to discriminate among solder joint shapes or classes. It is important to remark that only four of this cooling rates or a combination of the five will be used as input nodes for the neural network prediction methodology. After performing the multivariate analysis in MATLAB, multiple parameters describing the solder joint shape are determined being the most important: the P and d values, means for every variable describing the data (grand average cooling

rates), and the multivariate distances among solder joint geometries (i.e. accounts for the means distances among classes for all of the samples in function of the C_1, C_2, C_3, C_4, and C_5 variables describing the solder joint shape). Table 4.10 show the P and d values for the experimental data with no cover, one cover, and two covers. A *d* value of zero indicates the classes of data have the same means, a d value of 1 indicates that the data has different means and they fell along a line, and finally a d value of 2 means the group of data has different means and fell on a plane (maximum dimension is 2 for three classes: 60, 90, and 120). The P values describe the results of testing if the means lie in a dimension 0, 1, and 2. A P value less than 0.05 rejects the hypothesis of a n-dimensional space. As seen in Table 4.10, the classes have different means and fell along a line (d=1, P_1=0, P_2>0.05).

Table 4.10. P-values and d-value in function of number of covers.

No cover	***d-value***	1	
	P-values	0	0.94
One cover	***d-value***	1	
	P-values	0	0.33
Two covers	***d-value***	1	
	P-values	0	0.84

Tables 4.11 to 4.13 show the means of the different cooling rates classified by solder joint shape for no cover, one cover and two covers, respectively. As seen in the Tables 4.11 to 4.13 the means of the grand average cooling rate increase as the number of covers increase; the reason for this increase of cooling rate is that increasing the covers allows a higher temperature in the cover surface. The energy is more difficult to transfer by conduction trough the cover and air low thermal conductivities than through the solder high conductivity. This causes a higher temperature in the cover surface that is decreased by natural convection with the environment.

Table 4.11. Means of the grand average cooling rates classified by solder joint shape (no cover).

	C1	C2	C3	C4	C5
60	1.3	1.2	1.1	1.0	1.0
90	1.0	1.0	0.9	0.9	0.8
120	0.9	0.8	0.8	0.7	0.7

Table 4.12. Means of the grand average cooling rates classified by solder joint shape (one cover).

	C1	C2	C3	C4	C5
60	2.3	2.1	1.9	1.8	1.6
90	2.3	2.1	1.9	1.8	1.6
120	2.2	2.0	1.8	1.7	1.5

Table 4.13. Means of the grand average cooling rates classified by solder joint angle (two covers).

	C1	C2	C3	C4	C5
60	3.6	3.1	2.8	2.5	2.2
90	3.7	3.2	2.8	2.5	2.3
120	3.5	3.0	2.7	2.4	2.1

The difference of the means among 60 and 90 solder joints decreases significantly as the covers increase to one cover; this behavior is a direct consequence of the different composition of the surfaces under infrared thermography inspection when the cover is added. Another fact, that corroborates the reason of the sudden change in the difference of means between no cover and one cover, is that the difference of means between 60, 90, and 120 for one and two covers is quite similar (See red circles on Tables 4.14 to 4.16). It is important to remark that a direct conclusion of the difference of the means among closest class is the possibility of discriminating among classes. It is well known that small intraclass variations and large interclass variations are essential for a good

discrimination among classes [117]. The means difference among closest or contiguous classes accounts directly for interclass difference, while the data samples dispersion accounts for the intraclass variation (see Figure 4.15 for an example). Here and after, the average temperature and the average of the grand average cooling rate difference among closest or contiguous classes will be referred as T_{A-B} and CR_{A-B}; where A and B stands for class A (can be 60, 90, or 120) and class B (can be 60, 90, or 120), respectively. According to this nomenclature, the difference among closest classes for no cover (CR_{60-90}=10.91 and CR_{90-120}=4.4) provides a high possibility of discriminating among classes or solder joint shapes for this configuration, but the difference among closest classes for one cover (CR_{90-60}=0.526 and CR_{60-120}=1.8) and two covers (CR_{90-60}=0.7045 and CR_{60-120}=1.5) provides a lower possibility of discriminating among classes or solder joint shapes for these two configurations. These facts about discrimination capability will be corroborated in the prediction or classification section.

Table 4.14. Multivariate means distances of the grand average cooling rates classified by solder joint angle (no cover).

	60	**90**	**120**
60	0	10.91	28.2
90	10.91	0	4.4
120	28.2	4.4	0

Table 4.15. Multivariate means distances of the grand average cooling rates classified by solder joint angle (one cover).

	60	**90**	**120**
60	0	0.526	1.8
90	0.526	0	3.22
120	1.8	3.22	0

Table 4.16. Multivariate means distances of the grand average cooling rates classified by solder joint angle (two covers).

	60	90	120
60	0	0.7045	1.4938
90	0.7045	0	4.0655
120	1.4938	4.0655	0

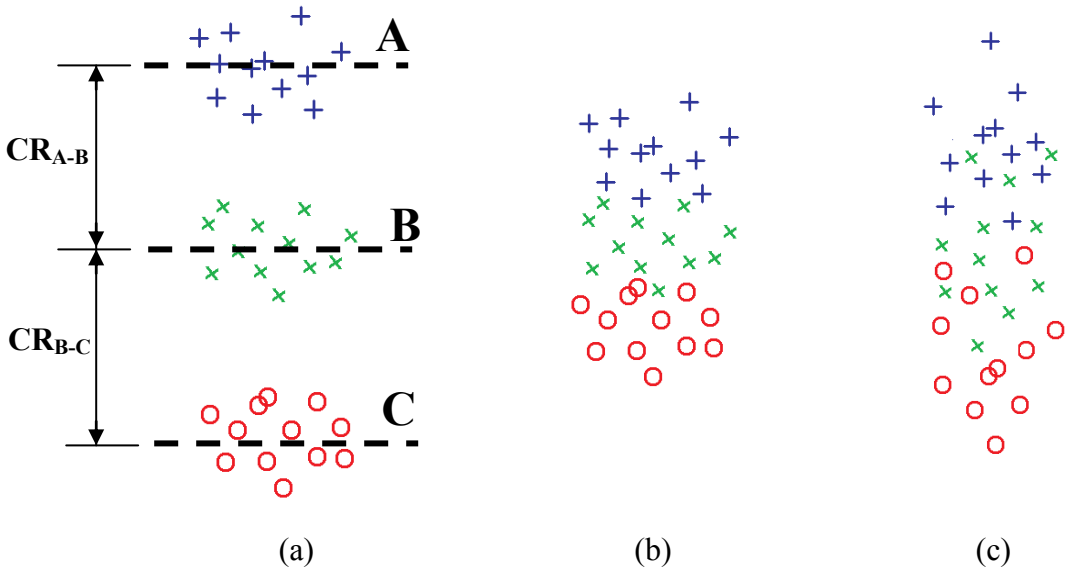

Figure 4.15. Chart showing: (a) large interclass distance and small intraclass distance, (b) small interclass distance, and (c) small interclass distance and large intraclass distance.

4.1.4. Classification Procedure

As explained in Section 2.4.1, artificial neural networks is one of the most simple, flexible and accurate prediction or classification approaches used up to date. In addition, the MATLAB Neural Network Toolbox has multiple training and transfer functions that permit to develop easily neural networks; moreover, these neural networks address the problems of over fitting. Therefore, neural networks is the perfect choice to develop models to discriminate among solder joint shapes or classes (60, 90, and 120) by means

of multiple variables or features (C_1, C_2, C_3, C_4, and C_5). According to Section 3.2.7, 7 alternatives were used as the input nodes for the neural networks; these input nodes were varied from two to four and were combinations of the variables C_1, C_2, C_3, C_4, and C_5. The output nodes were three (1, 0 and 0 for 60, 0, 1 and 0 for 90, and 0, 0 and 1 for 120). The number of hidden nodes was varied from three to nine initially. However, hidden nodes were increased to improve the capability of the neural network to approximate the solder joint behavior, because the classification accuracy was low for the boards with covers.

Table 4.17 shows the percent of accuracy obtained in the prediction by means of the neural networks developed (best accuracies obtained are marked in green and only the number of hidden nodes with best accuracy is presented). Trainrp was chosen as the training function, because this training function has proven to achieve a good accuracy in different classification problems [85, 127, 161]. According to these tables, it was determined that the difference in the behavior of each solder joint shape is so evident for the boards with no cover, that a good percentage of correct predictions is obtained with only two input nodes (74.5%, alternative 7, 7 hidden nodes). In addition, increasing the number of input nodes will always improve the predictions with a low number of hidden nodes if the additional input nodes discriminate clearly among the solder joint shapes (Best prediction for data: 84.3%, Alternative 4, 5 hidden nodes). It is very important to point out that the predictions accuracy for the board with no cover was used as a benchmark criterion for the prediction accuracies for the experimental data for one and two covers. It is obvious that no prediction accuracies as high as 84.3 % for the experiments with one and two covers can be obtained because the covers will prevent from getting a clear thermal signature. A clear evidence of this fact is the lower multivariate means distance among classes (60, 90, and 120) for one and two covers (See Tables 4.15 and 4.16).

Table 4.17. Epochs to converge and detection accuracy when using *TrainRP* with varying number of hidden nodes (no cover).

Alternative	Hidden Node for Best Prediction	Epochs	Training Average Error	% Accuracy (n=40)
1	**4**	3	0.173610	66.67
2	**4**	19	0.021833	75.00
3	**4**	17	0.112467	84.31
4	**5**	16	0.115655	84.31
5	**3**	32	0.111109	82.35
6	**9**	20	0.089285	80.39
7	**7**	17	0.143651	74.51

In the case of the boards with a cover, using the alternatives proposed generate maximum accuracies of 47% (See Table 4.18). The reason is that the means difference between the 90 and 60 was very small. Therefore, the transfer functions for the output and hidden nodes were varied in order to get better results by improving the neural network models. Not only the transfer function was varied, but also the number of hidden nodes was increased to a maximum of 20. A higher number of hidden nodes can follow or represent better the solder joint shape behavior. A total of 13 transfer functions available from Matlab were tested for the hidden and output nodes. The best combination with a 50.9% of accuracy was using hyperbolic tangent sigmoid transfer functions for both, the hidden nodes and the out put nodes.

Table 4.18. Epochs to converge and detection accuracy when using *TrainRP* with varying number of hidden nodes (one cover).

Alternative	Hidden Node for Best Prediction	Epochs	Training Average Error	% Accuracy (n=40)
1	9	10	0.1917	15.69
2	5	7	0.1413	41.67
3	4	25	0.1589	47.06
4	3	11	0.1876	47.06
5	4	9	0.2033	25.49
6	4	2	0.2224	23.53
7	7	7	0.2308	27.45

Table 4.19. Epochs to converge and detection accuracy when using *TrainRP* and *tansig-tansig* transfer functions with varying number of hidden nodes (alternative 3 and one cover).

Hidden nodes	Epochs	Training Average Error	% accuracy (n=40)
3	11	0.187616	47.06
4	8	0.178005	41.18
5	8	0.220217	37.25
6	8	0.176265	45.10
7	6	0.189175	41.18
8	2	0.192649	50.98
9	3	0.180474	45.10
10	8	0.198179	45.10
11	2	0.232858	19.61
12	6	0.197603	49.02
13	8	0.165735	47.06
14	4	0.206940	43.14
15	3	0.163658	37.25
16	7	0.191734	45.10
17	8	0.184357	49.02
18	2	0.198915	39.22
19	6	0.185000	33.33
20	7	0.224288	41.18

Table 4.20. Epochs to converge and detection accuracy when using *Traincgb* and *tansig-tansig* transfer functions with varying number of hidden nodes (alternative 4 and one cover).

Hidden nodes	Epochs	Training Average Error	% accuracy (n=40)
3	45	0.191805	11.76
4	42	0.177353	17.65
5	38	0.197086	25.49
6	40	0.258060	21.57
7	39	0.219309	23.53
8	28	0.228824	52.94
9	31	0.203632	39.22
10	28	0.212412	45.10
11	28	0.272126	45.10
12	49	0.202996	3.92
13	28	0.191563	45.10
14	30	0.189836	41.18
15	32	0.195568	37.25
16	47	0.173889	7.84
17	47	0.209814	7.84
18	44	0.198061	13.73
19	39	0.245142	23.53
20	33	0.219799	35.29

However, the percentage of accuracy was still low. A trial to increase the accuracy was done by testing different training functions with the same transfer function combination (tansig-tansig); a total of four training functions were tested for alternatives 3 and 4 (traincgb, trainbfg, trainlm, and trainrp). The best results were obtained with traincgb-alternative 4 (Powell-Beale conjugate gradient back propagation training function) and a 52.94% of accuracy, but trainrp-alternative 4 was still competitive with a 50.9% of accuracy (See Tables 4.19 and 4.20). Next, the influence of the data sets selected for training and testing was analyzed. Four random sets of data (random 1, random 2, random 3, and random 4) were produced and tested with the same transfer function combination (tansig-tansig) for alternatives 3 and 4 using training functions trainrp and traincgb. The best results obtained were for the random 4-traincgb-alternative 3

combination with a 70.6% of accuracy (See Table 4.21). It is important to remark that a total of 38 neural network models were developed in order to improve prediction results for one cover sets of data and that each neural network model was restarted several times to achieve the best accuracy (it is well known that random initial weights affect neural network performance). Only the best results achieved by means of the improvement procedure are presented in Tables 4.21 and 4.22. According to Tables 4.21 and 4.22, it is clear that the sample chosen from the whole amount of data influence the prediction accuracy, because the more representative is the sample the better predictions can be obtained. In addition, the highest the number of input nodes are used, the highest accuracy in the predictions is obtained (i.e. this is only true if the additional input nodes discriminate among classes in the same level as the original ones). For example, alternative 3 achieves better accuracies than alternative 4; even if alternative 4 uses four input nodes and alternative 3 three input nodes, alternative 3 uses a combination of the five cooling rates or variables with similar capability to discriminate among classes (as seen in Table 4.12 means distances among classes are similar for all cooling rates). Something to infer from neural networks models for boards without cover and one cover results is that the set of data with the highest multivariate distances (data for boards without cover) among classes discriminate better among such classes.

Table 4.21. Epochs to converge and detection accuracy when using different random training and test sets of data and *tansig-tansig* transfer functions with *trainrp* and *traincgb* training functions (alternative 3 and one cover).

Data set	training function	Hidden nodes	Epochs	Training Average Error	% accuracy (n=40)
random 1	Trainrp	9	94	0.233551	50.98
random 2	Trainrp	8	42	0.191207	49.00
random 3	Trainrp	20	179	0.186689	52.94
random 4	Trainrp	10	24	0.217404	60.78
random 1	Traincgb	6	27	0.265612	47.00
random 2	Traincgb	9	93	0.196127	56.86
random 3	Traincgb	5	125	0.195917	66.67
random 4	Traincgb	11	63	0.172983	70.59

Table 4.22. Epochs to converge and detection accuracy when using different random training and test sets of data and *tansig-tansig* transfer functions with *trainrp* and *traincgb* training functions (alternative 4 and one cover).

data set	training function	Hidden nodes	Epochs	Training Average Error	% accuracy (n=40)
random 1	Trainrp	6	175	0.240834	41.18
random 2	Trainrp	13	9	0.250442	45.00
random 3	Trainrp	9	206	0.220580	52.90
random 4	Trainrp	7	114	0.216411	47.06
random 1	Traincgb	6	49	0.245519	45.00
random 2	Traincgb	13	31	0.239390	49.00
random 3	Traincgb	12	38	0.231460	50.98
random 4	Traincgb	7	41	0.224493	50.98

As mentioned before, the multivariate means distances among classes (60, 90, and 120) for the sets of data for the board with two covers is quite similar to the sets of data for the board with one cover (See Tables 4.15 and 4.16). According to the similarity between these two sets of data, the best neural networks configurations obtained for the boards with one cover data sets were used for the boards with two covers data sets. The best configurations for the board with one cover data sets were the ones with tansig-tansig transfer functions and training function trainrp or traincgb. In addition, two random sets of data for training and testing of the neural network model were used. Tables 4.23 to 4.26 show the best neural networks configurations in function of the random set of data and training function used for the accustomed seven alternatives of the input nodes. According to the results, *trainrp* training function offers a better accuracy for the random set of data 1, but the *traincgb* offers a better behavior for set of data 2 (See average for percent of accuracy in Tables 4.23 to 4.26). In relation to the random sets of data, there is not a major difference in the accuracies achieve indicating a consistency in the population. Independently of the sets of data or training functions, Alternative 2 offers a better performance and Alternative 3 offers a close performance. Alternative 2 uses four input nodes, while Alternative 3 uses three nodes and a combination of the five cooling rates or discriminating variables. This supports the

theory that no only the amount of input nodes or data matters but also the quality of the data to discriminate or characterized the different classes (60, 90 and 120).

Table 4.23. Epochs to converge and detection accuracy when using different alternatives for the input nodes and *tansig-tansig* transfer functions with *trainrp* training function and random set of data 1 (two covers).

	Hidden nodes	Epochs	Training Average Error	% accuracy (n=40)
A1	5	22	0.194225	45.00
A2	9	9	0.247412	66.67
A3	10	4	0.195255	58.89
A4	11	14	0.165641	53.00
A5	14	5	0.197665	53.00
A6	9	9	0.180939	53.00
A7	5	9	0.211049	45.10
			Average	53.52

Table 4.24. Epochs to converge and detection accuracy when using different alternatives for the input nodes and *tansig-tansig* transfer functions with *traincgb* training function and random set of data 1 (two covers).

	Hidden nodes	Epochs	Training Average Error	% accuracy (n=40)
A1	3	4	0.204544	41.18
A2	7	9	0.153186	58.34
A3	4	12	0.183623	55.00
A4	6	5	0.258272	54.90
A5	14	3	0.253255	52.98
A6	9	20	0.171488	51.00
A7	3	16	0.219623	49.00
			Average	51.77

Table 4.25. Epochs to converge and detection accuracy when using different alternatives for the input nodes and *tansig-tansig* transfer functions with *trainrp* training function and random set of data 2 (two covers).

	Hidden nodes	Epochs	Training Average Error	% accuracy (n=40)
A1	5	5	0.236688	47.00
A2	6	10	0.170762	66.67
A3	5	5	0.224785	56.86
A4	11	8	0.251481	47.06
A5	10	8	0.196636	49.02
A6	14	13	0.212268	49.00
A7	15	10	0.317260	39.22
			Average	50.69

Table 4.26. Epochs to converge and detection accuracy when using different alternatives for the input nodes and *tansig-tansig* transfer functions with *traincgb* training function and random set of data 2 (two covers).

	Hidden nodes	Epochs	Training Average Error	% accuracy (n=40)
A1	5	98	0.248562	45.10
A2	3	9	0.2367	66.67
A3	15	37	0.183480	64.71
A4	14	12	0.219521	51.00
A5	16	1	0.215635	51.00
A6	5	22	0.196951	52.00
A7	16	4	0.262501	41.18
			Average	53.09

If the maximum accuracy predictions are compared among the experimental data for the boards with no cover (84.5%), one cover (70.6%) and two covers (66.67%), the boards with no cover data provide a much better accuracy prediction for the solder joint shape than the boards with covers. In addition, the accuracy of prediction for the boards with covers is similar. This is a clear evidence that sets of data with higher difference in the multivariate means among closest classes have better discrimination capability (difference among closest classes for no cover: $CR_{60\text{-}90}$=10.91 and $CR_{90\text{-}120}$=4.4;

difference among closest classes for one cover: $CR_{90\text{-}60}$=0.526 and $CR_{60\text{-}120}$=1.8; difference among closest classes for two covers: $CR_{90\text{-}60}$=0.7045 and $CR_{60\text{-}120}$=1.5).

4.1.5. Findings

According to the experimental results, temperatures and grand average cooling rates depend highly on the solder joint shapes for the PCB assembly with no cover. A clear dependence of the temperatures and grand average cooling rates, with respect to the solder joint angle, was determined for the assembly with no cover but not for the assemblies with covers. A 1-D analysis showed that a lower total surface area and cone angle reduce the energy lost by conduction and convection on the solder joints for the PCB assembly for no cover; therefore, the lower surface area available for energy dissipation as the cone angle decreases promotes higher temperatures and grand average cooling rates. In the case of the assemblies with covers, the addition of the covers limits the amount of energy reaching the solder joint shapes and completely eliminates the effect of the solder joint shape in the absorption of energy by radiation; this significantly weakens the difference between temperatures and grand average cooling rate signals among solder joint positions. The addition of the covers not only weaken signals differences but promotes a major role of the position versus the shape of the solder joint on the temperatures and grand average cooling rates. When the covers are added, the temperature on the surface of the cover is monitored introducing boundary conditions asymmetries; regions closer to the edged of the cover are affected by convection, while the region at the center is affected by the copper wires at its sides. This asymmetry conducted to higher temperatures and grand average cooling rates at the central position. Therefore, comparison of temperatures and grand average cooling rates are more reliable among the solder joint shapes at the sides, because these solder joints are under the same boundary conditions.

As mentioned in previous paragraph, the temperature and grand average cooling rate differences among solder joint shapes decrease as the number of covers increases. However, a MANOVA analysis proved that solder joint shapes are statistically different when described by the grand average cooling rates. Therefore, an artificial neural networks method was used to classify the experimental solder joint shapes in function of the grand averages cooling rates for no cover, one cover, and two covers assemblies. The classification accuracy reduces as the number of covers increases. This accuracy reduction is caused by the decrement of grand average cooling rate distances among solder joints as the number of covers increases.

4.2. Numerical Model

This section presents the results of the verification and validation procedures for the numerical model. Section 4.2.1 presents some of the aspects of the numerical model development as well as the verification process. Section 4.2.2 discuses the agreement found between the numerical model and the experimental model as well as the main causes for the disagreements between models.

4.2.1. Finite element Model Development and Verification

According to Section 3.3.1, the mesh on the model was generated according to the importance of the component in the thermal phenomena. In addition, the mesh is smaller close to the interfaces between the different components. Figure 4.16 shows the mesh generated for one cover PCB assembly. It can be seen that the mesh is fine close to the wires and coarse in the structure of the fixture. The reason for this is that high temperature gradients are expected in the interface between the wire and the cover but not in the bottom of the fixture because is blocked by the rest of the components.

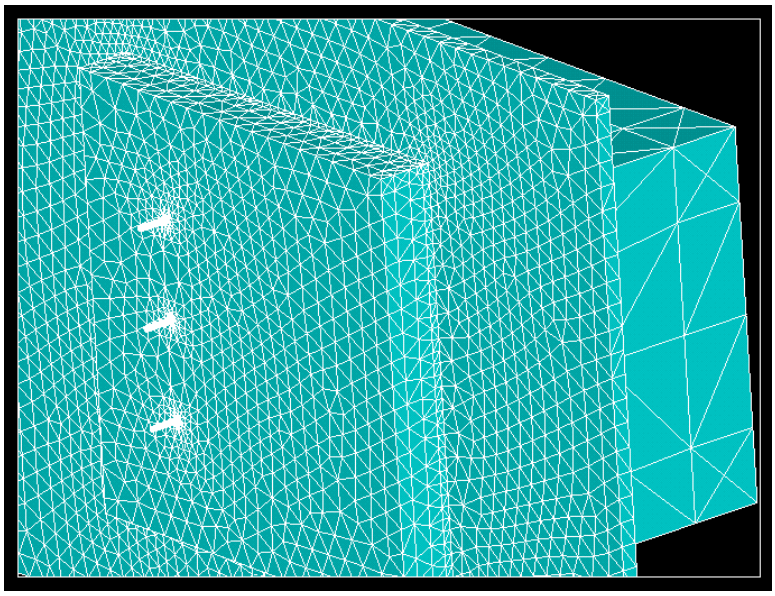

Figure 4.16. Mesh generated for the PCB assembly.

In order to verify spatial grid convergence, three different meshes were generated on the top parts of the assembly using three different levels of refinement with the SmartSize ANSYS function (7, 5, and 4 levels). The total numbers of elements obtained were 240,325, 165,534, and 105,757 for the fine, medium, and coarse meshes, respectively. The finite element model was solved for 30 s of heating time and 4918 W/m^2 for the heat flux. The temperatures at the 60, 90, and 120 solder joint positions were obtained. The total volume of the solid model was determined to be 0.0171 m^3 and the refinement factors among models were determined to be r_{21}=1.13 and r_{32}=1.16. According to group of Equations (20) and the temperatures determined at the different solder joint shapes positions, the grid convergence indexes were calculated and are shown in Table 4.27; important variables during the calculation procedure are shown too. According to Table 4.27, the numerical uncertainty ranges from 0.14 to 0.33% and 2.19 to 4.13% for the fine and medium meshes, respectively; the corresponding variation in temperatures are from 0.113 to 0.075 ºC and from 1.24 to 2.4 ºC. The highest discrepancy between the coarse

and the medium refinement with respect to the discrepancy between the medium and fine refinements verifies that the spatial grid convergence was achieved.

Table 4.27. Grid convergence indexes for three different levels of refinement on the numerical model.

Solder Joint position	f_1 (ºC)	f_2 (ºC)	f_3 (ºC)	φ_{21}	φ_{32}	E_{21}	E_{32}	$\%GCI_1$	$\%GCI_2$
90	56.42	56.50	56.92	0.089	0.413	0.0016	0.0073	0.20	-2.19
60	55.60	55.40	56.01	-0.200	0.610	0.0036	0.0110	0.33	-3.33
120	54.13	54.16	54.90	0.025	0.743	0.0005	0.0137	-0.14	-4.36

Next, a qualitative verification of the thermal distribution on the model is performed. With regards to the temperature distribution at the model (see Figure 4.17), it can be seen that the temperatures close to the edges at the cover are low because of thermal convection at the lateral surfaces, there is an important thermal gradient close to the interface between the wire and the cover caused by the differences in thermal conductivities, and the temperatures at the fixture support are very low because of the lack of heat transfer reaching this areas. These behaviors verify completely the agreement between the solution, the energy conservation, and the boundary conditions imposed to the model.

The code accuracy has been verified extensively by ANSYS. ANSYS is a program in commercial use since 1970. In addition, ANSYS provides multiple test cases that have a theoretical solution for verification. Unfortunately, the PCB assembly is too specific and complicated to obtain a full theoretical solution. However, simple theoretical solutions or numerical solutions to partial differential equations can be used to corroborate the veracity of the solution of the PCB assembly in some of the portions of the PCB assembly.

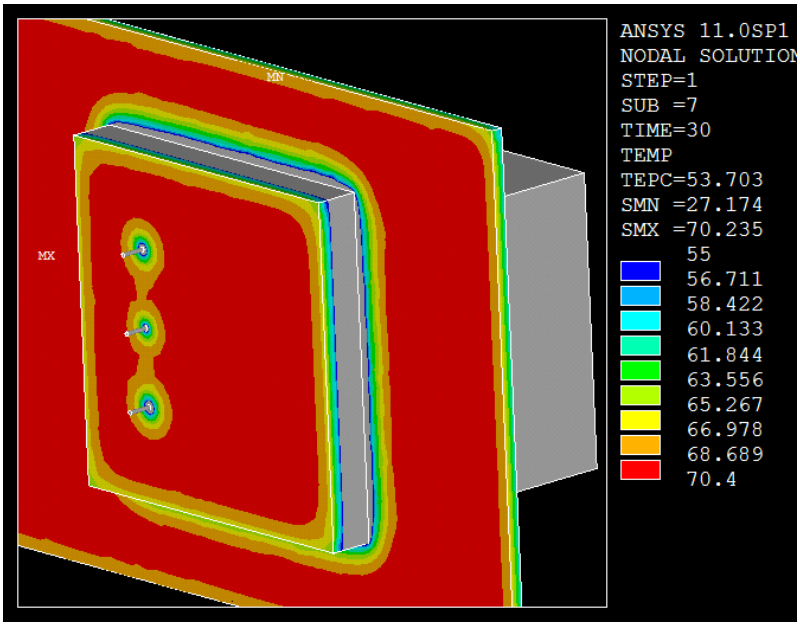

Figure 4.17. Temperature distribution at the PCB assembly after 30 s of heating time.

The cover of the model showed in Figure 4.18 was subject to a heat flux of 5087 W/m^2 for 30 s, the initial temperature of the model was uniform and equal to 28.7 °C, and the ambient temperature was 27 °C. In temperature ranges of 28.7 to 70.4 °C, the convective coefficient varies from 3 to 6 W/m^2 °C at the lateral surfaces and from 3.5 to 7.5 W/m^2 °C at the top cover. Now, if the cover of the PCB assembly is considered as an object with no dimensional temperature variations (Bio is much lower than 1, see Table 3.1) and with and adiabatic bottom surface ($k_{air} << k_{board}$), an analytical solution can be obtained considering a lumped capacitance model and it is given by Equation (28). Solving the temperature for the cover under the conditions already mentioned, a temperature for the cover at 30 s of heating can be calculated as 70.09 °C; temperature that agrees with the maximum numerical temperature (69.87 °C) at the top of the cover verifying the accuracy of the solution of the numerical model.

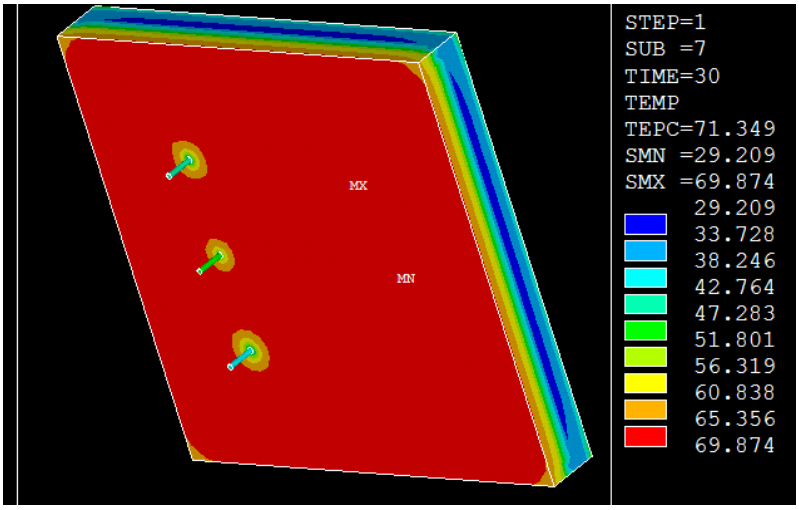

Figure 4.18. Temperature distribution at 30 s of heating after applying 5087 W/m^2 of heat flux to the top cover.

Moreover, the position of the numerical maximum temperature at the top of the cover is the location where the lateral heat transfer has a minimum effect; therefore, the temperature at this position can be considered as varying only in the perpendicular direction to the cover. A 1-D model of the PCB assembly at this location is shown in Figure 4.19. This model has the next governing equation:

$$\frac{\partial^2 T}{\partial z^2} = \frac{1}{\alpha}\frac{\partial T}{\partial t} \tag{30}$$

this is a partial differential equation that can be represented by the numerical explicit method of finite differences with the next expression:

$$\frac{T_{m+1}^{p} + T_{m-1}^{p} - 2T_{m}^{p}}{(\Delta x)^2} = \frac{1}{\alpha}\frac{T_{m}^{p+1} - T_{m}^{p}}{\Delta t} \tag{31}$$

where p is the p^{th} interval of time, m is the m^{th} grid point, and Δx is the one dimensional grid spacing. Equation (31) can be solved easily for the unknown times because all the temperatures in the previous time are known. More details about the method can be found at [151]. The method was applied at every portion of the PCB assembly, and the transient temperature was obtained for every component of the assembly.

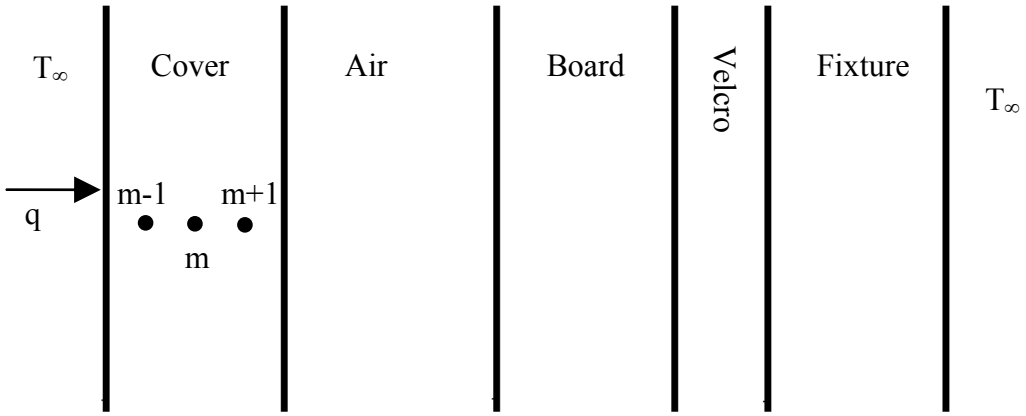

Figure 4.19. 1-D model of the PCB assembly.

Figure 4.20 shows the temperature distribution obtained for the 1-D PCB assembly model. The temperatures of the numerical model at the top surface and the bottom surface of the fixture platform are 69.87 and 29 °C. The temperatures determined with the 1-D model at this positions are 71.94 and 28.85 °C verifying again the accuracy in the calculations of the finite element model.

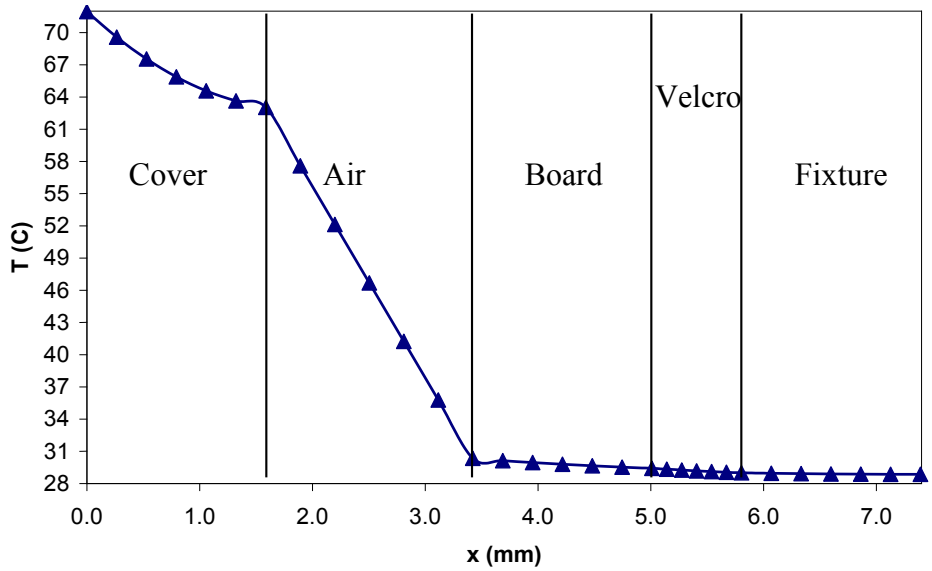

Figure 4.20. Temperature distribution for the1-D model of the PCB assembly at 30 s of heating.

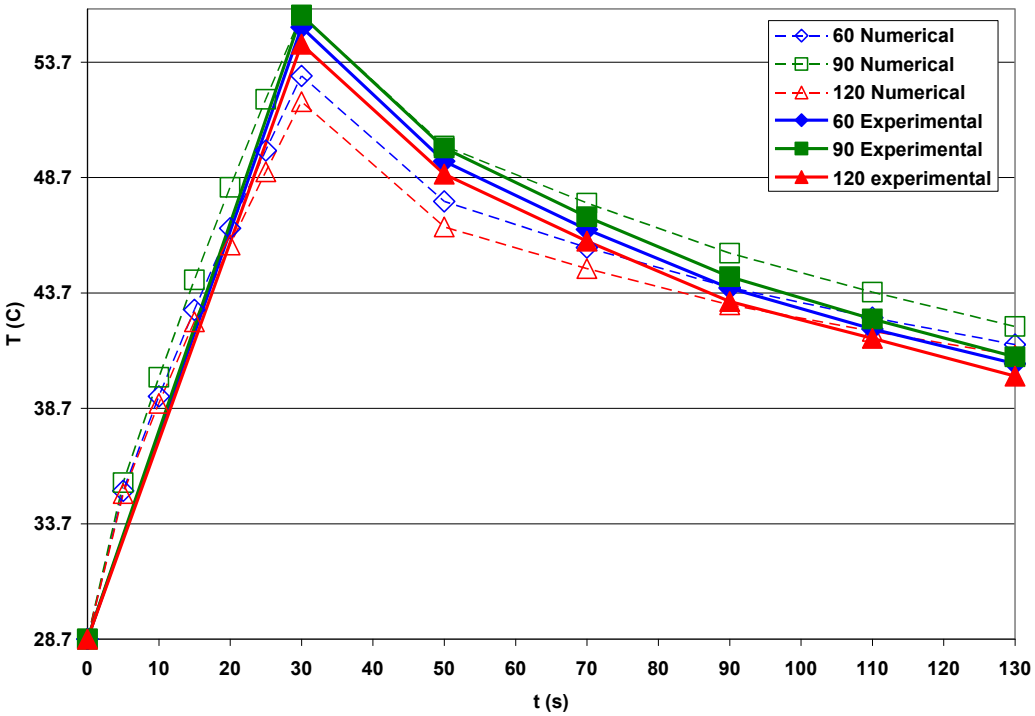

Figure 4.21. Average temperature at the different solder joint shape position (one cover).

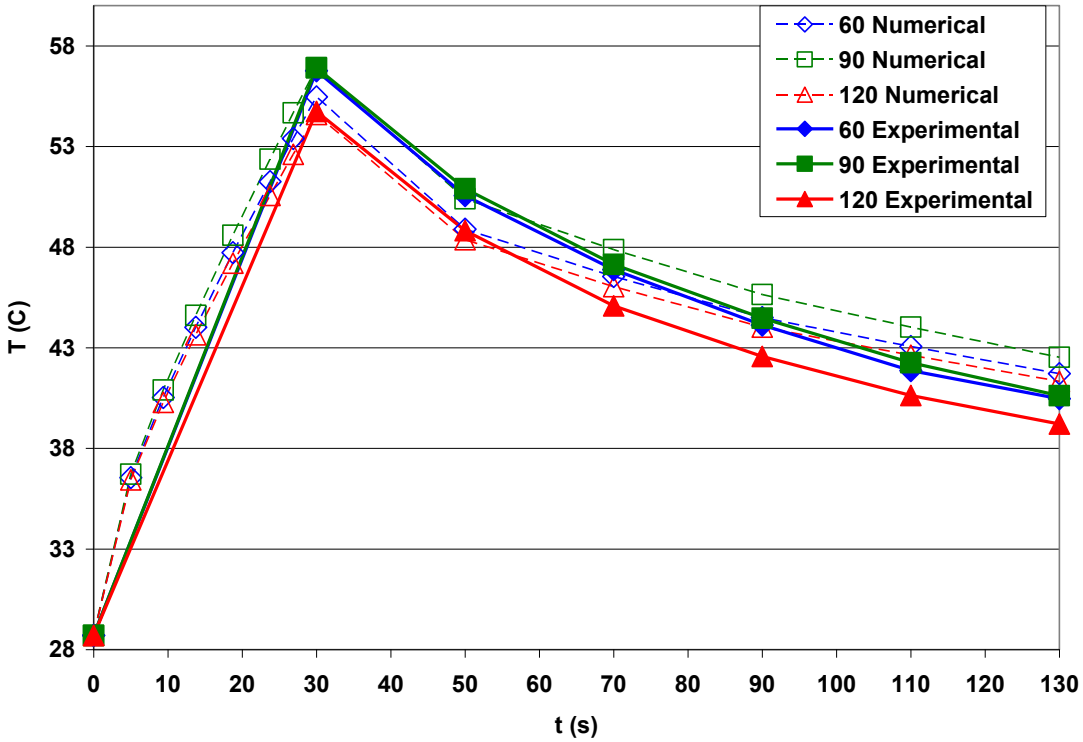

Figure 4.22. Average temperature at the different solder joint shape position (two covers).

4.2.2. Finite element Model Validation

Figures 4.21 and 4.22 show a comparison among the average temperatures at the solder joint positions between the experimental results and the numerical models for one and two covers, respectively. Tables 4.28 and 4.29 show the difference between experimental and numerical average temperatures over time at the 60, 90 and, 120 positions. It can be seen that experimental and numerical temperatures are within a margin of 2.5 °C (5%) and 2.13 °C (4%) of each other for one cover and two cover models, respectively. The main difference between the numerical and experimental models is the slope of the temperature curve. The temperature slope is higher for the experimental model than for the numerical model. The reason is that the numerical model neglects thermal convection in the gaps between covers and in the gaps between

the PCB and the first cover. In consequence, the temperatures in the experimental models drop faster than in the numerical model, because the energy lost by thermal convection is more significant than the energy lost by thermal conduction. The highest average temperature difference is at the extreme positions (i.e. this is a consequence of the non uniform heat flux from the lamp in the experimental model and the fact that the numerical model aims to have the same temperature as the experimental model at the central position at the end of heating process).

Table 4.28. Average temperature difference among experimental and numerical models (one cover).

time (s)	$(T_{60})_{exp}$-$(T_{60})_{num}$ (ºC)	$(T_{90})_{exp}$-$(T_{90})_{num}$ (ºC)	$(T_{120})_{exp}$-$(T_{120})_{num}$ (ºC)
30	2.11	-0.01	2.49
50	1.74	-0.09	2.29
70	0.78	-0.59	1.19
80	-0.03	-1.02	0.14
110	-0.49	-1.16	-0.30
130	-0.83	-1.32	-0.90

Table 4.29. Average temperature difference among experimental and numerical models (two covers).

Time (s)	$(T_{60})_{exp}$-$(T_{60})_{num}$ (ºC)	$(T_{90})_{exp}$-$(T_{90})_{num}$ (ºC)	$(T_{120})_{exp}$-$(T_{120})_{num}$ (ºC)
30	1.29	0.00	0.15
50	1.67	0.50	0.45
70	0.35	-0.74	-0.95
80	-0.37	-1.18	-1.45
110	-1.20	-1.77	-2.00
130	-1.26	-1.92	-2.13

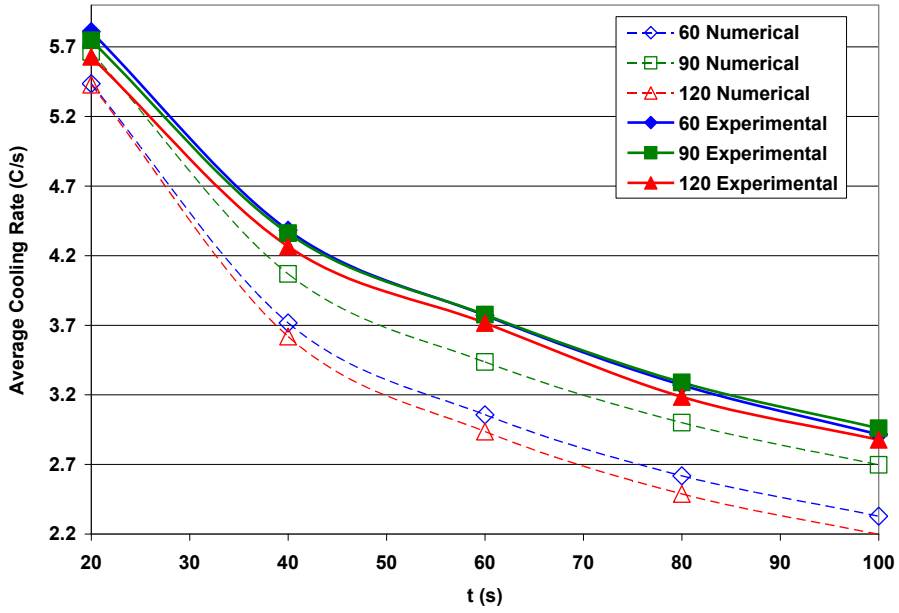

Figure 4.23. Grand average cooling rate at the different solder joint shape position (one cover).

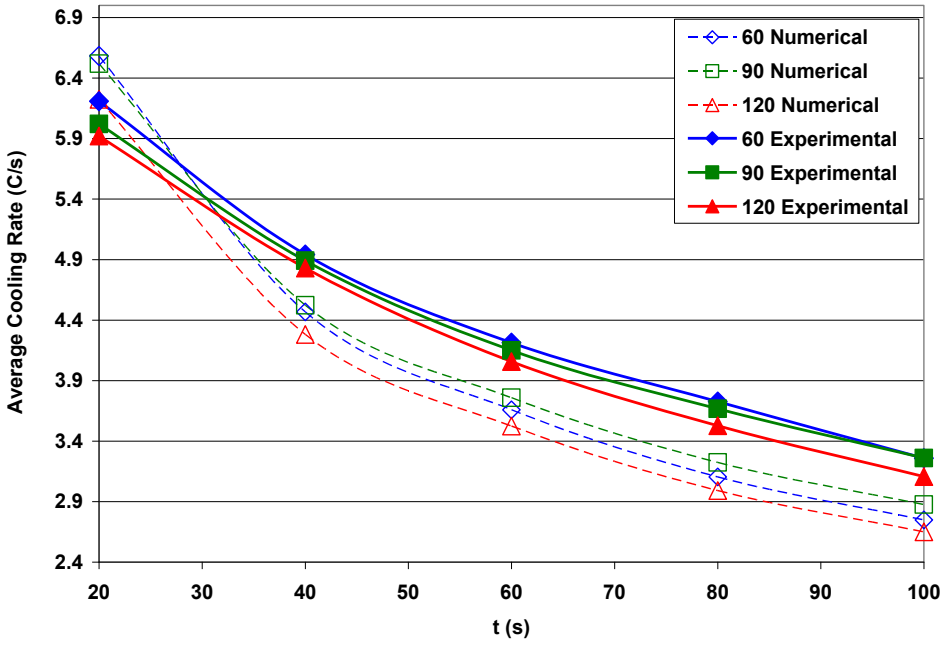

Figure 4.24. Grand average cooling rate at the different solder joint shape position (two covers).

Figures 4.23 and 4.24 show the grand average cooling rate comparison between experimental and numerical models for one and two covers, respectively. Tables 4.30 and 4.31 show the percentage of difference between experimental and numerical grand average cooling rates over time at the 60, 90 and, 120 positions. The maximum differences between models are in the extreme positions (60 and 120), although there is a higher difference for the cooling rate (20% maximum) than for temperature (5% maximum), because cooling rate is a characteristic describing not only temperature level, but also how the temperature drops over time. Some points to notice in both, numerical and experimental grand average cooling rate curves, are: the grand average cooling rate increase while the distances among classes decrease from one cover to two covers, two of the contiguous classes are very close at some point and even crossed paths (as an example see the grand average cooling rates for 60 and 90 positions for Figure 4.24), and the distances among classes are higher in the numerical model that considers a uniform heat flux. These differences are caused by a natural difference in the heating source between models that affects the initial temperature during cooling process, and by some variations in the properties for the board material (FR4) with a special emphasis on the specific heat that dictates how the temperature changes in the board cover.

Table 4.30. Grand average cooling rate difference between experimental and numerical models (one cover).

time (s)	ΔCR_{60} (%)	ΔCR_{90} (%)	ΔCR_{120} (%)
30	6.43	1.44	3.57
50	15.21	6.71	15.17
70	18.97	9.00	21.02
80	19.92	8.79	21.89
110	20.17	8.85	23.58

Table 4.31. Grand average cooling rate difference among experimental and numerical models (two covers).

time (s)	ΔCR_{60} (%)	ΔCR_{90} (%)	ΔCR_{120} (%)
30	6.43	1.44	3.57
50	15.21	6.71	15.17
70	18.97	9.00	21.02
80	19.92	8.79	21.89
110	20.17	8.85	23.58

As demonstrated in Sections 4.1.3 and 4.1.4, the variable differences (Temperature and grand average cooling rates) among contiguous classes (solder joint shapes) determine the discriminability among solder joint shapes. Solder joint shapes were discriminate with better accuracy for the sets of data with higher grand average cooling rate means differences (no cover 85%, one cover 72%, and two covers 67%). This indicates that a higher difference in temperature and grand average cooling rates among contiguous classes will provide a better discriminability among classes. Tables 4.32 to 4.36 show the absolute difference among contiguous classes for the experimental and numerical results analysis in no cover (only experimental), one cover, and two covers. It can be inferred from the experimental results, that increasing the number of covers reduces the temperature and grand average cooling rates differences among contiguous solder joint shapes. Although there are some discrepancies in the differences for the experimental results for the two covers model, this hypothesis is corroborated in the numerical differences for two covers. Two covers model that show a reduction in both the average temperature and grand average cooling rates differences with respect to those ones for one cover model. This hypothesis will be explored by varying the amount of covers and keeping the heat flux at the top cover constant in the parametric numeric analysis (Section 4.3.1).

Table 4.32. Experimental temperature and grand average cooling rate differences between contiguous solder joint shapes (no cover and 30 s heating time).

Time(s)	$T_{90\text{-}60}$	$T_{120\text{-}90}$	$CR_{90\text{-}60}$	$CR_{120\text{-}90}$
0	1.372	1.231		
20	1.161	0.955	0.211	0.276
40	1.100	0.774	0.136	0.229
60	1.062	0.606	0.103	0.208
80	1.030	0.480	0.086	0.188
100	0.970	0.335	0.080	0.179
Average	**1.116**	**0.730**	**0.123**	**0.216**

Table 4.33. Experimental temperature and grand average cooling rate differences between contiguous solder joint shapes (one cover and 30 s heating time).

Time(s)	$T_{90\text{-}60}$	$T_{60\text{-}120}$	$CR_{90\text{-}60}$	$CR_{60\text{-}120}$
0	0.511	0.737		
20	0.573	0.557	0.062	0.118
40	0.553	0.503	0.021	0.096
60	0.498	0.572	0.004	0.059
80	0.431	0.401	0.020	0.104
100	0.294	0.541	0.043	0.082
Average	**0.477**	**0.552**	**0.030**	**0.092**

Table 4.34. Experimental temperature and grand average cooling rate differences between contiguous solder joint shapes (two covers and 30 s heating time).

Time(s)	$T_{90\text{-}60}$	$T_{60\text{-}120}$	$CR_{90\text{-}60}$	$CR_{60\text{-}120}$
0	0.153	2.023		
20	0.340	1.737	0.187	0.100
40	0.256	1.800	0.051	0.061
60	0.342	1.557	0.063	0.093
80	0.393	1.228	0.060	0.139
100	0.147	1.261	0.001	0.154
Average	**0.272**	**1.601**	**0.072**	**0.109**

Table 4.35. Numerical temperature and grand average cooling rate differences between contiguous solder joint shapes (one cover and 30 s heating time).

Time(s)	T_{90-60}	T_{60-120}	CR_{90-60}	CR_{60-120}
0	2.630	1.111		
20	2.402	1.103	0.228	0.008
40	1.925	0.916	0.353	0.097
60	1.489	0.749	0.380	0.121
80	1.101	0.592	0.382	0.130
100	0.783	0.464	0.369	0.129
Average	**1.722**	**0.822**	**0.343**	**0.097**

Table 4.36. Numerical temperature and grand average cooling rate differences between contiguous solder joint shapes (two covers and 30 s heating time).

Time(s)	T_{90-60}	T_{60-120}	CR_{90-60}	CR_{60-120}
0	1.447	0.876		
20	1.511	0.517	0.064	0.358
40	1.337	0.503	0.055	0.186
60	1.149	0.472	0.099	0.134
80	0.968	0.425	0.120	0.113
100	0.812	0.382	0.127	0.099
Average	**1.204**	**0.529**	**0.093**	**0.178**

4.2.3. Findings

The numerical model maximum uncertainty was 0.33% when using a fine mesh with 240325 elements, and it was verified for spatial grid convergence. The numerical model was verified to model the heat transfer phenomena adequately by examining qualitatively the temperature distribution at 30s of heating; temperatures close to the edges are lower because of thermal convection, temperatures close to the copper wires show a significant temperature gradient caused by the high thermal conductivity difference between the cover and the wire, and the temperatures on the fixture support are considerably low because of the lack of energy transfer to this component. A lumped

capacitance model of the cover was used to verify the veracity the numerical model temperatures calculations at the top cover; the difference between the lumped model temperature and the numerical model maximum temperature was only 0.31%. In addition, a 1-D finite differences composite wall model of the PCB assembly further verify the numerical model temperature calculations; temperatures determined by finite differences were compared to the numerical temperatures at the most probable location following a 1-D thermal conduction model and were verified to have a maximum difference of 3%.

The agreement of the numerical model with the experimental model was validated. The level of disagreement of the temperatures at the solder joint 90 position was found to be within 3.21% (one cover) and 4.73% (two covers); in the case of grand average cooling rates, the level of disagreement was within 8.85% (one cover) and 13.36% (two covers). The higher disagreement for grand average cooling rate was caused by a discrepancy between models in the rate of temperature drop. The reason of the discrepancy is that the numerical model neglects thermal convection in the air gaps between covers, and between the PCB and the first cover. Thermal convection in air is a faster heat transfer mechanism than thermal conduction causing a higher temperature drop over time for the experimental model.

4.3. Prediction Model

A prediction model was developed to predict the optimum active thermography conditions required to achieve an adequate hidden solder joint shape characterization. First, a parametric numeric analysis was performed to determine the relationship between the number of covers and active thermography parameters (heat flux and heating time). After the parametric analysis was concluded, a linear regression model was used to generate a predictive model. The predictive model aims to determine the optimal infrared thermography conditions to discriminate among solder joint shapes.

4.3.1. Finite element Parametric Analysis

Three main parameters were varied in the parametric analysis: amount of heating time, number of covers, and heat flux. Next subsections will present the effects that these parameters caused in the capability to discriminate among solder joint shapes.

4.3.1.1. Number of Covers

Figures 4.25 and 4.26 show the average temperature and grand average cooling rate in function of the number of covers. According to Figure 4.25, the temperature differences decrease as the number of cover increases. The same behavior is detected in the grand average cooling rate differences (See Figure 4.26). After the four cover, is practically impossible to discriminate among solder joint shape positions by means of temperature. After the second cover, it is hard to see any difference among the solder joint shape positions by means of grand average cooling rate. According to the steady state 1-D models for one and two covers, the capacity of the system to dissipate energy by convection increases as the number of covers increases. Logically, the major capacity to dissipate energy reduces the thermal resistance of the PCB assembly as well as the energy reaching the solder joints through the copper wire. Therefore, it is important to keep in mind that energy conducted through the copper wire is lost to the surrounding air and the rest of the covers. The increment in amount of surface area in contact with the air as the number of covers increases (covers act like fins increasing energy lost) reduces the amount of energy reaching the solder joint shapes and causes a more uniform temperature distribution on the top cover. In addition, the lower energy reaching the solder joints decreases the effect of the solder joints shape on the cover temperatures at the side locations (60 and 120), and validates the hypothesis that increasing the number of covers reduces the capability of the inspection system to distinguish between solder joints geometries (comparison is reliable only between 60 and 120 solder joints that are subject to the same boundary conditions).

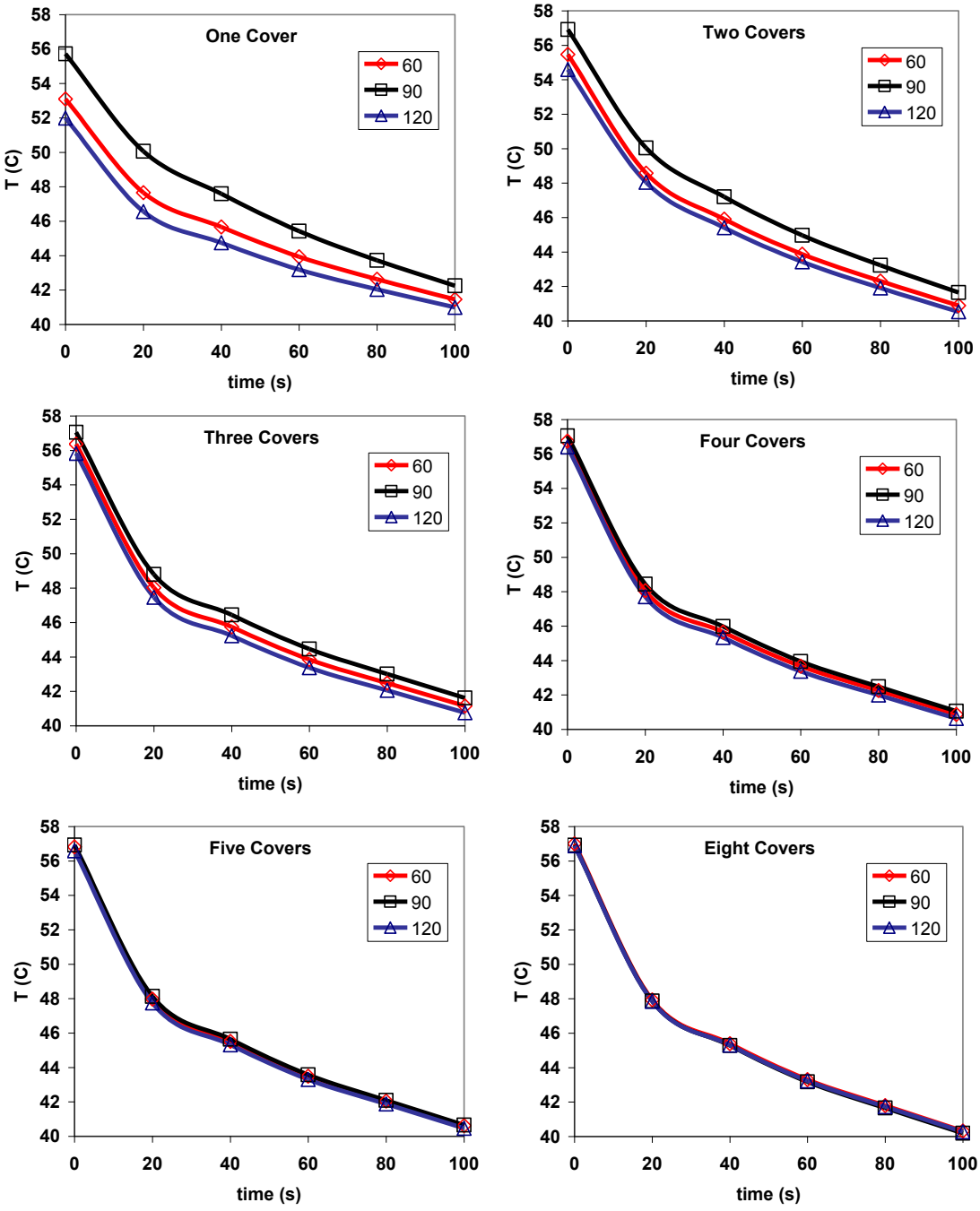

Figure 4.25. Average temperature as function of number of covers for constant heat flux.

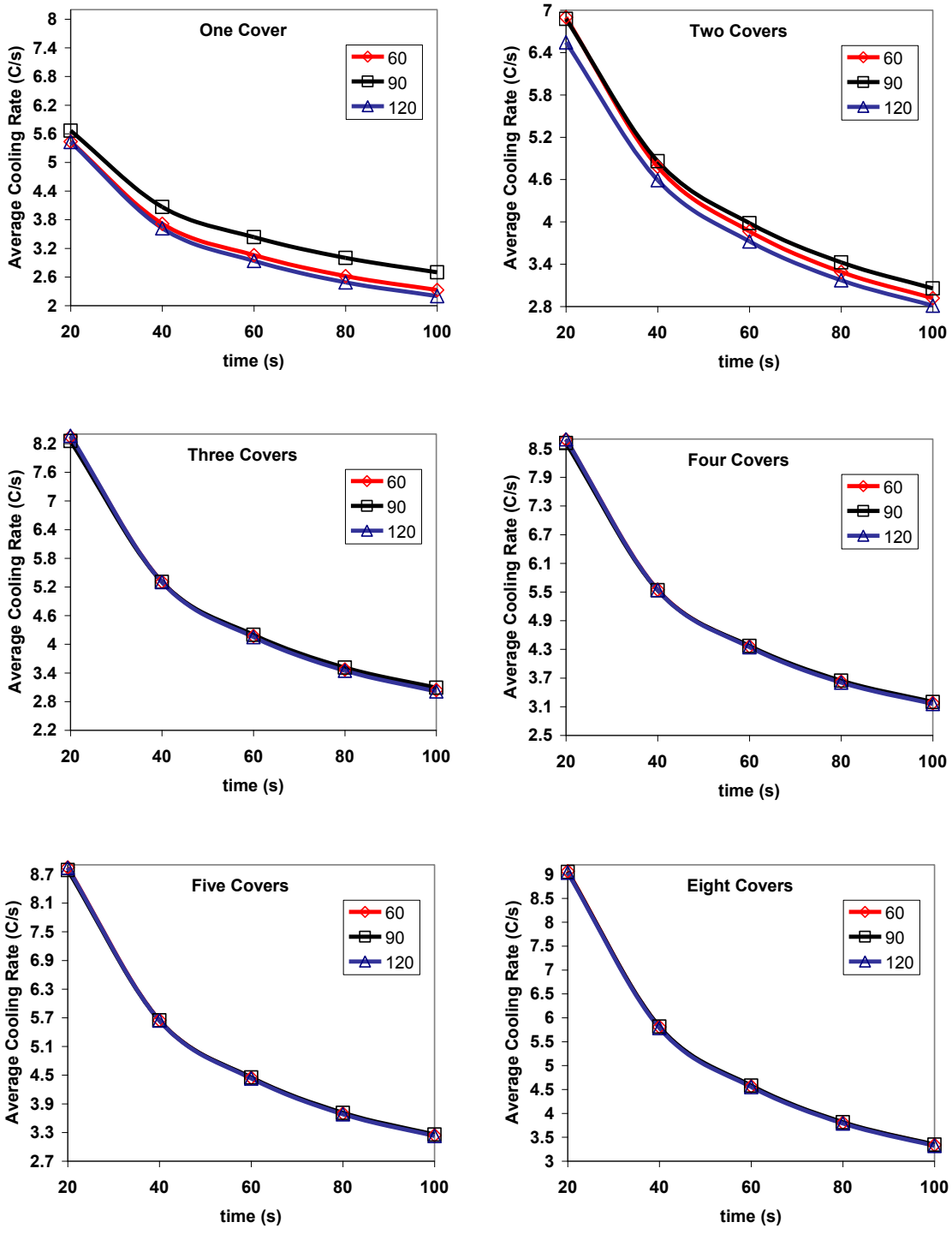

Figure 4.26. Grand average cooling rate as function of number of covers for constant heat flux.

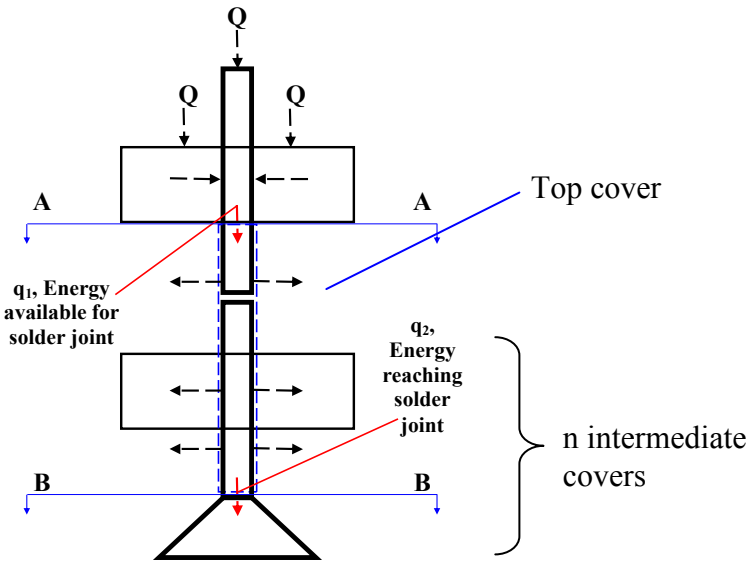

Figure 4.27. Schematic of multi covers PCB assembly showing the energy available for the solder joints and the energy reaching the solder joints.

In order to further corroborate that a minor energy reaching the solder joints as the number of covers increases is causing the poor capability to discriminate among solder joints, the energy lost in its way to the solder joints was determined for the numerical models for 1, 2, 3, 4, 5, and 8 covers at 30 seconds of heating. Referring to Figure 4.27, there are two ways for energy to get to the solder joints by means of the copper wire: direct irradiation, and conduction from the top cover to the wire. However, the total energy rate added to the wire can be considered as the energy rate added by conduction to the wire in the axial direction just below the top cover (q_1 energy crossing Plane A-A). On the other hand, the energy rate reaching the solder joint can be considered as the energy rate transfer by conduction (q_2) that is crossing Plane B-B. An estimate of the energy rate lost on its way to the cover can be determined by the difference between q_2 and q_1. Energy rate transfers q_1 and q_2 were determined by integration of the axial local numerical thermal flux over the copper wire transversal area on Planes A-A and B-B, respectively (energy rate into the wire in X-Y directions are neglected as they are only

3% of the axial thermal flux, see Figure 4.28). Energy rate q_1 plays an important role in the temperature on the top of the cover; a highest value of q_1 means a lower temperature in the cover because more energy rate is withdrawn from it.

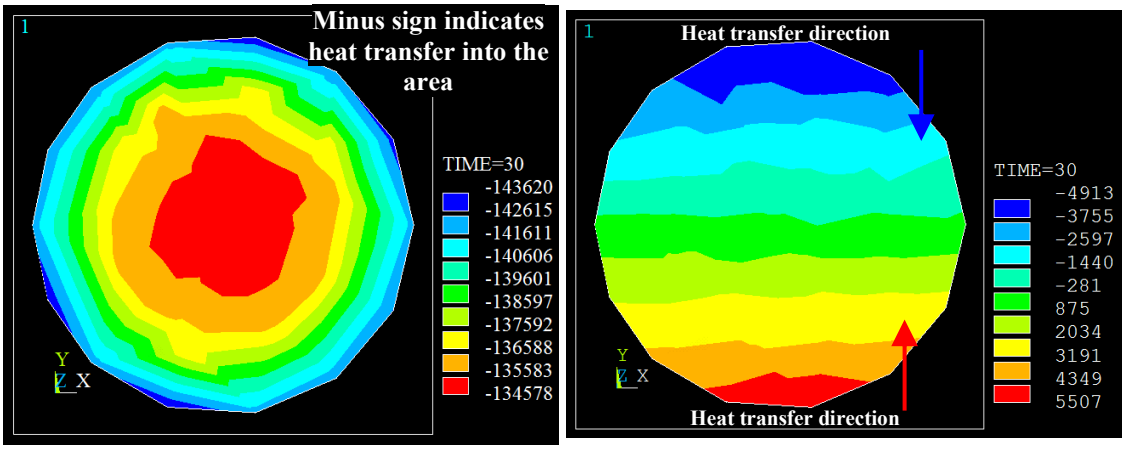

(a) **(b)**

Figure 4.28. Thermal fluxes for copper wire transversal section at Plane A-A in the: (a) z direction and (b) y direction.

Figure 4.29 shows the energy rate available for the solder joints; according to this figure, it can be concluded that temperatures at the 90 position will be the highest, because less energy is withdrawn from the cover in this position. By a similar logic, the temperature at the 60 position will be higher than the temperature at the 120 position corroborating the experimental temperature behavior over time for one and two covers.

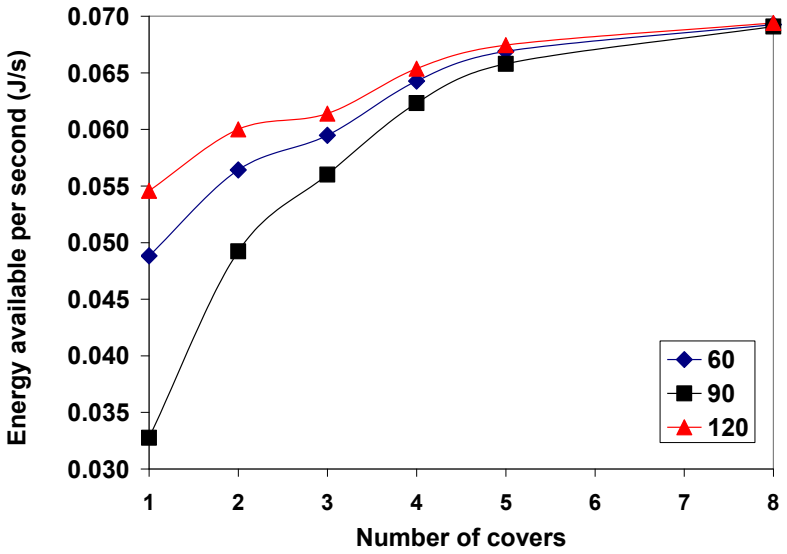

Figure 4.29. Energy rate available for the solder joints at the copper wire on Plane A-A.

Figure 4.30 shows the percentage of the amount of energy rate added to the copper wire that is lost on its way to the solder joint. It can be clearly seen that the amount of energy lost increases as the number of covers increases, and that almost no energy reaches the solder joints when 8 covers are used in the PCB assembly. This proves that the energy lost by axial heat transfer (in this case is axial heat transfer because convection in the gaps between covers and PCB is neglected in the numerical model) is the cause for the reduction in discriminability or ability to distinguish between the solder joint geometries (only between 60 and 120 solder joint geometries that are under the same boundary conditions). Finally, the trend on the energy lost among solder joints is identical to the trend found for the experimental and numerical temperature and grand average cooling rate; this links axial energy rate lost as the reason for the temperature and grand average cooling rate behaviors as the number of covers increases. Therefore a higher amount of energy must be provided in order to reach the solder joint shapes. Section 4.3.1.2 shows the effect of the increment in the amount of energy provide to the cover.

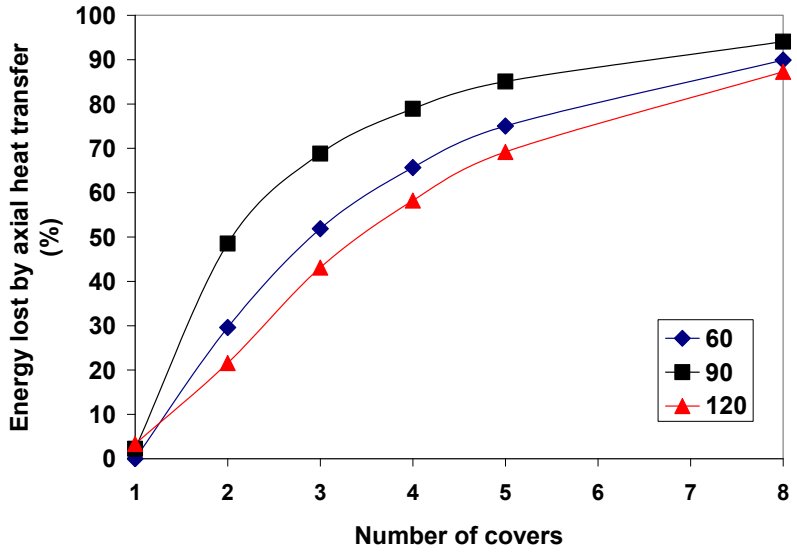

Figure 4.30. Percentage of energy rate lost by axial heat transfer before reaching the solder joints.

4.3.1.2. Amount of Heat Flux

As an example of the effect of increasing the amount of heat flux and the direct proportionality between temperature and grand average cooling rate differences, Table 4.37 shows the percentage of increment in the differences obtained by increasing the amount of energy applied to the cover. This clearly proves that the increment of heat flux provides and increment in the temperature and grand average cooling rate differences among contiguous classes and, therefore, an increment on discriminability too. However, energy can not be added without restriction to the cover; energy can be added only until the cover material reaches its glass transition temperature (150 ºC). In addition, no excess of energy should be added; energy should be added only until a good discriminability is reached.

Table 4.37. Percentage of increment in the numerical temperature and grand average cooling rate differences between contiguous positions obtained by increasing the heat flux for three and four covers numerical models.

	Increment (%)				
	Amount of energy	**T_{90-60}**	**T_{60-120}**	**CR_{90-60}**	**CR_{60-120}**
3 covers	156.124	140.175	136.889	147.355	143.599
4 covers	162	142.012601	133.766434	150.578158	131.306384

A good discriminability is dictated by the prediction accuracy. If temperature and cooling rate distances among solder joint shapes for the experimental results for no cover, one cover, and two covers (84.5%, 70.6%, and 66.7% accuracy discriminating among solder joint shapes) are compare to the numerical results for one and two covers, it can be inferred that a grand average cooling rate distance between all of the contiguous/closest classes of 0.123 is the minimum needed to reach a good prediction of 84.5% of accuracy (See Table 4.32), while a minimum distance of 0.1 between only two of the closest classes will lead to a regular prediction accuracy of 70.6% (See Tables 4.33 and 4.34). Therefore, grand average cooling rate discriminability is set "good" when $CR_{A-B}>0.12$ in all of the closest classes, "regular" when $CR_{A-B}>0.1$ in one of the closest classes, and "null" when $CR_{A-B}<0.1$ in all of the closest classes. According to this discriminability criterion, the heat flux on the cover was varied iteratively (a minimum of 18 finite element models were solved) until a good discriminability was reached or a maximum temperature of 140 °C in the cover was reached. Figure 4.31 shows the amount of energy to reach a minimum cooling rate difference of 0.1 (CR_{A-B}) or the maximum temperature allowable, the maximum and minimum cooling rate differences, and zones for "good", "regular" and "null" discriminability. It was not possible to reach the minimum cooling rate difference for a number of covers larger than 3 because a temperature in the cover higher than 140 °C is reached (see Figure 4.32).

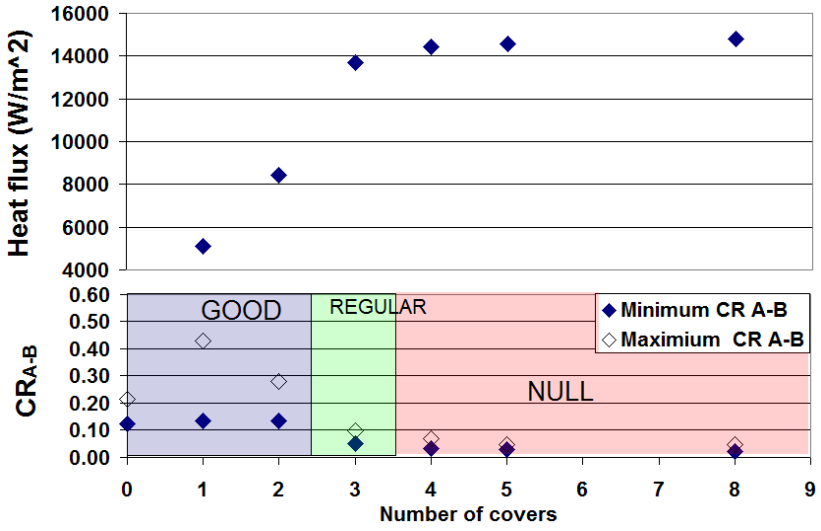

Figure 4.31. Heat flux required to obtain an adequate cooling rate difference between solder joint shapes.

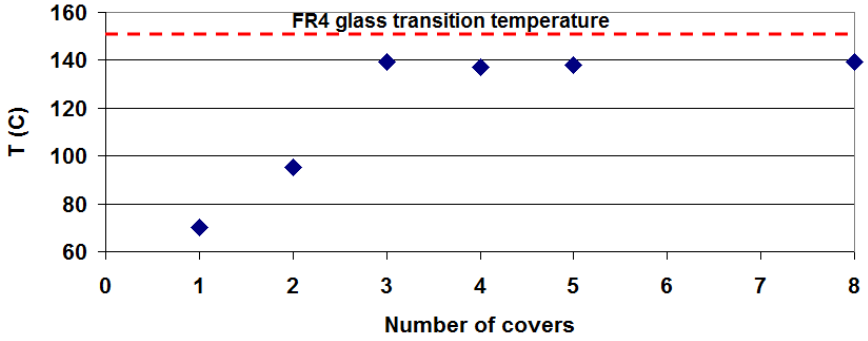

Figure 4.32. Maximum temperature achieved in the top cover surface.

4.3.1.3. Amount of Heating Time

So far, no heating time was varied for the finite element models; heating time is important to reduce inspection time and to determine the effect of higher energy sources. This section presents the amount of energy needed to achieve a good discriminability or a maximum temperature in the cover equal to 140 °C for 5, 15, and 30 s. In this case, the total amount of energy was used to compare among heating times, because the total

amount of energy applied to the top cover varies with the heating time and the heat flux. The total amount of energy applied to the cover is given by the next expression:

$$Q_{cover} = H_F \times H_T \times S_{cover} \tag{32}$$

where H_F, H_T, and S_{cover} are the heat flux applied to the top cover, the amount of heating time, and the top surface area of the cover, respectively. According to Figures 4.33 and 4.34, a heating time of *5 s* requires lower total amount of energy to reach an adequate cooling rate distance among closest classes.

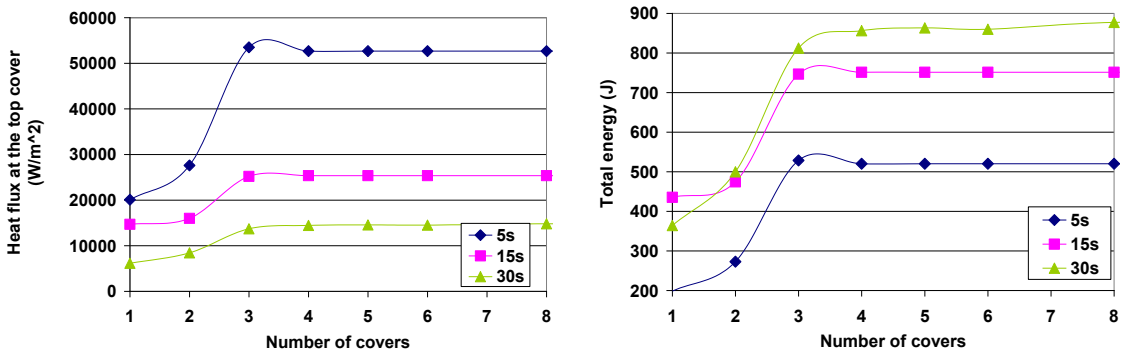

(a) (b)

Figure 4.33. Amount of (a) heat flux and (b) total energy required to achieve a good discriminability or a maximum temperature of 140 °C in the top cover in function of number of covers.

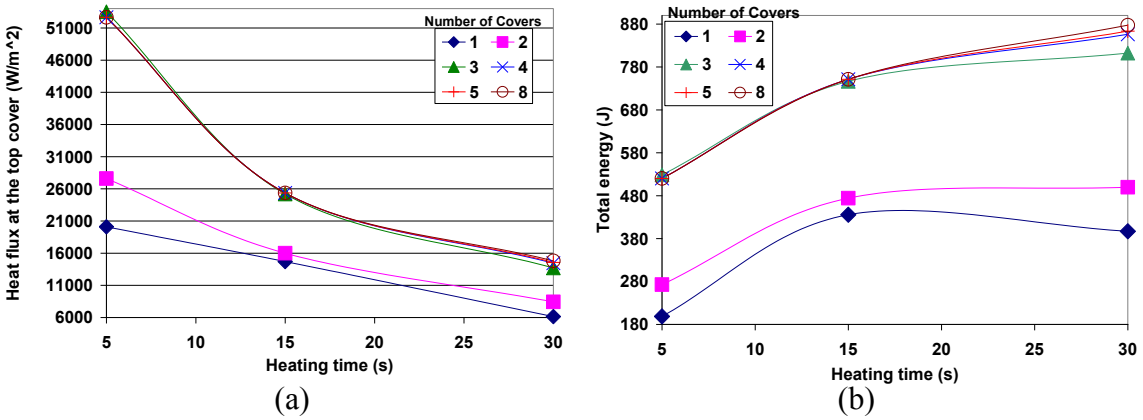

Figure 4.34. Amount of (a) heat flux and (b) total energy required to achieve a good discriminability or a maximum temperature of 140 °C in the top cover in function of heating time.

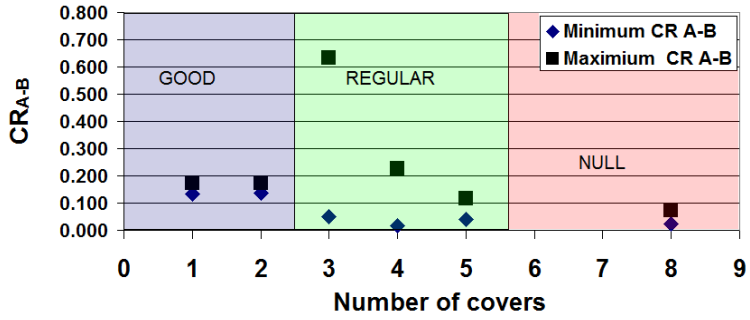

Figure 4.35. Grand average cooling rate distances between closest solder joint shapes for 5 s of heating time.

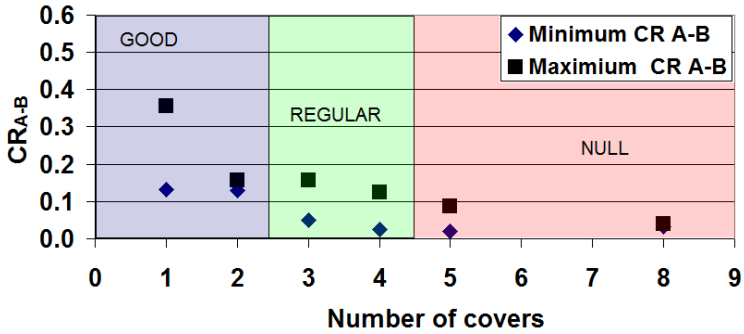

Figure 4.36. Grand average cooling rate distances between closest solder joint shapes for 15 s of heating time.

According to Figures 4.32, 4.35 and 4.36, it can be inferred that a heating time of 5 s provides a larger range of discriminability, but they are showing only the average of the differences between closest classes for the cooling rates from 20 to 100 s; if Tables 4.35, 4.38, and 4.39 are compared, the adequate difference among closest solder shapes only last a short period of time for 5s. Therefore, a faster infrared camera capable of acquiring pictures in a shorter period of time should be used. This means that as the inspection time decreases the cost of the equipment increases too, because more sophisticated cameras and high energy sources are needed.

Table 4.38. Numerical temperature and grand average cooling rate differences between contiguous solder joint shapes (one cover and 5 s heating time).

time(s)	T_{90-60}	T_{60-120}	CR_{90-60}	CR_{60-120}
0	1.625	0.493		
20	2.076	0.928	0.452	0.435
40	1.749	0.796	0.062	0.152
60	1.417	0.666	0.069	0.058
80	1.105	0.543	0.130	0.013
100	0.834	0.436	0.158	0.011
average	**1.468**	**0.644**	**0.174**	**0.134**

Table 4.39. Numerical temperature and grand average cooling rate differences between contiguous solder joint shapes (one cover and 15 s heating time).

time(s)	T_{90-60}	T_{60-120}	CR_{90-60}	CR_{60-120}
0	4.094	1.646		
20	4.181	1.880	0.087	0.234
40	3.496	1.601	0.299	0.022
60	2.815	1.330	0.426	0.105
80	2.189	1.082	0.476	0.141
100	1.663	0.870	0.486	0.155
average	**3.073**	**1.401**	**0.355**	**0.132**

4.3.2. Prediction Model Development

Two multiple linear regression models were developed to determine the appropriate amount of energy to achieve a "good" or "regular" solder joint classification in function of the number of covers and heating time. As seen in Figure 4.33, the curve for the amount of energy behaves like a quadratic polynomial for a number of covers equal or less than three and like a straight line for a number of covers larger than 3; therefore, non continuous regression models will achieve a much better accuracy approximating the curves behavior. On the other hand, the total amount of energy behaves like a quadratic function of heating time. According to this, the equations used for the multiple linear regression model are:

$$
\begin{aligned}
&C_N \le 3: \\
&Q_{cover} = H_T \times S_{cover} \times (p_1 C_N + p_2 C_N^2 + p_3 H_T + p_4 H_T^2 + p_5 C_N H_T \\
&\qquad + p_6 C_N^2 H_T + p_7 C_N H_T^2 + p_8) \\
&C_N > 3: \\
&Q_{cover} = H_T \times S_{cover} \left(r_1 C_N + r_2 H_T + r_3 H_T^2 + r_4 C_N H_T + r_5 C_N H_T^2 + r_6\right)
\end{aligned}
\tag{33}
$$

where Q_{cover}, C_N, H_T, and p_i and r_j are the total amount of energy provided to the cover, number of covers, heating time, and the polynomial constant coefficients ($i=1,2,...,8$ and $j=1,2,...,6$), respectively. The linear regression Excel function "LINEST" was used to determine the coefficients for Equations (33). This function determines the best coefficients fitting the finite element parametric model data using a least-squares method. The constant coefficients for the group of Equations (33) are given in Table 4.40; these constant coefficients provide coefficients of determination (R^2) values of 0.998 and 0.999 for $C_N \le 3$ and $C_N > 3$, respectively. As a verification, Table 4.41 shows a comparison between the total amount of energy determined by the prediction equation and that ones determined by the parametric analysis; it can be seen that maximum errors of 6% are obtained. Finally, it is important to remind that Equations (33) can be used to

determine the amount of energy needed to achieve a "good" discrimination for one and two covers, and a "regular discrimination" for 3 to 5 covers (refer to Figures 4.31, 4.35 and 4.36 for more detailed information). In addition, Equations (33) can be used to determine the maximum amount of energy to achieve a maximum temperature in the cover of 140 °C for a number of covers larger than 5.

Table 4.40. Constant coefficients determined for Equations (33) using multiple linear regression method.

p8	25554.446	**R6**	72256.677
p7	41.910	**R5**	0.231
p6	-296.669	**R4**	-4.611
p5	-797.230	**R3**	79.289
p4	-47.946	**R2**	-4316.781
p3	751.112	**R1**	17.292
p2	9820.858		
p1	-13706.652		

4.3.3. Prediction Model Validation

To corroborate the degree of agreement between the prediction model and the experimental active infrared thermography methodology proposed, experiments were conducted for one cover and two covers PCB assemblies and 30 s of heating time. In order to provide the same total amount of energy during the experiment as the one predicted by the linear regression model, heat flux sensors were attached to the cover of the one cover and two covers PCB assemblies. The heat flux sensor used was a typical bidirectional heat flux plate with and integrated thermocouple and a maximum measurement capability of 12600 W/m^2. After performing the experiments, it was possible to determine the experimental grand average cooling rate distances among solder joint shapes; these distances can be compared with the ones obtained in the parametric numerical analysis and should be similar.

Table 4.41. Error introduced by the fitting procedure in the determination of the total amount of energy.

C_N	H_T (s)	Fitting error (%)	Q_{cover} FEA (J)	Q_{cover} prediction model (J)
1	5	1.4	198.5	195.7
1	15	3.2	435.5	449.6
1	30	3.1	364.1	352.9
2	5	2.1	272.7	278.3
2	15	6.0	474.2	446.0
2	30	4.5	499.7	522.3
3	5	0.5	528.6	525.8
3	15	1.9	746.6	760.7
3	30	1.4	812.3	800.9
4	5	0.0	520.2	520.2
4	15	0.0	751.2	751.2
4	30	0.1	856.2	857.1
5	5	0.0	520.2	520.2
5	15	0.0	751.2	751.2
5	30	0.1	863.5	862.3
8	5	0.0	520.2	520.2
8	15	0.0	751.2	751.2
8	30	0.0	877.3	877.6

Unfortunately, the capacity of the halogen lamp available for this research (500 W halogen lamp) can not achieve the high amounts of energy required for PCB assemblies to achieve a good discriminability. The maximum amount of energy achieved in 30s with this kind of lamp was 203 J and the energies needed for one and two covers are 364.1 J and 522.3 J, respectively. In order to get an estimation of the experimental grand average cooling rate distances, experiments were performed with different amounts of energies in the range from 140 to 203 J. After the data was obtained, two different curves were fitted to the data, and the curves equations were used to extrapolate the distances to the energies required by the prediction model. Tables 4.42 and 4.43 show the obtained distances in function of the amount of energy for each experiment performed for one and two covers, respectively.

Table 4.42. Grand average cooling rates distances among solder joint shapes for one cover and in function of amount of energy provided.

Experiment	64.9 J		140.5 J		189.5 J	
	Maximum CR_{AB}	***Minimum CR_{AB}***	***Maximum CR_{AB}***	***Minimum CR_{AB}***	***Maximum CR_{AB}***	***Minimum CR_{AB}***
1	0.2468	0.0907	0.2877	0.0957	0.3103	0.1069
2	0.2451	0.1190	0.2885	0.0963	0.3300	0.1009
3	0.2256	0.0660	0.2777	0.0896	0.3095	0.1062
4	0.2126	0.0925	0.3050	0.0998	0.3004	0.1059
5	0.2320	0.0777	0.3307	0.0985	0.3299	0.1033
6	0.2598	0.1017	0.2875	0.0959	0.3064	0.1064
Average	0.2370	0.0913	0.2962	0.0960	0.3144	0.1049

Table 4.43. Grand average cooling rates distances among solder joint shapes for two covers in function of amount of energy provided.

Experiment	107.2 J		155.3 J		203.1 J	
	Maximum CR_{AB}	***Minimum CR_{AB}***	***Maximum CR_{AB}***	***Minimum CR_{AB}***	***Maximum CR_{AB}***	***Minimum CR_{AB}***
1	0.0857	0.2249	0.2328	0.0893	0.3581	0.0486
2	0.0948	0.2162	0.2029	0.0886	0.2927	0.0713
3	0.0862	0.2153	0.2429	0.1059	0.293	0.1006
4	0.0892	0.2209	0.2545	0.0932	0.2695	0.1275
5	0.0984	0.2114	0.2128	0.0845	0.2906	0.1231
6	0.0899	0.2124	0.2186	0.0940	0.3601	0.0957
Average	0.0907	0.2168	0.2274	0.0926	0.2667	0.0945

Exponential and linear curves were fitted to the average of the experimental grand average cooling rate distances. Table 4.44 and 4.45 show the fitting equations obtained with its respective coefficient of determination. Finally, Tables 4.46 to 4.49 show the error between the prediction model and the experimental results by means of the corresponding fitting equations. It can be seen that the errors between models are below 10%, with exception of the linear fitting case for two covers; however, this is the fitting model that has the lowest correlation ratio of all.

Table 4.44. Grand average cooling rate distances fitting equations for one cover.

	Distance	Fitting equation	R^2
Exponential	maximum CR_{A-B}	$0.206\ e^{0.00233\ Qcover}$	0.96
	minimum CR_{A-B}	$0.0843\ e^{0.00108\ Qcover}$	0.92
Linear	maximum CR_{A-B}	$0.000635\ Q_{cover} + 0.199$	0.97
	minimum CR_{A-B}	$0.000105\ Q_{cover} + 0.083$	0.91

Table 4.45. Grand average cooling rate distances fitting equations for two covers.

	Distance	Fitting equation	R^2
Exponential	maximum CR_{A-B}	$0.169\ e^{0.00216\ Qcover}$	0.91
	minimum CR_{A-B}	$0.086\ e^{0.00042\ Qcover}$	1.00
Linear	maximum CR_{A-B}	$0.00052\ Q_{cover} + 0.156$	0.90
	minimum CR_{A-B}	$0.00004\ Q_{cover} + 0.086$	1.00

Table 4.46. Percentage of error between the prediction and experimental models when using a linear equation to fit the experimental grand average cooling rate distances for one cover.

	Q (J)	Maximum CR_{A-B}	minimumCR_{A-B}
Prediction model	353	0.434	0.132
Experimental model	353	0.423	0.121
% error between models	----	2.594	9.346

Table 4.47. Percentage of error between the prediction and experimental models when using an exponential equation to fit the experimental grand average cooling rate distances for one cover.

	Q (J)	Maximum CR_{A-B}	minimumCR_{A-B}
Prediction model	353	0.434	0.132
Experimental model	353	0.469	0.123
% error between models	----	-7.520	6.931

Table 4.48. Percentage of error between the prediction and experimental models when using a linear equation to fit the experimental grand average cooling rate distances for two covers.

	Q (J)	Maximum CR_{A-B}	minimumCR_{A-B}
Prediction model	353	0.569	0.098
Experimental model	353	0.428	0.107
% error between models	----	33.003	-8.390

Table 4.49. Percentage of error between the prediction and experimental models when using an exponential equation to fit the experimental grand average cooling rate distances for two covers.

	Q (J)	Maximum CR_{A-B}	Minimum CR_{A-B}
Prediction model	353	0.569	0.098
Experimental model	353	0.522	0.108
% error between models	----	9.145	-9.384

4.3.4. Findings

The parametric analysis further verified that grand average cooling rate distances among hidden solder joint shapes decreases as the number of covers increases. The reduction of the grand average cooling rate distances is caused by an increment of energy lost in the transversal direction that reduces the energy reaching the solder joint shapes. Basically, the increment of covers provides a higher surface area for the dissipation of energy allowing a low effect of the solder joint shape at the cover temperature distribution and grand average cooling rate. Accordingly, it was corroborated that increasing the amount of heat flux at the top cover provides a higher difference in the grand average cooling rate distances among hidden solder joint shapes. In the case of heating time, the grand average cooling rate distances among solder joint shapes increases as the heating time decreases providing a better discrimination. This is caused by the very high heat flux provided that, unfortunately, will increase the cost of the energy source. As the heat flux is the main variable affecting the capacity to discriminate among solder joint shapes, its

value was varied until an appropriate discrimination between solder joint shapes was achieved for different number of covers and heating times. It was discovered that the heat flux needed to achieve a “good” or “regular” discriminability is a quadratic function for a number of covers less or equal than 3; after the third cover, it follows a linear function. A “good” discrimination means that it is possible to differentiate among the three solder joints, while a “regular” discrimination means that it is possible to discriminate only between two of the solder joints. After the third cover, it is only possible to achieve a “regular” or “null” discriminability because the heat flux applied to the top cover is limited by the glass transition temperature for the cover (150 °C). Therefore, it is not possible to keep increasing the heat flux to achieve a better discriminability after the fourth cover is added.

In order to validate the heat flux prediction model, active thermography experiments were performed with one and two covers PCB assemblies. The objective of these experiments was to establish the same heat flux as the one obtained from the prediction model; next, the obtained experimental distances among grand average cooling rates were compared to those obtained in the parametric analysis for the corresponding heat flux, heating time, and number of covers. Unfortunately and due to the low energy achievable by the halogen lamp, the needed heat flux was not achievable and a procedure to obtain an estimate of the grand average cooling rate distances was performed (see Section 4.3.3 for details). The prediction model showed an agreement higher than 90% with the experimental thermography model when comparing the maximum and minimum grand average cooling rate distances between models. Better agreements can be achieved if some issues are solved in the experimental model: a more uniform heat flux from the lamp should be achieved, the temperatures at the top cover should be monitored immediately after the heating process is ended, and no high speed movement of the fixture should be allowed (force convection affects in a different way zones close to the leading edge than zones close to the rear edge). A an example of the nonuniform heat flux, Figure 4.37 shows the heat flux measured at the different solder

joint shape positions. A percentage of difference of heat flux provided between the 90 position and the 60 and 120 positions can be determined as 11% and 4%, respectively. A better infrared technique avoiding uneven heating is lock-in thermography [69], although it is more complicated, expensive, and lengthy to apply.

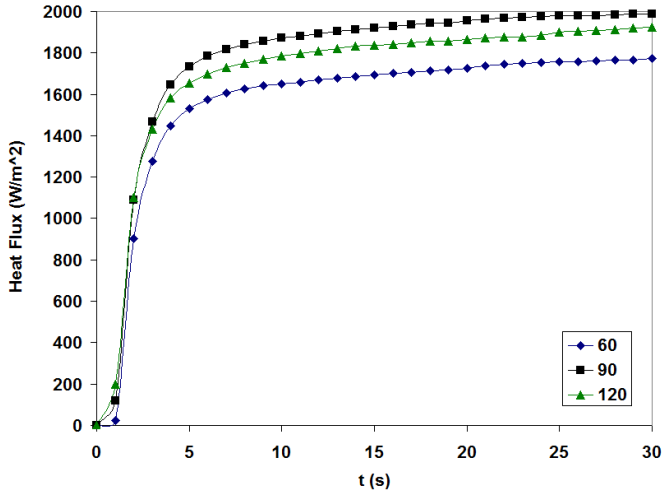

Figure 4.37. Heat flux at the three solder joint positions.

5. SUMMARY, CONCLUSIONS, AND FUTURE DIRECTIONS

5.1. Summary

Chip solder joints integrity is one of the most important factors for the proper reliability of electronics [4-8]. The main defects after assembly are usually related to improper solder joints [4]. In actuality, solder joints are especially important in the actuality because of the wide use of surface mount technology that relies completely in proper solder joints. Surface mounting technologies as Flip Chip Array and Ball Grid Array are one of the most used in actuality. These mounting methods in particular keep the solder joints hidden from view making its inspection very difficult. In addition, the wide use of board stacking keeps the solder joints hidden from view too. Multiple methods, like automatic optical inspection, automatic X-ray inspection, and laser ultrasound, are commonly used to detect electronic components solder joint quality after its assembly in manufacturing sites, but there are some limitations in these inspection methods. Active thermography base methodologies can be used to characterize solder joint shapes by means of its grand average cooling rate; it is relatively easy to implement, not harmful for technicians, portable, low cost, and automated. Such characteristics are suitable for a good nondestructive detection system.

The objectives of this research were to understand, model, and predict hidden solder joint shapes in order to achieve better electronics reliability. To understand how the solder joint shapes affect the component surface transient temperature after applying a heat flux, an experimental model was developed by means of an active infrared thermography nondestructive experimental setup. Transient thermal behavior was characterized by means of grand average cooling rate. The solder joint shapes were assumed as cones with three different angles (60^{o}, 90^{o}, and 120^{o}) to account for the solder joint integrity (60^{o} represents an adequate solder joint). These solder joints were visible and hidden by one and two covers. Ten different electronic board prototypes and

15 experiments were performed in the active thermography detection system. Five of the experiments were performed on the boards without a cover, while the rest of the experiments were performed on the boards with one and two covers. The experiments were performed inside an environmental chamber with two sections (heating and cooling sections). The experimental procedure consisted of heating the PCB assembly by a halogen lamp inside the heating section, moving the PCB assembly to a cooling section, and monitoring the thermal transient behavior during the cooling process by means of an infrared camera. A multi analysis of variance (MANOVA) was performed on the experimental data determining that the solder joint geometries were statistically different when described by the grand average cooling rates. Artificial neural networks classifying models based on the grand average cooling rate experimental data were developed; these models were used to test and establish the capability of grand average cooling rate to describe the different hidden solder joint shapes as the PCB assembly complexity increases.

A finite element model was used to simulate the heat transfer phenomena during the application of the active thermography technique. Sources of uncertainties during active thermography application (e.g. uneven heating, sample movement, and dead time between heating and cooling processes) were not modeled. First, the numerical model was validated with respect to the experimental model; second, a numerical parametric analysis was performed to further investigate the limitations and extend the applicability of active infrared thermography to characterize hidden solder joint shapes by means of grand average cooling rate. The parameters varied were the number of covers, amount of heat flux, and amount of heating time.

As a final step, a prediction model was developed to determine the optimum amount of heat flux required to achieve an adequate hidden solder joint shape characterization in function of the number of covers and heating time. In summary, this research provided the electronics industry with the knowledge to develop better infrared thermography

techniques to address hidden solder joint shapes quality inspection and improve electronics reliability.

5.2. Conclusions

According to the experimental model, temperatures and grand average cooling rates depend highly on the solder joint shapes for the PCB assembly with no cover. The lower surface area available for energy dissipation as the angle decreases promotes higher temperatures and grand average cooling rates. Temperatures and grand average cooling rates depend in a lower degree on the solder joint shapes for PCB assemblies with covers. The addition of the covers limits the amount of energy reaching the solder joint shapes weakening the temperature differences and grand average cooling rates among solder joint shape positions on the top cover. In addition, the covers promote a major role of the position versus the shape of the solder joints on the temperatures and grand average cooling rates at the top cover. Regions closer to the edge of the cover are affected in a higher degree by convection at the edge of the cover, while the region at the center is affected by the copper wires at its sides. This asymmetry conducted to higher temperatures and grand average cooling rates at the central position. Comparison of temperatures and grand average cooling rates are more reliable among the solder joint shapes at the sides, because these solder joints are under the same boundary conditions.

A multi analysis of variance (MANOVA) proved that solder joint shapes are statistically different when described by the experimental grand average cooling rates (C_1 to C_5). In addition, the statistical analysis determined that temperature and cooling rate differences among closest classes or solder joint shapes are inversely proportional to the number of covers.

After determining that solder joint shapes are statistically different when described by grand average cooling rates, a supervised classification model based on neural networks

and experimental grand average cooling rate was found to discriminate among solder joints with 84.3%, 70.6%, and 66.67% accuracies for visible, hidden by one cover, and hidden by two covers solder joints, respectively. It was determined that the addition of the covers diminished the discriminability by reducing the temperature and cooling rate differences between closest classes or solder joint shapes.

A finite element model was developed for the thermal processes during heating and cooling. The numerical model maximum uncertainty was 0.33% when using a fine mesh with 240325 elements and it was verified for spatial grid convergence. The numerical model was verified to model the heat transfer phenomena adequately by examining qualitatively the temperature distribution at 30 s of heating. A lumped capacitance analytical model of the cover and a 1-D finite differences composite wall model of the PCB assembly were used to verify the numerical model temperature calculations; a maximum difference of 3.21% between the numerical temperature and these two models was determined. The finite element model was validated to determine the average surface temperature at the 90 solder position with maximum errors of 3.21% (one cover) and 4.73% (two covers), and the grand average cooling rates at the same position with maximum errors of 8.85% (one cover) and 13.36% (two covers). The main cause for the differences between the numerical and the experimental model was that the thermal convection was neglected in the gaps between covers and in the gaps between the first cover and the PCB. Another possible factor contributing to this discrepancy is a thermal diffusivity difference between the value used for the numerical model and the real value for the cover material that should be determined by an experimental method.

After corroborating the degree of agreement between the experimental and numerical models, a finite element based parametric analysis was performed by varying the number of covers, heat flux at the top cover, and the heating time. The parametric analysis was able to determine that temperature and cooling rate differences among closest or contiguous solder joint shapes (classes) are directly proportional to heat flux, and

inversely proportional to the number of covers. The heating time was directly proportional to the time the temperatures should be monitored during the cooling process. As heating time reduces, higher heating sources and faster acquisition of images are needed, increasing the cost of the infrared thermography. In addition, the parametric analysis determined the capability of the infrared thermography to discriminate among hidden solder joint shapes as a "good" discriminability for a number of covers less than three, a "regular" discrimination for three to five covers, and a "null" discrimination for a number of covers larger than five. A "good" discrimination means that it is possible to differentiate among the three solder joints, while a "regular" discrimination means that it is possible to discriminate only between two of the solder joints. The heat flux needed to achieve a "good" or "regular" discriminability is a quadratic function of the number of covers when that number is less or equal than three; after the third cover, it follows a linear function.

The prediction model showed an agreement higher than 90% with the experimental thermography model when comparing the maximum and minimum grand average cooling rate distances. Better agreements can be achieved if some issues are solved in the experimental model: a more uniform heat flux from the lamp should be achieved, the temperatures at the top cover should be monitored immediately after the heating process is ended, and no high speed movement of the fixture should be allowed (force convection affects in a higher degree close to the leading edge than close to the rear edge of the assembly).

After the research methodology was applied, it can be concluded that the infrared thermography methodology proposed can discriminate among three solder joint shapes with 60°, 90°, and 120° cone angles hidden by a maximum of five covers PCB assembly. However, the discrimination between solder joint geometries is more reliable for solder joints located on the sides (60° and 120°) that exhibit symmetry with respect to the boundary conditions. Finally, grand average cooling rate and temperature distances

among solder joints are directly proportional to capability to discriminate among solder joints.

5.3. Future Directions

The three different solder joints were attached in only one board; therefore, it is important to develop models for each solder joint in individual covers so interactions among solder joints, as well as solder joint location effects, are avoided. So far, it is difficult to analyze the amount of interaction among solder joints as the three solder joints PCB assembly is too complex to analyze. However, separating the different solders in individual covers will triple the amount of effort to develop the experimental and numerical models.

The energy source should be further investigated. Energy sources providing a more uniform energy are expected to improve the discrimination capability and reliability of the active thermography methodology.

The finite element analysis was performed by considering the convective coefficient according to empirical convective correlations. A more complete finite element model could include a computational fluid dynamics analysis.

The finite element model was done considering only three different solder joints with a cone shape. The interval between cone angles was 30^{o}. The interval between cone angles can be decrease to further investigate the capabilities of the infrared thermography methodology. In addition, the angle increment can be added to the prediction model as an additional independent variable; therefore, the amount of energy, to reach an adequate discrimination, will be predicted in function of number of covers, heating time, and solder joint angle increment difference.

Finally, higher energy sources can be used to further validate the optimum heat flux prediction model and perform more complex active thermography techniques.

The prediction model objective was to determine the optimum active thermography conditions to discriminate adequately among three different solder joints with a conical shape. In reality, the PCB assemblies are attached to the component by several solder joints (as much as 600 in some BGA components). However, the methodology followed to develop the prediction model can be applied to any number of solder joint shapes. Therefore, the methodology should be tested with actual components. For instance, this methodology can be applied to generate a prediction model to discriminate among good solder balls, missing solder balls, open solder balls, and cracked solder balls on BGA components. However, PCB samples with these kinds of defects should be obtained to generate experimental models. Next, numerical models should be validated with respect to the experimental models. Once the numerical models are validated, a parametric analysis varying the amount and location of defectuous solder balls can be performed to generate a large scale and more realistic prediction model for the electronics industry.

REFERENCES

[1] H. Elliott, *Intel's recall will cost a mere $253 million*, Electronic News 46 (2000), p. 1.

[2] J. Mathew, *Intel to replace one million bad boards*, Electronic News 46 (2000), p. 1.

[3] S. Tiku, M. Azarian, and M. Pecht, *Using a reliability capability maturity model to benchmark electronics companies*, International Journal of Quality & Reliability Management 24 (2007), pp. 547-563.

[4] S. Beck, and R. Lieske, *Reducing defects and costs with adhesive printing*, Circuits assembly 11 (2000), p. 40.

[5] E.H. Amalu, N.N. Ekere, and S. Mallik, *Evaluation of rheological properties of lead-free solder pastes and their relationship with transfer efficiency during stencil printing process*, Materials & Design 32 (2011), pp. 3189-3197.

[6] I. Fidan, *CAPP for electronics manufacturing case study: Fine pitch SMT laser soldering*, Journal of Electronic Packaging 126 (2004), pp. 173-176.

[7] N.S.S. Mar, P.K.D.V. Yarlagadda, and C. Fookes, *Design and development of automatic visual inspection system for PCB manufacturing*, Robotics and Computer-Integrated Manufacturing 27 (2011), pp. 949-962. Available at: http://www.sciencedirect.com/science/article/B6V4P-52JW548-1/2/81361f2fa6c7d76af2e95316801e4170.

[8] B. Enterkin, *Minimizing SMT soldering defects, costs and losses through ultrasonic stencil cleaning*, Global SMT and Packaging IEEE 2 (2002), pp. 10-13.

[9] *Pennsylvania Inventors Develop Printed Circuit Board Stacking Connector*, US Fed News Service, Including US State News (2007). Available at: http://www.highbeam.com/doc/1P3-1297143191.html.

[10] A. Kanadjian, *High-density modules proliferate: Low-cost memory gives users an instant performance boost*, Electronic News 44 (1998), p. 40.

[11] D. Maliniak, *Memory-chip stacks send density skyward*, Electronic Design 42 (1994), pp. 69-70.

[12] E.J. Stefanides, *ZIF connectors simplify circuit board stacking*, Design News 46 (1990), pp. 102-103.

[13] W. Wong, *EPIC express rides the rails*, Electronic Design 54 (2006), p. 32.

[14] M. Dirjish, *Connector makers woo pitch, push power, get down to basics*, Electronic design 56 (2008), pp. 42-44.

[15] Hirose-Electric, *Applications of Hirose connectors*, (2011). Available at: http://www.hirose-connectors.com/connectors/index_ap.aspx.

[16] 3M, *3M™ board-to-board connectors*, (2012). Available at: http://solutions.3m.com/wps/portal/3M/en_US/Interconnect/Home/Products/ProductCatalog/Catalog/?PC_7_RJH9U5230O73D0ISNF9B3C3SI1_nid=BQXK50DDF8beWK7G49LP38gl.

[17] SAMTEC, *Samtec high speed board-to-board mezzanine strips*, (2011). Available at: http://www.samtec.com/highspeed/mezzanine_strips.aspx.

[18] Hirose-Electric, *PCB board-to-board connectors*, (2011). Available at: http://www.hirose-connectors.com/connectors/H216boardtoboardconnectors.aspx?p1=1&cat=07.

[19] J. Gao, *Machine vision based measurement of BGA connector solder balls, in Eighth ACIS International Conference on Software Engineering, Artificial Intelligence, Networking, and Parallel/Distributed Computing (SNPD 2007)*, Qingdao, China, 2007.

[20] Q. Cao, Z. Fu, N. Xia, and F.L. Lewis, *A binocular machine vision system for ball grid array package inspection*, Assembly Automation 25 (2005), pp. 217-222.

[21] G. Wagner, *Machine vision solves test challenges*, Lasers & Optronics 19 (2000), p. 25.

[22] F. Zhen, J.C. Gonzalez, T. Sea, M. Kurwa, and E. Krastev, *Can nondestructive techniques identify BGA defects?*, SMT: Surface Mount Technology 22 (2008), pp. 25-27.

[23] P. Brundy, *Whither analytical X-Ray*, Circuits Assembly 17 (2006), pp. 28-29.

[24] J. Feng, J. Basani, M. Kurwa, D. Bernard, and E. Krastev, *Modern 2D X-ray tackles BGA defects (cover story)*, SMT: Surface Mount Technology 22 (2008), pp. 22-24.

[25] A. Hirakimoto, S. Ohnishi, H. Maeda, T. Kishi, T. Shiota, T. Tamura, M. Ukita, S. Fujita, and M. Kamegawa, *Progress of microfocus X-ray systems for fluoroscopic and computed tomography*, Spectrochimica Acta Part B: Atomic Spectroscopy 59 (2004), pp. 1101-1106.

[26] T. Kangasvieri, O. Nousiainen, J. Putaala, R. Rautioaho, and J. Vähäkangas, *Reliability and RF performance of BGA solder joints with plastic-core solder balls in LTCC/PWB assemblies*, Microelectronics and Reliability 46 (2006), pp. 1335-1347.

[27] Kaufmann, *Nondestructive testing using microfocus x-rays*, Lasers & Optronics 18 (1999), p. 25.

[28] L.J. Ladani, A. Dasgupta, I. Cardoso, and E. Monlevade, *Effect of selected process parameters on durability and defects in surface mount assemblies for portable electronics*, IEEE Transactions on Electronics Packaging Manufacturing 31 (2008), pp. 51-60.

[29] J.C.C. Lo, B.F. Jia, Z. Liu, J. Zhu, and S.W.R. Lee, *Reliability study of surface mount printed circuit board assemblies with lead*, Soldering & Surface Mount Technology 20 (2008), pp. 30-38.

[30] SONOSCAN, *Sonoscan expands component screening program*, Advanced Packaging 12 (2003), p. 16.

[31] T. Adams, *Online inspection for hidden internal defects*, Sensors 17 (2000), pp. 58-61.

[32] L.W. Kessler, *Acoustic micro-imaging*, Advanced Materials & Processes 163 (2005), pp. 45-47.

[33] S.R. Martell, J.E. Semmens, and L.W. Kessler, *Nondestructive acoustic microimaging (AMI) analysis of MEMS materials, manufacturing, and*

packaging, in Reliability, Testing, and Characterization of MEMS/MOEMS, San Francisco, CA, USA, 2001.

[34] C. Miyasaka, and B.R. Tittmann, *Recent advances in acoustic microscopy for nondestructive evaluation*, Journal of Pressure Vessel Technology 122 (2000), pp. 374-378.

[35] O. Nousiainen, T. Kangasvieri, R. Rautioaho, and J. Vahakangas, *Characterization of Sn7In4.1Ag0.5Cu solder in lead*, Soldering & Surface Mount Technology 20 (2008), pp. 11-17.

[36] J. Putaala, T. Kangasvieri, O. Nousiainen, H. Jantunen, and M. Moilanen, *Detection of thermal cycling-induced failures in RF/microwave BGA assemblies*, IEEE Transactions on Electronics Packaging Manufacturing 31 (2008), pp. 240-247.

[37] S. Brand, P. Czurratis, P. Hoffrogge, and M. Petzold, *Automated inspection and classification of flip-chip-contacts using scanning acoustic microscopy*, Microelectronics and Reliability 50 (2010), pp. 1469-1473.

[38] J. Yang, *Non-destructive identification of defects in integrated circuit packages by scanning acoustic microscopy*, Microelectronics and Reliability 36 (1996), pp. 1291-1295.

[39] Y.L. Zhang, N. Guo, H. Du, and W.H. Li, *Automated defect recognition of C-SAM images in IC packaging using support vector machines*, International Journal of Advanced Manufacturing Technology 25 (2005), pp. 1191-1196.

[40] J. Baliga, *Laser pulses inspect solder joints*, Semiconductor International 23 (2000), p. 68.

[41] D.S. Erdahl, and I.C. Ume, *Determination of measurement limit for open solder bumps on a flip-chip package using a laser ultrasonic inspection system*, IEEE Transactions on Advanced Packaging 29 (2006), pp. 178-185.

[42] T. Howard, D. Erdahl, I.C. Ume, J. Gamalski, and A. Achari, *Development of an advanced system for inspection of flip chip and chip scale package interconnects*

using laser ultrasound and interferometric techniques, Proceedings of SPIE - The International Society for Optical Engineering 4828 (2002), pp. 136-142.

[43] L. Sheng, D. Erdahl, I.C. Ume, A. Achari, and J. Gamalski, *A novel approach for flip chip solder joint quality inspection: laser ultrasound and interferometric system*, IEEE Transactions on Components and Packaging Technologies 24 (2001), pp. 616-624.

[44] J.F. Head, *Cancer risk assessment with a second-generation infrared imaging system, in Infrared Technology and Applications XXIII*, Orlando, FL, USA, 1997.

[45] J.F. Head, *Computerized image analysis of digitized infrared images of breasts from a scanning infrared imaging system, in Infrared Technology and Applications XXIV*, San Diego, CA, USA, 1998.

[46] G.A. Santa Cruz, J. Bertotti, J. Marín, S.J. González, S. Gossio, D. Alvarez, B.M.C. Roth, P. Menéndez, M.D. Pereira, M. Albero, L. Cubau, P. Orellano, and S.J. Liberman, *Dynamic infrared imaging of cutaneous melanoma and normal skin in patients treated with BNCT*, Applied Radiation and Isotopes 67 (2009), pp. S54-S58.

[47] B. Ribeiro da Luz, and J.K. Crowley, *Identification of plant species by using high spatial and spectral resolution thermal infrared (8.0-13.5 micrometers) imagery*, Remote Sensing of Environment 114 (2010), pp. 404-413.

[48] H. Li, Z. Fan, and J. You, *Infrared imaging solar spectrograph at Purple mountain observatory*, Solar Physics 185 (1999), pp. 69-76.

[49] M. Carroll, *What we've learned about a strange new world*, Astronomy 38 (2010), p. 30.

[50] H. Wiggenhauser, *Active IR-applications in civil engineering*, Infrared Physics & Technology 43 (2002), pp. 233-238.

[51] E. Brocard, M. Schneebeli, and C. Matzler, *Deriving winds at cloud-base height with an infrared camera*, IEEE Transactions on Geoscience and Remote Sensing 47 (2009), pp. 3319-3325.

[52] E. Erdem, F. Arikan, and C.B. Erol, *DAMA Infrared sea modeling and analysis software*, IEEE Transactions on Geoscience and Remote Sensing 47 (2009), pp. 3581-3592.

[53] J.S. DiMarco, *Closed-loop guidance of imaging infrared missile seekers, in Infrared Imaging Systems: Design, Analysis, Modeling, and Testing X*, Orlando, FL, USA, 1999.

[54] T.J. Kulp, *Remote imaging of controlled gas releases using active and passive infrared imaging systems, in Infrared Technology and Applications XXIII*, Orlando, FL, USA, 1997.

[55] D.A. Roberts, E.S. Bradley, R. Cheung, I. Leifer, P.E. Dennison, and J.S. Margolis, *Mapping methane emissions from a marine geological seep source using imaging spectrometry*, Remote Sensing of Environment 114 (2010), pp. 592-606.

[56] O. Breitenstein, M. Langenkamp, F. Altmann, D. Katzer, A. Lindner, and H. Eggers, *Microscopic lock-in thermography investigation of leakage sites in integrated circuits*, Review of Scientific Instruments 71 (2000), pp. 4155-4160.

[57] G. Busse, C. Spiessberger, and A. Gleiter, *Application of data fusion to thermal wave imaging with lockin thermography, in 15th International Conference on Photoacoustic and Photothermal Phenomena*, Leuven, Belgium, 2010.

[58] P. Chaudhuri, P. Santra, S. Yoele, A. Prakash, D.C. Reddy, L.T. Lachhvani, J. Govindarajan, and Y.C. Saxena, *Non-destructive evaluation of brazed joints between cooling tube and heat sink by IR thermography and its verification using FE analysis*, Nondestructive Testing And Evaluation 39 (2006), pp. 88-95.

[59] D. Chen, C. Zhang, N. Wu, Z. Zeng, C. Xing, Y. Li, S. Zhao, and T. Ning, *Nondestructive testing of rocket engine injector panel using ultrasonic burst phase thermography, in 5th International Symposium on Advanced Optical Manufacturing and Testing Technologies*, Dalian, China, 2010.

[60] A.E. Dolinko, *Non-destructive visualization of defect borders in flawed plates inspected by thermal load*, Journal of Physics D: Applied Physics 41 (2008), p. 205503.

[61] R.A. Epperly, G.E. Heberlein, and L.G. Eads, *Thermography, a tool for reliability and safety*, IEEE Industry Applications Magazine 5 (1999), pp. 28-36.

[62] D.K. Fike, *Using infrared thermography as a manufacturing tool to analyze and repair defects in printed circuit boards, in Thermosense XIII*, Orlando, FL, USA, 1991.

[63] G. Giorleo, C. Meola, and A. Squillace, *Analysis of defective carbon-epoxy by means of lock-in thermography*, Research in Nondestructive Evaluation 12 (2000), pp. 241-250.

[64] A. Gleiter, C. Spiebberger, and G. Busse, *Lockin thermography with optical or ultrasound excitation*, Strojniski Vestnik/Journal of Mechanical Engineering 56 (2010), pp. 619-624.

[65] G.D. Harvel, and J.S. Chang, *Nondestructive evaluation of multiply connected electrical arc furnace graphite rod electrodes*, Research in Nondestructive Evaluation 20 (2009), pp. 215-229.

[66] T. Hierl, W. Gross, H. Scheuerpflug, A. Lutz, U. Schirl, and M.J. Schulz, *Infrared imaging of buried heat sources and material nonuniformities, in Infrared Technology and Applications XXIII*, Orlando, FL, USA, 1997.

[67] Y.Y. Hung, Y.S. Chen, S.P. Ng, L. Liu, Y.H. Huang, B.L. Luk, R.W.L. Ip, C.M.L. Wu, and P.S. Chung, *Review and comparison of shearography and active thermography for nondestructive evaluation*, Materials Science and Engineering R: Reports 64 (2009), pp. 73-112.

[68] C. Ibarra-Castanedo, and X.P.V. Maldague, *Interactive methodology for optimized defect characterization by quantitative pulsed phase thermography*, Research in Nondestructive Evaluation 16 (2005), p. 175.

[69] C. Ibarra-Castanedo, J.-M. Piau, S. Guilbert, N.P. Avdelidis, M. Genest, A. Bendada, and X.P.V. Maldague, *Comparative study of active thermography*

techniques for the nondestructive evaluation of honeycomb structures, Research in Nondestructive Evaluation 20 (2009), pp. 1-31.

[70] A. Kamoi, Y. Okamoto, and V. Vavilov, *Studying the inspection limits in detecting buried objects by using infrared thermography, in Thermosense XXV*, Orlando, FL, USA, 2003.

[71] W. Karpen, D. Wu, and G. Busse, *A theoretical model for the measurement of fiber orientation with thermal waves*, Research in Nondestructive Evaluation 11 (1999), pp. 179-197.

[72] A. Kozowska, F. Weik, J.W. Tomm, A. Mal, M. Latoszek, P. Wawrzyniak, M. Teodorczyk, L. Dobrzanski, M. Zbroszczyk, and M. Bugajski, *Thermal properties of high-power diode lasers investigated by micro-thermography, in High-Power Diode Laser Technology and Applications III*, San Jose, CA, USA, 2005.

[73] K. Kurita, M. Oyado, H. Tanaka, and S. Tottori, *Active infrared thermographic inspection technique for elevated concrete structures using remote heating system*, Infrared Physics and Technology 52 (2009), pp. 208-213.

[74] Y. Lu, Y. Cao, J.G. McDaniel, and M.L. Wang, *Finite element analysis of surface wave radiation for pavement debonding, in Nondestructive Characterization for Composite Materials, Aerospace Engineering, Civil Infrastructure, and Homeland Security*, San Diego, CA, USA, 2010.

[75] S. Marinetti, and V. Vavilov, *IR thermographic detection and characterization of hidden corrosion in metals: General analysis*, Corrosion Science 52 (2010), pp. 865-872.

[76] C. Meola, G.M. Carlomagno, U. Prisco, and A. Vitiello, *Nondestructive control of polyethylene blanket insulation by means of lock-in thermography*, Research in Nondestructive Evaluation 15 (2004), pp. 55-63.

[77] R. Montanini, *Quantitative determination of subsurface defects in a reference specimen made of Plexiglas by means of lock-in and pulse phase infrared thermography*, Infrared Physics and Technology 53 (2010), pp. 363-371.

[78] M. Morbidini, and P. Cawley, *A calibration procedure for sonic infrared nondestructive evaluation*, Journal of Applied Physics 106 (2009), pp. 023504-023513.

[79] A. Richards, and X. Han, *Ultrasound with IR imaging detects hidden defects*, Laser Focus World 36 (2000), p. S13.

[80] A. Wyckhuyse, and X. Maldague, *A study of wood inspection by infrared thermography, part II: Thermography for wood defects detection*, Research in Nondestructive Evaluation 13 (2001), pp. 13-21.

[81] A. Wyckhuyse, and X. Maldague, *A study of wood inspection by infrared thermography, part I: wood pole inspection by infrared thermography*, Research in Nondestructive Evaluation 13 (2001), pp. 1-12.

[82] L. Zhang, H. Shen, Z. Yang, and J. Jin, *Shunt removal and patching for crystalline silicon solar cells using infrared imaging and laser cutting*, Progress in Photovoltaics: Research and Applications 18 (2010), pp. 54-60.

[83] R. Mulaveesala, and S. Tuli, *Theory of frequency modulated thermal wave imaging for nondestructive subsurface defect detection*, Applied Physics Letters 89 (2006), p. 191913.

[84] T.C. Chai, B.S. Wong, W.M. Bai, A. Trigg, and Y.K. Lam, *A novel defect detection technique using active transient thermography for high density package and interconnections, in Electronic Components and Technology*, New Orleans, LA, USA, 2003.

[85] S.-J. Hsieh, R. Crane, and S. Sathish, *Understanding and predicting electronic vibration stress using ultrasound excitation, thermal profiling, and neural network modeling*, Nondestructive Testing And Evaluation 20 (2005), pp. 89-102.

[86] D.L. King, J.A. Kratochvil, M.A. Quintana, and T.J. McMahon, *Applications for infrared imaging equipment in photovoltaic cell, module, and system testing, in IEEE Photovoltaic Specialists Conference*, Anchorage, AK , USA, 2000.

[87] J. Varis, R. Lehtiniemi, and R. Vuohelainen, *Thermal inspection of solder quality of electronic components, in Thermosense XXI*, Orlando, FL, USA, 1999.

[88] B. Wiecek, E. De Baetselier, and G. De Mey, *Active thermography application for solder thickness measurement in surface mounted device technology*, Microelectronics Journal 29 (1998), pp. 223-228.

[89] T.L. Williams, *Thermal Imaging Cameras Characteristics and Performance*, CRC Press, Boca Raton, FL, 2009.

[90] Wikipedia, *Printed circuit board*, (2012). Available at: http://en.wikipedia.org/wiki/Printed_circuit_board.

[91] Wikipedia, *Surface-mount technology* (2012). Available at: http://en.wikipedia.org/wiki/Surface-mount_technology.

[92] Wikipedia, *Through-hole technology*, (2011). Available at: http://en.wikipedia.org/wiki/Through-hole_technology.

[93] A.H. Landzberg, *Microelectronics Manufacturing Diagnostics Handbook*, Van Nostrand Reinhold, New York, NJ, 1993.

[94] D. Upton, *AOI-AXI duo improves product yield*, EE: Evaluation Engineering 48 (2009), pp. 60-63.

[95] K.C. Koh, H.J. Choi, J.S. Kim, and H.S. Cho, *A statistical learning-based object recognition algorithm for solder joint inspection, in Optomechatronic Systems II*, Boston, MA, USA, 2001.

[96] T.S. Yun, K.J. Sim, and H.J. Kim, *Support vector machine-based inspection of solder joints using circular illumination*, Electronics Letters 36 (2000), pp. 949-951.

[97] D. Hong, H. Lee, M.Y. Kim, H. Cho, and J. Moon, *Sensor fusion of phase measuring profilometry and stereo vision for three-dimensional inspection of electronic components assembled on printed circuit boards*, Applied Optics 48 (2009), pp. 4158-4169.

[98] F.H. Kong, *A new method of inspection based on shape from shading, in 1st International Congress on Image and Signal Processing*, Sanya, China, 2008.

[99] G.T. Ayoub, *Flux inspection with UV fluorescence AOI*, Advanced Packaging 13 (2004), pp. 39-40.

[100] C. Faber, *Automatic optical inspection of IC connections*, Advanced Packaging 16 (2007), pp. 34-37.

[101] S. Liu, and I.C. Ume, *Vibration analysis based modeling and defect recognition for flip-chip solder-joint inspection*, Journal of Electronic Packaging 124 (2002), pp. 221-226.

[102] J.N. Reddy, *An Introduction to the Finite Element Method*, 3rd ed., *McGraw-Hill series in mechanical engineering*, McGraw-Hill Higher Education, New York, NY, 2006.

[103] A. Amri, *Thermal analysis of a three-dimensional breast model with embedded tumour using the transmission line matrix (TLM) method*, Computers in Biology and Medicine 41 (2011), pp. 76-86.

[104] K. Weide, *Impact of FEM simulation on reliability improvement of packaging*, Microelectronics and Reliability 39 (1999), pp. 1079-1088.

[105] Y.Y. Zhu, and S. Cescotto, *Transient thermal and thermomechanical analysis by mixed FEM*, Computers & Structures 53 (1994), pp. 275-304.

[106] I. Anteby, I. Shai, and A. Arbel, *Numerical calculations for combined conduction and radiation transient heat transfer in a semitransparent medium*, Numerical Heat Transfer Part A: Applications 37 (2000), pp. 359-371.

[107] I.A. Badruddin, Z.A. Zainal, P.A. Narayana, and K.N. Aswatha Seetharamu, *Numerical analysis of convection conduction and radiation using a non-equilibrium model in a square porous cavity*, International Journal of Thermal Sciences 46 (2007), pp. 20-29.

[108] K.A.R. Ismail, and C.S. Salinas, *Application of multidimensional scheme and the discrete ordinate method to radiative heat transfer in a two-dimensional enclosure with diffusely emitting and reflecting boundary walls*, Journal of Quantitative Spectroscopy & Radiative Transfer 88 (2004), pp. 407-422.

[109] H. Qi, Q. Zhang, E.C. Tinsley, M. Osterman, and M.G. Pecht, *High cycle cyclic torsion fatigue of PBGA Pb-free solder Joints*, IEEE Transactions on Components and Packaging Technologies 31 (2008), pp. 309-314.

[110] C.T. Peng, C.M. Liu, J.C. Lin, H.C. Cheng, and K.N. Chiang, *Reliability analysis and design for the fine-pitch flip chip BGA packaging*, IEEE Transactions on Components and Packaging Technologies 27 (2004), pp. 684-693.

[111] S.C. Chaparala, B.D. Roggeman, J.M. Pitarresi, B.G. Sammakia, J. Jackson, G. Griffin, and T. McHugh, *Effect of geometry and temperature cycle on the reliability of WLCSP solder joints*, IEEE Transactions on Components & Packaging Technologies 28 (2005), pp. 441-448.

[112] Y. Zhou, M. Al-Bassyiouni, and A. Dasgupta, *Vibration durability assessment of Sn3.0Ag0.5Cu and Sn37Pb solders under harmonic excitation*, Journal of Electronic Packaging 131 (2009), pp. 011016-011025.

[113] C. Kuo-Ning, and L. Chang-Ming, *A comparison of thermal stress/strain behavior of elliptical/round solder pads*, Journal of Electronic Packaging, Transactions of the ASME 123 (2001), pp. 127-131.

[114] T.S. Lee, T.P. Choi, and C.D. Yoo, *Finite element modeling of three-dimensional solder joint geometry in SMT*, Journal of Electronic Packaging, Transactions of the ASME 119 (1997), pp. 119-125.

[115] V. Eveloy, P. Rodgers, and M.S.J. Hashmi, *Application of numerical analysis to the optimisation of electronic component reliability screening and assembly processes*, Journal of Materials Processing Technology 155-156 (2004), pp. 1788-1796.

[116] X. P. Maldague and A. E. Rozlosnik (eds.), *Hybrid procedure to characterize hidden defects in composite materials,* Vol. 4710, SPIE - The International Society for Optical Engineering, Orlando, FL, USA, 2002, pp. 599-609.

[117] A. Jain, and Duin, *Statistical pattern recognition: A review*, IEEE Transactions on Pattern Analysis and Machine Intelligence 22 (2000), p. 4.

[118] T.-h. Kim, S.K. Bandyopadhyay, W. Adi, T.-h. Kim, and Y. Xiao, *Pattern recognition using artificial neural network: A review, in 4th International Conference on Information Security and Assurance*, Miyazaki, Japan, 2010.

[119] E. Cantú-Paz, *A survey of parallel genetic algorithms*, Calculateurs Paralleles, Reseaux et Systems Repartis 10 (1998), pp. 141–171.

[120] P.G. Espejo, S. Ventura, and F. Herrera, *A survey on the application of genetic programming to classification*, IEEE Transactions on Systems, Man, and Cybernetics, Part C: Applications and Reviews 40 (2010), pp. 121-144.

[121] D. Graupe, *Principles of Artificial Neural Networks*, 2nd ed., Vol. 6, *Advanced series on circuits and systems*, World Scientific, Hackensack, NJ, 2007.

[122] A. Cazorla, F.J. Olmo, and L. Alados-Arboledas, *Development of a sky imager for cloud cover assessment*, Journal of the Optical Society of America A: Optics, Image Science, and Vision 25 (2008), pp. 29-39.

[123] S. Chao Ton, and S. Long, *A neural network based information granulation approach to shorten the cellular phone test process*, Computers in Industry 57 (2006), pp. 412-423.

[124] C. Cheng, G. Sun, and C. Zhang, *Early detection of gastric cancer using wavelet feature extraction and neural network classification of FT-IR*, Spectroscopy 22 (2007), pp. 38-42.

[125] I. Gereige, S. Robert, S. Thiria, F. Badran, G. Granet, and J.J. Rousseau, *Recognition of diffraction-grating profile using a neural network classifier in optical scatterometry*, Journal of the Optical Society of America A: Optics, image science, and vision 25 (2008), pp. 1661-1667.

[126] C. Gope, N. Kehtarnavaz, and D. Nair, *Neural network classification of EEG signals using time-frequency representation, in International Joint Conference on Neural Networks*, Piscataway, NJ, USA, 2005.

[127] S.-J. Hsieh, *Artificial neural networks and statistical modeling for electronic stress prediction using thermal profiling*, Electronics Packaging Manufacturing, IEEE Transactions on 27 (2004), pp. 49-58.

[128] D. Mittal, V. Kumar, S.C. Saxena, N. Khandelwal, and N. Kalra, *Neural network based focal liver lesion diagnosis using ultrasound images*, Computerized Medical Imaging and Graphics 35 (2011), pp. 315-323.

[129] C. Mu Chen, and S. Long, *An information granulation based data mining approach for classifying imbalanced data*, Information Sciences 178 (2008), pp. 3214-3227.

[130] S. Ozcelik, and N. Hardalac, *The statistical measurements and neural network analysis of the effect of musical education to musical hearing and sensing*, Expert Systems with Applications 38 (2011), pp. 9517-9521.

[131] L. Wang, and C. Silván, *Neural network classification of mangrove species from multi-seasonal Ikonos imagery*, Photogrammetric Engineering and Remote Sensing 74 (2008), pp. 921-927.

[132] Y. Zhang, Z. Dong, L. Wu, and S. Wang, *A hybrid method for MRI brain image classification*, Expert Systems with Applications 38 (2011), pp. 10049-10053.

[133] R. Duca, and F. Del, *Hyperspectral and multiangle CHRIS–PROBA images for the generation of land cover maps*, IEEE Transactions on Geoscience and Remote Sensing 46 (2008), pp. 2857-2866.

[134] A.C. Gonzalez-Garcia, J.H. Sossa-Azuela, and E.M. Felipe-Riveron, *Image retrieval based on wavelet computation and neural network classification, in 8th International Workshop on Image Analysis for Multimedia Interactive Services*, Santorini, Greece, 2007.

[135] I. Kucuk, T. Yildirim, N.M. Gasanly, and H. Ozkan, *Estimation of thermally stimulated current in as grown TlGaSeS layered single crystals by multilayered perceptron neural network*, Expert Systems with Applications 38 (2011), pp. 7192-7194.

[136] I. Maglogiannis, H. Sarimveis, C.T. Kiranoudis, A.A. Chatziioannou, N. Oikonomou, and V. Aidinis, *Radial basis function neural networks classification for the recognition of idiopathic pulmonary fibrosis in microscopic images*, IEEE Transactions on Information Technology in Biomedicine 12 (2008), pp. 42-54.

[137] R. Vilar, J. Zapata, and R. Ruiz, *An automatic system of classification of weld defects in radiographic images*, Nondestructive Testing and Evaluation International 42 (2009), pp. 467-476.

[138] C.J. Huberty, *Applied MANOVA and Discriminant Analysis*, 2nd ed., Wiley-Interscience, Hoboken, NJ, 2006.

[139] M. Castellani, and H. Rowlands, *Evolutionary artificial neural network design and training for wood veneer classification*, Engineering Applications of Artificial Intelligence 22 (2009), pp. 732-741.

[140] C.-F.J. Kuo, C.-J. Lee, and C.-C. Tsai, *Using a neural network to identify fabric defects in dynamic cloth inspection*, Textile Research Journal 73 (2003), pp. 238-244.

[141] J. Liu, B. Zuo, X. Zeng, P. Vroman, and B. Rabenasolo, *Wavelet energy signatures and robust Bayesian neural network for visual quality recognition of nonwovens*, Expert Systems With Applications 38 (2011), pp. 8497-8508.

[142] A. Marcano-Cedeno, J. Quintanilla-Dominguez, and D. Andina, *WBCD breast cancer database classification applying artificial metaplasticity neural network*, Expert Systems with Applications 38 (2011), pp. 9573-9579.

[143] F. Moghadas Nejad, and H. Zakeri, *An expert system based on wavelet transform and radon neural network for pavement distress classification*, Expert Systems with Applications 38 (2011), pp. 7088-7101.

[144] H. Muzhou, and H. Xuli, *The multidimensional function approximation based on constructive wavelet RBF neural network*, Applied Soft Computing Journal 11 (2011), pp. 2173-2177.

[145] A. Oishi, K. Yamada, S. Yoshimura, G. Yagawa, S. Nagai, and Y. Matsuda, *Neural network-based inverse analysis for defect identification with laser ultrasonics*, Research in Nondestructive Evaluation 13 (2001), pp. 79-95.

[146] B. Samata, and K.R. Al-Balushi, *Use of time domain features for the neural network based fault diagnosis of a machine tool coolant system*, Proceedings of the Institution of Mechanical Engineers, Part I (Journal of Systems and Control Engineering) 215 (2001), pp. 199-207.

[147] J. Wang, and W. Zhang, *Predicting bond qualities of fabric composites after wash and dry wash based on principal-BP neural network model*, Textile Research Journal 77 (2007), pp. 142-150.

[148] N. Subramanian, A. Yajnik, and R.S.R. Murthy, *Artificial neural network as an alternative to multiple regression analysis in optimizing formulation parameters of cytarabine liposomes*, AAPS Pharmscitech 5 (2004), pp. 11-19.

[149] MathWorks, *Multilayer Networks and Backpropagation Training*, (2012). Available at: http://www.mathworks.com/help/toolbox/nnet/ug/bss33r9.html.

[150] M. Modest, *Radiative Heat Transfer*, 2nd ed., Academic Press, Boston, MA, 2003.

[151] F.P. Incropera, *Fundamentals of Heat and Mass Transfer*, 6th ed., John Wiley, Hoboken, NJ, 2007.

[152] C.O. Popiel, *Free convection heat transfer from vertical slender cylinders: A review*, Heat Transfer Engineering 29 (2008), pp. 521-536.

[153] N.K. Abdul-Jabbar, *Natural convective heat transfer coefficient – a review: I. Isolated vertical and horizontal surfaces*, Energy Conversion and Management 42 (2001), pp. 491-504.

[154] T.H. Wang, C.C. Lee, Y.-S. Lai, and C.-E. Huang, *Correlation between power cycling and thermal cycling fatigue reliabilities of chip-scale packages, in 29th International Electronics Manufacturing Technology Symposium IEEE/CPMT/SEMI*, San Jose, CA, USA, 2004.

[155] H. Caiying, L. Zuyao, W. Hongxia, W. Lei, L. Feng, and R. Hongfeng, *Thermo-mechanical simulation and optimization analysis for warpage-induced PBGA solder joint failures, in SMNTA International*, Shangai, China, 2010.

[156] Plastics-International, *Plastic sheets, rods & tube*, (2011). Available at: http://www.plasticsintl.com.

[157] NASA, *Verification Assessment*, (2008). Available at: http://www.grc.nasa.gov/WWW/wind/valid/tutorial/verassess.html.

[158] M. Ozturk, and M.C. Aydin, *Verification of a 3-D numerical model for spillway aerator*, Mathematical and Computational Applications 14 (2009), pp. 21-30.

[159] I. Babuska, and J.T. Oden, *Verification and validation in computational engineering and science: Basic concepts*, Computer Methods in Applied Mechanics and Engineering 193 (2004), pp. 4057-38.

[160] K.S. Kim, H.H. Choi, C.S. Moon, and C.W. Mun, *Comparison of k-nearest neighbor, quadratic discriminant and linear discriminant analysis in classification of electromyogram signals based on the wrist-motion directions*, Current Applied Physics 11 (2011), pp. 740-745.

[161] S.-J. Hsieh, and S. Ling, *A methodology for microcontroller signal frequency stress prediction*, Microelectronics and Reliability 45 (2005), pp. 1243-1251.

APPENDIX A

Artificial Neural Networks MATLAB script for Alternative 3

```
%
%************************************************************************
%
%  A Neural Network program to do PCB recognition any Inputs 3 Outputs
%
%************************************************************************
%

clear all;

%--Begin--------Opening and formating Modelling Data and test Data----------------------------

    %+++++++++training Data+++++++++

fid1 = fopen('C:\BEN\matlab_analysis\numerical\Pin_Model_3In_Hi_3Out_all_num.dat','r');  % Read training data from a file
All_Data = fscanf(fid1,'%f');                                                           % Matrix holding data
fclose(fid1);
N = max(size(All_Data))

  %------------Reading training data
l = 1;
for k = 1:8:N-7,
  S1(l)= All_Data(k+3)+All_Data(k+4);                                  % (C4+C5)
  S2(l)= (abs(All_Data(k+2)-All_Data(k+1))+abs(All_Data(k+1)-All_Data(k)))/2;          % average of rates from C1 to C3
  S3(l)= (All_Data(k)+All_Data(k+1)+All_Data(k+2))/3;                  % (C1+C2+C3)/3
  Out1(l)= All_Data(k+4);
  Out2(l)= All_Data(k+5);
  Out3(l)= All_Data(k+6);
  l=l+1;
end;
  %-------------Reading   training data

ORIG_Data =[S1; S2; S3];
Target_Data=[Out1;Out2;Out3];          %Outputs

Norm_S1= S1

Norm_S2= S2

Norm_S3= S3
Norm_Data = [Norm_S1;Norm_S2;Norm_S3];   %Matrix data for training neural network


  %         +++++++++TESTing DATA++++++++++++

fid2 = fopen('C:\BEN\matlab_analysis\numerical\Pin_test_3In_Hi_3Out_all_num.dat','r');
T_Data = fscanf(fid2,'%f');                                                          % Matrix holding data

M = max(size(T_Data));
fclose(fid2);


h = 1;

for p = 1:8:M-7,
  T1(h)= T_Data(p+3)+T_Data(p+4);                                      % (C4+C5)
  T2(h)= (abs(T_Data(p+2)-T_Data(p+1))+abs(T_Data(p+1)-T_Data(p)))/2;   % average of rates from C1 to C3
  T3(h)= (T_Data(p)+T_Data(p+1)+T_Data(p+2))/3;                        % (C1+C2+C3)/3
  TOut1(h)= T_Data(p+4);
  TOut2(h)= T_Data(p+5);
  TOut3(h) = T_Data(p+6);
  h=h+1;
end;
```

```
Test_Data =[T1; T2; T3];
Test_Target_Data=[TOut1; TOut2; TOut3];  %test outputs

Norm_T1= T1

Norm_T2= T2
Norm_T3= T3


Norm_Test_Data = [Norm_T1;Norm_T2;Norm_T3];   %Matrix data for testing neural network


%--End-------Opening and formating Modelling Data and test Data--------------------------


zz=1;
%z=12;


for z = 5:18   %--------------For to vary number of hidden nodes form 5 to 18

%-----------BEGIN----Creating feed-forward backpropagation network--------------

  rand('state',0);
  net = newff(minmax(Norm_Data),Target_Data,[z],{'tansig' 'tansig'});

    %--NOTE---z are the HIDDEN NODES in previous line----


%-----------END----Creating feed-forward backpropagation network---


%--BEGIN-----preparing a custom network to be initialized with initwb-----------------


    net.layers{1}.initFcn = 'initwb';
    net.layers{2}.initFcn = 'initwb';

    net.inputweights{1,1}.initFcn = 'rands';
    net.layerweights{2,1}.initFcn = 'rands';

    net.biases{1,1}.initFcn ='rands';
    net.biases{2,1}.initFcn ='rands';

%--END-----preparing a custom network to be initialized with initwb-----------------

%--BEGIN-------(initializes layer weights and biases functions (i.e. rands)----

   %----initializing the network-----
     net = init(net);
   %----initializing the network-----


   %----training parammeters----
     net.trainParam.epochs=100000;
     net.trainParam.lr=0.05;
     net.trainParam.show=1000;
     net.trainParam.goal=0.001;
   %----training parammeters----

%--END-------(initializes layer weights and biases functions (i.e. rands)----

%----training-----
[net,tr]=train(net,Norm_Data,Target_Data);

a = sim(net,Norm_Data);

%----saving training performance, state, and regression-----

h1=plotperform(tr);
legend('Location','SouthOutside','Orientation','horizontal');
saveas(h1,['C:\Users\Ben\Documents\MATLAB\A4_newff_back_3in_hddvariable\A4_performance_newff_hn' int2str(z)], 'm');
close(h1)
```

```
h2=plottrainstate(tr);
saveas(h2,['C:\Users\Ben\Documents\MATLAB\A4_newff_back_3in_hddvariable\A4_train_state_newff_hn' int2str(z)], 'm');
close(h2)
h4=plotregression(Target_Data,a);
saveas(h4,['C:\Users\Ben\Documents\MATLAB\A4_newff_back_3in_hddvariable\A4_regression_newff_hn' int2str(z)], 'm');
close(h4)



%*********************************************************
%                                   TESTING NEURAL NETWORK
%*********************************************************

tn = sim(net,Norm_Test_Data);

tot_err = 0;
tot_good=0;
Samp_Num = M/8;

%------------determining accuracy o neural network developed

for i = 1:Samp_Num
  if int8(Test_Target_Data(1,i))==int8(tn(1,i))
     if int8(Test_Target_Data(2,i))==int8(tn(2,i))
       if int8(Test_Target_Data(3,i))==int8(tn(3,i))
         tot_good=tot_good+1;
       else
         tot_err=tot_err+1;
       end
     else
       tot_err=tot_err+1;
     end
  else
    tot_err=tot_err+1;
  end
end
  tot_err
  tot_good
  Percent_correct=100*(tot_good/(tot_good+tot_err))
  hn_number(zz)=z;
  hn_err(zz)=tot_err;
  hn_good(zz)=tot_good;
  hn_percent(zz)=Percent_correct;
  zz=zz+1;

  clear net.layers{1}
  .initFcn
  clear net.layers{2}.initFcn
  clear net.inputweights{1,1}.initFcn
  clear net.layerweights{2,1}.initFcn
  clear net.biases{1,1}.initFcn
  clear net.biases{2,1}.initFcn
  clear net
  clear tn
  clear a
end

hn_results=[hn_number; hn_err; hn_good; hn_percent;];  %storing accuracies in terms hidden number

save C:\Users\Ben\Documents\MATLAB\A4_newff_back_3in_hddvariable\A4_backpropagation.dat

                                                %----------previous line saves all data as well as neural network
```

APPENDIX B

Vertical Plate [151]

$$h = \left(\frac{k}{L}\right)\left(0.68 + \frac{0.67 Ra_L^{1/4}}{\left[1 + (0.492/\mathrm{Pr})^{9/16}\right]^{4/9}}\right) \qquad Ra \le 10^9 \tag{B-1}$$

Horizontal plate [153]

Upper surface of heated plate or lower surface of cooled plate

$$h = 1.32\left(\frac{T_s - T_\infty}{L}\right)^{1/4} \qquad Ra \le 10^9 \tag{B-2}$$

Lower surface of heated plate or upper surface of cooled plate

$$h = 0.59\left(\frac{T_s - T_\infty}{L}\right)^{1/4} \tag{B-3}$$

Vertical slender cylinder [152]

$$h = \left(\frac{k}{D}\right)\left(0.36 + \frac{0.67\left(Ra_D D/L\right)^{1/4}}{\left[1 + (0.492/\mathrm{Pr})^{9/16}\right]^{4/9}}\right) \qquad Ra_D D/L < 10^9 \tag{B-4}$$

Ra is the Rayleigh number and is given by the next expressions:

$$Ra_L = \frac{g\beta(T_s - T_\infty)L^3}{\nu\alpha}$$

$$Ra_D = \frac{g\beta(T_s - T_\infty)D^3}{\nu\alpha} \tag{B-5}$$

where g, β, T_s, T, L, D, ν, and α are the local gravitational acceleration, thermal expansion coefficient, surface temperature, ambient temperature, length, diameter, kinematic viscosity, and thermal diffusivity. Finally, it is important to mention that the fluid properties should be evaluated at the film temperature that is given by the next expression:

$$T_{film} = \frac{T_s + T_\infty}{2} \tag{B-6}$$

APPENDIX C

Finite element model ANSYS script for eight covers

```
!USE DATA:
!CONVECTIVE COEFFICIENT=correlations
!AMBIENT TEMPERATURE heat Chamber=27c
!AMBIENT TEMPERATURE cool Chamber=28.7c

/FILNAME,heating,1

!--------ALL dimensions are in meters unless especified----------



/PREP7

/PNUM,AREA,1              !Controls entity numbering/coloring on plots

!load convective coefficient correlations, file, "convective_coefficient_correlations", should exist in working directory
PARRES,,convective_coefficient_correlations,,

cover=8

w=0.3048                  !12" width chamber
l_c=0.36                  !12" lenght cooling chamber
l_h=0.19                  !length heating chamber
l=l_c+l_h                 !12" total length
h=0.515                   !height chamber              GEOMETRIC pARAMETERS
thk1=0.005                !1/4" thickness acrylic              FOR
thk2=0.01                 !1/2" thickness styrofoam            CHAMBER

!--------------Fixture platform------------------
wb=0.096                  !1-3/4"  width
lb=0.07                   !1-3/4"   length
hb=0.0015875              !1/16"  height

!----------SIMPLE---FIXTURE-------

wf=0.005                  !
lf=0.04                   !
hf=0.0475                 !
lf_gc=lb/2+0.05     !0.065              !fixture "y" geometric center

!----------board---------
wb2=0.04445               !1-3/4" width
lb2=0.04445               !1-3/4" lenght
hb2=0.0015875             !1/16"  thickness
```

```
!-------velcro---------
hv=0.0015875              !1/16" height


!----------Lamp dimensions-----------------------
!-----bottom and top bases-----
wl_b=6.25/100
ll_b=9.75/100
wl_t=4.35/100
ll_t=5.25/100
thk3=1/1000



!----------Pin-dimensions--------
r60=0.1054*2.54/200
h60=0.0913*2.54/100
V60=3.1416*(r60**3)/(3*tan(30*3.1416/180))

r82=0.122*2.54/200
h82=3*V60/(3.1416*(r82**2))
r90=0.1265*2.54/200
h90=0.0633*2.54/100
r100=0.1338*2.54/200
h100=3*V60/(3.1416*(r100**2))
r120=0.152*2.54/200
h120=0.044*2.54/100

!!all comments relate to cone dimenssions estart with !==================
!!====================cone dimenssions should be added here as:=============

!theta82=82                              !angle
!r82=(3*V60*tan (0.5*theta82*3.1416/180)/3.1416)**0.3334   !radious
!h82=r82/tan (0.5*theta82*3.1416/180)                     !height

!add cones until three
!end of comment for cone dimenssions


!++++++++++++++++++++++fixture update++++++++++++++++++++++++++++

!upper vertical prism
v_f_w=0.75/100
v_f_l=3.75/100
v_f_h=2.25/100

!horizontal rectangular prism
h_f_w=5.75/100
h_f_l=3.75/100
h_f_l=0.75/100
```

```
!square bottom supports (by two)
s_f_w=0.75/100
s_f_h=1.5/100

!TRIANGULAR PRISM HEIGHT
t_f_h=1.25/100

!hole position from midpoint X/Y
h_p=0.625/100
h_r=0.625/200

!--------------Lamp Filament position and dimensions-----------------
lfil=4.25/100
dfil=1/1000
xf=w/2-0.0105
yf=lf_gc+l_c-0.5*ll_b+2.75/100
zf=17.3/100

!-------------------------pin wire dimensions----------------------------
w_r=0.022*2.54/200  !radious
w_l=1/100           !lenght

!-------------------------cover height

!==================== next line should be modified for smallest cone angle for example if
!45 is smallest cone angle:
!c_h=h45-w_r*(h45/r45)

c_h=h60-w_r*(h60/r60)    !space between cover and board or between covers
w_l=(1/100)+(cover-2)*(c_h+hb)       !pin wire lenght updated so same length beyond cover is consistent for any number of covers


!-----------------------Material Properties-------------------------

MP,DENS,1,105             !acrylic as
MP,KXX,1,0.036            !Glass fiber, organic bonded (Incropera)
MP,KYY,1,0.036
MP,KZZ,1,0.036
MP,C,1,795
!alpha=4.313e-7

MP,DENS,2,16              !styrofoam (Polystyrene molded beads, Incropera)
MP,KXX,2,0.04
MP,KYY,2,0.04
MP,KZZ,2,0.04
MP,C,2,1210
!alpha=2.066e-6

MP,DENS,3,8420        !solder--Data from
MP,KXX,3,51           !2004 IEEE/SEMI Int'l Electronics Manufacturing Technology Symposium
```

```
MP,KYY,3,51          !Correlation Between Power Cycling and Thermal Cycling Fatigue Reliabilities
MP,KZZ,3,51
MP,C,3,176
!alpha=3.441e-5

!MP,DENS,4,1920     !board (Substrate)
!MP,KXX,4,0.81      !data from:
!MP,KYY,4,0.81      !Journal of Materials Processing Technology 155–156 (2004) 1788–1796
!MP,KZZ,4,0.29      !Application of numerical analysis to the optimisation of electronic
!MP,C,4,1300
!alpha=3.245e-7


MP,DENS,4,1870                    !board EXP
MP,KXX,4,0.525
MP,KYY,4,0.525                    !0.27
MP,KZZ,4,0.525
MPTEMP,1,25,30,70,120,240            ! Create temperature table
MPDATA,C,4,1,1210,1210,1380,1500,1650  !Create CP table
MPPLOT,C,4,,,,,


MP,DENS,5,2790     !lamp (case)
MP,KXX,5,237       !data from:
MP,KYY,5,237       !fundamentals of heat transfer
MP,KZZ,5,237       !Incropera
MP,C,5,798
!alpha=1.064e-4

MP,DENS,6,19300    !fillament (tungsten)
MP,KXX,6,100       !data from:
MP,KYY,6,100       !fundamentals of heat transfer
MP,KZZ,6,100       !Incropera
MP,C,6,167
!alpha=3.103e-5

MP,DENS,7,8940     !copper
MP,KXX,7,401       !data from:
MP,KYY,7,401       !fundamentals of heat transfer
MP,KZZ,7,401       !Incropera tin-plated copper for pin wire
MP,C,7,390

MP,DENS,8,1150      !nylon_for velcro
MP,KXX,8,0.25       !data from:
MP,KYY,8,0.25       !plastics International + w
MP,KZZ,8,0.25       !
MP,C,8,1883.95
!alpha=1.739e-4

MP,DENS,9,1.1769            !air
MP,KXX,9,0.02624            !incropera
```

```
MP,KYY,9,0.02624
MP,KZZ,9,0.02624
MP,C,9,1007.3
!alpha=2.2156e-5

PTXY,0,0,w,0,w,l,0,l        !acrylic shell generation
PRISM,0,h
PTXY,thk1,thk1,w-thk1,thk1,w-thk1,l-thk1,thk1,l-thk1
PRISM,thk1,h-thk1
VSBV,1,2,SEPO, ,keep
VSEL,S,VOLU,,3
VATT,1              !ASSIGNING ACRYLIC PROPERTIES
ALLSEL


!------------------------------Styrofoam shell generation
PTXY, thk1+thk2,thk1+thk2,w-thk1-thk2,thk1+thk2,w-thk1-thk2,l_c-thk2,thk1+thk2,l_c-thk2
PRISM,thk1+thk2,h-thk1-thk2
VSBV,2,1,SEPO, ,
VSEL,S,VOLU,,4
VATT,2              !ASSIGNING styrofoam PROPERTIES
ALLSEL

PTXY,(w-h_f_w)/2,l_c+lf_gc-(v_f_l/2),v_f_w+(w-h_f_w)/2,l_c+lf_gc-(v_f_l/2),v_f_w+(w-h_f_w)/2,l_c+lf_gc+(v_f_l/2),(w-
h_f_w)/2,l_c+lf_gc+(v_f_l/2)        !fixture generation
PRISM,thk1+thk2+s_f_h+v_f_w,thk1+thk2+s_f_h+v_f_w+v_f_h
PTXY,-v_f_w+(w+h_f_w)/2,l_c+lf_gc-(v_f_l/2),(w+h_f_w)/2,l_c+lf_gc-(v_f_l/2),(w+h_f_w)/2,l_c+lf_gc+(v_f_l/2),-
v_f_w+(w+h_f_w)/2,l_c+lf_gc+(v_f_l/2)        !fixture generation
PRISM,thk1+thk2+s_f_h+v_f_w,thk1+thk2+s_f_h+v_f_w+v_f_h
PTXY,(w-h_f_w)/2,l_c+lf_gc-(v_f_l/2),(w+h_f_w)/2,l_c+lf_gc-(v_f_l/2),(w+h_f_w)/2,l_c+lf_gc+(v_f_l/2),(w-
h_f_w)/2,l_c+lf_gc+(v_f_l/2)        !fixture generation
PRISM,thk1+thk2+s_f_h,thk1+thk2+s_f_h+v_f_w
!PTXY,(w-s_f_w)/2,l_c+lf_gc-(v_f_l/2),(w+s_f_w)/2,l_c+lf_gc-(v_f_l/2),(w+s_f_w)/2,l_c+lf_gc-(v_f_l/2)+s_f_w,(w-s_f_w)/2,l_c+lf_gc-
(v_f_l/2)+s_f_w        !fixture generation
!PRISM,thk1+thk2,thk1+thk2+s_f_h
!PTXY,(w-s_f_w)/2,l_c+lf_gc+(v_f_l/2),(w+s_f_w)/2,l_c+lf_gc+(v_f_l/2),(w+s_f_w)/2,l_c+lf_gc+(v_f_l/2)-s_f_w,(w-s_f_w)/2,l_c+lf_gc+(v_f_l/2)-
s_f_w        !fixture generation
!PRISM,thk1+thk2,thk1+thk2+s_f_h
VSEL,S,VOLU,,1,2,,1
VATT,1              !ASSIGNING fixture ACRYLIC PROPERTIES
VSEL,S,VOLU,,5,,,1
VATT,1
K,1020,(w-h_f_w)/2,l_c+lf_gc-(v_f_l/2)+1e-3,thk1+thk2+s_f_h+v_f_w+v_f_h
K,1021,(w-h_f_w)/2,l_c+lf_gc+(v_f_l/2)-1e-3,thk1+thk2+s_f_h+v_f_w+v_f_h
K,1022,(w-h_f_w)/2,l_c+lf_gc,thk1+thk2+s_f_h+v_f_w+v_f_h-t_f_h
K,1023,v_f_w+(w-h_f_w)/2,l_c+lf_gc-(v_f_l/2)+1e-3,thk1+thk2+s_f_h+v_f_w+v_f_h
K,1024,v_f_w+(w-h_f_w)/2,l_c+lf_gc+(v_f_l/2)-1e-3,thk1+thk2+s_f_h+v_f_w+v_f_h
K,1025,v_f_w+(w-h_f_w)/2,l_c+lf_gc,thk1+thk2+s_f_h+v_f_w+v_f_h-t_f_h
V,1020,1021,1022,1023,1024,1025

K,1026,(w+h_f_w)/2,l_c+lf_gc-(v_f_l/2)+1e-3,thk1+thk2+s_f_h+v_f_w+v_f_h
```

```
K,1027,(w+h_f_w)/2,l_c+lf_gc+(v_f_l/2)-1e-3,thk1+thk2+s_f_h+v_f_w+v_f_h
K,1028,(w+h_f_w)/2,l_c+lf_gc,thk1+thk2+s_f_h+v_f_w+v_f_h-t_f_h
K,1029,-v_f_w+(w+h_f_w)/2,l_c+lf_gc-(v_f_l/2)+1e-3,thk1+thk2+s_f_h+v_f_w+v_f_h
K,1030,-v_f_w+(w+h_f_w)/2,l_c+lf_gc+(v_f_l/2)-1e-3,thk1+thk2+s_f_h+v_f_w+v_f_h
K,1031,-v_f_w+(w+h_f_w)/2,l_c+lf_gc,thk1+thk2+s_f_h+v_f_w+v_f_h-t_f_h
V,1026,1027,1028,1029,1030,1031
allsel
VSBV,1,6,SEPO
VSBV,2,7,SEPO
ALLSEL


!------------------generating board----------

PTXY,(w/2)-(wb2/2),l_c+lf_gc-(lb2/2),(w/2)+(wb2/2),l_c+lf_gc-(lb2/2),(w/2)+(wb2/2),l_c+lf_gc+(lb2/2),(w/2)-(wb2/2),l_c+lf_gc+(lb2/2)        !board
generation
PRISM,thk1+thk2+s_f_h+v_f_w+v_f_h+1.5*hb,thk1+thk2+s_f_h+v_f_w+v_f_h+2.5*hb
VSEL,S,VOLU,,2
VATT,4              !ASSIGNING board PROPERTIES
ALLSEL

!--------------------------------solder generation----------------------------------

CSWPLA,21,0                !Defines a local coordinate system at the origin of the working plane.
WPLANE,2 ,0,0,thk1+thk2+s_f_h+v_f_w+v_f_h+2.5*hb,1,0,thk1+thk2+s_f_h+v_f_w+v_f_h+2.5*hb,0,1,thk1+thk2+s_f_h+v_f_w+v_f_h+2.5*hb

!=================== in next three lines, the radious and height should be change
!for the three angles that will be use. for example in the case of 45,70, and 100
!the three lines will be:

!CON4, (w/2)-0.0105,l_c+lf_gc-0.01,r45,,h45
!CON4, (w/2)-0.0105,l_c+lf_gc,r70,,h70
!CON4, (w/2)-0.0105,l_c+lf_gc+0.01,r100,,h100


CON4, (w/2)-0.0105,l_c+lf_gc-0.01,r120,,h120
CON4, (w/2)-0.0105,l_c+lf_gc,r90,,h90
CON4, (w/2)-0.0105,l_c+lf_gc+0.01,r60,,h60
VSEL,S,VOLU,,6,7,
VATT,3              !ASSIGNING solder
VSEL,S,VOLU,,9
VATT,3              !ASSIGNING solder
ALLSEL

!+--------------add the pin wires-------------
WPLANE,2 ,0,0,thk1+thk2+s_f_h+v_f_w+v_f_h+2.5*hb,1,0,thk1+thk2+s_f_h+v_f_w+v_f_h+2.5*hb,0,1,thk1+thk2+s_f_h+v_f_w+v_f_h+2.5*hb
CYL4,(w/2)-0.0105,l_c+lf_gc-0.01,w_r,,,,w_l
CYL4,(w/2)-0.0105,l_c+lf_gc,w_r,,,,w_l
CYL4,(w/2)-0.0105,l_c+lf_gc+0.01,w_r,,,,w_l
WPCSYS,,21
allsel
```

```
VSBV,9,12,SEPO,,keep
VSBV,7,11,SEPO,,keep
VSBV,6,10,SEPO,,keep

!--------------------fixture support holes generation-------------

WPLANE,3,0,0,thk1+thk2+s_f_h+v_f_w,1,0,thk1+thk2+s_f_h+v_f_w,0,1,thk1+thk2+s_f_h+v_f_w
CYL4,(w/2)-h_p,l_c+lf_gc-h_p,h_r,360,,,-v_f_w
CYL4,(w/2)+h_p,l_c+lf_gc-h_p,h_r,360,,,-v_f_w
CYL4,(w/2)+h_p,l_c+lf_gc+h_p,h_r,360,,,-v_f_w
CYL4,(w/2)-h_p,l_c+lf_gc+h_p,h_r,360,,,-v_f_w
allsel
VSBV,5,16,SEPO
VSBV,17,6,SEPO
VSBV,5,14,SEPO
VSBV,6,15,SEPO
allsel

WPCSYS,,21

!-------------------------generating fixture-----------------------------

PTXY,(w/2)-(wb/2),l_c+lf_gc-(lb/2),(w/2)+(wb/2),l_c+lf_gc-(lb/2),(w/2)+(wb/2),l_c+lf_gc+(lb/2),(w/2)-(wb/2),l_c+lf_gc+(lb/2)
PRISM,thk1+thk2+s_f_h+v_f_w+v_f_h,thk1+thk2+s_f_h+v_f_w+v_f_h+hb
VSEL,S,VOLU,,6
VATT,4              !ASSIGNING fix-board PROPERTIES

!-----------------------------generating velcro---------------------------

PTXY,(w/2)-(wb2/2),l_c+lf_gc-(lb2/2),(w/2)+(wb2/2),l_c+lf_gc-(lb2/2),(w/2)+(wb2/2),l_c+lf_gc+(lb2/2),(w/2)-(wb2/2),l_c+lf_gc+(lb2/2)
PRISM,thk1+thk2+s_f_h+v_f_w+v_f_h+hb,thk1+thk2+s_f_h+v_f_w+v_f_h+1.5*hb
VSEL,S,VOLU,,14
VATT,8              !ASSIGNING velcro PROPERTIES


!-----------------------------LAMP MODEL-----------------------------------
K,1001,-0.0105+(w-wl_b)/2,lf_gc+l_c-0.5*ll_b,0.15          !Defines a keypoint------bottom keypoints of lamp-------
K,1002,-0.0105+(w+wl_b)/2,lf_gc+l_c-0.5*ll_b,0.15
K,1003,-0.0105+(w+wl_b)/2,lf_gc+l_c-0.5*ll_b+ll_b,0.15
K,1004,-0.0105+(w-wl_b)/2,lf_gc+l_c-0.5*ll_b+ll_b,0.15
K,1005,-0.0105+(w-wl_t)/2,lf_gc+l_c-0.5*ll_b+(ll_b-ll_t)/2,0.189          !Defines a keypoint------bottom keypoints of lamp
K,1006,-0.0105+(w+wl_t)/2,lf_gc+l_c-0.5*ll_b+(ll_b-ll_t)/2,0.189
K,1007,-0.0105+(w+wl_t)/2,lf_gc+l_c-0.5*ll_b+(ll_b+ll_t)/2,0.189
K,1008,-0.0105+(w-wl_t)/2,lf_gc+l_c-0.5*ll_b+(ll_b+ll_t)/2,0.189
V, 1001, 1002, 1003, 1004, 1005, 1006, 1007, 1008      !Defines a volume through keypoints.
K,1009,-0.0105+thk3+(w-wl_b)/2,lf_gc+l_c-0.5*ll_b+thk3,0.15          !Defines a keypoint------top keypoints of lamp-----
K,1010,-0.0105-thk3+(w+wl_b)/2,lf_gc+l_c-0.5*ll_b+thk3,0.15
K,1011,-0.0105-thk3+(w+wl_b)/2,lf_gc+l_c-0.5*ll_b+ll_b-thk3,0.15
K,1012,-0.0105+thk3+(w-wl_b)/2,lf_gc+l_c-0.5*ll_b+ll_b-thk3,0.15
K,1013,-0.0105+thk3+(w-wl_t)/2,lf_gc+l_c-0.5*ll_b+thk3+(ll_b-ll_t)/2,0.189-thk3          !Defines a keypoint------bottom keypoints of lamp
K,1014,-0.0105-thk3+(w+wl_t)/2,lf_gc+l_c-0.5*ll_b+thk3+(ll_b-ll_t)/2,0.189-thk3
```

```
K,1015,-0.0105-thk3+(w+wl_t)/2,lf_gc+l_c-0.5*ll_b-thk3+(ll_b+ll_t)/2,0.189-thk3
K,1016,-0.0105+thk3+(w-wl_t)/2,lf_gc+l_c-0.5*ll_b-thk3+(ll_b+ll_t)/2,0.189-thk3
V, 1009, 1010, 1011, 1012, 1013, 1014, 1015, 1016      !Defines a volume through keypoints.
VSBV,15,16,SEPO

!++++++++++++++Filament generation++++++++++++++++++++++++++++++++
WPLANE,,xf,yf,zf,xf+0.1,yf,zf,xf,yf+0.1,zf
WPROTA,,-90      !Rotates the working plane
CYL4,0,0,dfil/2,360,,,lfil
WPCSYS,,21

allsel

VGEN,2,17,,,wl_b+wl_b/10,,,,1,0          !Generates additional volumes from a pattern of volumes.
VGEN,2,17,,,-(wl_b+wl_b/10),,,,1,0

!------continuing----------------Styrofoam shell generation
PTXY, thk1+thk2,l_c,w-thk1-thk2,l_c,w-thk1-thk2,l_c+l_h-thk1,thk1+thk2,l_c+l_h-thk1
PRISM,thk1+thk2,h-thk1-thk2
VSBV,4,19,SEPO, ,
VSEL,S,VOLU,,20
VATT,2              !ASSIGNING styrofoam PROPERTIES
ALLSEL

!----continuing-------------------acrylic shell generation
PTXY,thk1+thk2,l-thk1,w-thk1-thk2,l-thk1,w-thk1-thk2,l,thk1+thk2,l
PRISM,thk1+thk2,h-thk1-thk2
VSBV,3,4,SEPO,,keep

allsel


!gluing surfaces in contact to generate common surfaces (non-radiating surfaces)
VGLUE,19,20    !chamber walls


VGLUE,13,2   !pins+board
VGLUE,20,9
VGLUE,7,2

VGLUE,20,10   !wire+board
VGLUE,2,11
VGLUE,21,12

VGLUE,7,10   !wire+pin
VGLUE,20,9
VGLUE,12,13

VGLUE,6,14   !board-fix+velcro
VGLUE,14,2   !velcro+board
```

```
VGLUE,9,2   !pins+board again
VGLUE,2,7
VGLUE,2,11

VGLUE,20,2   !wire+board again
VGLUE,2,10
VGLUE,21,2

VGLUE,1,12    !fix+vs
VGLUE,8,14

VGLUE,1,5    !4hole+vs
VGLUE,8,14

allsel

!------------------assigning convective coefficient at SURFACES-----------------------------



!------------------------------mylar surfaces of heating cham---------------------------

ASEL,S,AREA,,15,16,,1              !mylar surfaces of heating cham
!SFA,ALL,,RDSF,0.37,1                !E=0.37,ENCLOSURE1,mylar 0.0625mm
SFA,ALL,,conv,%HH_W_V%,27
ASEL,S,AREA, ,152,,,1
!SFA,ALL,,RDSF,0.37,1
SFA,ALL,,conv,%HH_W_V%,27
ASEL,S,AREA, ,13,,,1
!SFA,ALL,,RDSF,0.37,1
SFA,ALL,,conv,%HH_W_H_T%,27
ASEL,S,AREA, ,14,,,1
!SFA,ALL,,RDSF,0.37,1
SFA,ALL,,conv,%HH_W_H_B%,27
ASEL,S,AREA, ,27,,,1              !black cover chamber
!SFA,ALL,,RDSF,0.91,1
SFA,ALL,,conv,%HH_W_V%,27


!-----------------------------------fix_board---------------------------------------

ASEL,S,AREA,,90,91,,1
SFA,ALL,,conv,%HH_THK%,27
ASEL,S,AREA,,48,,,1
SFA,ALL,,conv,%HH_THK%,27
ASEL,S,AREA,,85,,,1
SFA,ALL,,conv,%HH_THK%,27
ASEL,S,AREA,,24,,,1
SFA,ALL,,conv,%HH_FX_B%,27
```

```
ASEL,S,AREA,,56,57,,1          !V SURFACE FIXTURE (MIGHT NOT BE ADDED)
!SFA,ALL,,RDSF,0.37,1          !E=0.37, Mylar 0.0625mm thick
SFA,ALL,,conv,%HH_V_V%,27
ASEL,S,AREA,,60,61,,1
!SFA,ALL,,RDSF,0.37,1
SFA,ALL,,conv,%HH_V_V%,27
ASEL,S,AREA,,58,59,,1
SFA,ALL,,conv,%HH_ANG%,27


ASEL,S,AREA,,44,45,,1          !other V SURFACE FIXTURE (MIGHT NOT BE ADDED)
!SFA,ALL,,RDSF,0.37,1          !E=0.37, Mylar 0.0625mm thick
SFA,ALL,,conv,%HH_V_V%,27
ASEL,S,AREA,,4,5,,1
!SFA,ALL,,RDSF,0.37,1
SFA,ALL,,conv,%HH_V_V%,27
ASEL,S,AREA,,43,,,1
SFA,ALL,,conv,%HH_ANG%,27
ASEL,S,AREA,,6,,,1
SFA,ALL,,conv,%HH_ANG%,27



ASEL,S,AREA,,39,40,,1
!SFA,ALL,,RDSF,0.37,1
SFA,ALL,,conv,%HH_V_hV%,27
ASEL,S,AREA,,17,,,1
!SFA,ALL,,RDSF,0.37,1
SFA,ALL,,conv,%HH_V_hV%,27
ASEL,S,AREA,,84,,,1
!SFA,ALL,,RDSF,0.37,1
SFA,ALL,,conv,%HH_V_hV%,27
ASEL,S,AREA,,97,,,1
!SFA,ALL,,RDSF,0.37,1
SFA,ALL,,conv,%HH_V_h_b%,27

ASEL,S,AREA,,37,38,,1
SFA,ALL,,conv,%HH_V_hV%,27
ASEL,S,AREA,,41,42,,1
SFA,ALL,,conv,%HH_V_hV%,27
ASEL,S,AREA,,86,,,1
SFA,ALL,,conv,%HH_V_h_t%,27
ASEL,S,AREA,,88,89,,1
SFA,ALL,,conv,%HH_V_hV%,27
ASEL,S,AREA,,94,95,,1
SFA,ALL,,conv,%HH_V_hV%,27

allsel

/PSF,conv,hcoef,3,1,ON
LPLOT
```

```
ASEL,S,AREA,,156,,,1   !cooling walls
SFA,ALL,,conv,%HC_W_H_T%,28.7
ASEL,S,AREA,,157,,,1   !cooling walls
SFA,ALL,,conv,%HC_W_H_B%,28.7
ASEL,S,AREA,,158,161,,1   !cooling walls
SFA,ALL,,conv,%HC_W_V%,28.7

allsel
/PSF,conv,hcoef,3,1,ON
LPLOT


!-----------------------generating---board cover-------------------------

PTXY,(w/2)-(wb2/2),l_c+lf_gc-(lb2/2),(w/2)+(wb2/2),l_c+lf_gc-(lb2/2),(w/2)+(wb2/2),l_c+lf_gc+(lb2/2),(w/2)-(wb2/2),l_c+lf_gc+(lb2/2)        !board
generation
PRISM,thk1+thk2+s_f_h+v_f_w+v_f_h+2.5*hb+c_h,thk1+thk2+s_f_h+v_f_w+v_f_h+2.5*hb+c_h+hb
VSEL,S,VOLU,,14
VATT,4              !ASSIGNING board PROPERTIES
ALLSEL
VSBV,14,20,SEPO,,keep
VSBV,21,10,SEPO,,keep
VSBV,14,11,SEPO,,keep


VGLUE,20,21    !GLUING WIRES TO COVER
VGLUE,22,10
VGLUE,22,11

!-----------------------air----gap-------------------------

PTXY,(w/2)-(wb2/2),l_c+lf_gc-(lb2/2),(w/2)+(wb2/2),l_c+lf_gc-(lb2/2),(w/2)+(wb2/2),l_c+lf_gc+(lb2/2),(w/2)-(wb2/2),l_c+lf_gc+(lb2/2)        !board
generation
PRISM,thk1+thk2+s_f_h+v_f_w+v_f_h+2.5*hb,thk1+thk2+s_f_h+v_f_w+v_f_h+2.5*hb+c_h
ALLSEL
VSBV,11,9,SEPO,,keep
VSBV,23,7,SEPO,,keep
VSBV,11,20,SEPO,,keep
VSBV,23,13,SEPO,,keep
VSBV,11,10,SEPO,,keep
vdele,21


VGLUE,9,7,13,20,10,23,2,22,14    !GLUING air TO pin+wire


ASEL,S,AREA,,68,,,1        !60 location
SFA,ALL,,conv,%HH_C_V%,27
ASEL,S,AREA,,47,,,1
SFA,ALL,,conv,%HH_C_V%,27
```

```
ASEL,S,AREA,,147,,,1   !90 location
SFA,ALL,,conv,%HH_C_V%,27
ASEL,S,AREA,,100,,,1
SFA,ALL,,conv,%HH_C_V%,27

ASEL,S,AREA,,151,,,1   !120 location
SFA,ALL,,conv,%HH_C_V%,27
ASEL,S,AREA,,153,,,1
SFA,ALL,,conv,%HH_C_V%,27

!-----------------------generating surface squares to calculate cooling rate-------------
PTXY,(w/2)-0.0105-r120,l_c+lf_gc-0.01-r120,(w/2)-0.0105+r120,l_c+lf_gc-0.01-r120,(w/2)-0.0105+r120,l_c+lf_gc-0.01+r120,(w/2)-0.0105-
r120,l_c+lf_gc-0.01+r120,         !board generation
PRISM,thk1+thk2+s_f_h+v_f_w+v_f_h+2.5*hb+c_h+hb,thk1+thk2+s_f_h+v_f_w+v_f_h+2.5*hb+c_h+2*hb

PTXY,(w/2)-0.0105-r120,l_c+lf_gc-r120,(w/2)-0.0105+r120,l_c+lf_gc-r120,(w/2)-0.0105+r120,l_c+lf_gc+r120,(w/2)-0.0105-
r120,l_c+lf_gc+r120,         !board generation
PRISM,thk1+thk2+s_f_h+v_f_w+v_f_h+2.5*hb+c_h+hb,thk1+thk2+s_f_h+v_f_w+v_f_h+2.5*hb+c_h+2*hb

PTXY,(w/2)-0.0105-r120,l_c+lf_gc+0.01-r120,(w/2)-0.0105+r120,l_c+lf_gc+0.01-r120,(w/2)-0.0105+r120,l_c+lf_gc+0.01+r120,(w/2)-0.0105-
r120,l_c+lf_gc+0.01+r120,         !board generation
PRISM,thk1+thk2+s_f_h+v_f_w+v_f_h+2.5*hb+c_h+hb,thk1+thk2+s_f_h+v_f_w+v_f_h+2.5*hb+c_h+2*hb

VGLUE,28,7,9,10    !cubes to cover
vdele,13,14,1,1
vdele,20,,,1

!---------------convection at lateral surfaces of covers-------------------------
ASEL,S,AREA,,9,12,1,1              !brd
SFA,ALL,,conv,%HH_THK%,27
ASEL,S,AREA,,78,79,1,1             !Velcro
SFA,ALL,,conv,%HH_THK%,27
ASEL,S,AREA,,75,,,1                !Velcro
SFA,ALL,,conv,%HH_THK%,27
ASEL,S,AREA,,46,,,1                !Velcro
SFA,ALL,,conv,%HH_THK%,27

ASEL,S,AREA,,166,,,1               !cover
SFA,ALL,,conv,%HH_THK%,27
ASEL,S,AREA,,155,,,1               !cover
SFA,ALL,,conv,%HH_THK%,27
ASEL,S,AREA,,148,,,1               !cover
SFA,ALL,,conv,%HH_THK%,27
ASEL,S,AREA,,146,,,1               !cover
SFA,ALL,,conv,%HH_THK%,27

ASEL,S,AREA,,202,204,1,1           !air
SFA,ALL,,conv,%HH_THK%,27
ASEL,S,AREA,,197,,,1               !air
SFA,ALL,,conv,%HH_THK%,27
```

```
allsel

!---------------------assigning properties foR EACH VOLUME--------------------------------
VSEL,S,VOLU,,21       !90 PIN MATERIAL
VATT,3
!VSEL,S,VOLU,,28       !BOARD MATERIAL
VATT,4
VSEL,S,VOLU,,12       !BOARD MATERIAL
VATT,4
VSEL,S,VOLU,,2       !BOARD MATERIAL
VATT,4
VSEL,S,VOLU,,22       !BOARD MATERIAL
VATT,4
VSEL,S,VOLU,,24       !60 PIN MATERIAL
VATT,3
VSEL,S,VOLU,,11       !120 PIN MATERIAL
VATT,3
VSEL,S,VOLU,,3       !STYROFOAM WALLS
VATT,2
VSEL,S,VOLU,,25,27       !WIRE MATERIAL? silver?
VATT,7
VSEL,S,VOLU,,29       !air
VATT,9
VSEL,S,VOLU,,6     !ASSIGNING velcro PROPERTIES
VATT,8
VSEL,S,VOLU,,16,18    !lamp case
VATT,5
VSEL,S,VOLU,,15      !fillament
VATT,6
VSEL,S,VOLU,,19
VATT,1              !ASSIGNING fixture ACRYLIC PROPERTIES
VSEL,S,VOLU,,4
VATT,1              !ASSIGNING fixture ACRYLIC PROPERTIES
VSEL,S,VOLU,,1       !FIXTURE PART STYROFOAM?
VATT,2
VSEL,S,VOLU,,8       !FIXTURE PART STYROFOAM? VERTICAL PART
VATT,2
VSEL,S,VOLU,,5       !FIXTURE PART STYROFOAM? HORIZONTAL PERFORATED PART
VATT,2

allsel

!-------------------Erasing lamps and filament for heat flux model----------------------

VDELE,15,18,1,1


!------------adding HeatFlux at top fixturesurface and cover----------------------

/PSF,hflux,,3,1,on
```

```
LPLOT

!-----heat flux is consider constant in wires tips and convection is neglected in tip
!-----update heat flux value as needed

ASEL,S,AREA,,73,,,1   !60 location
SFA,ALL,,HFLUX,20090.28571

                !90 location
ASEL,S,AREA,,69,,,1
SFA,ALL,,HFLUX,20090.28571


ASEL,S,AREA,,65,,,1
SFA,ALL,,HFLUX,20090.28571

ASEL,S,AREA,,33,35,,1   !EXTERIOR walls
SFA,ALL,,conv,%HH_WO_v%,27
ASEL,S,AREA,,31,,,1   !cooling walls
SFA,ALL,,conv,%HH_WO_HT%,27
ASEL,S,AREA,,32,,,1   !cooling walls
SFA,ALL,,conv,%HH_WO_HB%,27

ASEL,S,AREA,,164,,,1   !cooling walls
!SFADELE,all,,CONV
SFA,ALL,,conv,%HH_WO_v%,27
ASEL,S,AREA,,29,,,1   !cooling walls
SFADELE,all,,CONV
SFA,ALL,,conv,%HH_WO_v%,27


!---------------second cover generation---------------------------------

!-----------------------air----board-------------------------

PTXY,(w/2)-(wb2/2),l_c+lf_gc-(lb2/2),(w/2)+(wb2/2),l_c+lf_gc-(lb2/2),(w/2)+(wb2/2),l_c+lf_gc+(lb2/2),(w/2)-(wb2/2),l_c+lf_gc+(lb2/2)        !board
generation
PRISM,thk1+thk2+s_f_h+v_f_w+v_f_h+3.5*hb+c_h,thk1+thk2+s_f_h+v_f_w+v_f_h+3.5*hb+2*c_h
ALLSEL
vclear,all
VSBV,7,25,SEPO,,keep
VSBV,9,26,SEPO,,keep
VSBV,7,27,SEPO,,keep   !becomes 9 air

!-----------------------2 COVER----board-------------------------
allsel
PTXY,(w/2)-(wb2/2),l_c+lf_gc-(lb2/2),(w/2)+(wb2/2),l_c+lf_gc-(lb2/2),(w/2)+(wb2/2),l_c+lf_gc+(lb2/2),(w/2)-(wb2/2),l_c+lf_gc+(lb2/2)        !board
generation
zztemp=thk1+thk2+s_f_h+v_f_w+v_f_h+2.5*hb
PRISM,zztemp+2*c_h+hb,zztemp+2*c_h+2*hb
allsel
```

```
VSBV,7,25,SEPO,,keep
VSBV,10,26,SEPO,,keep
VSBV,7,27,SEPO,,keep !second cover become 10

!-----------------------generating surface squares to calculate cooling rate-------------
PTXY,(w/2)-0.0105-r120,l_c+lf_gc-0.01-r120,(w/2)-0.0105+r120,l_c+lf_gc-0.01-r120,(w/2)-0.0105+r120,l_c+lf_gc-0.01+r120,(w/2)-0.0105-
r120,l_c+lf_gc-0.01+r120,         !board generation
PRISM,zztemp+2*c_h+2*hb,zztemp+2*c_h+3*hb

PTXY,(w/2)-0.0105-r120,l_c+lf_gc-r120,(w/2)-0.0105+r120,l_c+lf_gc-r120,(w/2)-0.0105+r120,l_c+lf_gc+r120,(w/2)-0.0105-
r120,l_c+lf_gc+r120,          !board generation
PRISM,zztemp+2*c_h+2*hb,zztemp+2*c_h+3*hb

PTXY,(w/2)-0.0105-r120,l_c+lf_gc+0.01-r120,(w/2)-0.0105+r120,l_c+lf_gc+0.01-r120,(w/2)-0.0105+r120,l_c+lf_gc+0.01+r120,(w/2)-0.0105-
r120,l_c+lf_gc+0.01+r120,         !board generation
PRISM,zztemp+2*c_h+2*hb,zztemp+2*c_h+3*hb

VGLUE,14,13,7,10    !cubes to cover becomes 18
vdele,15,17,1,1
allsel
VGLUE,9,18,22,25,26,27


VSEL,S,VOLU,,14       !air2
VATT,9
VSEL,S,VOLU,,17       !air
VATT,9

VSEL,S,VOLU,,15       !cover2
VATT,4
VSEL,S,VOLU,,9        !cover
VATT,4
VSEL,S,VOLU,,7        !wire
VATT,7
VSEL,S,VOLU,,10       !wire
VATT,7
VSEL,S,VOLU,,13       !wire
VATT,7

ASEL,S,AREA,,175,,,1   !cover1
SFA,ALL,,conv,%HH_THK%,27
ASEL,S,AREA,,177,,,1   !cover1
SFA,ALL,,conv,%HH_THK%,27
ASEL,S,AREA,,179,,,1   !cover1
SFA,ALL,,conv,%HH_THK%,27
ASEL,S,AREA,,167,,,1   !cover1
SFA,ALL,,conv,%HH_THK%,27

ASEL,S,AREA,,137,,,1   !cover2
SFA,ALL,,conv,%HH_THK%,27
ASEL,S,AREA,,138,,,1   !cover2
```

```
SFA,ALL,,conv,%HH_THK%,27
ASEL,S,AREA,,136,,,1   !cover2
SFA,ALL,,conv,%HH_THK%,27
ASEL,S,AREA,,150,,,1   !cover2
SFA,ALL,,conv,%HH_THK%,27



ASEL,S,AREA,,70,,,1   !air
SFA,ALL,,conv,%HH_THK%,27
ASEL,S,AREA,,76,,,1   !air
SFA,ALL,,conv,%HH_THK%,27
ASEL,S,AREA,,66,,,1   !air
SFA,ALL,,conv,%HH_THK%,27
ASEL,S,AREA,,77,,,1   !air
SFA,ALL,,conv,%HH_THK%,27

!-----------------------Third cover generation---------------------------------------

!-----------------------air----board-------------------------
zztemp=thk1+thk2+s_f_h+v_f_w+v_f_h+2.5*hb
PTXY,(w/2)-(wb2/2),l_c+lf_gc-(lb2/2),(w/2)+(wb2/2),l_c+lf_gc-(lb2/2),(w/2)+(wb2/2),l_c+lf_gc+(lb2/2),(w/2)-(wb2/2),l_c+lf_gc+(lb2/2)        !board
generation
PRISM,zztemp+2*c_h+2*hb,zztemp+3*c_h+2*hb
ALLSEL
VSBV,7,17,SEPO,,keep
VSBV,16,13,SEPO,,keep
VSBV,7,10,SEPO,,keep   !becomes 16 air

!-----------------------COVER----board-------------------------
allsel
PTXY,(w/2)-(wb2/2),l_c+lf_gc-(lb2/2),(w/2)+(wb2/2),l_c+lf_gc-(lb2/2),(w/2)+(wb2/2),l_c+lf_gc+(lb2/2),(w/2)-(wb2/2),l_c+lf_gc+(lb2/2)        !board
generation
PRISM,zztemp+3*c_h+2*hb,zztemp+3*c_h+3*hb
allsel
VSBV,7,17,SEPO,,keep
VSBV,22,13,SEPO,,keep
VSBV,7,10,SEPO,,keep !second cover become 22

!-----------------------generating surface squares to calculate cooling rate-------------
PTXY,(w/2)-0.0105-r120,l_c+lf_gc-0.01-r120,(w/2)-0.0105+r120,l_c+lf_gc-0.01-r120,(w/2)-0.0105+r120,l_c+lf_gc-0.01+r120,(w/2)-0.0105-
r120,l_c+lf_gc-0.01+r120,        !board generation
PRISM,zztemp+3*c_h+3*hb,zztemp+3*c_h+4*hb

PTXY,(w/2)-0.0105-r120,l_c+lf_gc-r120,(w/2)-0.0105+r120,l_c+lf_gc-r120,(w/2)-0.0105+r120,l_c+lf_gc+r120,(w/2)-0.0105-
r120,l_c+lf_gc+r120,        !board generation
PRISM,zztemp+3*c_h+3*hb,zztemp+3*c_h+4*hb

PTXY,(w/2)-0.0105-r120,l_c+lf_gc+0.01-r120,(w/2)-0.0105+r120,l_c+lf_gc+0.01-r120,(w/2)-0.0105+r120,l_c+lf_gc+0.01+r120,(w/2)-0.0105-
r120,l_c+lf_gc+0.01+r120,        !board generation
PRISM,zztemp+3*c_h+3*hb,zztemp+3*c_h+4*hb
```

```
VGLUE,22,23,7,24    !cubes to cover becomes 28
vdele,25,27,1,1
allsel
VGLUE,10,13,17,16,28,15

allsel
VSEL,S,VOLU,,7        !air3
VATT,9
VSEL,S,VOLU,,22       !cover3
VATT,4
VSEL,S,VOLU,,23       !wire
VATT,7
VSEL,S,VOLU,,24       !wire
VATT,7
VSEL,S,VOLU,,25       !wire
VATT,7


ASEL,S,AREA,,193,,,1   !cover3
SFA,ALL,,conv,%HH_THK%,27
ASEL,S,AREA,,192,,,1   !cover3
SFA,ALL,,conv,%HH_THK%,27
ASEL,S,AREA,,191,,,1   !cover3
SFA,ALL,,conv,%HH_THK%,27
ASEL,S,AREA,,196,,,1   !cover3
SFA,ALL,,conv,%HH_THK%,27



ASEL,S,AREA,,100,,,1   !air3
SFA,ALL,,conv,%HH_THK%,27
ASEL,S,AREA,,101,,,1   !air3
SFA,ALL,,conv,%HH_THK%,27
ASEL,S,AREA,,102,,,1   !air3
SFA,ALL,,conv,%HH_THK%,27
ASEL,S,AREA,,106,,,1   !air3
SFA,ALL,,conv,%HH_THK%,27

!++++++++++++++++++++++++++++++generation of fourth board

!----------------------air----board-------------------------
zztemp=thk1+thk2+s_f_h+v_f_w+v_f_h+2.5*hb
PTXY,(w/2)-(wb2/2),l_c+lf_gc-(lb2/2),(w/2)+(wb2/2),l_c+lf_gc-(lb2/2),(w/2)+(wb2/2),l_c+lf_gc+(lb2/2),(w/2)-(wb2/2),l_c+lf_gc+(lb2/2)        !board
generation
PRISM,zztemp+3*c_h+3*hb,zztemp+4*c_h+3*hb
ALLSEL
VSBV,10,24,SEPO,,keep
VSBV,13,25,SEPO,,keep
VSBV,10,23,SEPO,,keep   !becomes 13 air
```

```
!-----------------------COVER----board-------------------------
allsel
PTXY,(w/2)-(wb2/2),l_c+lf_gc-(lb2/2),(w/2)+(wb2/2),l_c+lf_gc-(lb2/2),(w/2)+(wb2/2),l_c+lf_gc+(lb2/2),(w/2)-(wb2/2),l_c+lf_gc+(lb2/2)        !board
generation
PRISM,zztemp+4*c_h+3*hb,zztemp+4*c_h+4*hb
allsel
VSBV,10,24,SEPO,,keep
VSBV,16,25,SEPO,,keep
VSBV,10,23,SEPO,,keep !second cover become 16

!-----------------------generating surface squares to calculate cooling rate-------------
PTXY,(w/2)-0.0105-r120,l_c+lf_gc-0.01-r120,(w/2)-0.0105+r120,l_c+lf_gc-0.01-r120,(w/2)-0.0105+r120,l_c+lf_gc-0.01+r120,(w/2)-0.0105-
r120,l_c+lf_gc-0.01+r120,        !board generation
PRISM,zztemp+4*c_h+4*hb,zztemp+4*c_h+5*hb

PTXY,(w/2)-0.0105-r120,l_c+lf_gc-r120,(w/2)-0.0105+r120,l_c+lf_gc-r120,(w/2)-0.0105+r120,l_c+lf_gc+r120,(w/2)-0.0105-
r120,l_c+lf_gc+r120,         !board generation
PRISM,zztemp+4*c_h+4*hb,zztemp+4*c_h+5*hb

PTXY,(w/2)-0.0105-r120,l_c+lf_gc+0.01-r120,(w/2)-0.0105+r120,l_c+lf_gc+0.01-r120,(w/2)-0.0105+r120,l_c+lf_gc+0.01+r120,(w/2)-0.0105-
r120,l_c+lf_gc+0.01+r120,        !board generation
PRISM,zztemp+4*c_h+4*hb,zztemp+4*c_h+5*hb

VGLUE,26,17,10,16    !cubes to cover becomes30
vdele,27,29,1,1
allsel
VGLUE,24,25,23,30,13,22


VSEL,S,VOLU,,10       !air4
VATT,9
VSEL,S,VOLU,,17       !cover4
VATT,4
VSEL,S,VOLU,,16       !cover3
VATT,4
VSEL,S,VOLU,,26       !wire
VATT,7
VSEL,S,VOLU,,28       !wire
VATT,7
VSEL,S,VOLU,,27       !wire
VATT,7

ASEL,S,AREA,,186,,,1   !cover3
SFA,ALL,,conv,%HH_THK%,27
ASEL,S,AREA,,188,,,1   !cover3
SFA,ALL,,conv,%HH_THK%,27
ASEL,S,AREA,,215,,,1   !cover3
SFA,ALL,,conv,%HH_THK%,27
ASEL,S,AREA,,216,,,1   !cover3
SFA,ALL,,conv,%HH_THK%,27
```

```
ASEL,S,AREA,,225,,,1   !cover4
SFA,ALL,,conv,%HH_THK%,27
ASEL,S,AREA,,226,,,1   !cover4
SFA,ALL,,conv,%HH_THK%,27
ASEL,S,AREA,,224,,,1   !cover4
SFA,ALL,,conv,%HH_THK%,27
ASEL,S,AREA,,227,,,1   !cover4
SFA,ALL,,conv,%HH_THK%,27



ASEL,S,AREA,,111,,,1   !air4
SFA,ALL,,conv,%HH_THK%,27
ASEL,S,AREA,,112,,,1   !air4
SFA,ALL,,conv,%HH_THK%,27
ASEL,S,AREA,,115,,,1   !air4
SFA,ALL,,conv,%HH_THK%,27
ASEL,S,AREA,,116,,,1   !air4
SFA,ALL,,conv,%HH_THK%,27

!++++++++++++++++++++++++++++++ generating fith board

!----------------------air----board-------------------------
zztemp=thk1+thk2+s_f_h+v_f_w+v_f_h+2.5*hb
PTXY,(w/2)-(wb2/2),l_c+lf_gc-(lb2/2),(w/2)+(wb2/2),l_c+lf_gc-(lb2/2),(w/2)+(wb2/2),l_c+lf_gc+(lb2/2),(w/2)-(wb2/2),l_c+lf_gc+(lb2/2)        !board
generation
PRISM,zztemp+4*c_h+4*hb,zztemp+5*c_h+4*hb
ALLSEL
VSBV,13,26,SEPO,,keep
VSBV,22,27,SEPO,,keep
VSBV,13,28,SEPO,,keep   !becomes 22 air

!----------------------COVER----board-------------------------
allsel
PTXY,(w/2)-(wb2/2),l_c+lf_gc-(lb2/2),(w/2)+(wb2/2),l_c+lf_gc-(lb2/2),(w/2)+(wb2/2),l_c+lf_gc+(lb2/2),(w/2)-(wb2/2),l_c+lf_gc+(lb2/2)        !board
generation
PRISM,zztemp+5*c_h+4*hb,zztemp+5*c_h+5*hb
allsel
VSBV,13,26,SEPO,,keep
VSBV,23,27,SEPO,,keep
VSBV,13,28,SEPO,,keep   !becomes 23 cv

!----------------------generating surface squares to calculate cooling rate-------------
PTXY,(w/2)-0.0105-r120,l_c+lf_gc-0.01-r120,(w/2)-0.0105+r120,l_c+lf_gc-0.01-r120,(w/2)-0.0105+r120,l_c+lf_gc-0.01+r120,(w/2)-0.0105-
r120,l_c+lf_gc-0.01+r120,        !board generation
PRISM,zztemp+5*c_h+5*hb,zztemp+5*c_h+6*hb

PTXY,(w/2)-0.0105-r120,l_c+lf_gc-r120,(w/2)-0.0105+r120,l_c+lf_gc-r120,(w/2)-0.0105+r120,l_c+lf_gc+r120,(w/2)-0.0105-
r120,l_c+lf_gc+r120,        !board generation
PRISM,zztemp+5*c_h+5*hb,zztemp+5*c_h+6*hb
```

```
PTXY,(w/2)-0.0105-r120,l_c+lf_gc+0.01-r120,(w/2)-0.0105+r120,l_c+lf_gc+0.01-r120,(w/2)-0.0105+r120,l_c+lf_gc+0.01+r120,(w/2)-0.0105-
r120,l_c+lf_gc+0.01+r120,        !board generation
PRISM,zztemp+5*c_h+5*hb,zztemp+5*c_h+6*hb

VGLUE,13,24,25,23    !cubes to cover becomes32
vdele,29,31,1,1
allsel
VGLUE,26,27,28,32,17,22

allsel
VSEL,S,VOLU,,13       !air5
VATT,9
VSEL,S,VOLU,,23       !cover5
VATT,4
VSEL,S,VOLU,,17       !cover4
VATT,4
VSEL,S,VOLU,,24       !wire
VATT,7
VSEL,S,VOLU,,29       !wire
VATT,7
VSEL,S,VOLU,,25       !wire
VATT,7

allsel
/PSF,conv,hcoef,3,1,on
LPLOT


ASEL,S,AREA,,246,,,1   !cover5
SFA,ALL,,conv,%HH_THK%,27
ASEL,S,AREA,,247,,,1   !cover5
SFA,ALL,,conv,%HH_THK%,27
ASEL,S,AREA,,248,,,1   !cover5
SFA,ALL,,conv,%HH_THK%,27
ASEL,S,AREA,,244,,,1   !cover5
SFA,ALL,,conv,%HH_THK%,27

ASEL,S,AREA,,146,,,1   !air5
SFA,ALL,,conv,%HH_THK%,27
ASEL,S,AREA,,147,,,1   !air5
SFA,ALL,,conv,%HH_THK%,27
ASEL,S,AREA,,148,,,1   !air5
SFA,ALL,,conv,%HH_THK%,27
ASEL,S,AREA,,127,,,1   !air5
SFA,ALL,,conv,%HH_THK%,27

!++++++++++++++++++++++++++++++sixth board generation

!----------------------air----board-------------------------
zztemp=thk1+thk2+s_f_h+v_f_w+v_f_h+2.5*hb
```

```
PTXY,(w/2)-(wb2/2),l_c+lf_gc-(lb2/2),(w/2)+(wb2/2),l_c+lf_gc-(lb2/2),(w/2)+(wb2/2),l_c+lf_gc+(lb2/2),(w/2)-(wb2/2),l_c+lf_gc+(lb2/2)        !board
generation
PRISM,zztemp+5*c_h+5*hb,zztemp+6*c_h+5*hb
ALLSEL
VSBV,22,24,SEPO,,keep
VSBV,26,29,SEPO,,keep
VSBV,22,25,SEPO,,keep   !becomes 26 air

!----------------------COVER----board-------------------------
allsel
PTXY,(w/2)-(wb2/2),l_c+lf_gc-(lb2/2),(w/2)+(wb2/2),l_c+lf_gc-(lb2/2),(w/2)+(wb2/2),l_c+lf_gc+(lb2/2),(w/2)-(wb2/2),l_c+lf_gc+(lb2/2)        !board
generation
PRISM,zztemp+6*c_h+5*hb,zztemp+6*c_h+6*hb
allsel
VSBV,22,24,SEPO,,keep
VSBV,27,29,SEPO,,keep
VSBV,22,25,SEPO,,keep   !becomes 27 cv

!----------------------generating surface squares to calculate cooling rate-------------

PTXY,(w/2)-0.0105-r120,l_c+lf_gc-0.01-r120,(w/2)-0.0105+r120,l_c+lf_gc-0.01-r120,(w/2)-0.0105+r120,l_c+lf_gc-0.01+r120,(w/2)-0.0105-
r120,l_c+lf_gc-0.01+r120,        !board generation
PRISM,zztemp+6*c_h+6*hb,zztemp+6*c_h+7*hb

PTXY,(w/2)-0.0105-r120,l_c+lf_gc-r120,(w/2)-0.0105+r120,l_c+lf_gc-r120,(w/2)-0.0105+r120,l_c+lf_gc+r120,(w/2)-0.0105-
r120,l_c+lf_gc+r120,        !board generation
PRISM,zztemp+6*c_h+6*hb,zztemp+6*c_h+7*hb

PTXY,(w/2)-0.0105-r120,l_c+lf_gc+0.01-r120,(w/2)-0.0105+r120,l_c+lf_gc+0.01-r120,(w/2)-0.0105+r120,l_c+lf_gc+0.01+r120,(w/2)-0.0105-
r120,l_c+lf_gc+0.01+r120,        !board generation
PRISM,zztemp+6*c_h+6*hb,zztemp+6*c_h+7*hb

VGLUE,30,28,22,27    !cubes to cover becomes34
vdele,31,33,1,1
allsel
VGLUE,29,24,25,26,23,34

allsel
VSEL,S,VOLU,,22       !air6
VATT,9
VSEL,S,VOLU,,27       !cover6
VATT,4
VSEL,S,VOLU,,23       !cover5
VATT,4
VSEL,S,VOLU,,28       !wire
VATT,7
VSEL,S,VOLU,,31       !wire
VATT,7
VSEL,S,VOLU,,30       !wire
VATT,7
```

```
allsel
/PSF,conv,hcoef,3,1,on
LPLOT


ASEL,S,AREA,,271,,,1   !cover6
SFA,ALL,,conv,%HH_THK%,27
ASEL,S,AREA,,272,,,1   !cover6
SFA,ALL,,conv,%HH_THK%,27
ASEL,S,AREA,,273,,,1   !cover6
SFA,ALL,,conv,%HH_THK%,27
ASEL,S,AREA,,269,,,1   !cover6
SFA,ALL,,conv,%HH_THK%,27

ASEL,S,AREA,,178,,,1   !air6
SFA,ALL,,conv,%HH_THK%,27
ASEL,S,AREA,,180,,,1   !air6
SFA,ALL,,conv,%HH_THK%,27
ASEL,S,AREA,,185,,,1   !air6
SFA,ALL,,conv,%HH_THK%,27
ASEL,S,AREA,,187,,,1   !air6
SFA,ALL,,conv,%HH_THK%,27

!++++++++++++++++++++++++++++++seventh board generation

!-----------------------air----board-------------------------
zztemp=thk1+thk2+s_f_h+v_f_w+v_f_h+2.5*hb
PTXY,(w/2)-(wb2/2),l_c+lf_gc-(lb2/2),(w/2)+(wb2/2),l_c+lf_gc-(lb2/2),(w/2)+(wb2/2),l_c+lf_gc+(lb2/2),(w/2)-(wb2/2),l_c+lf_gc+(lb2/2)        !board
generation
PRISM,zztemp+6*c_h+6*hb,zztemp+7*c_h+6*hb
ALLSEL
VSBV,24,28,SEPO,,keep
VSBV,25,31,SEPO,,keep
VSBV,24,30,SEPO,,keep   !becomes 25 air

!-----------------------COVER----board-------------------------
allsel
PTXY,(w/2)-(wb2/2),l_c+lf_gc-(lb2/2),(w/2)+(wb2/2),l_c+lf_gc-(lb2/2),(w/2)+(wb2/2),l_c+lf_gc+(lb2/2),(w/2)-(wb2/2),l_c+lf_gc+(lb2/2)        !board
generation
PRISM,zztemp+7*c_h+6*hb,zztemp+7*c_h+7*hb
allsel
VSBV,24,28,SEPO,,keep
VSBV,26,31,SEPO,,keep
VSBV,24,30,SEPO,,keep   !becomes 26 cv

!-----------------------generating surface squares to calculate cooling rate-------------

PTXY,(w/2)-0.0105-r120,l_c+lf_gc-0.01-r120,(w/2)-0.0105+r120,l_c+lf_gc-0.01-r120,(w/2)-0.0105+r120,l_c+lf_gc-0.01+r120,(w/2)-0.0105-
r120,l_c+lf_gc-0.01+r120,        !board generation
PRISM,zztemp+7*c_h+7*hb,zztemp+7*c_h+8*hb
```

```
PTXY,(w/2)-0.0105-r120,l_c+lf_gc-r120,(w/2)-0.0105+r120,l_c+lf_gc-r120,(w/2)-0.0105+r120,l_c+lf_gc+r120,(w/2)-0.0105-
r120,l_c+lf_gc+r120,        !board generation
PRISM,zztemp+7*c_h+7*hb,zztemp+7*c_h+8*hb

PTXY,(w/2)-0.0105-r120,l_c+lf_gc+0.01-r120,(w/2)-0.0105+r120,l_c+lf_gc+0.01-r120,(w/2)-0.0105+r120,l_c+lf_gc+0.01+r120,(w/2)-0.0105-
r120,l_c+lf_gc+0.01+r120,        !board generation
PRISM,zztemp+7*c_h+7*hb,zztemp+7*c_h+8*hb

VGLUE,32,29,24,26    !cubes to cover becomes36
vdele,33,35,1,1
allsel
VGLUE,28,31,30,27,25,36

allsel
VSEL,S,VOLU,,24       !air7
VATT,9
VSEL,S,VOLU,,29       !cover7
VATT,4
VSEL,S,VOLU,,26       !cover6
VATT,4
VSEL,S,VOLU,,32       !wire
VATT,7
VSEL,S,VOLU,,34       !wire
VATT,7
VSEL,S,VOLU,,33       !wire
VATT,7

allsel
/PSF,conv,hcoef,3,1,on
LPLOT


ASEL,S,AREA,,268,,,1   !cover6
SFA,ALL,,conv,%HH_THK%,27
ASEL,S,AREA,,199,,,1   !cover6
SFA,ALL,,conv,%HH_THK%,27
ASEL,S,AREA,,270,,,1   !cover6
SFA,ALL,,conv,%HH_THK%,27
ASEL,S,AREA,,200,,,1   !cover6
SFA,ALL,,conv,%HH_THK%,27

ASEL,S,AREA,,299,,,1   !cover7
SFA,ALL,,conv,%HH_THK%,27
ASEL,S,AREA,,300,,,1   !cover7
SFA,ALL,,conv,%HH_THK%,27
ASEL,S,AREA,,301,,,1   !cover7
SFA,ALL,,conv,%HH_THK%,27
ASEL,S,AREA,,302,,,1   !cover7
SFA,ALL,,conv,%HH_THK%,27

ASEL,S,AREA,,201,,,1   !air7
```

```
SFA,ALL,,conv,%HH_THK%,27
ASEL,S,AREA,,205,,,1   !air7
SFA,ALL,,conv,%HH_THK%,27
ASEL,S,AREA,,207,,,1   !air7
SFA,ALL,,conv,%HH_THK%,27
ASEL,S,AREA,,208,,,1   !air7
SFA,ALL,,conv,%HH_THK%,27

!++++++++++++++++++++++++++++++eighth board

!-----------------------air----board-------------------------
zztemp=thk1+thk2+s_f_h+v_f_w+v_f_h+2.5*hb
PTXY,(w/2)-(wb2/2),l_c+lf_gc-(lb2/2),(w/2)+(wb2/2),l_c+lf_gc-(lb2/2),(w/2)+(wb2/2),l_c+lf_gc+(lb2/2),(w/2)-(wb2/2),l_c+lf_gc+(lb2/2)        !board
generation
PRISM,zztemp+7*c_h+7*hb,zztemp+8*c_h+7*hb
ALLSEL
VSBV,25,32,SEPO,,keep
VSBV,27,34,SEPO,,keep
VSBV,25,33,SEPO,,keep   !becomes 27 air

!-----------------------COVER----board-------------------------
allsel
PTXY,(w/2)-(wb2/2),l_c+lf_gc-(lb2/2),(w/2)+(wb2/2),l_c+lf_gc-(lb2/2),(w/2)+(wb2/2),l_c+lf_gc+(lb2/2),(w/2)-(wb2/2),l_c+lf_gc+(lb2/2)        !board
generation
PRISM,zztemp+8*c_h+7*hb,zztemp+8*c_h+8*hb
allsel
VSBV,25,32,SEPO,,keep
VSBV,28,34,SEPO,,keep
VSBV,25,33,SEPO,,keep   !becomes 28 cv

!-----------------------generating surface squares to calculate cooling rate-------------

PTXY,(w/2)-0.0105-r120,l_c+lf_gc-0.01-r120,(w/2)-0.0105+r120,l_c+lf_gc-0.01-r120,(w/2)-0.0105+r120,l_c+lf_gc-0.01+r120,(w/2)-0.0105-
r120,l_c+lf_gc-0.01+r120,         !board generation
PRISM,zztemp+8*c_h+8*hb,zztemp+8*c_h+9*hb

PTXY,(w/2)-0.0105-r120,l_c+lf_gc-r120,(w/2)-0.0105+r120,l_c+lf_gc-r120,(w/2)-0.0105+r120,l_c+lf_gc+r120,(w/2)-0.0105-
r120,l_c+lf_gc+r120,         !board generation
PRISM,zztemp+8*c_h+8*hb,zztemp+8*c_h+9*hb

PTXY,(w/2)-0.0105-r120,l_c+lf_gc+0.01-r120,(w/2)-0.0105+r120,l_c+lf_gc+0.01-r120,(w/2)-0.0105+r120,l_c+lf_gc+0.01+r120,(w/2)-0.0105-
r120,l_c+lf_gc+0.01+r120,         !board generation
PRISM,zztemp+8*c_h+8*hb,zztemp+8*c_h+9*hb

VGLUE,31,30,25,28    !cubes to cover becomes38
vdele,35,37,1,1
allsel
VGLUE,32,34,33,29,27,38

allsel
VSEL,S,VOLU,,28       !air8
```

```
VATT,9
VSEL,S,VOLU,,30       !cover8
VATT,4
VSEL,S,VOLU,,25       !cover7
VATT,4
VSEL,S,VOLU,,31       !wire
VATT,7
VSEL,S,VOLU,,36       !wire
VATT,7
VSEL,S,VOLU,,35       !wire
VATT,7

allsel
/PSF,conv,hcoef,3,1,on
LPLOT


ASEL,S,AREA,,238,,,1   !cover7
SFA,ALL,,conv,%HH_THK%,27
ASEL,S,AREA,,239,,,1   !cover7
SFA,ALL,,conv,%HH_THK%,27
ASEL,S,AREA,,240,,,1   !cover7
SFA,ALL,,conv,%HH_THK%,27
ASEL,S,AREA,,241,,,1   !cover7
SFA,ALL,,conv,%HH_THK%,27

ASEL,S,AREA,,324,,,1   !cover8
SFA,ALL,,conv,%HH_THK%,27
ASEL,S,AREA,,325,,,1   !cover8
SFA,ALL,,conv,%HH_THK%,27
ASEL,S,AREA,,326,,,1   !cover8
SFA,ALL,,conv,%HH_THK%,27
ASEL,S,AREA,,327,,,1   !cover8
SFA,ALL,,conv,%HH_THK%,27

ASEL,S,AREA,,263,,,1   !air8
SFA,ALL,,conv,%HH_THK%,27
ASEL,S,AREA,,264,,,1   !air8
SFA,ALL,,conv,%HH_THK%,27
ASEL,S,AREA,,267,,,1   !air8
SFA,ALL,,conv,%HH_THK%,27
ASEL,S,AREA,,269,,,1   !air8
SFA,ALL,,conv,%HH_THK%,27


ASEL,S,AREA,,338,,,1        !60 location
!SFA,ALL,,RDSF,0.182,1
SFA,ALL,,conv,%HH_C_V%,27
ASEL,S,AREA,,339,,,1
!SFA,ALL,,RDSF,0.182,1
SFA,ALL,,conv,%HH_C_V%,27
```

```
ASEL,S,AREA,,342,,,1   !90 location
!SFA,ALL,,RDSF,0.182,1
SFA,ALL,,conv,%HH_C_V%,27
ASEL,S,AREA,,343,,,1
!SFA,ALL,,RDSF,0.182,1
SFA,ALL,,conv,%HH_C_V%,27

ASEL,S,AREA,,340,,,1   !120 location
!SFA,ALL,,RDSF,0.182,1
SFA,ALL,,conv,%HH_C_V%,27
ASEL,S,AREA,,341,,,1
!SFA,ALL,,RDSF,0.182,1
SFA,ALL,,conv,%HH_C_V%,27



!---------convective coefficient plus heat flux is consider for board and fixture surfaces------

! HF=Costant heat flux + h * (T-Tambient)    !!!!(h=convective coefficient that is function
                                    !!!! of Temperature and time)

!functions %Hh_fx_tf% and %Hh_bd_tf% should be updated every time heat flux is change

!convective coefficient need be updated when ambient temperature changes too
!to do so open menu:
!      parameters
!           functions
!                define/edit
! in that order, then open functions Hh_fx_tf and Hh_bd_tf and modify as desire.

ASEL,S,AREA,,74,,,1   !fix_board
SFA,ALL,,HFLUX,%Hh_fx_tf%


ASEL,S,AREA,,73,,,1          !60 location
SFA,ALL,,HFLUX,33319.81678

ASEL,S,AREA,,69,,,1          !90 location
SFA,ALL,,HFLUX,33319.81678

ASEL,S,AREA,,65,,,1          !120 location
SFA,ALL,,HFLUX,33319.81678


ASEL,S,AREA,,334,,,1   !60 location
SFA,ALL,,HFLUX,%Hh_bd_tf%

                !90 location
ASEL,S,AREA,,332,,,1
SFA,ALL,,HFLUX,%Hh_bd_tf%
```

```
                !120 location
ASEL,S,AREA,,330,,,1
SFA,ALL,,HFLUX,%Hh_bd_tf%

ASEL,S,AREA,,335,,,1   !cover location

SFA,ALL,,HFLUX,%Hh_bd_tf%

/PSF,conv,hcoef,3,1,on
LPLOT

!-----------------------------------------------------------meshing-------------------------------------------------------

ET,1,SOLID90

MSHAPE,1,3D                !To specify element shapes
MSHKEY,0                   !Specifies whether free meshing or mapped meshing

!+++NOTE select only walls of chamber and try coarse mesh 10 use comand "vmesh,all" after selecting++++++++++++++

SMRTSIZE,10                !SIZLVL,FAC,EXPND,TRANS,ANGL,ANGH,GRATIO,SMHLC,SMANC,MXITR,SPRX   !Specifies meshing
parameters for automatic (smart) element sizing.
VSEL,none
vsel,s,volu,,3,4,1,1
vsel,a,volu,,19,,,
VMESH,all

!+++select fixture support then stablish smart size 7 and use comand "vmesh,all" after selecting ++++++++++++++
SMRTSIZE,7                 !SIZLVL,FAC,EXPND,TRANS,ANGL,ANGH,GRATIO,SMHLC,SMANC,MXITR,SPRX   !Specifies meshing
parameters for automatic (smart) element sizing.
vsel,none
vsel,a,volu,,1,,,
vsel,a,volu,,5,,,
vsel,a,volu,,8,,,
VMESH,all


!+++NOTE select solder+wires+board+fixture+velcro+cover ++++++++++++++
SMRTSIZE,5                 !SIZLVL,FAC,EXPND,TRANS,ANGL,ANGH,GRATIO,SMHLC,SMANC,MXITR,SPRX   !Specifies meshing
parameters for automatic (smart) element sizing.
vsel,none
vsel,s,volu,,3,5,1,1
vsel,a,volu,,19,,,
vsel,a,volu,,1,,,
vsel,a,volu,,8,,,
vsel,inve,volu
VMESH,all

FINISH
/SOLU
```

```
TUNIF, 28.7
ANTYPE,TRANSIEnt,new !Antype, Status, LDSTEP, SUBSTEP, Action       !Specifies the analysis type and restart status.
TIME,15
KBC,1              !Specifies NO ramp loading within a load step.

SOLCONTROL,on
DELTIM,2.5,2.5,5,off
NEQIT,30
ALLSEL
SAVE,heating                    !Saves all current database information
OUTRES,ALL,ALL
/OUTPUT,heating,txt
SOLVE
FINISH


/post1

FILE,heating,rth   !sets results file to heating.rth
set,last          !sets results to last time that should be 5,15, or 30s

nSEL,all,,,,,,1
*VGET,TEMP_heat,NODE,all,temp   !saves last results to use as initial conditions
                        !for cooling
FINISH

!**********************COOLING ANALYSIS START HERE***********************************

/FILNAME,cooling,1



/PREP7

allsel

VSEL,NONE
NSEL,none

VSEL,s,volu,,3
VSEL,a,volu,,4
VSEL,a,volu,,19

vsel,inve,volu,

VGEN,1,all,,,,-0.5*(l_c+l_h),,,,1


allsel
```

```
/PSF,conv,hcoef,3,1,ON
LPLOT

!*********************************NOTE*****************************************

!****wherever the tables starting by "%HRC" are locate,
!the convective coefficient is considered as:
!
!hT= h_conv + h_radiation, where h radiation is considere as:
!       E*S*(T+T_environment)*(T^2+T_environment^2)
!where:
!      E is emissivity, S ->Stefan-Boltzmann constant, and T surface temperature
!Temperature are absolute Temperatures
!  Both coefficients (h_conv and h_radiation) are functions of temperature...
! and time

!*********************end Note************************************************

!-------------------UPDATING convective coefficient at surfaces

!+++++++++++++++modify top surface board+++++++++++++++++
ASEL,S,AREA,,335,,,1      !BOARD
SFADELE,all,,RDSF
SFADELE,all,,hflux
!SFA,ALL,,RDSF,0.9,2
!SFA,ALL,,conv,%HC_BD_T%,28.7
SFA,ALL,,conv,%HRC_BD_T%,28.7

ASEL,S,AREA,,334,,,1      !120PIN
SFADELE,all,,RDSF
SFADELE,all,,hflux
SFADELE,all,,conv
!SFA,ALL,,RDSF,0.9,2       !E=1, ENCLOSURE1,--lead gray oxidized--
!SFA,ALL,,conv,%HC_BD_T%,28.7
SFA,ALL,,conv,%HRC_BD_T%,28.7

ASEL,S,AREA, ,332,,,1      !90PIN
SFADELE,all,,RDSF
SFADELE,all,,hflux
SFADELE,all,,conv
!SFA,ALL,,RDSF,0.9,2       !E=1, ENCLOSURE1,-----CHECK E----
!SFA,ALL,,conv,%HC_BD_T%,28.7
SFA,ALL,,conv,%HRC_BD_T%,28.7

ASEL,S,AREA, ,330,,,1      !60 PIN
SFADELE,all,,RDSF
SFADELE,all,,hflux
!SFA,ALL,,RDSF,0.9,2       !E=1, ENCLOSURE1,-----CHECK E----
!SFA,ALL,,conv,%HC_BD_T%,28.7
SFA,ALL,,conv,%HRC_BD_T%,28.7
```

```
!-------------------------ELECTRIC WIRE-------------------------
!60
ASEL,S,AREA,,73,,,1   !TIP
SFADELE,all,,hflux
SFA,ALL,,conv,%HRC_PN_T%,28.7

ASEL,S,AREA,,69,,,1   ! TIP 90 location
SFADELE,all,,hflux
SFA,ALL,,conv,%HRC_PN_T%,28.7

ASEL,S,AREA,,65,,,1   ! TIP 120 location
SFADELE,all,,hflux
SFA,ALL,,conv,%HRC_PN_T%,28.7

ASEL,S,AREA,,338,,,1        !60 location
SFA,ALL,,conv,%HRC_C_V%,28.7
ASEL,S,AREA,,339,,,1
SFA,ALL,,conv,%HRC_C_V%,28.7
ASEL,S,AREA,,342,,,1   !90 location
SFA,ALL,,conv,%HRC_C_V%,28.7
ASEL,S,AREA,,343,,,1
SFA,ALL,,conv,%HRC_C_V%,28.7
ASEL,S,AREA,,340,,,1   !120 location
SFA,ALL,,conv,%HRC_C_V%,28.7
ASEL,S,AREA,,341,,,1
SFA,ALL,,conv,%HRC_C_V%,28.7


ASEL,S,AREA,,74,,,1   !fix_board
SFADELE,all,,RDSF
SFADELE,all,,hflux
SFA,ALL,,conv,%HRC_FX_T%,28.7
ASEL,S,AREA,,90,91,,1
SFA,ALL,,conv,%HC_THK%,28.7
ASEL,S,AREA,,48,,,1
SFA,ALL,,conv,%HC_THK%,28.7
ASEL,S,AREA,,85,,,1
SFA,ALL,,conv,%HC_THK%,28.7
ASEL,S,AREA,,24,,,1
SFA,ALL,,conv,%HC_FX_B%,28.7

ASEL,S,AREA,,9,12,1,1   !brd
SFA,ALL,,conv,%HC_THK%,28.7
ASEL,S,AREA,,78,79,1,1   !Velcro
SFA,ALL,,conv,%HC_THK%,28.7
ASEL,S,AREA,,75,,,1   !Velcro
SFA,ALL,,conv,%HC_THK%,28.7
ASEL,S,AREA,,46,,,1   !Velcro
SFA,ALL,,conv,%HC_THK%,28.7

ASEL,S,AREA,,175,,,1   !cover1
```

```
SFA,ALL,,conv,%HC_THK%,28.7
ASEL,S,AREA,,177,,,1   !cover1
SFA,ALL,,conv,%HC_THK%,28.7
ASEL,S,AREA,,179,,,1   !cover1
SFA,ALL,,conv,%HC_THK%,28.7
ASEL,S,AREA,,167,,,1   !cover1
SFA,ALL,,conv,%HC_THK%,28.7

ASEL,S,AREA,,137,,,1   !cover2
SFA,ALL,,conv,%HC_THK%,28.7
ASEL,S,AREA,,138,,,1   !cover2
SFA,ALL,,conv,%HC_THK%,28.7
ASEL,S,AREA,,136,,,1   !cover2
SFA,ALL,,conv,%HC_THK%,28.7
ASEL,S,AREA,,150,,,1   !cover2
SFA,ALL,,conv,%HC_THK%,28.7

ASEL,S,AREA,,202,204,1,1   !air1
SFA,ALL,,conv,%HC_THK%,28.7
ASEL,S,AREA,,197,,,1   !air1
SFA,ALL,,conv,%HC_THK%,28.7

ASEL,S,AREA,,70,,,1   !air2
SFA,ALL,,conv,%HC_THK%,28.7
ASEL,S,AREA,,76,,,1   !air2
SFA,ALL,,conv,%HC_THK%,28.7
ASEL,S,AREA,,66,,,1   !air2
SFA,ALL,,conv,%HC_THK%,28.7
ASEL,S,AREA,,77,,,1   !air2
SFA,ALL,,conv,%HC_THK%,28.7

ASEL,S,AREA,,215,,,1   !cover3
SFA,ALL,,conv,%HC_THK%,28.7
ASEL,S,AREA,,216,,,1   !cover3
SFA,ALL,,conv,%HC_THK%,28.7
ASEL,S,AREA,,188,,,1   !cover3
SFA,ALL,,conv,%HC_THK%,28.7
ASEL,S,AREA,,186,,,1   !cover3
SFA,ALL,,conv,%HC_THK%,28.7



ASEL,S,AREA,,100,,,1   !air3
SFA,ALL,,conv,%HC_THK%,28.7
ASEL,S,AREA,,101,,,1   !air3
SFA,ALL,,conv,%HC_THK%,28.7
ASEL,S,AREA,,102,,,1   !air3
SFA,ALL,,conv,%HC_THK%,28.7
ASEL,S,AREA,,106,,,1   !air3
SFA,ALL,,conv,%HC_THK%,28.7
```

```
ASEL,S,AREA,,226,,,1   !cover4
SFA,ALL,,conv,%HC_THK%,28.7
ASEL,S,AREA,,225,,,1   !cover4
SFA,ALL,,conv,%HC_THK%,28.7
ASEL,S,AREA,,224,,,1   !cover4
SFA,ALL,,conv,%HC_THK%,28.7
ASEL,S,AREA,,227,,,1   !cover4
SFA,ALL,,conv,%HC_THK%,28.7



ASEL,S,AREA,,115,,,1   !air4
SFA,ALL,,conv,%HC_THK%,28.7
ASEL,S,AREA,,116,,,1   !air4
SFA,ALL,,conv,%HC_THK%,28.7
ASEL,S,AREA,,111,,,1   !air4
SFA,ALL,,conv,%HC_THK%,28.7
ASEL,S,AREA,,112,,,1   !air4
SFA,ALL,,conv,%HC_THK%,28.7


ASEL,S,AREA,,246,,,1   !cover5
SFA,ALL,,conv,%HC_THK%,28.7
ASEL,S,AREA,,247,,,1   !cover5
SFA,ALL,,conv,%HC_THK%,28.7
ASEL,S,AREA,,248,,,1   !cover5
SFA,ALL,,conv,%HC_THK%,28.7
ASEL,S,AREA,,244,,,1   !cover5
SFA,ALL,,conv,%HC_THK%,28.7

ASEL,S,AREA,,146,,,1   !air5
SFA,ALL,,conv,%HC_THK%,28.7
ASEL,S,AREA,,147,,,1   !air5
SFA,ALL,,conv,%HC_THK%,28.7
ASEL,S,AREA,,148,,,1   !air5
SFA,ALL,,conv,%HC_THK%,28.7
ASEL,S,AREA,,127,,,1   !air5
SFA,ALL,,conv,%HC_THK%,28.7

ASEL,S,AREA,,178,,,1   !air6
SFA,ALL,,conv,%HC_THK%,28.7
ASEL,S,AREA,,180,,,1   !air6
SFA,ALL,,conv,%HC_THK%,28.7
ASEL,S,AREA,,185,,,1   !air6
SFA,ALL,,conv,%HC_THK%,28.7
ASEL,S,AREA,,187,,,1   !air6
SFA,ALL,,conv,%HC_THK%,28.7

ASEL,S,AREA,,268,,,1   !cover6
SFA,ALL,,conv,%HC_THK%,28.7
ASEL,S,AREA,,199,,,1   !cover6
```

```
SFA,ALL,,conv,%HC_THK%,28.7
ASEL,S,AREA,,270,,,1   !cover6
SFA,ALL,,conv,%HC_THK%,28.7
ASEL,S,AREA,,200,,,1   !cover6
SFA,ALL,,conv,%HC_THK%,28.7

ASEL,S,AREA,,201,,,1   !air7
SFA,ALL,,conv,%HC_THK%,28.7
ASEL,S,AREA,,205,,,1   !air7
SFA,ALL,,conv,%HC_THK%,28.7
ASEL,S,AREA,,207,,,1   !air7
SFA,ALL,,conv,%HC_THK%,28.7
ASEL,S,AREA,,208,,,1   !air7
SFA,ALL,,conv,%HC_THK%,28.7

ASEL,S,AREA,,238,,,1   !cover7
SFA,ALL,,conv,%HC_THK%,28.7
ASEL,S,AREA,,239,,,1   !cover7
SFA,ALL,,conv,%HC_THK%,28.7
ASEL,S,AREA,,240,,,1   !cover7
SFA,ALL,,conv,%HC_THK%,28.7
ASEL,S,AREA,,241,,,1   !cover7
SFA,ALL,,conv,%HC_THK%,28.7

ASEL,S,AREA,,324,,,1   !cover8
SFA,ALL,,conv,%HC_THK%,28.7
ASEL,S,AREA,,325,,,1   !cover8
SFA,ALL,,conv,%HC_THK%,28.7
ASEL,S,AREA,,326,,,1   !cover8
SFA,ALL,,conv,%HC_THK%,28.7
ASEL,S,AREA,,327,,,1   !cover8
SFA,ALL,,conv,%HC_THK%,28.7

ASEL,S,AREA,,263,,,1   !air8
SFA,ALL,,conv,%HC_THK%,28.7
ASEL,S,AREA,,264,,,1   !air8
SFA,ALL,,conv,%HC_THK%,28.7
ASEL,S,AREA,,267,,,1   !air8
SFA,ALL,,conv,%HC_THK%,28.7
ASEL,S,AREA,,269,,,1   !air8
SFA,ALL,,conv,%HC_THK%,28.7

ASEL,S,AREA,,56,57,,1          !V SURFACE FIXTURE (MIGHT NOT BE ADDED)
!SFA,ALL,,RDSF,0.37,1          !E=0.37, Mylar 0.0625mm thick
SFA,ALL,,conv,%HC_V_V%,28.7
ASEL,S,AREA,,60,61,,1
!SFA,ALL,,RDSF,0.37,1
SFA,ALL,,conv,%HC_V_V%,28.7
ASEL,S,AREA,,58,59,,1
SFA,ALL,,conv,%HC_ANG%,28.7
```

```
ASEL,S,AREA,,44,45,,1                !other V SURFACE FIXTURE (MIGHT NOT BE ADDED)
!SFA,ALL,,RDSF,0.37,1                !E=0.37, Mylar 0.0625mm thick
SFA,ALL,,conv,%HC_V_V%,28.7
ASEL,S,AREA,,4,5,,1
!SFA,ALL,,RDSF,0.37,1
SFA,ALL,,conv,%HC_V_V%,28.7
ASEL,S,AREA,,43,,,1
SFA,ALL,,conv,%HC_ANG%,28.7
ASEL,S,AREA,,6,,,1
SFA,ALL,,conv,%HC_ANG%,28.7



ASEL,S,AREA,,39,40,,1
SFA,ALL,,conv,%HC_V_hV%,28.7
ASEL,S,AREA,,17,,,1
SFA,ALL,,conv,%HC_V_hV%,28.7
ASEL,S,AREA,,84,,,1
SFA,ALL,,conv,%HC_V_hV%,28.7
ASEL,S,AREA,,97,,,1
SFA,ALL,,conv,%HC_V_h_b%,28.7

ASEL,S,AREA,,37,38,,1
SFA,ALL,,conv,%HC_V_hV%,28.7
ASEL,S,AREA,,41,42,,1
SFA,ALL,,conv,%HC_V_hV%,28.7
ASEL,S,AREA,,86,,,1
SFA,ALL,,conv,%HC_V_h_t%,28.7
ASEL,S,AREA,,88,89,,1
SFA,ALL,,conv,%HC_V_hV%,28.7
ASEL,S,AREA,,94,95,,1
SFA,ALL,,conv,%HC_V_hV%,28.7

allsel
/PSF,conv,hcoef,3,1,ON
LPLOT

FINISH
/SOLU

allsel

icdele
*DO,JJ,1,660394              !660394 should be modify to the right total nodes
  IC,JJ,TEMP,TEMP_heat(JJ)   !Specifies initial conditions at nodes.
*ENDDO

ANTYPE,TRANSIEnt,new   !Specifies the analysis type and restart status.
TIME,100               !solution for 100 seconds
KBC,1                  !Specifies NO ramp loading within a load step.
```

```
SOLCONTROL,on
DELTIM,2,2,20,off       !start with a 2 seconds time using minimum increment of 2s....
NEQIT,40                !and maximum of 20s
ALLSEL

SAVE,cooling                    !Saves all current database information...
OUTRES,ALL,ALL                  !to restart analysis
/OUTPUT,cooling,txt             !all solution info saved at this file "cooling.txt"
SOLVE
FINISH

! In order to determine the average temperatures in the cover surfaces at the solder joint positios,
!the areas for every solder position should be selected using the command "asel", then the nodes
!forming this area should be determine and listed as shown in the next loops to determine average temperatures

!*****************NOTE: nodes numbers change with changes in geometries and mesh size**************


!++++++++++++++++++++++Average temperatures determination at every surface at solder joint positions++++++++++++++++++++

*DIM,TMP_AVG_60,,11       ! wherever 11 is found, means the number of substeps in the solution file
*DIM,TMP_AVG_90,,11       !appropiate solution file should be load to determine
*DIM,TMP_AVG_120,,11      !the average temperatures needed (cooling or heating results)
*DIM,TMP_AVG_mx,,11

*DO,II,1,11       ! For II = 1 to 3:
 set,1,II

*GET,TEMP_60,NODE,440892,temp   !440892 modify for node at maximum temperature
*SET,TMP_AVG_mx(II),TEMP_60

!!!!++++++++60 PIN
*SET,TMP_AVG_60(II),0
*SET,NODE_SUM,0

  *GET,TEMP_60,NODE,50388,temp
  *SET,NODE_SUM,NODE_SUM+1
  *SET,TMP_AVG_60(II),TMP_AVG_60(II)+TEMP_60

  *GET,TEMP_60,NODE,50387,temp
  *SET,NODE_SUM,NODE_SUM+1
  *SET,TMP_AVG_60(II),TMP_AVG_60(II)+TEMP_60


*DO,KK,50397,50400
  *GET,TEMP_60,NODE,KK,temp
  *SET,NODE_SUM,NODE_SUM+1
  *SET,TMP_AVG_60(II),TMP_AVG_60(II)+TEMP_60
*ENDDO

*DO,KK,58033,58062
```

```
  *GET,TEMP_60,NODE,KK,temp
  *SET,NODE_SUM,NODE_SUM+1
  *SET,TMP_AVG_60(II),TMP_AVG_60(II)+TEMP_60
*ENDDO

*DO,KK,58271,58298

  *GET,TEMP_60,NODE,KK,temp
  *SET,NODE_SUM,NODE_SUM+1
  *SET,TMP_AVG_60(II),TMP_AVG_60(II)+TEMP_60
*ENDDO

*DO,KK,442782,442985
  *GET,TEMP_60,NODE,KK,temp
  *SET,NODE_SUM,NODE_SUM+1
  *SET,TMP_AVG_60(II),TMP_AVG_60(II)+TEMP_60
*ENDDO

*SET,TMP_AVG_60(II),TMP_AVG_60(II)/NODE_SUM

!!!!++++++++90 PIN
*SET,TMP_AVG_90(II),0
*SET,NODE_SUM,0

*DO,KK,50389,50394
  *GET,TEMP_90,NODE,KK,temp
  *SET,NODE_SUM,NODE_SUM+1
  *SET,TMP_AVG_90(II),TMP_AVG_90(II)+TEMP_90
*ENDDO

*DO,KK,58093,58120
  *GET,TEMP_90,NODE,KK,temp
  *SET,NODE_SUM,NODE_SUM+1
  *SET,TMP_AVG_90(II),TMP_AVG_90(II)+TEMP_90
*ENDDO

*DO,KK,58151,58180
  *GET,TEMP_90,NODE,KK,temp
  *SET,NODE_SUM,NODE_SUM+1
  *SET,TMP_AVG_90(II),TMP_AVG_90(II)+TEMP_90
*ENDDO

*DO,KK,442986,443185
  *GET,TEMP_90,NODE,KK,temp
  *SET,NODE_SUM,NODE_SUM+1
  *SET,TMP_AVG_90(II),TMP_AVG_90(II)+TEMP_90
*ENDDO

*SET,TMP_AVG_90(II),TMP_AVG_90(II)/NODE_SUM

!!!!++++++++120 PIN
```

```
*SET,TMP_AVG_120(II),0
*SET,NODE_SUM,0

*GET,TEMP_120,NODE,50395,temp
*SET,NODE_SUM,NODE_SUM+1
*SET,TMP_AVG_120(II),TMP_AVG_120(II)+TEMP_120
*GET,TEMP_120,NODE,50396,temp
*SET,NODE_SUM,NODE_SUM+1
*SET,TMP_AVG_120(II),TMP_AVG_120(II)+TEMP_120


*DO,KK,50341,50344
  *GET,TEMP_120,NODE,KK,temp
  *SET,NODE_SUM,NODE_SUM+1
  *SET,TMP_AVG_120(II),TMP_AVG_120(II)+TEMP_120
*ENDDO

*DO,KK,56825,56838
  *GET,TEMP_120,NODE,KK,temp
  *SET,NODE_SUM,NODE_SUM+1
  *SET,TMP_AVG_120(II),TMP_AVG_120(II)+TEMP_120
*ENDDO

*DO,KK,56854,56860
  *GET,TEMP_120,NODE,KK,temp
  *SET,NODE_SUM,NODE_SUM+1
  *SET,TMP_AVG_120(II),TMP_AVG_120(II)+TEMP_120
*ENDDO

*DO,KK,56876,56882
  *GET,TEMP_120,NODE,KK,temp
  *SET,NODE_SUM,NODE_SUM+1
  *SET,TMP_AVG_120(II),TMP_AVG_120(II)+TEMP_120
*ENDDO

*DO,KK,58181,58210
  *GET,TEMP_120,NODE,KK,temp
  *SET,NODE_SUM,NODE_SUM+1
  *SET,TMP_AVG_120(II),TMP_AVG_120(II)+TEMP_120
*ENDDO

*DO,KK,443186,443385
  *GET,TEMP_120,NODE,KK,temp
  *SET,NODE_SUM,NODE_SUM+1
  *SET,TMP_AVG_120(II),TMP_AVG_120(II)+TEMP_120
*ENDDO

*SET,TMP_AVG_120(II),TMP_AVG_120(II)/NODE_SUM

*ENDDO
```

VITA

Name: Jose Benjamin Dolores Giron Palomares

Address: Zhejiang University, Zijingang Branch, No. 388 Yuhangtang Road, Room 468, Building A
College of Agriculture and Biotechnology
Hangzhou, Zhejiang 310058 China

Email Address: tiny_ikari@yahoo.com.mx

Education: B.A., Mechanical Engineering, The University of Guanajuato, 2002
M.S., Mechanical Engineering, The University of Guanajuato, 2004
Ph. D., Mechanical Engineering, Texas A&M University, 2012